Numerical Modelling of Inhomogeneous Liquefied Natural Gas (LNG) Vapour Cloud Explosions

Reza Khodadadi Azadboni

Department of Mechanical and Automotive Engineering

Kingston University London

This dissertation is submitted for the degree of

Doctor of Philosophy

April, 2019

Acknowledgements

I would like to express my sincere appreciation to my supervisory team, Professor Jennifer Wen and Dr. Ali Heidari, for their great support during my PhD. Their help and knowledge have been fundamental in order to produce the work presented in this thesis.

I would also like to thank the European Commission for giving me this opportunity to take on such an important research project (SafeLNG project) and for supporting me and Kingston University during these four years.

My sincere thanks, also go to all my colleagues in the SafeLNG project for the helpful discussions on the topic and the pleasant time spent together. Also, I would like to thank Dr. Antoine Hubert, Dr. Marco Macchi, Dr. Konstantinos Lyras, Dr. Dinesh Bhatia, Toby Godwin, George Heinemann and Dr. Ali Rabiee, for offering great bits of help.

I thank my loving family for their continuous support, and for helping me both emotionally and spiritually.

Last but not least, I would like to thank my fiancée Rojin, for helping me with any difficulty and her emotional supports during these years.

Abstract

The main hazard of Liquified Natural Gas (LNG) is the flammable vapour cloud, which can extend to kilometres as a greenhouse gas or be ignited resulting in fire and explosions. This work aims to carry out a safety study on the vapour cloud explosion of LNG. Since most of the experimental research works are available for Hydrogen/Air mixture, in this present work, the first goal is to extend the existing physical understanding of deflagration-to-detonation transition (DDT), in hydrogen/air mixtures with transverse concentration gradients in closed channels. Explosions in homogenous (uniform) reactive mixtures have been widely investigated, both experimentally and numerically. However, in real accident scenarios, mixtures are usually inhomogeneous due to the localised nature of most fuel releases, buoyancy effects and the finite time between release and ignition. It is imperative to determine whether mixture inhomogeneity can increase the explosion hazard beyond what is known for homogeneous mixtures. Hence, extensive knowledge on these processes has been built up over decades for homogeneous mixtures. The approach is to identify similarities and differences caused by concentration gradients compared to homogenous mixtures with equal average hydrogen concentration.

The dynamics of deflagration to detonation transition (DDT), and explosion modelling, have been studied using the newly assembled density-based solvers (VCEFoam) within the frame of OpenFOAM CFD toolbox. In order to evaluate the convective fluxes contribution, Harten–Lax–van Leer–Contact (HLLC) scheme is used for accurate shock capturing. The numerical code is initially verified by four sets of verification test cases. In addition to shock capturing verification, the capability of the current numerical code in capturing the detonation cellular structure has been examined. The CFD results have been compared against both quantitatively and qualitatively with the other previous works as well as an experimental observation.

Then, numerical studies have been conducted to investigate flame acceleration and transition to detonation in both homogeneous and inhomogeneous hydrogen-air mixtures in obstructed and unobstructed channel configurations (in medium scale). The developed VCEFoam solver has been used within OpenFOAM, for these simulations. For the considered experiment (Boeck *et al.*, 2016), different sets of configurations and fuel concentration have been studied. Three different geometry configuration such as BR00 (0% Blockage ratio, smooth channel), BR30

(30 % blockage ratio), and BR60 (60% blockage ratio), have been considered in this study. Also, in order to study the effect of a concentration gradient, different mixture concentrations have been investigated in both homogenous and inhomogeneous mixtures. A total of 17 conditions were simulated for different hydrogen concentrations in both homogeneous and inhomogeneous mixtures with and without obstructions. A high resolution grid is provided by using adaptive mesh refinement (AMR) method, which leads to 30 grid points per half reaction length (HRL). The numerical predictions were compared against previous experiments. Overall, the predicted flame tip velocities, overpressures, and locations of detonation onset are in good reasonably agreement with the measurements.

It is found that, the transverse concentration gradients can either strengthen or weaken flame acceleration, depending on average hydrogen concentration and channel obstruction. The role of hydrodynamic instabilities and the effect of baroclinic torque and Richtmyer Meshkov (RM) instability have also been studied. The results support that RM instability is the primary source of turbulence generation in the present case.

Then vapour cloud explosion study has been carried out for industrial scale scenarios (very large scale). A robust CFD methodology has been presented for modelling very large scale, vapour cloud explosions scenarios. A specific model has been considered for modelling the impact of flame-instabilities, particularly the thermal diffusive instabilities, and Darrieus Landau (DL) instabilities in large-scale models. The numerical model has initially been validated with the largest ever conducted indoor DDT and explosion experiments in the RUT facilities. Good qualitative agreement between the numerical prediction results and experimental measurements of RUT facilities has achieved. After demonstrating the code verification, LNG vapour cloud explosion scenarios, generated from the release of an evaporated liquefied natural gas have been studied. Two different possible incidents in LNG VCE have been studied; explosion modelling in onshore LNG plant and offshore LNG shipping. For the onshore LNG explosion study; an LNG plant has been considered to have fuel leakage from one of its storage tanks. In both onshore and offshore scenarios, the maximum recorded overpressure was below 1.2 bar, which is far below the CJ detonation limit (CJ detonation pressure, for stoichiometric methane/air mixtures, is 16.6 bar). Therefore, in this scenario, LNG flame acceleration was not enough to cause a detonation, and only a flame

deflagration has been noticed. The results of the current study can be used in the context of safety to assess the potential risks of explosions in the energy industry.

Contents

List of Figures

List of Tables

Nomenclature

A	Area / Pre-exponential factor
A_s	Reference Sutherland viscosity
a	Speed of sound
C	cell
Co	Courant number
C_p	Specific heat at constant pressure
c	Progress variable
c	flame front
D	critical diameter for the onset of detonation
D	deformation gradient tensor
D	mass diffusion
D_{CJ}	CJ detonation velocity
E	Energy
E_t	total energy
E_a	Activation energy

e	specific internal energy
F_*	intermediate flux
f	Flame
f	face
G	Wrinkling factor
G_Ξ	generation rate
H	Height
H	Heaviside function
h	Enthalpy
h_s	sensible enthalpy
i	Shock wave
J	Diffusion Flux
j	diffusive heat flux
k	Turbulent kinetic energy
k	index for species
k	Thermal conductivity
k_{RT}	unstable wavenumber
M	Mean molar mass
m	Mach stem
Ma	Mach number

N	Total species
L	length scale
p	Pressure
q	Total energy release per unit mass
$\dot{Q}$	Heat transfer rate
q_j	diffusive flux
R	Specific gas constant
R_u	Universal gas constant
Re_t	Turbulent Reynolds number
R_Ξ	Reduction rate
ri	Reflection of shock wave
S	surface
S_u	Laminar flame speed
S_L	Laminar flame speed
S_h	enthalpy source
s	Obstacle spacing
T	Temperature
T_s	Sutherland temperature
TV	Total variation

t	Time
tr	Trace of a tensor
U	Velocity
u'	rms velocity fluctuations
V	Volume
W	Molar weight
x	Horizontal cartesian coordinate
x_i	Mole fraction
Y	Species mass fraction
y	Vertical Cartesian coordinate
z	Third Cartesian coordinate

Greek symbol

α	thermal conductivity
Δ	turbulent filter size
ε	Dissipation rate
η	Kolmogorov length scale
θ	Wedge angel
λ	detonation cell size
λ_c	cutoff wavelength
υ	Kinematic viscosity

μ	Dynamic viscosity
μ_T	Eddy viscosity parameter
μ_t	Turbulent viscosity
ρ	Density
ρ_u	Unburned gas density
σ	expansion ratio
Ξ	Flame wrinkling factor
Ξ_{Ξ}	Equilibrium flame wrinkling
Ξ_{eq}^{*}	Turbulent flame wrinkling factor
Ξ_{DL}	wrinkling factor due to the DL instability
Σ	Flame surface density
τ	viscous stress tensor
τ	Auto ignition time scale
τ_{ij}	Stress tensor
τ'_{ij}	Reynolds stress tensor
τ_η	Kolmogorov length scale
ϕ	arbitrary quantity
Q^{ϕ}	source term

φ	General variable
Φ	Equivalence ratio
φ	Equivalence ratio
$\dot{\omega}$	rate of formation
ω_{ip}	weighting function
$\Re$	universal gas constant
$J^{\phi,C}$	convection flux
$J^{\phi,D}$	diffusion flux
J^{ϕ}	total flux
R_u	Reynolds number
Le	Lewis number
Sc_t	Turbulent Schmidt number

Subscripts

CJ	Chapman Jouguet
c	cell
def	deflagrative
eff	Effective
eq	Equilibrium
F	Flame
f	Face

H2	Hydrogen molecule
i	species index
ip	integration point
ip(f)	number of integration points along surface f
ign	ignition
k	Specific turbulent kinetic energy
k	Species index
K	Wave index
L	Laminar
L	Left
m	mixture
max	Maximum
min	Minimum
N2	Nitrogen
O2	Oxygen
R	Right
S	Shock
s	Surface-averaged
T	turbulent
u	Unburned

∞	environmental properties

Abbreviations

2D	Two Dimensional
3D	Three Dimensional
AMR	Adaptive Mesh Refinement
BLEVE	boiling liquid expanding vapour explosion
CFD	Computational Fluid Dynamics
CFL	Courant Friedrichs Lewy
CJ	Chapman Jouguet
DDT	Deflagration to Detonation Transition
dev	deviatoric component
DL	Darrieus Landau
DNS	Direct Numerical Simulation
FA	Flame Acceleration
FVM	Finite Volume Method
HLLC	Harten Lax van Leer with Contact
HRL	Half reaction length
KH	Kelvin Helmholtz
LES	Large Eddy Simulation
LNG	Liquified Natural Gas

MILES	Monotone Integrated Large Eddy Simulation
NG	Natural gas
OpenFOAM	Open Field Operation And Manipulation
PISO	Pressure Implicit with Splitting of Operators
RM	Ritchmeyr Meshkov
RT	Ryleigh Taylor
STL	Stereo Lithographic surface
SWACER	Shock Wave Amplification by Coherent Energy Release
TNT	Tri-Nitro-Toluene
tr	Trace of a tensor
TVD	Total Variation Diminishing
URANS	Unsteady Reynolds Averaged Navier Stokes
VCE	Vapour cloud explosion
ZND	Zeldovich von Neumann Döring

Chapter 1 Introduction

1.1 Liquefied natural gas (LNG)

The most common fuel in industry and residential usage is natural gas, which mainly, contains methane (CH4). One of the primary usages of natural gas is heating purposes. Among the concerns about natural gas is the transportation and storage. In order to transport natural gas, usually, it should be cooled and converted to liquid form. The liquefied form is 1/600th of the volume of natural gas in the gaseous form (Speight, 2007).

Liquefied natural gas (LNG) is considered as a clean fuel and an environmentally favourable to other hydrocarbon fuels. LNG industry and technology have a significant improvement in the utilisation of the world's energy resources. The main hazards of handling this fuel is: fire and explosion, cryogenic freeze burns, embrittlement of metals and plastics, and confined spaces hazards (Mokhatab *et al.*, 2014). Some hazard such as rapid phase transition, boiling liquid expanding vapour explosion (BLEVE), and vapour cloud explosions, are only possible under certain special circumstances in LNG transportations (Speight, 2007).

Due to LNG leakage and spills from LNG facilities, fire and explosion hazards can occur. The fuel leakage can usually happen during LNG fuel transportation procedures, which could be during the loading and unloading process. Then, in scenarios without fast ignition, the LNG will vaporise rapidly, spread, and then carry downwind with no injurious effects after diluting below flammable limits (Mokhatab *et al.*, 2014). Although if the LNG fuel ignites through a strong ignition source, then the released LNG fuel presents 4 potential hazards: jet fire, vapour cloud flash fire, pool fire, and vapour cloud explosion (Mokhatab *et al.*, 2014).

The thermal characteristics of vaporised LNG and natural gas are similar. Compared with other hydrocarbon fuels, natural gas has higher ignition energy, and has lower laminar burning velocity. Natural gas vapour in open areas (unconfined spaces), has less possibility to lead to

vapour cloud explosions (VCE), than in a confined area (Foss *et al.*, 2003). Several factors of the LNG vapour cloud to impact the possibility of trigger an explosion, such as: the size and concentration of the vapour cloud, the chemical structure of the vapour molecules, the strength of the ignition source, and the degree of confinement of the vapour cloud (Mokhatab *et al.*, 2014).

illustrates the formation of an LNG pool and vapour cloud for a large-scale spill. The flammability range for vaporised LNG (methane) in the air is relatively narrow, 5% lower flammability limit (LFL) – 15% upper flammability limit (UFL) compared with many other flammable gases, but if ignited the emissive power from methane is higher than for example from propane. Methane is, in contrast to propane, lighter than air and vaporised LNG from small leakages will, therefore, dissipate relatively quickly. For a large LNG spill, the visible white cloud of cold vaporised LNG will, however, initially have neutral buoyancy in the air (Algell, Bakosch and Forsman, 2012).

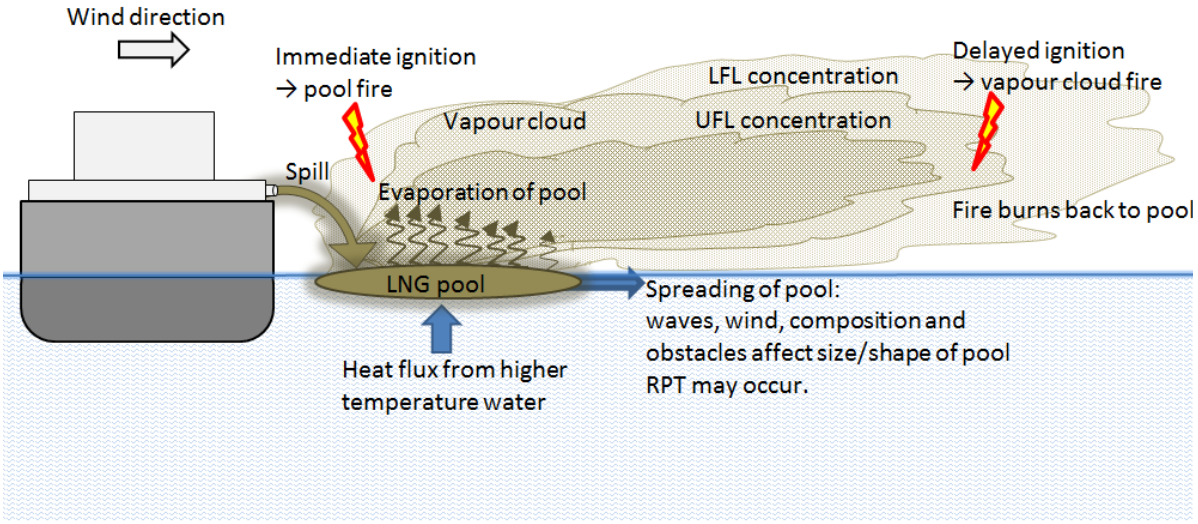

Figure 1-1: Possible outcome of LNG spill over water. Source: (Algell, Bakosch and Forsman, 2012).

1.2 Introduction to Explosion and detonation

Detonation stems from the Latin word “detonare”, which means “to expend thunder”. For a specific condition of fuel and oxidiser combustion phenomenon containing a supersonic flow which leads to a shock wave propagating, we can have detonation.

There are two modes for detonation initiation, which is related to the energy of spark ignitor. The first mode is known as slow mode, and the second one is known as a fast mode. In the slow mode initiation, spark ignition is usually weak, and detonation will occur by flame acceleration. Therefore, slow mode is usually called deflagration to detonation transition (DDT). However, for the fast mode initiation, spark igniter is strong, and so far, detonation will form immediately. In this scenario, a blast wave which can be produced by a strong igniter can initiate detonation. Moreover, in some literature fast mode initiation is called as direct initiation or blast initiation and contrary, slow mode is called as self-initiation. Therefore, there are two important factors for the initiation; transition distance for self-initiation and igniter energy for direct initiation (Lee, 1977).

In gas explosions phenomena, the interaction of flame front with surrounding flow, will result in a positive feedback : flame will accelerate, and it will increase the hydrodynamic instabilities which results to increasing the reaction rate. Figure 1-2 shows a schematic diagram of flame acceleration and transition to detonation processes. The accelerated flame front can either propagates as a deflagration or detonation (Breitung *et al.*, 2000). In order to model DDT phenomena, a numerical model which can take into account the different stages of flame propagation and transition to detonation, need to be considered. In the flame acceleration and deflagrations stage, the transport processes such as diffusion will play an important role. In the turbulent stage, transport of heat and mass, in reaction zone, will play an important role. In detonations stage, shock capturing will be crucial. Shock waves would compress the reactants and they can reach to auto-ignition point (Breitung *et al.*, 2000).

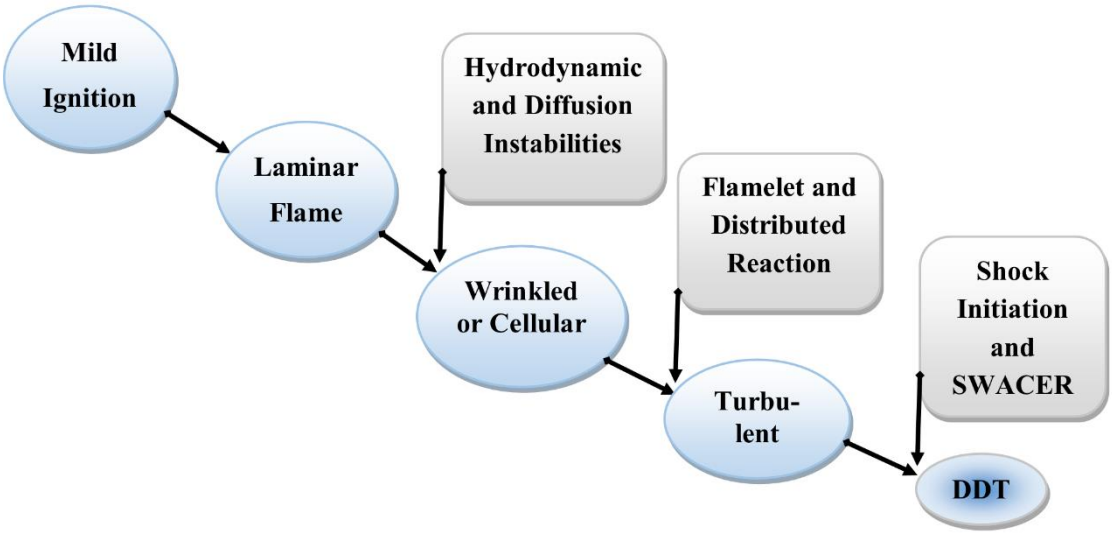

Figure 1-2: Flame acceleration and transition to detonation (DDT) processes, reproduced from (Breitung *et al.*, 2000).

1.3 Motivation and Objective

1.3.1 Aims and Objectives

Explosions in homogeneous reactive mixtures have been widely studied both experimentally and numerically. However, in practice, combustible mixtures are usually inhomogeneous and subject to both vertical and horizontal concentration gradients (Khodadadi Azadboni, Heidari and Wen, 2017a). There is still a very limited understanding of the explosion characteristics in such situations. Significant knowledge gaps exist in the underpinning science.

Research is needed to address the uncertainty associated with the potential built up and ignition of non-homogeneous LNG vapours within the congestion underneath storage tanks and the inventories and overpressures produced. Most LNG tanks are supported by piles which elevate the tank base above the ground. This creates an air gap between the base of the LNG tank and the ground, reducing the heat transfer between the cold tank and the ground (Ohnishi *et al.*, no date). This design eliminates the need for ground heating which consumes a large amount of energy and had been proved to be unreliable in preventing ground movement leading to tank support failure. However, the air gap presents a potential explosion hazard should flammable gas accumulate there. This is especially the case as the tank cannot be 100% leak tight. The explosion of non-homogeneous LNG vapours itself is also an under-researched scientific topic.

1.3.2 Contributions and Novelty

In recent years many studies on fire and explosion in homogenous reactive mixtures have been carried out. However, in practice, usually, the combustible mixtures are inhomogeneous and are subject to a vertical concentration gradient due to gravitational effects. Therefore, the present numerical work aims to study deflagration to detonation transition (DDT) phenomena in inhomogeneous mixtures. The research will focus on the effect of non-uniform gas concentrations on explosion development in clouds of NG/LNG in the air giving particular relevance to under-tank gas accumulation and explosions.

Since most of the experimental research works are available for Hydrogen/Air mixture, so for the first step, DDT phenomena in Hydrogen-Air inhomogeneous mixture will be investigated. Also, in order to study the effect of a concentration gradient, different mixture concentrations have been considered in both homogenous and inhomogeneous mixtures.

This work aims to carry out a safety study on vapour cloud explosion of LNG. Since most of the experimental research works are available for Hydrogen/Air mixture, in this present work, first aims to extend the existing physical understanding of DDT in hydrogen air mixtures with transverse concentration gradients in closed channels. Since extensive knowledge on these processes has been built up over decades for homogeneous mixtures, the approach is to identify similarities and differences caused by concentration gradients compared to homogenous mixtures with equal average hydrogen concentration.

1.3.3 Methodology

This work numerically investigates three different geometry configuration such as: BR00 (0% Blockage ratio, smooth channel), BR30 (30 % blockage ratio), and BR60 (60% blockage ratio), cases that were studied experimentally by (Boeck *et al.*, 2016) (which are in medium laboratory scale). Experimental data is used for model validation, and novel insight is gained from the simulations that could not be obtained from the experiments: continuous histories of pressure and flame location and speed are produced, as well as fields of density and pressure which reveal the mechanisms of flame acceleration and onset of detonation. In order to study the effect of a concentration gradient, different mixture concentrations have been considered in both homogenous and inhomogeneous mixtures. Also, the current numerical approach for the medium scale scenario, will aim to capture small scale features (e.g. hydrodynamic instabilities) which have influence in DDT.

Addition to the above-mentioned study, in the present work, vapour cloud explosion in industrial scale will be investigated. A robust numerical methodology for DDT and explosion modelling in large scale will develop. The numerical model for very large-scale scenarios, aims to capture the correct overpressure and location of transition to detonation. After validating the numerical code with a largest ever experiment in DDT and detonation (which are available for

hydrogen/air mixtures), LNG vapour cloud explosion modelling will be studied. Two different scenarios: onshore LNG explosion and offshore LNG explosion will be studied. And these studies aim to investigate the LNG flame acceleration and prediction of maximum overpressure for safety purposes.

1.4 Thesis Organisation

This thesis begins with presenting some of the introduction background on explosions and detonation in Chapter one. Also, this chapter includes objectives and an outline of the research methodology.

Chapter two provides a brief literature review of previous related works on gas explosions. This chapter includes review of DDT in different geometry configurations (obstructed and smooth channel), as well as DDT in mixtures with concentration gradients.

Chapter 3 provides the governing Equations and numerical schemes and discretisation methods. This chappter ends with presenting the numerical methodology developed in this work.

Chapter 4 presents verification of the developed numerical code. In this chapter different verification test cases will be used to approve the accuracy of the developed numerical model.

Results and their discussion are divided into two different chapters: DDT in inhomogeneous mixture with a medium scale test case has analysed in Chapter 5. This chapter presents the flame acceleration procedures and the onset of detonation in mixtures with concentration gradients.

DDT in very large-scale (industrial sales) scenarios is discussed separately in Chapter 6. In this chapter vapour cloud explosion of hydrogen and LNG will be studied.

This research work ends with a conclusion remarks and future works in chapter 7.

Chapter 2 Literature Review

2.1 Detonation

Mallard and Le Chatelier (1881), and Berthelot and Vielle (1882) have done the earliest observations of detonations waves. They have measured the detonation speed in hydrogen and some other hydrocarbon fuels. Mallard and Le Chatelier observed a deflagration to detonation transition by using a drum camera (Mallard and Le Chatelier, 1881).

Rankine (1870) and Hugoniot (1887) have developed the theoretical physics and explanation of detonation. Their studies defined the thermophysical changes such as pressure, velocity, temperature and density, through a shock wave by using the conservation equations in a stationary wave (Gaathaug, 2015).

Chapman (1899) demonstrated the minimum required detonation speed. Jouguet (1905) examined the entropy variation through the Hugoniot curve and same as what Chapman reported, and he stated that the minimum detonation velocity. As it has demonstrated in Lee (2008), the Chapman-Jouguet (CJ) point is where the Rayleigh line matches the Hugoniot curve, and also the slope of tangents is also equal to each other. More comprehensive details on CJ theories can be found in (Fickett and Davis, 2000; Lee, 2008; Law, 2010; Toro, 2013). In Figure 2-1**Error! Reference source not found.**, detonation pressure ratio, based on CJ theory, has been calculated by STANJAN software (Reynolds, 1986). Figure 2-1**Error! Reference source not found.** shows that the CJ detonation pressure ratio, varies by fuel equivalence ratio, for hydrogen-air and methane-air mixtures. The maximum calculated CJ pressure ratio is 15.6, for stochiometric hydrogen/air mixture (29.9 % hydrogen concentration).

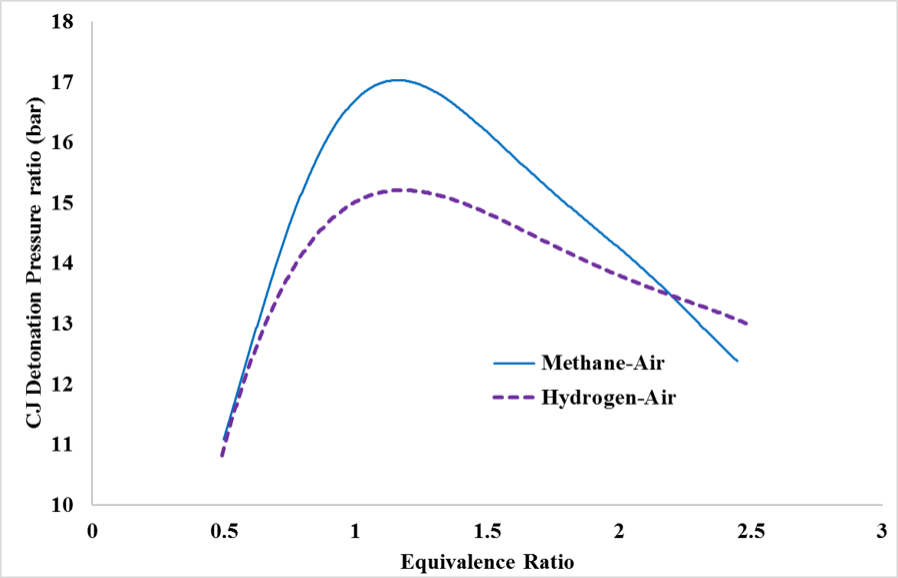

Figure 2-1: Detonation pressure ratio, based on CJ theory, has been calculated by STANJAN.

Later Zeldovich (1950), Von Neumann (1942) and Döring (1943) added more details progress on the CJ theory of detonations. The one-dimensional ZND (Zeldovich Neumann Döring) theory, takes into account the chemical reaction time and length associated with a shock wave propagating in front of the reaction zone. In ZND theory, the leading shock wave is usually followed by an induction zone.

Lee (2008) demonstrated a theory for computing the ZND detonation structure, based on the initial detonation velocity computed from CJ theory, for a certain ratio of specific heats and energy. Rankine-Hugoniot relations determine the condition behind a shock wave. The conservation of momentum, mass, and energy equation with a single step chemical reaction is combined between the shock and the CJ condition. A diagram of the ZND detonation structure is shown in Figure 2-2**Error! Reference source not found.**.

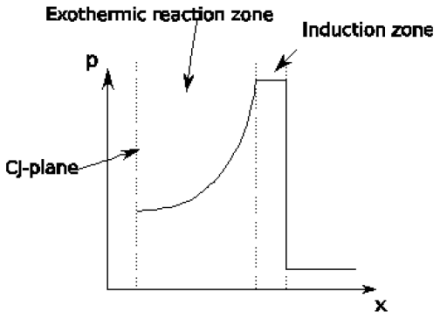

Figure 2-2– Schematic diagram of the ZND detonation structure (Vågsæther, 2010).

In Detonation front, due to the rapid energy release, the reaction zone is subsonic in the frame of the shock and supersonic concerning the undisturbed gas. Interaction of the incident shock and transverse waves generates Mach stems and triple points. Usually, there is a huge energy release on the triple points of detonation structure, and as a result, new shock waves can be generated from the triple points dynamically. The trajectory of the triple points will generate a cellular structure pattern. Shock wave interaction can increase the pressure on Mach stems. Eventually, the triple points trajectory forms the characteristic fish-like shape which indicates "detonation cells".

In a detonation front, a characteristic length λ defines the size of the detonation cell (λ is shown in Figure 2-3). Distribution of triple points depends on some factors such as geometry configuration, the initial condition and the reactivity of mixture. Having more triple-nodes can make the detonation front more unstable, and as a result, the length scale λ will be smaller.

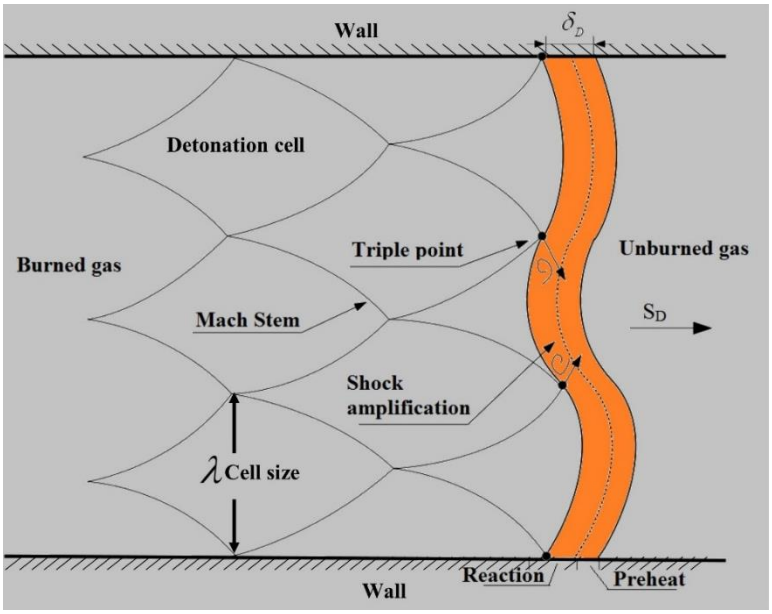

Figure 2-3: Schematic of the premixed SWACER mechanism and detonation cell structure. Reproduced from (Yu, 2015).

SWACER (Shock wave amplification by coherent energy release) mechanism which was proposed by Lee et al. (2008) is based on the Zeldovich mechanism. The schematic diagram of the SWACER mechanism is shown in Figure 2-3. The SWACER mechanism proposes that in a planar detonation front, the shock propagation and the chemical reaction are developing at the same time. However, on the unstable detonation front, the chemical reaction rate is not uniform, and it will increase by the shock triple point interactions.

One of the first physical descriptions of detonation initiation mechanism, in the presence of spatial distribution of induction period of self-ignition has formulated based on SWACER mechanism. The SWACER mechanism repersents a means of generating very strong waves locally in a reacting medium without the use of any external concentrated energy source. Therefore, the SWACER mechanism is not limited to photochemical initiation, and in fact it plays the main role in the transition of deflagration to detonation as well. Hence, in the deflagration stage, the physical processes can be thought of as the agents accountable for preparing the necessary conditions for the SWACER mechanism.

2.2 Hydrogen/Air half reaction length

Different values for half reaction length (HRL) are reported in the literature. This depends on the reaction mechanism and the initial condition of that reaction as well. Gamezo, Ogawa and Oran, (2007), reported half reaction length of hydrogen-air mixture is 0.1927 mm, however, Kumar et al. (Kumar *et al.*, 2015), showed that half-reaction length of hydrogen-air reaction is different for different reaction mechanism and in their study with changing the initial temperature that varied from 0.02 mm to 0.1 mm. Moreover, as shown by Stamps, Benedick and Tieszen, (1991), the HRL changes considerably with the mixture equivalence ratio. In the present study, the average volumetric hydrogen concentration is 30% which is close to the stoichiometric value with HRL 0.3 mm. However, with the presence of the concentration gradients, the actual equivalence ratio varies from 0.338 to 1.69, across the channel height. According to Figure 2-4, the HRL varies between 0.3 mm (stoichiometric mixture) and 0.39 mm (rich mixture) (Khodadadi Azadboni *et al.*, 2017).

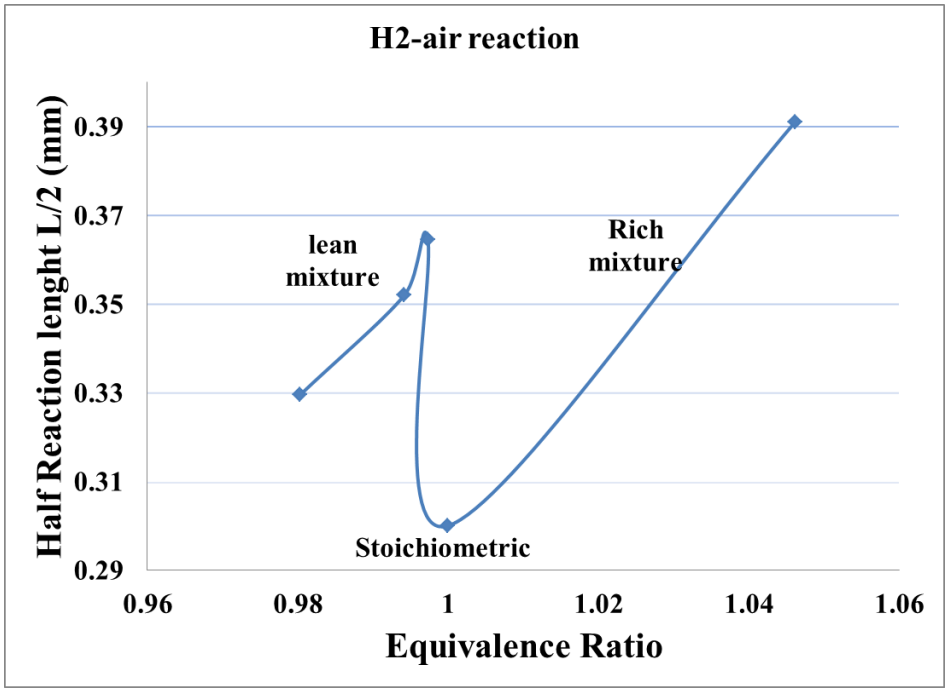

Figure 2-4: The half reaction length of hydrogen-air flame verse equivalence ratio (Reproduced from (Stamps, Benedick and Tieszen, 1991)).

2.3 Deflagration to Detonation Transition (DDT)

A comprehensive literature on various types of DDT has been reported by Thomas (2012), where he explained difference between macroscopic and microscopic DDT terminology.

The macroscopic terminology is a large-scale DDT which includes the procedure of flame acceleration (deflagration), and up to the transition of deflagration to detonation stage. The microscopic terminology, is a small-scale DDT, which it directs the onset of detonation, where the combustion procedure varies from a state which is controlled by diffusion to a condition where shock heating is playing a role (Khodadadi et al., 2017a). In this research study, the term DDT, is used in the wider content which includes both flame acceleration (deflagration), and onset of detonation. Also, Thomas (2012) stated that in a weak DDT process, detonation does not trigger through a strong reflected shock wave. Although he mentioned the importance of non-isotropic and non-equilibrium turbulence features, under flame acceleration and hot spots generations. This will create transverse waves which can be coupled with strong pressure waves, and can lead to formation of a shock/reaction complex which is known as a detonation front (Thomas, 2012; Khodadadi et al., 2017a).

2.3.1 DDT in unobstructed pipes/channels

Gas explosions inside tubes (or pipes) have been studied in the past. Most of these studies were carried out for industrial safety purposes and to describe the general mechanisms of flame propagation (Khodadadi *et al.*, 2016a). The majority of the works carried out for understanding the phenomena related to flame acceleration (FA) and DDT in tubes (Kristoffersen, 2004).

In the industry, there are a lot of hazardous combustible materials in pipelines and equipment. The combustible mixtures denote a possible risk when a probable ignition source is present or when the pressure or temperature in the tubes rises above the self-ignition situations (Kristoffersen, 2004; Khodadadi et al., 2018).

The study of transition from deflagration to detonation in smooth pipes, usually includes flame acceleration in confined area like circular/rectangular pipes without any obstruction. One of the earliest study in flame acceleration and DDT in smooth pipes carried out by Urtiew and Oppenheim (1966). They used a laser illumination with an ultra-fast camera technique to capture shock and flame fronts. They showed that DDT can happen either at the vicinity of turbulent flame front, (which is usually behind a leading shock wave) or at the shock contact surface (while two shock waves merged). They also noted that there are many possible causes to the DDT and not only one single macroscopic phenomenon is responsible for it. "An explosion within explosion" is a term named by Oppenheim (Urtiew and Oppenheim, 1966) which describes the phenomena which leads to the onset of detonation. In the “explosion within the explosion” desorption, reactant burns very fast in compared with the rest of the combustion process. Also, it is known as constant volume combustion, local explosion or hot spot. The “explosion within the explosion” could lead to a locally high-pressure region and pressure waves propagating into the system. Also, these local explosions are strong enough to trigger DDT by shock compression and heating. The experimental observation done by Meyer, Urtiew and Oppenheim, (1970) indicates that an explosion within the explosion can occur far behind the leading edge of the flame front. They have shown that a sequence of two local explosions can lead to a DDT. The first explosion decomposed to a shock wave as it turns to be isolated through the combustion products. The next explosion turns on to the onset of detonation. Additionally, Meyer et al. (Meyer, Urtiew and Oppenheim, 1970), demonstrated that the pure gas dynamic compression heating triggered by the shock waves developing in front of the accelerated flame, was not strong enough to ignite the reactants behind the shock waves. Figure 2-5 shows the schlieren records of the transition to detonation with onset between flame and shock from the experimental observation done by Meyer et al. (Meyer, Urtiew and Oppenheim, 1970).

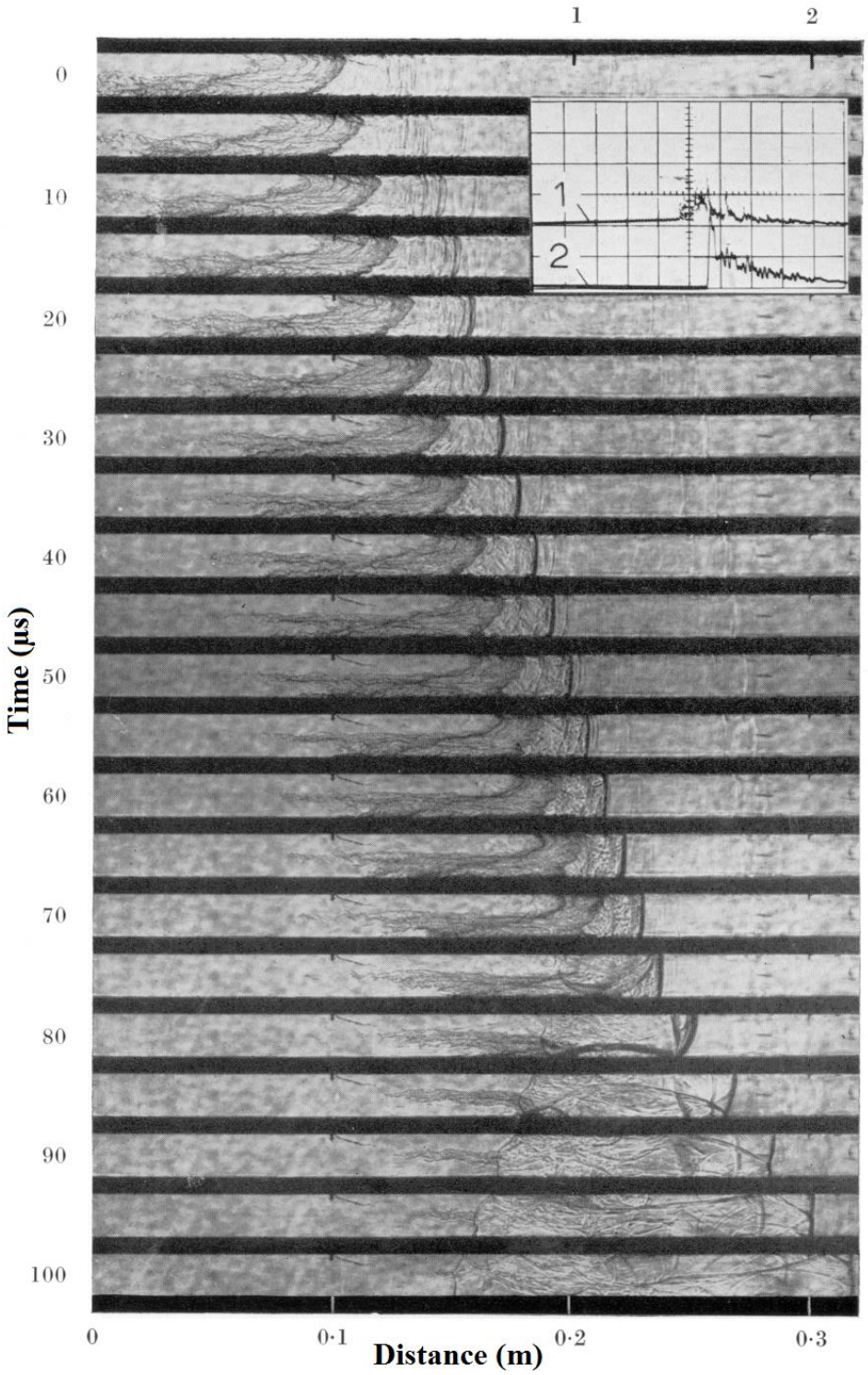

Figure 2-5: Schlieren records of the transition to detonation with onset between flame and shock Meyer et al. (Meyer, Urtiew and Oppenheim, 1970).

Peraldi et al. (1988) showed that for onset of detonation the tube diameter criteria should be at least equivalent to the detonation cell size. Later, Lindstedt and Michels (1989) demonstrated that for a circular pipe, the critical diameter for the onset of detonation is $D > \lambda/\pi$ (where λ is the detonation cell size). A comprehensive discussion on the critical diameter of a tube for onset of detonation and other characteristics of detonation conditions is described by Ciccarelli and Dorofeev (2008). Chao (2006) studied the DDT phenomena in a smooth channel, and he stated that due to hot spot generation downstream of the flame front, and local explosion generation will trigger the one set of detonation (Gaathaug, 2015).

Usually, for the onset of detonations a flame speed increases and generally it reaches a supersonic speed (Urtiew and Oppenheim, 1966; Lee, Knystautas and Chan, 1985; Peraldi, Knystautas and Lee, 1988; Dorofeev *et al.*, 2001; Kuznetsov *et al.*, 2005). The procedure of flame acceleration can significantly be affected by obstructions along the flame propagation (Lee, Knystautas and Chan, 1985; Peraldi, Knystautas and Lee, 1988; Dorofeev *et al.*, 2001). In smooth channels/pipes, different physical mechanisms are excepted to play a role. Shchelkin (1947) and Soloukhin (1961) have showed that the flame acceleration and transition to detonation in smooth channels are strongly affected by flame wall interactions and channel/tube wall roughness. They reported that flame acceleration would be promoted by turbulent boundary layer generation downstream of the flame front. Furthermore, during flame propagation in a smooth tube, the flame shape usually turns into a characteristic “tulip” shape with a leading edge close to the tube walls. Soloukhin (Soloukhin, 1961)also, stated that the local explosion, which lastly results in the onset of detonation, occurs close to the tube wall in the vicinity of flame wall interactions.

2.3.2 DDT in obstructed pipes/channels

DDT in obstructed pipes (or channels) is one of the most broadly studied geometry configurations, in the DDT literatures. Many studies have been carried out to examine flame acceleration (deflagrations), and DDT in obstructed channels. Comprehensive literature on these studies is available in Moen and Lee, (1980), Lee, Knystautas and Chan, (1985) and

Teodorczyk, Lee and Knystautas, (1989, 1991), Teodorczyk, (2008). Frolov (2012) reported that the Shchelkin spiral method is a well-known technique for accelerating a deflagration up to a detonation point. The Shchelkin spiral is a device that supports the transition from deflagration (in subsonic combustion regime) to detonation in a pulse detonation engine. Teodorczyk et al. (Teodorczyk, Lee and Knystautas, 1989) investigated the quasi-detonation phenomena, when detonation velocities as low as 40% of the normal Chapman-Jouguet (CJ) detonation velocity. As it has demonstrated in (Lee, 2008), the Chapman-Jouguet (CJ) point is where the Rayleigh line matches the Hugoniot curve, and also the slope of tangents is also equal to each other. Their experimental observation showed that in an obstructed channel, the obstruction could cause a detonation failure via diffraction and also shock reflections from the top and bottom walls can cause re-initiation. Chan (1995) observed that the reflecting shock waves from obstacles could lead to detonation initiation; and suggested that a local explosion is not enough to trigger an onset of detonation. Gamezo, Ogawa and Oran (2007) have carried out a numerical study on the DDT experiment done by Teodorczyk (2008) in obstructed channels. Vågsæther (2010) also studied this geometry configuration for stoichiometric hydrogen/air mixture and his description of the DDT process is presented in Figure 2-6. Figure 2-6 shows that the accelerated flame (deflagration) has been accelerated enough to generate a shock wave in front of the flame front. The flame is marked with “f”, and the shock wave is “i”. Mach stem is shown by “m”, and the reflection of the shock wave “i” at the obstacle is shown by “ri”. The Mach stem and reflection shock can lead to a shock flame interaction and a high-pressure region at the bottom of the obstacle (f2). Thus, a shock wave “b” will propagate from this local explosion. The diffraction of “b” around the obstacle is marked by “bd”, and the reflection at the top wall is shown as “rb”. The Mach stem at the top wall is shown by “mrb”. Moreover, when “rb” and “mrb” catch up with “f”, it will lead to DDT. Vågsæther (2010) reported that the reaction wave propagates with a velocity among 800m/s to 2100m/s, relative to the laboratory frame. For a stoichiometric mixture of hydrogen/air, the CJ detonation velocity is 1976m/s (this is calculated by using the Cantera software along with shock and detonation toolbox) (*Explosion Dynamics Laboratory*).

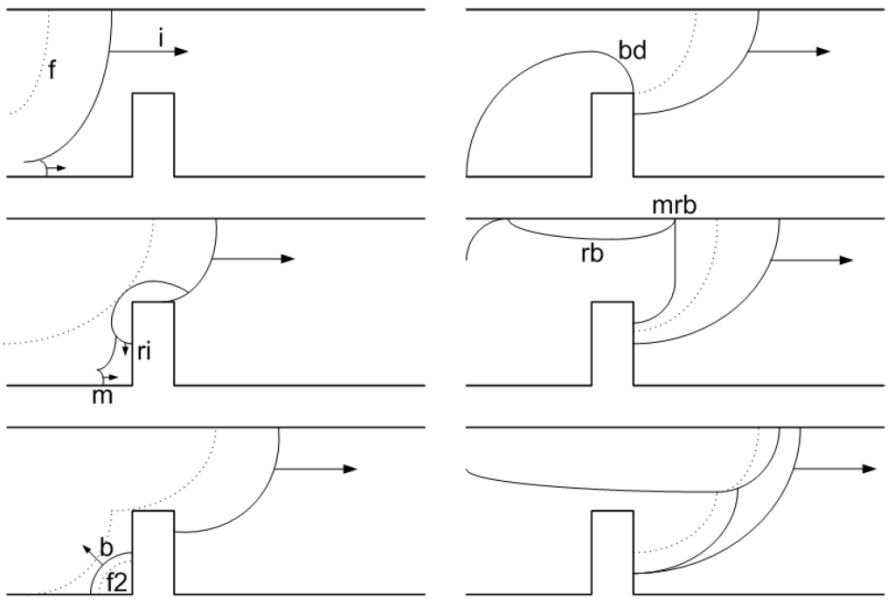

Figure 2-6: Explanation of DDT in obstructed channels (Vågsæther, 2010).; i) incident shock wave, b) shock wave generated from local explosion, bd) diffraction around the obstacle, rb) reflection at the top wall, ri) reflection of the shock wave "i" at the obstacle, mrb) Mach stem at the top wall.

Dorofeev et al. (2000) investigated the effect of scale on the onset of detonation. They compared different large-scale and laboratory-scale experiments (Lee, Knystautas and Chan, 1985; Sherman, Tieszen and Benedick, 1989; Teodorczyk, Lee and Knystautas, 1989; Chan and Dewit, 1996; Ciccarelli and Boccio, 1998; Kuznetsov, Alekseev and Dorofeev, 2000) and reported an experimental correlation for the critical detonation onset condition. The comparison of large amounts of experimental results leads to the correlation of $L \approx 7\lambda$ (Gaathaug, 2015). L is the length scale which is assumed to be the average of lengths in a room; however, for an obstructed channel, it is given by a series of compartments. Figure 2-7 shows the schematic view of an obstructed channel, in which the obstacle spacing is marked with S and the channel height is shown by H. The report by Dorofeev *et al.*, (2000) showed that the length scale criterion is necessary, but not enough criterion to trigger detonation in an obstructed channel. Flame acceleration and reactivity gradients generation must also be present. They also calculated the detonation cell sizes based on the works done by (Gavrikov, Efimenko and Dorofeev, 2000).

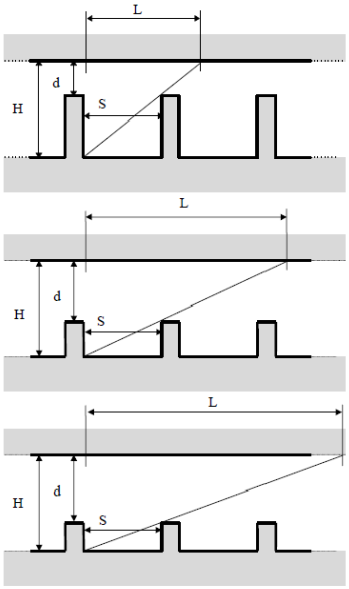

Figure 2-7: Schematic diagram for describing the effect of length scale on the onset of detonation by (Dorofeev *et al.*, 2000).

2.3.3 DDT in inhomogeneous mixtures

While DDT in homogeneous mixtures has been widely investigated (Ciccarelli and Dorofeev, 2008), fewer studies have addressed the effect of spatial gradients in mixture composition. Grune *et al.*, (2013) conducted large-scale experiments of flame acceleration (FA) and DDT in an obstructed semi-confined flat layer of a hydrogen-air mixture with transverse (vertical) concentration gradients (Khodadadi Azadboni *et al.*, 2019). The authors found that DDT propensity is increased by mixture inhomogeneity for globally lean mixtures, and may be correlated with the maximum local hydrogen concentration within the layer. Vollmer, Ettner and Sattelmayer, (2012) and Boeck, Hasslberger and Sattelmayer, (2014); Boeck, (2015); L. R. Boeck *et al.*, (2016) reported a strong effect of concentration gradients on FA and DDT phenomena in an entirely closed channel at laboratory-scale (Khodadadi Azadboni, Heidari and Wen, 2017a). Boeck et al. (Boeck *et al.*, 2016) observed that in a channel with obstructions, concentration gradients promoted FA and DDT only in globally lean mixtures with an average hydrogen concentration below about 24%; for richer mixtures, the presence of gradients led to

weaker FA and delayed DDT. The authors proposed that a mixture-averaged flame speed parameter (σS_L) may predict this effect, taking into account the integral rate of combustion and expansion which drives flame acceleration in a closed channel. By contrast, for unobstructed channels, gradients always led to stronger FA and earlier DDT, independent of the average hydrogen concentration; this was attributed to flame surface area enlargement driven by concentration gradients (Khodadadi Azadboni *et al.*, 2019).

The present work purposes at extending the existing physical understanding of DDT in hydrogen/air mixtures with transverse concentration gradients in closed channels. Since extensive knowledge on these processes has been built up over decades for homogeneous mixtures, the approach is to identify similarities and differences caused by concentration gradients compared to homogenous mixtures with equal average hydrogen concentration. Apart from this fact that hydrogen is one of most volatile fuel, and due to the high reactivity nature of hydrogen, this fuel has been considered as a worst-case scenario, most of the experimental research works are available for Hydrogen/Air mixture, and there is no available DDT experiment for inhomogeneous mixture of LNG/Air. Hence, for the first step, DDT phenomena in Hydrogen-Air inhomogeneous mixture will be investigated. This work numerically investigates seventeen cases that were studied experimentally by (Boeck *et al.*, 2016). Experimental data is used for model validation, and novel insight is gained from the simulations that could not be obtained from the experiments: continuous histories of pressure and flame location and speed are produced, as well as fields of density and pressure which reveal the mechanisms of flame acceleration and onset of detonation (Khodadadi Azadboni *et al.*, 2019).

2.4 Summary

In this chapter a comprehensive literature review on detonation and DDT phenomena has been presented. The earliest observations of detonations waves have been carried out by Mallard and Le Chatelier (1881), and Berthelot and Vielle (1882). They have measured the detonation speed in hydrogen and some other hydrocarbon fuels. The theoretical physics and explanation of detonation have developed by Rankine (1870) and Hugoniot (1887). Then, Chapman (1899)

demonstrated the minimum required detonation speed and Jouguet (1905) examined the entropy variation through the Hugoniot curve and same as what Chapman reported, and he stated that the minimum detonation velocity. Therefore, the Chapman-Jouguet (CJ) point for detonation pressure ratio, and detonation velocity (DCJ) are one of the important criteria in detonation. Later, another one-dimensional detonation theory has been developed by Zeldovich (1950), Von Neumann (1942) and Döring (1943) which is known as ZND theory. The ZND detonation theory, has added more details progress on the CJ theory of detonations.

Although most of the detonation and explosions scenarios in industry are deflagrations, a worst-case scenario can emerge if transition from deflagration to detonation occurs during an explosion. Deflagrations which generates from flame acceleration, require congestion and confinement to generate significant overpressures; by contrast, detonations inherently produce high overpressure and have the potential to propagate across large unobstructed and unconfined distances without substantial weakening. Thomas (2012) gave a comprehensive discussion on various mechanisms of deflagration-to-detonation transition (DDT) and differentiated the terminology between global DDT and local DDT. Global DDT includes both flame acceleration (FA) and the onset of detonation. Local DDT refers to the actual onset of detonation at the location where the combustion mechanism changes from diffusion-controlled to auto-ignition controlled. In this work, the term DDT is used in the global sense and includes both FA and the onset of detonation.

While DDT in homogeneous mixtures has been widely investigated (Ciccarelli and Dorofeev, 2008), fewer studies have addressed the effect of spatial gradients in mixture composition. Vollmer, Ettner and Sattelmayer, (2012); Grune et al., (2013); Boeck, Hasslberger and Boeck, (2015); Boeck et al., (2016), have conducted laboratory-scale experiments of flame acceleration (FA) and DDT in an obstructed semi-confined flat layer of a hydrogen-air mixture with transverse (vertical) concentration gradients. Boeck et al. (Boeck *et al.*, 2016) observed that in a channel with obstructions, concentration gradients promoted FA and DDT only in globally lean mixtures (hydrogen concentration below 24%), and for richer mixtures, the presence of gradients led to weaker FA and delayed DDT. The present work purposes at

extending the existing physical understanding of DDT in mixtures with transverse concentration gradients (inhomogeneous mixtures) in closed channels. Since most of the experimental research works are available for Hydrogen/Air mixture, and there is no available DDT experiment for inhomogeneous mixture of LNG/Air, therefore, in this research DDT phenomena in Hydrogen-Air inhomogeneous mixture will be investigated.

Chapter 3 Governing equations and Numerical schemes

3.1 Introduction

The present numerical study aims to investigate the dynamics of Deflagration to Detonation Transition (DDT) and vapour cloud explosion phenomena in inhomogeneous and homogeneous mixtures such as Hydrogen/Air and LNG/Air for medium and large-scale cases. Modelling discontinuities, such as shocks and contact surfaces, in high-speed compressible flows require numerical schemes that can predict and capture these features while avoiding spurious oscillations. The DDT phenomena have two major stages; flame acceleration (FA), during which the flow is in the subsonic regime, and the transition-to-detonation stage, in which the combustion wave undergoes a transition to the supersonic state.

3.2 Governing equations

The standard governing equations for solving the flow field in a Eulerian framework are listed below (Greenshields *et al.*, 2010):

Mass conservation:

$$\frac{\partial \rho}{\partial t} + \nabla .(\rho U) = 0 \tag{3.1}$$

Conservation of momentum (neglecting body forces):

$$\frac{\partial(\rho u)}{\partial t}+\nabla\bullet\left[u(\rho u)\right]+\nabla p+\nabla\bullet\tau=0 \tag{3.2}$$

Conservation of total energy:

$$\frac{\partial(\rho E)}{\partial t}+\nabla\bullet\left[u(\rho E)\right]+\nabla\bullet\left[up\right]+\nabla\bullet\left(\tau\bullet u\right)+\nabla\bullet\, j=0 \tag{3.3}$$

Where ρ is density, U is velocity and p is pressure. In Eq. 3.2, τ is the viscous stress tensor, which can be defined using equation 4.5 (Greenshields *et al.*, 2010). The energy equation can also be written in the sensible enthalpy equation format (Eq. 3.4) (Greenshields *et al.*, 2010; Khodadadi, Heidari and Wen, 2018; Khodadadi, Wen and Heidari, 2019):

$$\frac{\partial(\rho h_s)}{\partial t}+\nabla\bullet\left[u\left(\rho h_s\right)\right]-\nabla\bullet\left[\alpha\nabla h_s+\sum_{i=1}^{n}h_i J_i\right]-\nabla\bullet\left(\tau\bullet u\right)=\frac{\partial p}{\partial t}+S_h \tag{3.4}$$

where, u, P, h_s, T, S_h are the gas density, velocity, pressure, sensible enthalpy, temperature and enthalpy source respectively. α is defined as ($\alpha=k/c_p$), where k is the thermal conductivity and c_p is the specific heat at constant pressure.

$$\tau=-2\mu\, dev(D) \tag{3.5}$$

Where, in Eq. 3.5, dev stands for the deviatoric component, μ is the dynamic viscosity (which can be calculated from Sutherland's equation (Eq.4.6) (White and Corfield, 2006)), D is the deformation gradient tensor, which is defined by Eq. 3.7.

$$\mu=A_S\frac{T^{1.5}}{T+T_S} \tag{3.6}$$

$$D\equiv\frac{1}{2}\left[\nabla u+\left(\nabla u\right)^{\tau}\right] \tag{3.7}$$

In Eq. 3.6, A_S and T_S are constant values, which are dependent on the molecular transport properties of species.

Any second rank tensor (3×3 tensor matrix with 9 component) can be written as a combination of its deviatoric and hydrostatic components:

$$D = \underbrace{D - (\frac{1}{3})tr(D)I}_{deviatoric} + \underbrace{(\frac{1}{3})tr(D)I}_{hydrostatic} = dev(D) + hyd(D) \tag{3.8}$$

where, I is the unit tensor, and "tr" refers to the "Trace" of a tensor. The trace of a tensor *D* is a scalar, calculated by summing the diagonal components (Eq. 3.9):

$$tr\ (D)\ =\ D_{11}\ +\ D_{22}\ +\ D_{33} \tag{3.9}$$

In Eq. 3.8, dev stands for the deviatoric component (Greenshields *et al.*, 2010), and referring to Eq. 3.8, this deviatoric component will be:

$$dev(D) \equiv D - (\frac{1}{3})tr(D)I. \tag{3.10}$$

In Eq. 4.3, j is the diffusive heat flux (Eq. 3.11), and E_t is the total energy density (Eq. 3.12) which can be defined as (Poinsot and Veynante, 2005):

$$\mathbf{j} = -k\nabla T \tag{3.11}$$

$$E_t = e + |u|^2 / 2 \tag{3.12}$$

Where *T* is temperature and k is conductivity factor in Eq. 3.11 and *e* is the specific internal energy, and u is velocity in Eq. 3.12.

Therefore, the viscous stress tensor, τ, can be rewritten in vector form and is defined by the following:

$$\tau \equiv \mu(\nabla u + (\nabla u)^{\tau} - \tfrac{2}{3}(\nabla \bullet uI)) \tag{3.13}$$

The energy conservation equation can be rewritten in the following format:

$$\frac{\partial(\rho E_t)}{\partial t} + \frac{\partial}{\partial x_j}((\rho E_t + p)u_j) + \frac{\partial q_j}{\partial x_j} - \frac{\partial}{\partial x_j}(\tau_{ij} u_i) = 0 \tag{3.14}$$

In Eq. 3.14, q_j is the diffusive flux, which can be decomposed into two parts; the enthalpy flux because of species diffusion, and the heat flux due to heat conduction (Hirschfelder *et al.*, 1964). By utilising Fourier's law;

$$q_j = \underbrace{-\lambda \frac{\partial T}{\partial x_j}}_{heat\ flux} + \underbrace{\rho \sum_{k=1}^{N} h_k j_{k,j}}_{enthalpy\ flux} \tag{3.15}$$

where, k is an index for species. The species diffusion $j_{k,j}$ can be rewritten using Fick's law (Kee, Coltrin and Glarborg, 2003):

$$j_{k,j} = -D_k \frac{\partial Y_k}{\partial x_j}. \tag{3.16}$$

where, y_k is the mass fraction of species k, and D_k is the mass diffusivity of species k. However, the diffusive flux of species in the above equation, follows the Fick's law (Kee, Coltrin and Glarborg, 2003), but the individual species diffusivities D are not considered in this approach.

Finally, the energy transport equation can be written as the following:

$$\underbrace{\frac{\partial}{\partial t}(\rho Y_k)}_{\text{unsteady term}} + \underbrace{\frac{\partial}{\partial x_j}(\rho u_j Y_k)}_{\text{convection term}} - \underbrace{\frac{\partial}{\partial x_j}\left[\rho\left(D_k \frac{\partial Y_k}{\partial x_j}\right)\right]}_{\text{diffusion term}} = \underset{\substack{\text{source term:}\\ \text{production rate}}}{\dot{\omega}_k} \tag{3.17}$$

where, $\dot{\omega}_k$ is the rate of formation of species k in a chemical reaction.

The equation of state is required to close the above set of system of equations. In gas explosion, which is within extreme high pressure conditions, the validity of ideal gas assumption, can be questioned. However, for gaseous detonation, the pressure range is low enough to keep the ideal gas assumption valid and hence adopted in the present study. And also, since the flow is not about to change to the condensed phase, this assumption is valid.

$$p = \rho RT \tag{3.18}$$

In Eq. 3.17 R represents the specific gas constant of the mixture, p is pressure, ρ is density, and T is temperature.

In a mixture with N species, only N-1 transport equations need to be solved, the remaining species' mass fraction results from the condition in which all mass fractions must sum to unity:

$$y_N = 1 - \sum_{k=1}^{N-1} y_k. \tag{3.19}$$

Also, it should metion that Newtonian fluid assumption is used for modelling the viscous terms in the equations. In a Newtonian flow, the shear forces have a linear dependent on the velocity gradient and the dynamic and bulk viscosity of the fluid.

3.3 Numerical schemes and Discretisation

Computational Fluid Dynamics (CFD) is a numerical approach, used to solve the fluid governing equations, i.e. mass, momentum and energy. In CFD the highly non-linear PDEs can be solved through an iterative procedure. CFD modelling has been widely used, and is acceptable as a valid engineering approach in the industry as well as academia. The governing equations include the Navier-Stokes equations, in which there are a set of partial differential equations that cannot be solved using analytical methods (Versteeg and Malalasekera, 2007).

Nevertheless, through CFD, an approximate solution can be attained using a discretisation method that linearises the partial differential equations and replaces them with a set of algebraic equations. The solution of the linearized governing equations predicts the solution of the original governing equations at some pre-determined locations (grid points) and times (time steps) inside the computational domain. There are many different discretisation techniques in fluid dynamic problems; the two most common one can be classified as the finite difference method and the finite volume method.

In the finite difference method, the partial differential equations will be linearized by using a truncated Taylor series expansion. One of the primary advantages of the finite difference method is that high order schemes can be applied easily. However, this method is limited to structured grids, so it cannot be used for complex geometries. Conservation laws are also not necessarily guaranteed to be conserved by this numerical scheme.

The finite volume method (FVM) is a discretisation method for partial differential equations. In the FVM, the computational domain is divided into non-overlapping control volumes (CV), and a volume integral formulation is applied in a computational domain, to discretise the PDEs.

The mesh for the solution domain only defines the boundary of each control volume, which can either be a face (i.e. it is shared with a neighbouring control volume) or the boundary of the domain itself.

Nowadays, the FVM is one of the most common methods for discretising computational fluid dynamics problems.

In the FVM the computational node is defined as the cell centre of each control volume. Therefore, values can be determined at the centroid of each computational cell, and the quantities can also be interpolated from two adjacent cells. The FVM complies with the conservation of the quantities, because in this method, the integral of quantities on the common faces between two neighbouring cells are similar. In the FVM, the computational mesh does not have to be aligned with any coordinate system; hence this method is appropriate for both structured and unstructured meshes. This method can, therefore, be simply implemented on

complex geometries. However, constructing high order schemes (higher than second order) is challenging in the FVM (Ferziger and Peric, 2012). Due to the advantages of the FVM discretisation, in the current study, the finite volume method will be used.

3.3.1 Finite volume discretisation

The discretisation procedures include two main steps: discretising the governing equations to derive a set of linearised algebraic equations, and discretising the computational domain to define pre-determined locations, which are referred to as control volumes or computational cells/grids. In time-dependent problems (transient problems), the time is also divided into smaller time steps.

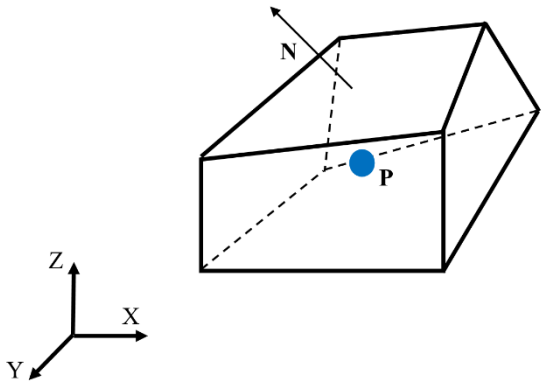

Figure 3-1: Schematic representation of a computational cell, control volume.

Figure 3-1 shows a schematic representation of a computational cell in a control volume. In Figure 3-1, the centroid of the cell (or cell centre), is shown by the marked point P, and all dependent variables and material properties are stored at the cell centre P. The normal vector to one of the surfaces (faces) are shown by vector **N**.

The first step of the FVM discretisation is to integrate over the finite volumes into which the computational domain has been divided. Formerly, the Gauss law would transform the volume

integrals of the convection and diffusion terms into surface integrals. In fluid dynamics, any governing equations can be stated in the form of a generalised transport equation, such as the one shown in Eq. 3.20, which is also known as the general conservation equation for an arbitrary quantity ϕ (Moukalled, Mangani and Darwish, 2016).

$$\underbrace{\frac{\partial(\rho\phi)}{\partial t}}_{\text{transient term}} + \underbrace{\nabla\cdot(\rho\mathbf{v}\phi)}_{\text{convective term}} = \underbrace{\nabla\cdot(\Gamma^{\phi}\nabla\phi)}_{\text{diffusion term}} + \underbrace{Q^{\phi}}_{\text{source term}} \tag{3.20}$$

where, **v** is the velocity vector, $(\cdot)$ is the dot product operator and, Q^{ϕ} represents a source term.

By neglecting the unsteady term, the steady form of the Eq. 3.20, can be written as:

$$\nabla\cdot(\rho\mathbf{v}\phi) - \nabla\cdot(\Gamma^{\phi}\nabla\phi) = Q^{\phi} \tag{3.21}$$

Figure 3-2 shows conservation terms in a discrete cell (C), which are described in Eq. 3.20.

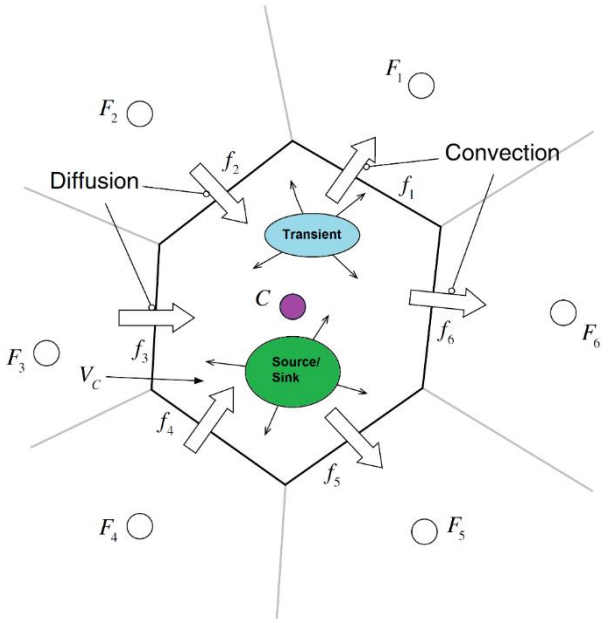

Figure 3-2: Conservation terms in a discrete cell volume. Reproduced from (Moukalled, Mangani and Darwish, 2016).

In Figure 3-2, F_1, F_2, F_3, F_4, F_5 and F_6, are the neighbour cells of the centre cell (C). Also, f_1, f_6 and f_5, are convection fluxes which are moving out from cell C, and f_2, f_3, and f_4, are the diffusion fluxes coming into the cell C.

By integrating Eq. 3.21 over the volume of the cell C (which is shown in Figure 3-2), the above equation can be rewritten as:

$$\int_{V_C} \nabla\cdot\left(\rho\mathbf{v}\phi\right)dV - \int_{V_C} \nabla\cdot\left(\Gamma^{\phi}\nabla\phi\right)dV = \int_{V_C} Q^{\phi}dV \tag{3.22}$$

Based on the divergence theorem, which is also known as Gauss' theorem (Byron and Fuller, 1992) the net flux of a vector field through a surface is equal to the total volume of all sources and sinks over the region inside the surface (Byron and Fuller, 1992; Moukalled, Mangani and Darwish, 2016):

$$\int_{V} \left(\nabla\cdot\mathbf{v}\right)\mathrm{d}V = \oint_{S} \mathbf{v}\,.\,\mathbf{n}\;dS \tag{3.23}$$

where, **v** is a vector field on volume V, and n is the normal vector to the surface S. Then, by using divergence theorem on the Eq. 3.22, the volume integrals of the diffusion and convection terms can be replaced by surface integrals (Moukalled, Mangani and Darwish, 2016):

$$\oint_{\partial V_C} \left(\rho\mathbf{v}\phi\right)\cdot d\mathbf{S} - \oint_{\partial V_C} \left(\Gamma^{\phi}\nabla\phi\right)\cdot d\mathbf{S} = \int_{V_C} Q^{\phi}dV \tag{3.24}$$

where, **S** is the surface vector, ϕ is the conserved quantity, and $\oint_{\partial V_C}$ is the surface integral over the volume V_C.

3.3.1.1 The discretisation of time and domain

The discretisation of the numerical domain produces the computational mesh, which is a set of control volumes. The control volumes or cells, depending on the domain's structure, can have any form, as shown in Figure 3-1.The coordinates of all cell centre, corners and, constructing faces should be accurately determined as an input to the discretised equations. Some CFD codes have been developed which can only work with a structured mesh, such as cubic cells; however, the flexibility and quality of the computational mesh can be very limited in these codes.

The time variable in the equations acts as a parabolic coordinate (Patankar, 1980); hence the computational solution, which is obtained from marching on time, should be initialised with an initial condition throughout the whole computational domain, at the start time.

The computational domain can be decomposed into a finite number of control volumes, such that the computational cells may not completely cover the whole computational domain. Therefore, the uniformity of the computational domain can depend on the grid resolution, and whether the mesh grid is structured or unstructured.

3.3.1.2 Determining the flux Integral over surfaces

Denoting the convection and diffusion flux terms by $J^{\phi,C}$ and $J^{\phi,D}$, respectively, their expressions are given by:

$$J^{\phi,C} = \rho \mathbf{v} \phi \tag{3.25}$$

$$J^{\phi,D} = -\Gamma^{\phi} \nabla \phi \tag{3.26}$$

Additionally, the total flux J^{ϕ} can be written as the sum of the convection and diffusion fluxes:

$$J^{\phi} = J^{\phi,C} + J^{\phi,D} \tag{3.27}$$

Therefore, the surface integrals over the cell C, of the convection, diffusion, and total fluxes can be written as:

$$\oint_{\partial V_C} \left(J^{\phi,C} \right) \cdot d\mathbf{S} = \sum_{f \in faces(V_C)} \left(\int_f (\rho \mathbf{v} \phi) \cdot d\mathbf{S} \right) \tag{3.28}$$

$$\oint_{\partial V_C} \left(J^{\phi,D} \right) \cdot d\mathbf{S} = \sum_{f \in faces(V_C)} \left(\int_f (\Gamma \nabla \phi) \cdot d\mathbf{S} \right) \tag{3.29}$$

$$\oint_{\partial V_C} \left(J^{\phi} \right) \cdot d\mathbf{S} = \sum_{f \in faces(V_C)} \left(\int_f (J_f^{\phi}) \cdot d\mathbf{S} \right) \tag{3.30}$$

It can be noted that in Eq. 3.29 and 3.30, the surface fluxes are calculated at the faces of the cell, rather than integrated within it. In order to evaluate the volume integral of the source term, a Gaussian quadrature is applied over the integral at the face "f" of the cell:

$$\int_f (J^{\phi}) \cdot d\mathbf{S} = \int_f (J^{\phi} \cdot n) \cdot dS = \sum_{ip \in ip(f)} (J^{\phi} \cdot n)_{ip} \omega_{ip} S_f \tag{3.31}$$

where, "ip" denotes an integration point, "ip(f)" the number of integration points along surface f and ω_{ip} is the weighting function. The general discretised formula, for the convection and diffusion terms, can be written as:

$$\oint_{\partial V_C} (\rho \mathbf{v} \phi) \cdot d\mathbf{S} = \sum_{f \in faces(V)} \sum_{ip \in ip(f)} \left((\rho \mathbf{v} \phi)_{ip} \omega_{ip} \cdot \mathbf{S}_f \right) \tag{3.32}$$

$$\oint_{\partial V_C} \left(-\Gamma^{\phi} \nabla \phi \right) \cdot d\mathbf{S} = \sum_{f \in faces(V)} \sum_{ip \in ip(f)} \left((-\Gamma^{\phi} \nabla \phi)_{ip} \omega_{ip} \cdot \mathbf{S}_f \right) \tag{3.33}$$

The Eq. 3.32, which is a general conservation transport equation, includes, a convection term, a diffusion term, and a source term. In the FVM, all of these terms need to be discretised and have a proper interpolation profile applied to them, before any iterative solution methods can

be used. More detailed information regarding the discretisation of these terms, and different methods for interpolation (e.g. upwind, central difference, backwards, Blending Differencing, TVD...), can be found in (Heidari, 2012; Moukalled, Mangani and Darwish, 2016).

3.3.1.3 Numerical tool set

The OpenFOAM (Open Field Operation and Manipulation) toolbox (*OpenFOAM Ltd*, 2015), which is used as the primary framework for the code developments in the present work, is based on the finite volume method. OpenFOAM is an open source, and object-oriented, CFD toolbox (Greenshields, 2015) that contains several CFD classes and functions that can be used to create new continuum solvers. The main package of OpenFOAM contains some solvers for chemical reactions, turbulence and heat transfer, solid dynamics and, electromagnetic calculations(Greenshields, 2015).

The CFD parts of OpenFOAM are based on a finite volume numerical approach. During the past few years, OpenFOAM users have been increased dramatically, and thousands of researchers are involved in research developments for this toolbox. The available solvers for combustion simulations in OpenFOAM can be used to simulate simple phenomena such as low-speed deflagrations and simple laminar and turbulent flames. However, to simulate more complex phenomena like high-speed deflagrations and detonations, new solvers must be developed (Greenshields, 2015).

OpenFOAM can be considered a high-level and advanced programming language that is specifically developed for CFD. In lower-level programming languages, the developer has access to some mathematical operators such as add, subtract, and multiplication power. However, OpenFOAM users have access to high-level operators such as divergence, gradient, Laplacian, etc.. Therefore, developers can create more efficient and reliable solvers in a shorter time. The object-oriented structure of OpenFOAM helps developers to follow a very systematic and standard pattern in their code developments. Weller et al. (Weller, 1993; Weller *et al.*,

1998; Tabor and Weller, 2004) provided excellent insight into the main code structure and capabilities of OpenFOAM. Considering the benefits of using such a compelling package as the base of research work, the author of the current work used OpenFOAM toolbox to develop CFD solvers for simulating different combustion regimes, especially the DDT phenomenon.

3.4 Solution algorithms

Simulating discontinuities, such as shocks and contact surfaces, in high-speed compressible flows requires numerical schemes that can capture these features while avoiding spurious oscillations. There are two main solution algorithms for solving the flow fields; pressure based and density-based approaches. Both approaches are examined in the present study.

In the pressure-based approach of OpenFOAM solvers (such as sonicFoam (*OpenFOAM Ltd*, 2015)), a non-iterative method, for handling the coupling of implicitly discretised time-dependent fluid flow equations, is utilised. The method is known as PISO (Pressure Implicit with the Splitting of Operators). It is based on applying pressure and velocity as dependent variables and applies to both the incompressible and compressible forms of the transport equations. The method is based on splitting the solution process into a series of steps, where operations on pressure are decoupled from operations on velocity (Issa, 1986).

Common methods for non-oscillatory solutions, shock and discontinuity capturing, and the generation of numerical fluxes, are typically involve Riemann solvers, Jacobian evaluation and characteristic decomposition. In which implementing of these complex characteristics features on a polyhedral mesh including number of faces, will be difficult (Greenshields *et al.*, 2010). However, an alternative approach, without Riemann solvers can provide accurate non-oscillatory solutions using the "central schemes" method. The central schemes, method, which have been developed by (Kurganov and Tadmor, 2000), are available in OpenFOAM (Kurganov and Tadmor, 2000; Kurganov, Noelle and Petrova, 2001; Greenshields *et al.*, 2010). Khodadadi et al. (Khodadadi Azdaboni *et al.*, 2013), carried out shock capturing studies using different OpenFOAM solvers to solve the Sod's problem (Sod, 1978) , and concluded that the

available central scheme and density-based solver in OpenFOAM can provide the most accurate shock capturing. They also mentioned that the proposed density-based solution could generate some oscillations in the contact surface of shock. These oscillations may be linked to the numerical schemes. Hence, to provide the most appropriate numerical scheme, for shock capturing, a similar shock tube modelling by using Sod's condition, has been conducted in this study.

The shock tube problem by Sod (Sod, 1978) has become a standard test case for compressible flow. The initial conditions for this problem consist of two semi-infinite states separated by a diaphragm at time t = 0 (Khodadadi Azdaboni, Malekbala and Azadboni, 2013). The left and right states are set to the following conditions (Table 3-1). For the numerical modelling, 100 cells have been considered in the computational domain, for comparison with the analytical solution.

Table 3-1: The initial condition of Sod's problem.

Compartment	X > 0.5 Left (driver)	X < 0.5 Right (driven)
Pressure	$P_L = 1$	$P_R = 0.1$
Density	$\rho_L = 1$	$\rho_R = 0.125$
Velocity	$U_L = 0$	$U_R = 0$

The existing central scheme density-based solver "rhoCentralFoam", and the pressure-based solver "sonicFoam", are used in this study (Kurganov and Tadmor, 2000; Greenshields, 2015).

The Sod problem was modelled with three different interpolation schemes:

1 Upwind schemes for density, temperature, and velocity.
2 VanLeer TVD method for density and temperature, and upwind for the velocity.
3 VanLeer for all of the parameters.

The solution of the existing pressure-based solver, "sonicFoam" has also been provided for a better comparison between the numerical methods and analytical solution.

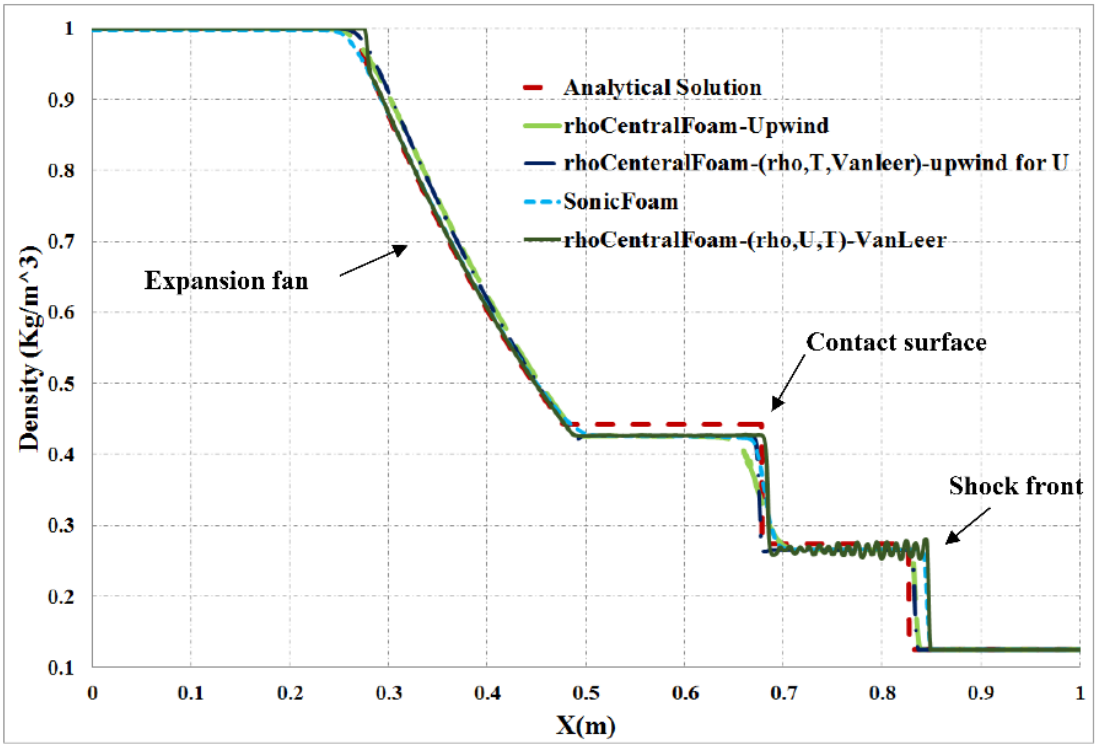

Figure 3-3: Density distribution in the shock tube using 100 cells.

The results in Figure 3-3 show a shock wave moving to the right, a rarefaction wave (expansion fan) moving to the left and the contact surface discontinuity, separating the shock and rarefaction waves, moving to the right (Sod, 1978). These results show that the density-based solutions can provide a better shock capturing than the pressure-based solver (dashed blue line, sonicFoam) with comparison to the analytical solutions. Moreover, it is seen that using the upwind method in the solution of the density-based solver (green line rhoCentralFoam-Upwind in Figure 3-3), can provide an adequate estimation of the shock front, but it will not model a shock contact surface or expansion fan accurately. In order to improve discontinuity modelling, TVD type schemes (Van Leer, 1974) are used. Figure 3-3 also shows that the VanLeer scheme (Van Leer, 1974) can produce an accurate shock contact surface modelling, but there are some oscillations in the leading shock contact surface (Khodadadi Azadboni, Wen and Heidari, 2019).

Additionally, Figure 3-3 shows that by changing the velocity interpolation scheme from VanLeer to the upwind, and using VanLeer for density and temperature interpolation in

rhoCentralFoam solver, the shock front, contact surface and expansion fan predictions will closely match with the analytical solution, without any oscillation in the shock contact surface.

Borm, Jemcov and Kau, (2011) implemented a Godunov-type scheme to create a new density-based solver in OpenFOAM ”dbnsTurbFoam” (Borm, Jemcov and Kau, 2011). This method is based on the HLLC (Harten-Lax-van Leer-Contact) (Batten, Leschziner and Goldberg, 1997) scheme, and the time discretisation, which includes the dual time scheme and the physical time step, is based the Runge–Kutta scheme (Ascher, Ruuth and Spiteri, 1997). The same method is used in creating a new density-based solver, “VCEFoam” (Vapour Cloud Explosion Foam) in the current work (Khodadadi Azadboni *et al.*, 2017). Adaptive Mesh Refinement (AMR), HLLC schemes and a chemical reactions solver are utilised in VCEFoam to simulate high Mach number reactive flows (Khodadadi Azadboni, Wen and Heidari, 2019).

In order to include the chemical reaction and species transport terms, the energy equation needs to be changed from the total energy to the sensible enthalpy, as in Eq. 3.34:

$$\frac{\partial(\rho h_s)}{\partial t}+\nabla\bullet\left(\rho u h_s\right)-\frac{\partial p}{\partial t}=\nabla\bullet\left[\alpha\nabla h_s+\sum_{i=1}^{n}h_i J_i\right]+\nabla\bullet\left(\tau\bullet u\right)+S_h \tag{3.34}$$

where, ρ, u, P, hs, T, S_h are the density, velocity, pressure, sensible enthalpy, temperature and enthalpy source respectively. α is k/c_p, k is the thermal conductivity and c_p is the specific heat at constant pressure. The viscous stress tensor is defined in Eq. 3.5.

Species transport and diffusion coefficient are added, so the species conservation equation is:

$$\frac{\partial(\rho Y_i)}{\partial t}+\nabla\bullet\left(\rho u Y_i\right)=\nabla\bullet J_i+R_i \tag{3.35}$$

where Y_i is the mass fraction and J_i is the diffusion flux of species i and is defined as Eq. 3.36:

$$J_i = -\rho D_{i,m} \nabla Y_i \tag{3.36}$$

where the binary diffusion coefficient, $D_{i,m}$, for species i in the mixture can be derived using Wilke's equation (Wilke, 1950).

3.4.1.1 HLLC Solver

Harten, Lax and van Leer developed an approximate Godunov-type method to solving the Riemann problem, known as HLL (Harten, Lax and van Leer, 1983). The resulting HLL-type Riemann solvers form the bases of very efficient and robust approximate Godunov–type methods (Toro, 2009a). However, one of the drawbacks of this scheme is the assumption of a two-wave configuration (Toro, 2009b). This assumption is only applicable for hyperbolic systems of two equations, such as the 1D shallow water equations. However, in larger systems, such as the Euler equations (e.g. 2D shallow water equations), the two–wave assumption is incorrect. Therefore, a different approach was introduced by (Toro, Spruce and Speares, 1994). They advised that the HLLC Riemann solver (in which, C stands for Contact) be applied to a tranisent Euler equations. HLLC is a "three–wave model", resulting in two–star states for the intermediate region of the Riemann–problem solution fan. The approximate wave structure of the HLLC scheme includes all the characteristic fields of the exact problem. One of the most common applications of the HLLC scheme is supersonic flow (Toro and Chakraborty, 1994). Also, another application of HLLC scheme is the two-dimensional transient shallow water equations (Fraccarollo and Toro, 1993, 1995). There are four possible solutions (U_L, U^*_L, U^*_R, U_R) when a small finite flow moves for a short time Δt. U_L and U_R are the discretized scalars; U^*_L and U^*_R are approximate vectors of the conserved variables (see Figure 3-4).

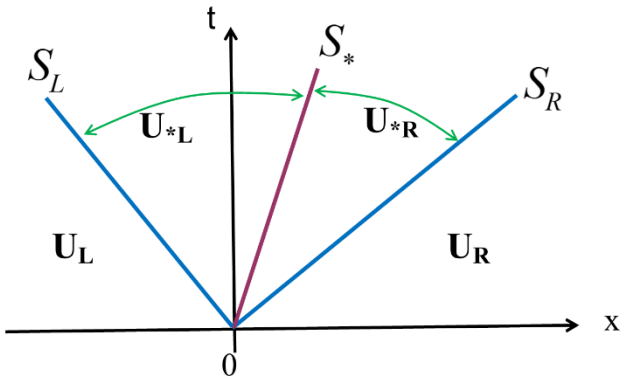

Figure 3-4: Solution of HLLC Riemann solver (reproduced from (Toro, 2009b)).

Figure 3-4 shows a schematic solution of the HLLC Riemann solver. In Figure 3-4, S_L and S_R are the slowest and fastest signal speeds and $S*$ is a middle wave speed. The solution in the star region consists of two constant states, separated by a wave in the middle of speed S_*. By considering the flow speed S_*, the rarefaction and shock wave speed can be found to be S_L and S_R respectively.

In order to compute the HLLC flux scheme, the following steps need to be taken.

Firstly, an estimate for the pressure $p*$ in the Star Region needs to be calculated:

$$p_* = \max\left(0, p_{pvrs}\right) \tag{3.37}$$

$$p_{pvrs} = \frac{1}{2}(p_L + p_R) - \frac{1}{2}(u_L - u_R)\bar{\rho}\bar{a} \tag{3.38}$$

$$\bar{\rho} = \frac{1}{2}(\rho_L + \rho_R), \qquad \bar{a} = \frac{1}{2}(a_L + a_R) \tag{3.39}$$

Step 2: Estimating the wave speed S_L and S_R.

Assuming the estimate for the pressure in the Star Region, p∗ has been calculated, the following wave speeds can then be chosen:

$$S_L = u_L - a_L q_L, \quad S_R = u_R - a_R q_R \tag{3.40}$$

q_R can be calculated using the following:

$$q_R = \begin{cases} 1 & \text{if } p_* \le pk \\ \left[1 + \frac{\gamma+1}{2\gamma}\left(p_* / pk - 1\right)\right]^{1/2} & \text{if } p_* > pk \end{cases} \tag{3.41}$$

K can be either L or R. If the K wave (K = L or K = R) is a rarefaction wave then the speed S_K corresponds to the characteristic speed of the head of the rarefaction wave, which carries the fastest signal. If the wave is a shock wave, then the speed also corresponds to an approximation of the actual shock speed.

The intermediate speed S_* can then be written based on S_L and S_R:

$$S_* = \frac{p_R - p_L + \rho_L u_L (S_L - u_L) - \rho_R u_R (S_R - u_R)}{\rho_L (S_L - u_L) - \rho_R (S_R - u_R)} \tag{3.42}$$

Step 3: Calculating the HLLC flux. The intermediate U_* is computed as:

$$U_{*K} = \left(\frac{S_K - u_K}{S_K - S_*}\right)\begin{pmatrix} \rho_K \\ \rho_K S_* \\ \rho_K u_K \\ \rho_K w_K \\ \rho_K \dfrac{E_K}{\rho_K} + \rho_K\left(S_* - u_K\right) \\ \rho_K Y_K \end{pmatrix} \quad \begin{matrix} \\ \\ \\ \\ \left[S_* + \dfrac{p_K}{\rho_K\left(S_K - u_K\right)}\right] \\ \\ \end{matrix} \tag{3.43}$$

The intermediate flux F_* is:

$$F_{*K} = F_K + S_K\left(U_{*K} - U_K\right) \tag{3.44}$$

Finally, the HLLC flux can be written as:

$$F^{hllc}_{i+\frac{1}{2}} = \begin{cases} F_L & \text{if} \quad 0 \le \mathrm{S_L} \\ F_{*L} & \text{if} \quad \mathrm{S_L} \le 0 \le \mathrm{S_*} \\ F_{*R} & \text{if} \quad \mathrm{S_*} \le 0 \le \mathrm{S_R} \\ F_R & \text{if} \quad 0 \ge \mathrm{S_R} \end{cases} \tag{3.45}$$

3.4.2 The transition between Low Mach number and High Mach number flows

In the flame acceleration and transition to detonation phenomena, the flow Mach number increases (transitioning from a subsonic regime into a supersonic regime). The transition mechanism in this work is due to the interaction of reflected shock from the obstacles to the flame front. Therefore, the shock capturing capability of the model has a substantial effect on the accuracy of the predictions. Moreover, the DDT phenomena can be divided into two main stages: flame acceleration (deflagration) in the subsonic regime, and detonation in the supersonic regime. Since the density-based solver is not suitable for modelling low Mach number problems, it is recommended to use a pressure-based approach for the flame

acceleration stage and then subsequently switch to the density-based solution for the supersonic flow (Khodadadi Azadboni, Wen and Heidari, 2019).

3.5 CFD methodology

In this section CFD methodology for medium scale and small scale scenario will descericbe and for large scale scenario additional CFD methodology will decribe in chapter 6. Two different solution approaches, developed in OpenFOAM, have been used for modelling DDT; pressure based and density based solution. A pressure based solver using the flame wrinkling combustion model (Weller *et al.*, 1998) "RMXiFoam" is used for uniform hydrogen/air mixture DDT modelling as well as for the prediction of Baroclinic torque and RM instabilities. Baroclinic torque ($\left(\nabla\rho\times\nabla p/\rho^2\right)$) is generated as a result of strong misalignment of the density gradient and pressure gradient. In high velocity reacting flows, such as deflagration and detonation waves, hydrodynamic instabilities are one of the critical factors in enhancing turbulence through shock-flame interaction. Therefore, Baroclinic vorticities have been predicted using this solver to examine the RM instability.

For mixtures with concentration gradients, the FA stage, which occurs at relatively low Mach numbers, has been modelled by using the pressure-based algorithm. The transition stage, which is supersonic and includes strong shock waves, has been modelled using the density-based solver. To evaluate the convective fluxes' contribution, and ensure accurate shock capturing, the HLLC (Batten, Leschziner and Goldberg, 1997; Toro, 2009b) scheme is used. The compressible Navier–Stokes equations are solved with species conservation equation (with a reduced chemical reaction mechanisem). For turbulence modelling, the Monotone Integrated Large Eddy Simulation (MILES) technique has been used (Grinstein, Margolin and Rider, 2007). The solver and numerical schemes are initially tested by various verification test cases (which will be discussed in the following).

3.5.1 Monotone Integrated Large Eddy Simulation (MILES)

Monotone Integrated Large Eddy Simulation (MILES) is a method that presented by (Boris *et al.*, 1992). This technique is inspired by the principles behind shock capturing schemes used for compressible flows. The idea is that turbulence is characterised by high levels of fluctuating vorticity, and therefore sharp velocity gradients. The main principle of the MILES method is to use an appropriate constructed scheme so that the numerical error acts as a turbulence model in such a way as to emulate the physical effects of small-scale viscous dissipation (Aspden, 2006). Therefore, high-order monotone schemes are required to resolve such flow features correctly. The "convenient conspiracy", as it was called by (Oran and Boris, 1993), is that these high-order monotone schemes have an inherent truncation error that acts as a numerical diffusion, which can emulate the effects of physical viscosity (Grinstein, Margolin and Rider, 2007).

In LES models the small-scale features are removed, and at that point the energy cascade process is truncated. The energy of the smallest scales solved on the grid cannot be moved to the following scales, producing a pile-up of energy at these scales. Subgrid scale models introduce the dissipation needed to avoid this effect. Therefore, most of the LES methods are based on centred discretization. Also, this will not introduce enough dissipation into the uniform grid cells, and they imperatively need any explicit subgrid scale (SGS) model. But, in upwind discretization methods introduce certainly a specific amount of dissipation. The Implicit Large-Eddy Simulation (ILES) methods, assume that the subgrid scales is purely dissipative (Sagaut, 2006). In non-oscillatory finite volume approaches, the Monotone Integrated Large Eddy Simulation (MILES) states the relationship between leading numerical error terms and tensorial subgrid viscosities (Boris *et al.*, 1992; Nogueira *et al.*, 2010). The MILES method, monotonicity preserving implicit LES (ILES), a class of practical methods for simulating turbulent high Reynolds number flows with complicated, compressible physics and complex geometry. A comprehensive discussion about MILES approaches is available in (Grinstein, Margolin and Rider, 2007).

3.6 Summary

In this chapter the required governing equations and numerical schemes for solving Deflagration to Detonation Transition (DDT) and vapour cloud explosion phenomena in inhomogeneous and homogeneous mixtures such as Hydrogen/Air and LNG/Air, have been presented. In modelling discontinuities, such as shocks and contact surfaces, in high-speed compressible flows require numerical schemes that can predict and capture these features while avoiding spurious oscillations. The DDT phenomena have two major stages; flame acceleration (FA), during which the flow is in the subsonic regime, and the transition-to-detonation stage, in which the combustion wave undergoes a transition to the supersonic state. For numerical modelling, a density-based solver, within the framework of the open source CFD code OpenFOAM, has developed. The developed density-based code VCEFoam (Khodadadi Azadboni et al., 2017; Khodadadi Azadboni, Heidari and Wen, 2018; Khodadadi Azadboni, Wen and Heidari, 2019) is integrated with a Monotone Integrated Large Eddy Simulation (MILES) approach. Within VCEFoam, compressible Navier–Stokes equations with a hydrogen-air reaction mechanism which contains 9 species and 21 detailed reactions (Ó Conaire et al., 2004) are solved. The HLLC scheme (Batten, Leschziner and Goldberg, 1997) for shock capturing and the Runge-Kutta scheme (Borm, Jemcov and Kau, 2011) for the time discrete schemes are used, which include the dual time scheme and the physical time step. At the end of this chapter, a CFD methodology for medium scale and small scale scenario has desceribed and for large scale scenario additional CFD methodology will decribe in chapter 6. The two different solution approaches, which are developed in OpenFOAM, for modelling DDT, pressure based and density based solution, have been disscused.

In the next chapter, code verification the developed numerical model will be discussed. For the code verification porpose, four sets of verification problem will be considered:

1. Shock capturing: 1D Sod's shock tube problem
2. Supersonic wedge: 2D oblique shock
3. DDT test case: comparison between pressure-based and density-based solution
4. 2-D detonation initiation test case: cellular structure

Chapter 4 Code Verification

For verification of the developed numerical model, four sets of verification problem have been considered. In these verification test cases, shock and cellular detonation capturing capability, and accuracy of the solver will be examined. Initially, Sod shock tube problem for shock capturing, and supersonic wedge for oblique shock capturing, capability verification, has been modelled. In addition, a DDT test case has been modelled to investigate the comparison between pressure-based and density-based solution methods. Eventually, in order to verify the capability of the numerical code in capturing detonation cell, a 2D detonation initiation test case has been modelled. The detonation cell size has been compared with the other previous works as well as an experimental observation.

4.1 Sod shock Tube problem

The Sod problem (Sod, 1978) was first chosen to validate the code regarding its ability to capture discontinuities such as shock waves. The test case consists of a one-dimensional Riemann problem. The initial states for this problem consist of two semi-infinite states separated by a diaphragm at the initial time (Figure 4-1). The region with the highest pressure is called the driver section of the shock tube, and the low-pressure part is the driven section. A diaphragm has separated these two sections, and the sudden breakdown of the diaphragm produces a high-speed flow, which propagates in the driven section of the shock tube.

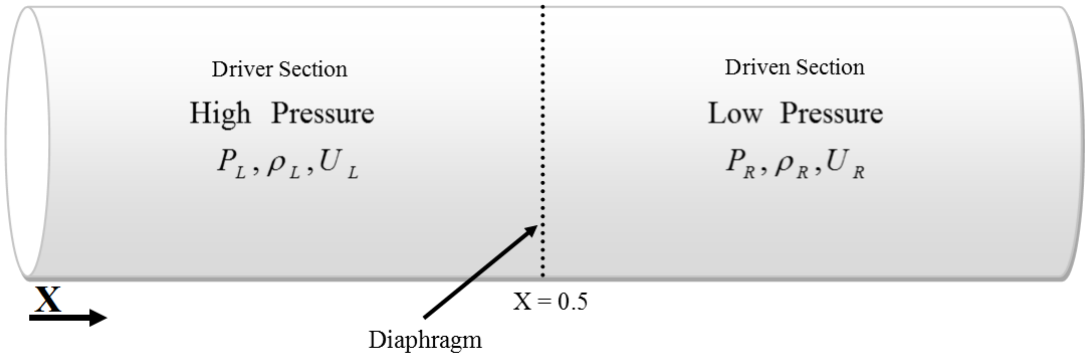

Figure 4-1: Schematic diagram of Sod's shock tube problem (at time=0).

The initial condition of the driver and driven sections are described in the following table. (Table 4-1). In this test case, all the variables are non-dimensional.

Table 4-1: Initial condition of Sod's shock tube problem

Compartment	$X > 0.5$ Left (driver)	$X < 0.5$ Right (driven)
Pressure	$P_L = 1$	$P_L = 0.1$
Density	$\rho_L = 1$	$\rho_L = 0.125$
Velocity	$U_L = 0$	$U_L = 0$

As soon as the membrane diaphragm is removed, the shock and the contact discontinuity will begin to travel into the low-pressure region, whereas the rarefaction wave (or expansion wave) will travel into the initially high-pressure region (Figure 4-2).

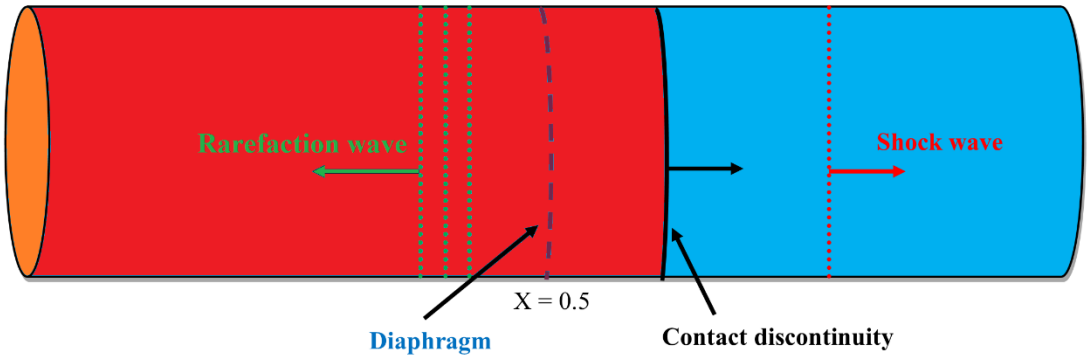

Figure 4-2: Schematic diagram of Sod's shock tube problem (after breaking the diaphragm).

One of the challenging issues in the Sod shock tube verification problem is how accurate the numerical code is capable of capturing the shock and contact surface of shock and other discontinuities. This case has been modelled with the numerical code, as well as with the available analytical solution (exact solution) (Khodadadi Azdaboni, Malekbala and Azadboni, 2013). The predicted numerical result at time t = 225 μs (around this time, the leading shock located in the middle of the domain), has been compared against the analytical solution (Figure 4-3). To satisfy the grid independency of the model, the calculations were carried out with 500, 1000, and 2000 grid points. By increasing the grid points from 500, to 1000, it has noticed that the predicted pressure, temperature, density, and velocity distributions are in excellent agreement with the analytical solutions. And there were no oscillations were found at the discontinuities. Then by increasing the grid points from 1000 to 2000, not much differences have been noticed in the results. Since, by refining the mesh from 1000 to 2000 cells, the results do not change much, therefore, it can be concluded that the results on the 1000 grid points, are mesh independent. Figure 4-3 shows the results of the model with the 1000 grid points.

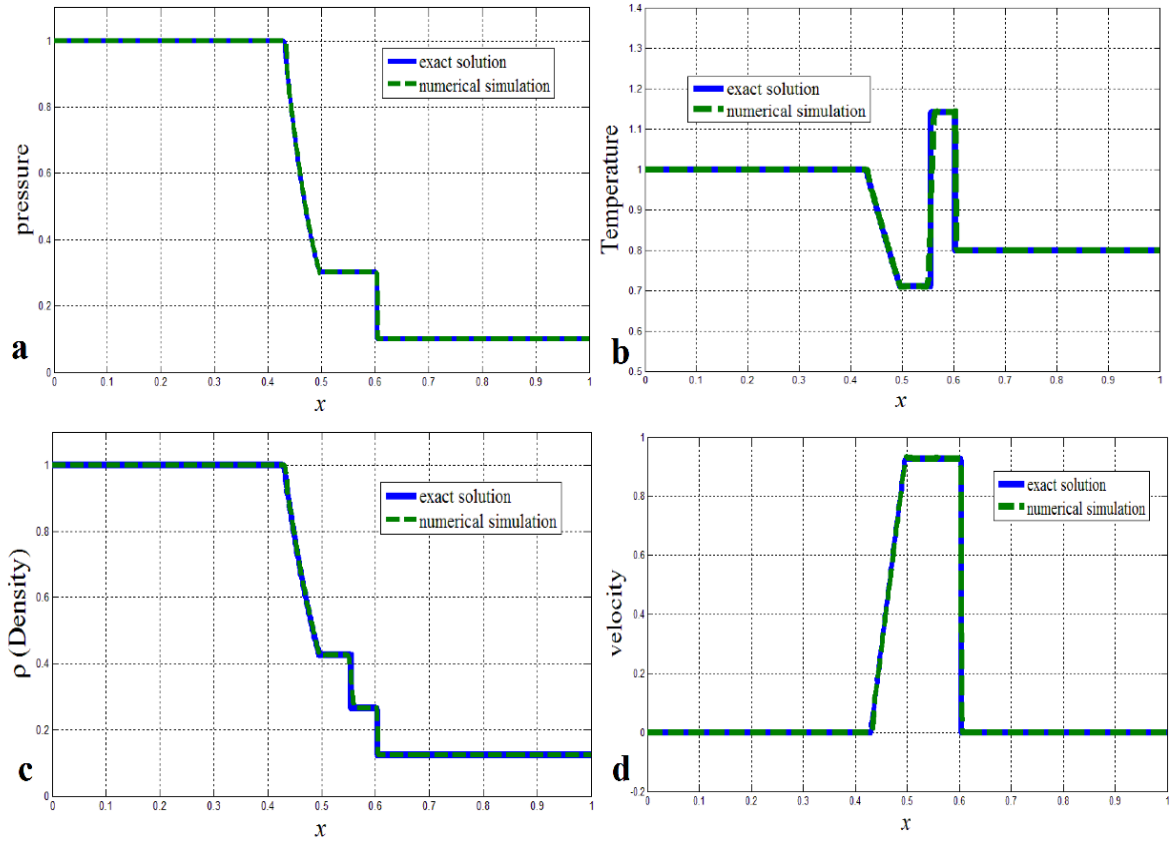

Figure 4-3. Density distribution in the shock tube with using 1000 cell; a) Pressure, b) Temperature, c) Density and d) Velocity distributions (Khodadadi Azadboni, Heidari and Wen, 2018).

As shown in Figure 4-3, the predicted pressure, temperature, density, and velocity distributions are in excellent agreement with the analytical solutions. The present results accurately capture the above-mentioned important characteristics of the flow, i.e. the rarefaction wave, the contact discontinuity, and the shock discontinuity. No oscillations were found at the discontinuities. At the contact region, the predictions show steep gradients due to molecular diffusion which was captured by the code. Figure 4-3 demonstrate movement of a shock wave to the right-hand side of the tube, and a rarefaction wave (expansion fan) moving to the left side. Also, the density and temperature plots show that the contact surface discontinuity will separate the shock and rarefaction waves which is moving to the right (Sod, 1978). These results demonstrate that the

density-based solutions can provide accurate shock capturing (Khodadadi Azadboni, Heidari and Wen, 2018).

4.2 2D test case: Supersonic wedge problem

The supersonic wedge problem involving two-dimensional oblique shock waves are prevalent in the study of super- and hypersonic flows, so it is crucial that a compressible flow solver is able to handle them well. Although one-dimensional Euler equations can represent the Sod shock tube problem, the supersonic wedge problem requires two-dimensional equations. The computational domain is shown in Figure 4-4. A horizontal stream with $M_\infty = 2$ meets a wedge whose axis of symmetry is parallel to the flow direction. The supersonic flow is then "turned into itself" resulting in an oblique shock wave, after which the flow is again parallel and uniform. The wedge angle is chosen 15 degrees. The analytical solution of this problem is well known and a MATLAB code, based on the provided theory in (Anderson, 1990), has been provided (Khodadadi Azadboni, Heidari and Wen, 2018).

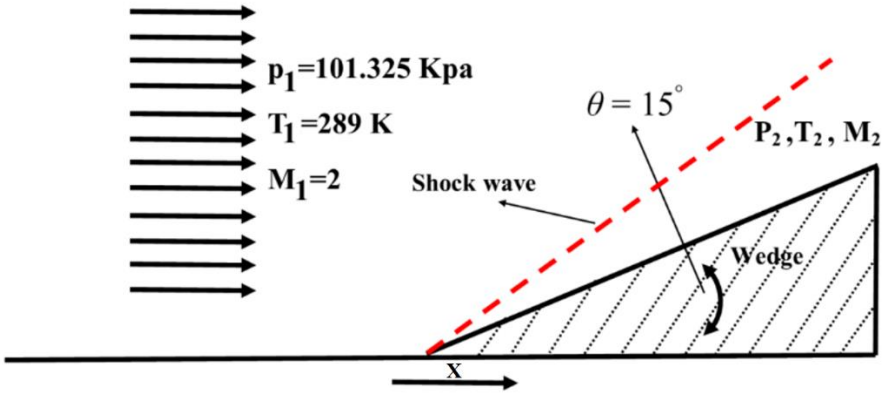

Figure 4-4. Schematic of the computational domain of the supersonic wedge problem.

The initial conditions of the two-dimensional wedge problem, as well as the computational domain, is shown in Figure 4-4.

To satisfy the grid independency of the model, the calculations were carried out with 20000, 50000, and 90000 grid points. By increasing the grid points from 20000, to 50000, it has noticed that the predicted pressure and temperature, distributions are in excellent agreement with the analytical solutions. And there were no oscillations were found at the discontinuities. Also, by increasing the grid points from 50000 to 90000, there were not many differences in the results. Therefore, it can be concluded that the results on the 50000 grid points, are mesh independent. Hence, 50000 hexahedral cells have been considered for this simulation. To avoid having any reflection from the incoming waves, a transmissive-wave boundary condition has been chosen for the outlet boundary condition. The upper boundary and the horizontal part of the lower boundary have been considered as a symmetry type, and for the rest of the regions, a zero gradient type has been implemented to the boundary conditions (Khodadadi Azadboni, Heidari and Wen, 2018).

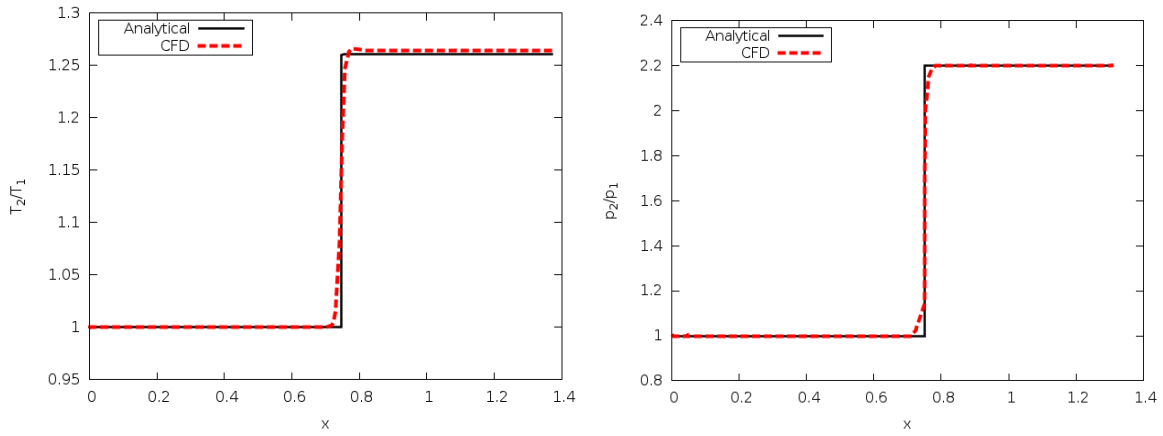

Figure 4-5: The predicted temperature ratio distribution in the wedge problem (right) and pressure ratio distribution in the wedge problem (left).

Figure 4-5 shows the predicted pressure and temperature ratios across the oblique shock in comparison with analytical solutions. Both figures give good results for the shock position and show an excellent agreement with the analytical solutions.

4.3 DDT test case: comparison between a pressure-based and density-based solution

The present DDT test case aims to study the dynamics of Deflagration to Detonation Transition (DDT) in inhomogeneous and homogeneous mixtures. For the numerical model, two different solution approaches, i.e. the pressure based and density-based methods, have been adopted using the OpenFOAM CFD toolbox. The reactive density-based developed solver (VCEFoam) using the HLLC scheme has been used for this verification study (Khodadadi Azadboni, Wen and Heidari, 2019). The predictions are in reasonably good qualitative and quantitative agreement with the experiments. The DDT phenomena have two major stages; flame acceleration (FA), during which the flow is in the subsonic regime, and the transition to detonation stage in which the combustion wave undergoes a transition to the supersonic state. The present study indicates that it is viable to use the pressure-based algorithm for studying the FA, but a density-based method is required for modelling DDT.

4.3.1 Methodology

The present study aims to provide an appropriate numerical method for modelling DDT phenomena in horizontal obstructed channels with two different blockage ratios: 60% and 30%. The tube is filled with hydrogen/air mixture with an average 30 percent hydrogen by volume.

Two different solvers developed in OpenFOAM have been used. A pressure-based solver using the flame wrinkling combustion model (Weller *et al.*, 1998) has been developed and named as RMXiFoam (which is based on the available XiFoam solver in OpenFOAM). The solver is used for uniform hydrogen/air mixture DDT modelling as well as prediction of Baroclinic torque and RM instabilities.

For mixtures with concentration gradients, the FA stage which occurs at relatively low Mach numbers has been modelled by using a pressure-based algorithm and the transition stage, which is supersonic and includes strong shock waves, has been modelled with a density-based solver. To evaluate the convective fluxes contribution, and accurate shock capturing, HLLC scheme is used (Batten, Leschziner and Goldberg, 1997; Toro, 2009b). The compressible Navier–

Stokes equations with a single step Arrhenius reaction mechanism are solved. This reaction has been introduced by (Gamezo, Ogawa and Oran, 2007). For turbulence modelling, the Monotone Integrated Large Eddy Simulation (MILES) technique has been used (Grinstein, Margolin and Rider, 2007). For numerical validation, an experimental inhomogeneous DDT test case (Boeck *et al.*, 2016) has been selected.

4.3.2 Numerical setup

The experiments of Boeck et al. (Boeck et al., 2016) involving inhomogeneous and homogeneous DDT in a hydrogen-air mixture are simulated. The experiments were conducted in a horizontal obstructed channel with 30% and 60% blockage ratios. There are 7 obstacles has been installed in the channel, and the first obstacle installed at 0.25m, and then 6 more obstacles with 0.3m spacing have installed, therefore the last obstacle (obstacle 7), is installed at 2.05m from the ignition point. The schematic of the computational domain is shown in Figure 4-6. It was initially filled with an inhomogeneous hydrogen-air mixture, which was on average 30% hydrogen by volume. In this study, adaptive mesh refinement (AMR) was used to provide a minimum cell size of 20 μm, equivalent to a minimum of 20 grid points per half-reaction length (more information regarding the grid size, and boundary conditions will be provided in section 5.3.1). In the present AMR method, the flame surface will be refined based on the high temperature gradients criteria. Therefore, the solver will track the flame front and refines the mesh in regions with high temperature gradients.

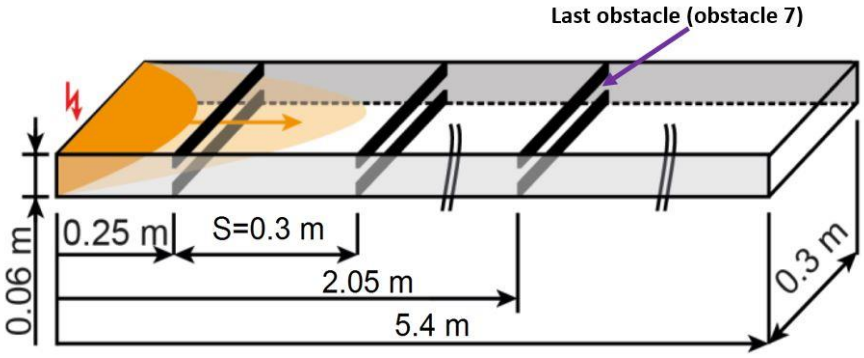

Figure 4-6: Schematic of the computational domain (Reproduced from (Boeck et al., 2016)).

4.3.3 Predictions using the pressure-based solver

Deflagration to detonation transition, for the 30 % inhomogeneous hydrogen-air mixture, in the obstructed channel with 60 % blockage ratio, has been modeled by RMXiFoam solver.

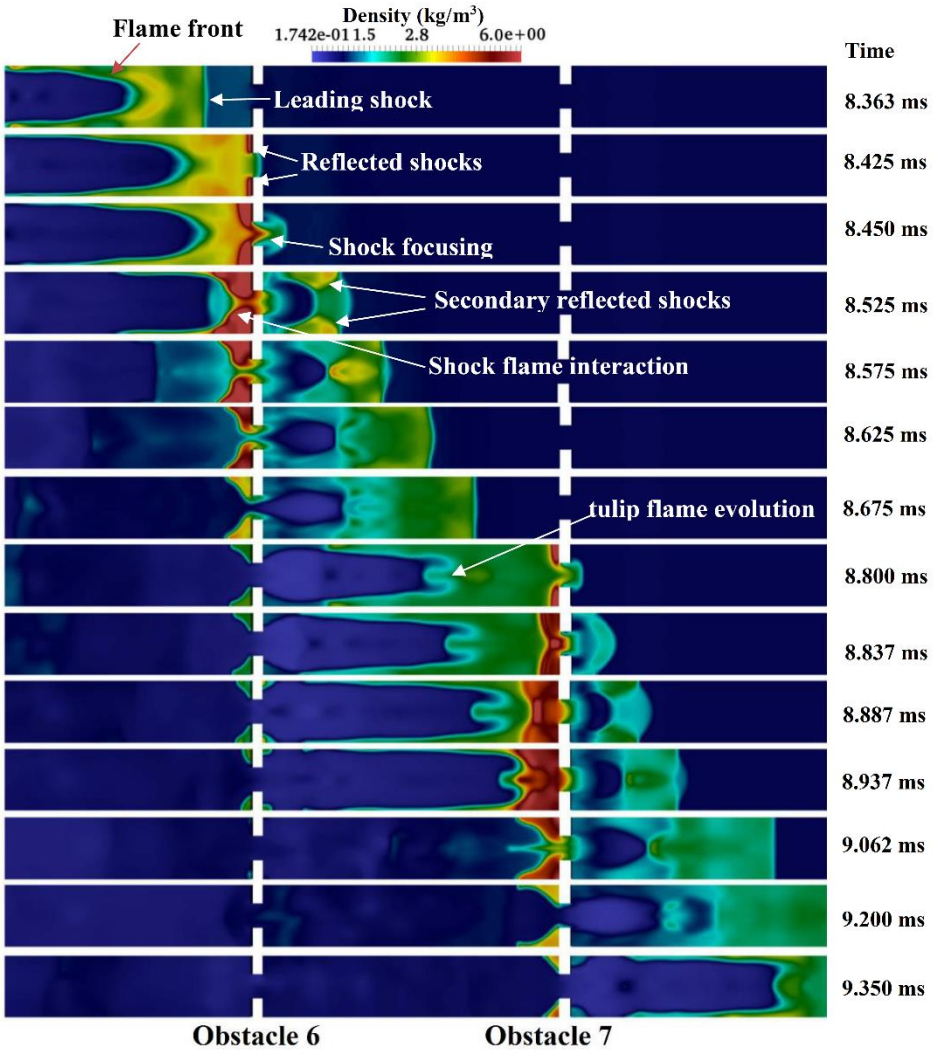

Figure 4-7: Density distribution contours of deflagration of Homogenous H2/Air mixture of 30% Vol and BR60, with the pressure-based solution.

Figure 4-7 shows the density counter of the flame while it propagates through obstacles 6 and 7 (obstacle 6 located at x=1.75m and obstacle 7 located at x=2.05m). In the first frame, it can be seen that a weak shock wave has been generated in the flame front before interacting with obstacle 6 and leading to a reflected shock moving upstream of the flow. At 8.45 ms the reflected shocks interact in the middle of the tube, where shock focusing phenomena occur, generating a stronger shock wave. At 8.825 ms, the reflected shock interacts with the flame front, and the first local explosion appears, which increases the pressure up to 20 bars.

However, at 8.625 ms, the detonation fails, and the leading shock wave and flame front are decoupled (Khodadadi Azadboni, Wen and Heidari, 2019).

The predicted Baroclinic torque in the tube is not strong enough to trigger RM instability.

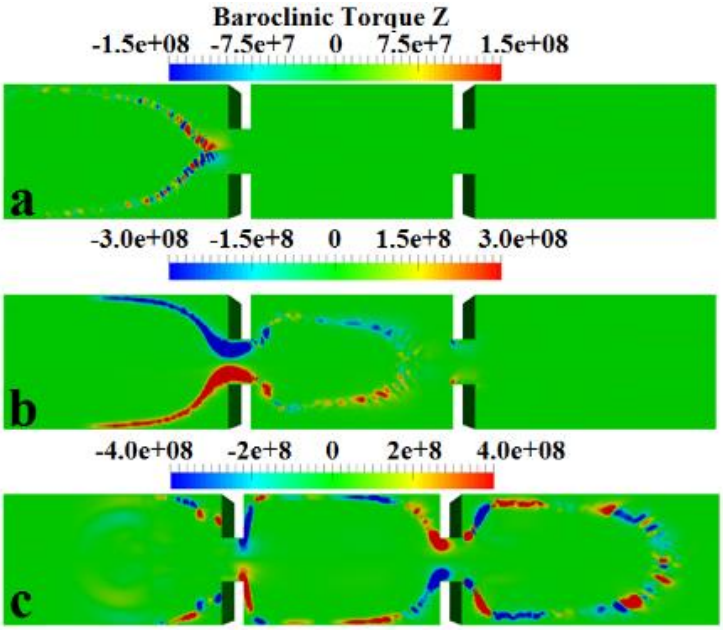

Figure 4-8: Baroclinic torque contour in the Z direction of flame acceleration of Hydrogen flame simulation with RMXiFoam solver, for BR=60 % at a) time=1.86ms, b) time=2.16ms and c) time=2.409ms.

Figure 4-8 shows the Baroclinic torques during the flame acceleration stage. It contains different directions of the Baroclinic vorticities (red: out of the plane, and blue: into the plane). Xiao et al. (Xiao, Houim and Oran, 2015), presented the Baroclinic torque field at different times during the initiation of the tulip flame and predicted the magnitude of Baroclinic torque to be in the range of -2e+8 to +2e+8. The present predictions are consistent with their findings as shown in Figure 4-8-a. They also predicted that the Baroclinic torque increases with time (around -1e+9 to +1e+9). The present predictions are, however, smaller; and as a result, no DDT or RM instability occurred.

The pressure-based RMXiFoam solver provides a reasonably good prediction of flame acceleration in the obstructed channel, but the accelerated flame did not undergo a transition to the detonation.

4.3.4 Predictions using the density-based solver

For better shock and detonation capturing, the newly assembled density-based solver is used. In this study, adaptive mesh refinement was used to provide a minimum cell size of 20 µm, equivalent to a minimum of 20 grid points per half-reaction length (more information regarding the grid size will be provided in section 5.3.1).

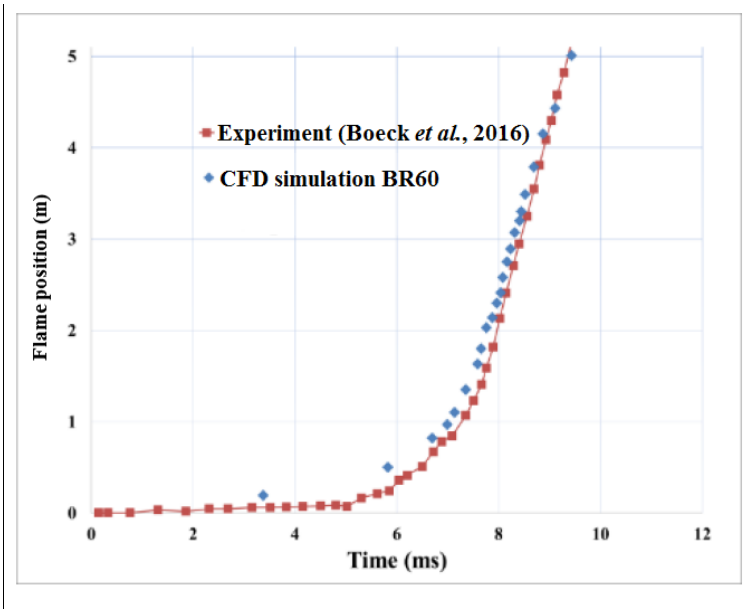

Figure 4-9: Comparison between the predicted and measured flame position for BR60% and homogeneous mixture 30 % Vol. hydrogen on average.

Figure 4-9 shows that there is a good quantitative agreement between the measurement and the present predictions.

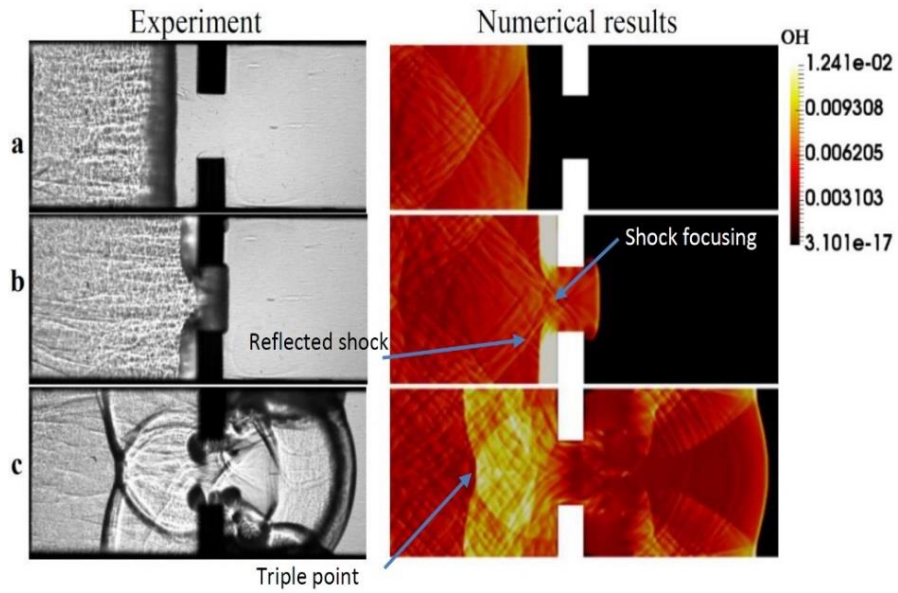

Figure 4-10: Comparison of experimental results of DDT of homogenous 30% Vol. hydrogen in BR 60 %, and x=2 m, (obstacle 7), with numerical results of OH distribution from VCEFoam in; a) time=9.42ms, b) time=9.44ms, c) time=9.48ms.

Figure 4-10 shows an excellent qualitative agreement between the experimental observations and the predicted OH distribution of homogeneous hydrogen flame DDT with the density-based solver. In Figure 4-10-a flame front is planer and moving toward the obstacle (the 7th obstacle in the tube), and two strong shock waves are generated behind the top and bottom obstacles. Figure 4-10-b shows that these two reflected shock waves are interacting in the middle of the tube and, as the results of shock focusing phenomena, a refraction shock wave will be generated in the downstream of flow. Then the generated shock wave interacts with the flame front and triggers a transition to detonation (Figure 4-10-c). Following DDT, the shock detonation structure can be seen, including a strong reflected shock wave as well as leading shock ahead of the flame front. Moreover, pressure gradient frames show the mechanism of shock and explosion generation (Figure 4-11) (Khodadadi Azadboni, Wen and Heidari, 2019).

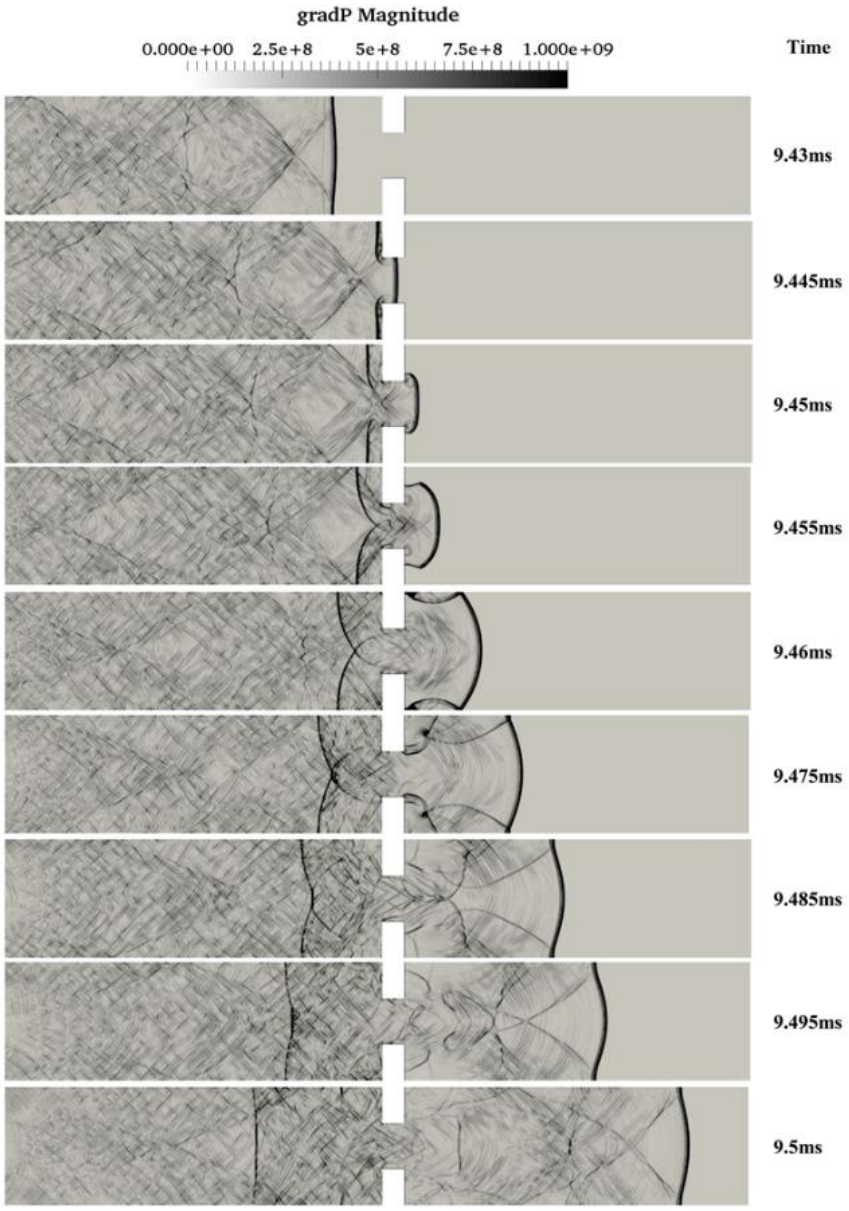

Figure 4-11: The magnitude of pressure gradient contours of deflagration to detonation for homogenous H2/Air mixture of 30% Vol and BR60.

Figure 4-11, shows the distribution of pressure gradient magnitude in the tube around obstacle 7. These results illustrate the evaluation of the shock waves. At 9.43 ms, a planner flame is moving toward the obstacle with a strong shock wave ahead of the flame front, as well as some weaker shock waves in the upstream of the flow field. Additionally, the reflected shock waves

from the upper and lower wall are interacting in the middle of the tube. Later, it can be observed that the leading shock is interacting with the obstacle and, as a result, a strong reflected shock is generated in the flow. The reflected shocks from the upper and lower obstacle interact in the middle of the tube causing a shock focusing (Figure 4-11, time=9.455ms). The reflected shock will generate a triple point in the detonation structure. Some part of the leading shock passes through the obstacle, slowly growing with the flame, until it reaches the upper and lower wall of the tube (Figure 4-11, time= 9.46 ms). At 9.475 ms, it can be seen that the reflected shock from the wall causes secondary triple point in the shock-flame structure. After 9.495 ms, the reflected shock waves from the upper and lower wall meet in the middle of the tube resulting in shock focusing phenomena in the downstream of the flow field. These results also illustrate that the obstacles and walls in the tube have a significant effect on shock generation ahead of the flame front.

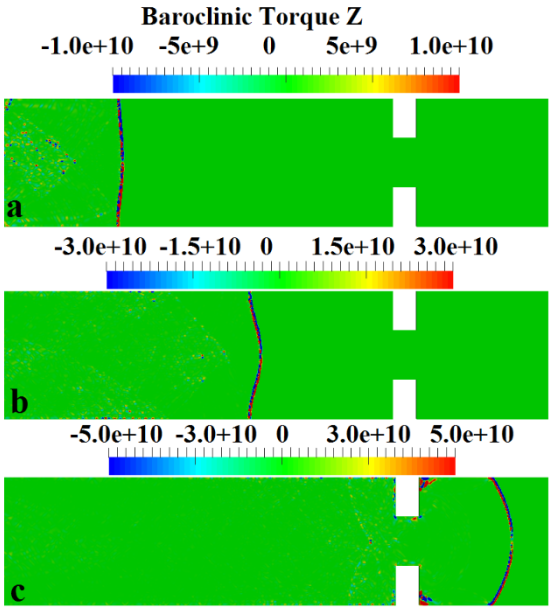

Figure 4-12: Baroclinic torque contour in the Z direction of DDT of homogenous hydrogen flame simulation with the density based solver, for BR=60 %, 30% H2 at a) time=9.0ms, b) time=9.14ms and c) time=9.18ms.

Figure 4-12 shows the predicted baroclinic torque distribution in the Z direction with the density-based solution. The baroclinic torque increases with time (Figure 4-12.a to Figure 4-12.c), so the pressure gradient has been increased respectively. Moreover, as shown in Figure

4-12.c, the magnitude of the Baroclinic torque (-5e+10 to +5e+10) is considerably higher than the predictions of the pressure-based model for the uniform mixture (as shown in Figure 4-8). Hence, the developed density-based solver has better capability of modelling shock-detonation phenomena (Khodadadi Azadboni, Wen and Heidari, 2019).

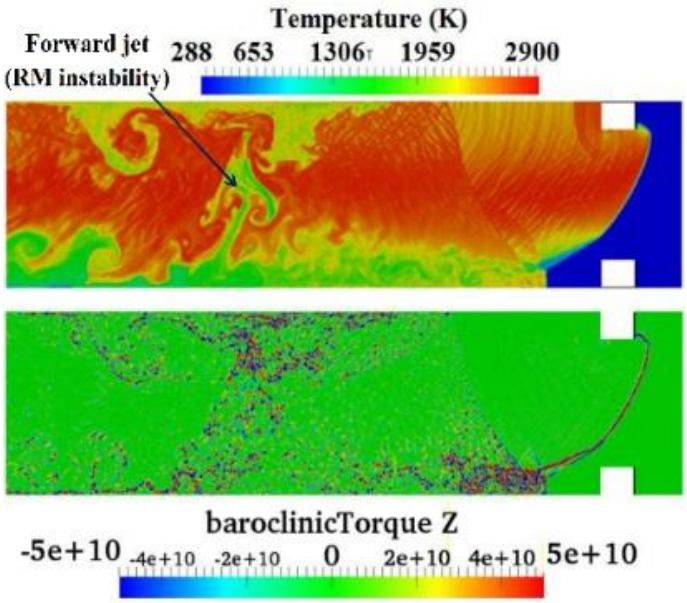

Figure 4-13: Inhomogeneous hydrogen-air with 30% Vol. on average mixture in the case with BR 30% and time=4.7ms; Top: temperature contour, Bottom: the predicted Baroclinic torque in the Z direction.

Figure 4-13 shows that DDT has occurred in the accelerated non-uniform hydrogen flame. The temperature contour indicates the formation of mushroom shape forward jets in the flame surface which is known as RM instabilities.

Furthermore, the predictions demonstrate that the overpressure at the DDT stage is higher in the non-uniform mixtures compared to the homogeneous mixtures under similar conditions. Besides, the results highlight that the Baroclinic torque and resulting RM instability has a substantial effect on flame acceleration and DDT. The results also suggest that higher baroclinic torque in the flow field would induce more RM instability, and hence increase the possibility of DDT (Khodadadi Azadboni, Wen and Heidari, 2019).

4.4 Detonation test case

4.4.1 Detonation cellular structure

As it has been described in Chapter 2, detonation is a high pressure supersonic strong explosion, where the speed of the explosion wave exceeds the local speed of sound. The appearance of a shock wave is the main feature of detonation. Due to the rapid energy release, the reaction zone is subsonic in the frame of the shock and supersonic concerning the undisturbed gas. When the shock waves interact with each other, Mach stems and cells are formed. In premixed combustion, the reactive detonation front is carried by the shock with supersonic speed.

The cellular structure of detonation has shown can be observed in chapter 2, as well as here in Figure 4-14.

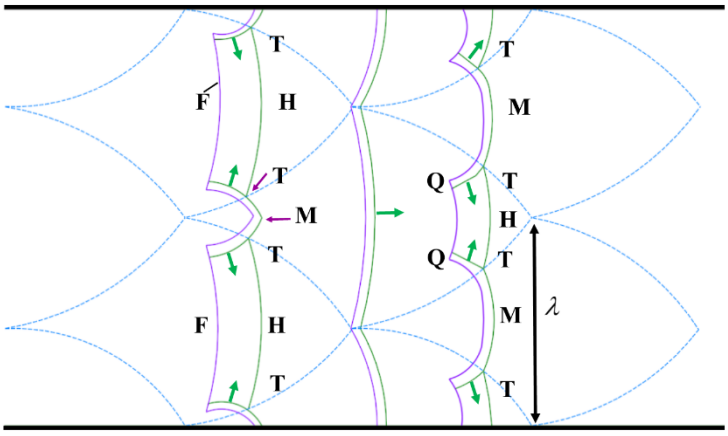

Figure 4-14: Cellular structure schematic, reproduced from (Hasslberger, 2017); flame-coloured in purple and shocks coloured by green.

Detonation can be defined as a shock-induced combustion wave. The one-dimensional theories such as CJ and ZND can calculate a decent prediction of detonation characteristic parameters. However, experimental works have shown that the detonation front is not planar, and it is a multi-dimensional structure. Multi-dimensional instabilities in the form of perpendicular shock waves to the main propagation direction on the detonation front also exist. In a detonation front, because of the interaction of a transversally running shock (TS) with a main running shock

(LS), a Mach stem (M) progresses. Based on shock superposition theory, pressure and temperature of unburned gas behind the longitudinally running main shock (LS), is lower than behind the Mach stem (Hasslberger, 2017). The interaction points of transverse shock, Mach stem and longitudinal shock is the triple point (T). Ultimately, the triple points trajectory (which is shown by dashed line) forms the characteristic fish-like shape which indicates "detonation cells" and the development of detonation cells will produce the detonation cellular structure. The perpendicular (to the main propagation direction) dimension of that cell is represented as the detonation cell size (it is marked by λ in Figure 4-14). The cellular patterns of various mixtures are distinguished with the cell's characteristic length L, width λ, as well as the irregularity of the pattern.

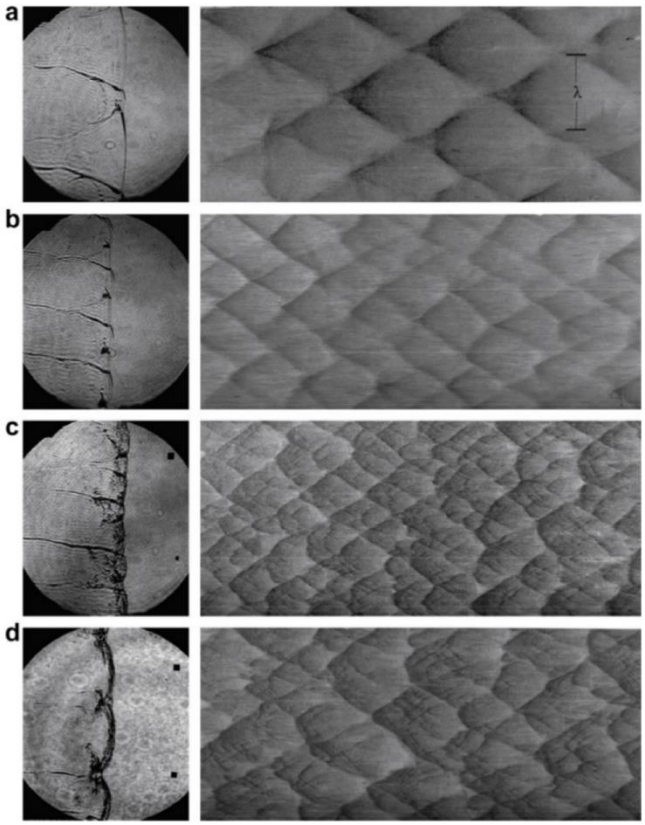

Figure 4-15: cellular detonation structure for different mixtures. (a) 2H2 + O2 + 17Ar, (b) 2H2 + O2 + 12Ar, (c) H2 + N2O + 1.33N2, (d) C3H8 + 5O2 + 9N2. Left hand side: Schlieren of density, right hand side: smoke foil (Shepherd, 2009).

Figure 4-15 shows different examples of detonation front and cellular structure of detonation (Shepherd, 2009). Figure 4-15 demonstrates that the detonation front has a curvature shape, and triple points are the discontinuities of the curvatures (which are the intersections of the main shock wave and transverse waves) Figure 4-15-a and Figure 4-15-b shows a regular detonation pattern and Figure 4-15-c and Figure 4-15-d shows unstable detonation and very irregular cellular pattern.

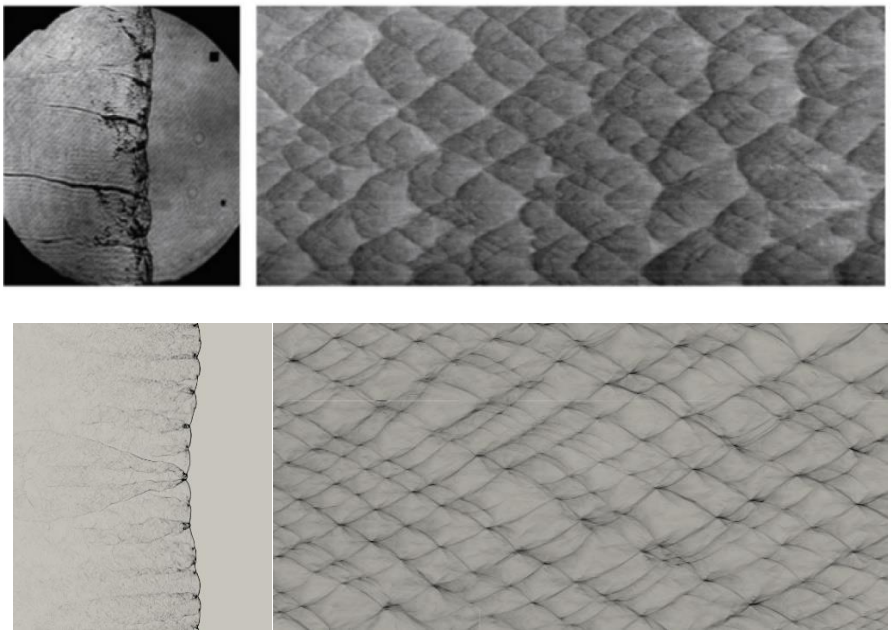

Figure 4-16: Structure of detonation front and cells for hydrogen/air mixture. Left: density Schlieren, right: smoke foil. Top row: Images from(Shepherd, 2009), bottom row: CFD results.

Figure 4-16 shows an irregular cellular structure of the detonation front and for hydrogen/air mixture. On the left-hand side, density Schlieren, and on the right-hand side, smoke foil presented. The top row is the experimental observation images from(Shepherd, 2009), bottom row: CFD results (note that the CFD setup is not exactly the same as the observation in (Shepherd, 2009)).

In order to capture the details of the detonation structure accurately, a high-resolution mesh is required. Also, to resolve the detonation front based on the literature (Mazaheri, Mahmoudi and Radulescu, 2012), it has been recommended that at least 20 grids within the detonation half reaction length (HRL) should be provided. Also, in order to capture small scale features such as KH or RM instabilities, even higher grid resolution is needed. Mazaheri, Mahmoudi and Radulescu, (2012) recently analysed high resolution two-dimensional numerical simulations of gaseous detonations both in high and low activation energies. In their research study, they mentioned that in the case of having high activation energy ($\frac{E_a}{RT_0} = 20$), which will cause an irregular detonation structure, much higher grid resolution (e.g. 300 per half reaction

length) is required to capture the effect of KH and RM instabilities in detonation propagation. However, they found that for lower activation energies $\frac{E_a}{RT_0} = 10$, which will be a regular detonation structure due to non-appearance of the small scales, using 50 grids per HRL is sufficient to capture most of the details.

In this section, a reasonably high-resolution (20 grid points per half-reaction length) 2D simulation of hydrogen/air mixture detonation in a 6 by 50 cm tube is modelled. The detonation is initiated by using three initial high pressure and temperature regions in the left-hand side of the domain, and the detonation wave propagates from left to right side of the domain (see Figure 4-20). This test case will show the capability of VCEFoam code in predicting the detonation cellular structure. The half-reaction length and detonation cell size for hydrogen/air mixture are about 167.3 µm and 1-2 cm respectively (the detonation cell size will differ by many factors, such as initial ambient pressure or initial ambient temperature as well as the fuel equivalence ratio). A 4.64 µm grid size is chosen which gives about 36 cells per half reaction length. The Courant number is set at 0.2 to avoid large time steps during the solution.

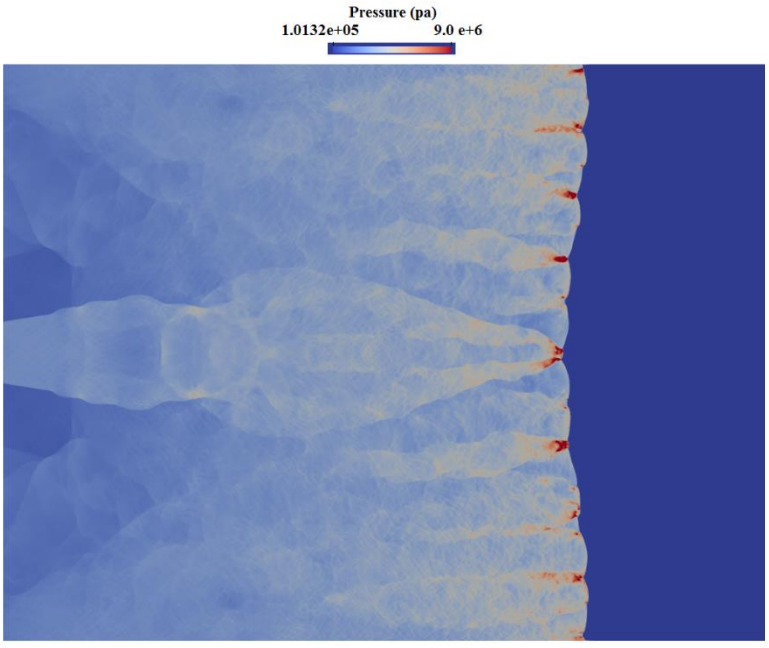

Figure 4-17: High-resolution detonation simulation, 33 points within the half reaction zone.

Figure 4-17 shows a pressure distribution of the detonation front. The triple points, as well as the transverse waves behind the detonation front, can be found in this snapshot. A schematic diagram of a triple point, as well as the Mach stem interaction with the incident shock and the reflected shock (also known as a transverse wave), is shown in Figure 4-18. The triple point is propagated to the downstream end by a strong shock wave called Mach stem. The reflected shock and the Mach stem enclose the slip line and the contact discontinuity. The shock front inside the detonation cell propagates. While two Mach stems propagate from point A to the line BC, the shock front in the detonation wave will move too. The triple point configuration has been reversed in the points B and C, and the detonation front in the cell turns into the incident shock. End to end of the symmetry line AD the change is smooth, and the shock strength reduced continuously. The two triple points in point D combine to a single triple point. Then, the incident shock disappears entirely, and the slip line, which was necessary for a study triple point formation between Mach stem and incident shock, will tear apart and remains behind the shock. Subsequently, two new triple points with two new slip lines will develop (Deiterding, 2005).

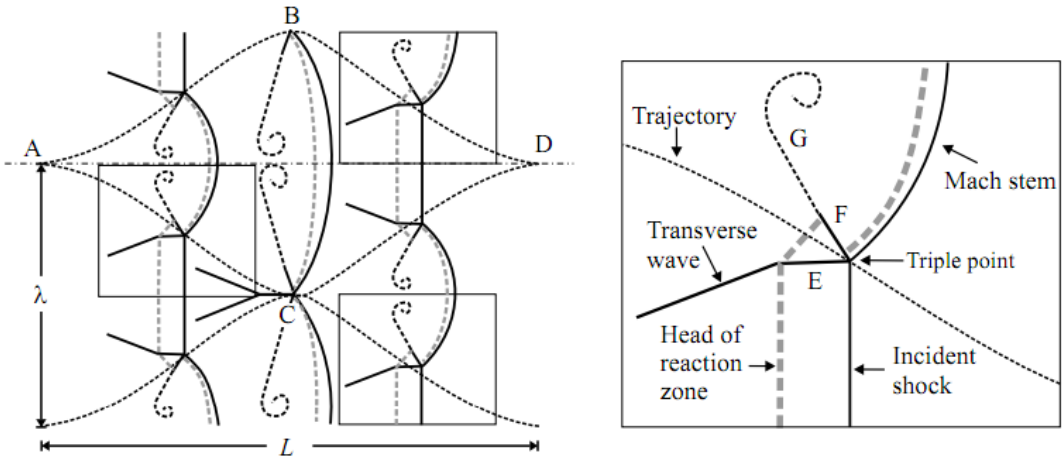

Figure 4-18: The schematic of triple point reproduced from (Deiterding, 2003).

In the present study, the detonation cellular structure has been recorded by tracing the triple points. Therefore, in order to track the triple points, the locus of the maximum pressure points

has been tracked, as they are sweeping over the domain while the detonation front propagates forward. Figure 4-19 represents an irregular cellar detonation pattern, which is resulted from a high activation energy. In this mixture, the CJ detonation velocity, is D_{CJ}=1980 m/s (Heidari, 2012), whilst the average recorded detonation velocity in the current high-resolution simulation, is D=1989 m/s (which is in good agreement with the theoretical CJ detonation velocity).

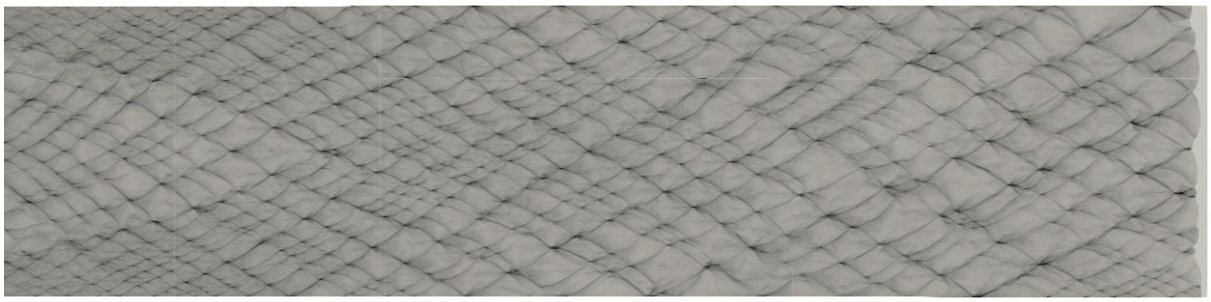

Figure 4-19: Numerical schlieren of soot foil for high activation energy case, and relatively irregular cellular detonation pattern.

In the following, a two-dimensional test case has been modelled to validate the capability of the current numerical model in capturing the detonation cellular structure. Moreover, the test case has been verified by numerous previous numerical works as well as an experimental observation.

4.4.2 Predictions of cellular detonation-verification test case

A two-dimensional test case has been selected to examine the capability of VCEFoam in capturing the cellular detonation structures. The schematic of the rectangular domain is shown in Figure 4-20. High pressure ($1000 \times p_0$ (atm)) and temperature perturbation ($25 \times T_0$ (K)) were initiated to trigger the detonation waves in the red regions. All four sides of the domain were assumed to have a wall with no-slip boundary conditions.

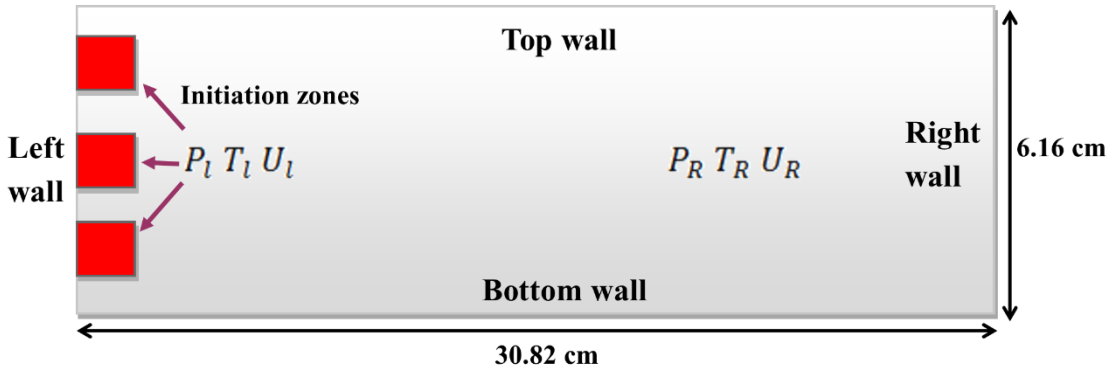

Figure 4-20: Schematic of a two-dimensional rectangular channel.

As mentioned previously, the mesh resolution has a significant impact in capturing the details of the detonation structure as well as having a direct relation with the induction length. The induction time in the unburned combustible mixture is $\tau_i \approx 119\ \mu s$ and the induction length is $L_i \approx 1.3\ mm$. In this test case, the grid resolution is 0.065 mm, providing 20 points in the induction length. The maximum Courant number has been set to 0.15. The Marinov's (Marinov, Westbrook and Pitz, 1996) hydrogen/air reaction mechanism is used. An important factor affecting the detonation cell size is the mixture equivalence ratio, e.g. rich mixture (high reactivity) produces smaller detonation cell size. Therefore, a hydrogen/oxygen mixture diluted with argon was used to capture the cell with lower computational costs. Argon dilution will decrease the mixture reactivity and result in overprediction of the detonation cell size (Marcantoni, Tamagno and Elaskar, 2017). The stoichiometric hydrogen/oxygen mixture diluted with argon is $2H_2$: O_2: 7Ar. It is presumed that the diluent Ar substitutes and plays a similar role to N_2 as inert species in the Marinov's reaction mechanism (Marinov, Westbrook and Pitz, 1996).

Table 4-2: H_2/Air reaction mechanism (Marinov, Westbrook and Pitz, 1996)[units: s, mol, cm^3, cal and K].

Reaction	A	b	Ea
(1) $OH + H2 \rightleftarrows H + H_2O$	2.14E+08	1.52	3449.0
(2) $O + OH \rightleftarrows O_2 + H$	2.02E+14	-0.4	0.0
(3) $O + H_2 \rightleftarrows OH + H$	5.06E+04	2.67	6290.0
(4) $H + O_2(+M) \rightleftarrows HO_2(+M)$	4.52E+13	0.0	0.0
low	1.05E+19	-1.257	0.0
(5) $H + O_2(+N_2) \rightleftarrows HO_2(+N_2)$	4.52E+13	0.0	0.0
low	2.03E+20	-1.59	0.0
(6) $H + O_2(+H_2) \rightleftarrows HO_2(+H_2)$	4.52E+13	0.0	0.0
low	1.52E+19	-1.133	0.0
(7) $H + O_2(+H_2O) \rightleftarrows HO_2(+H_2O)$	4.52E+13	0.0	0.0
low	2.10E+23	-2.437	0.0
(8) $OH + HO_2 \rightleftarrows H_2O + O_2$	2.13E+28	-4.827	3500.0
(8b) $OH + HO_2 \rightleftarrows H_2O + O_2$	9.10E+14	0.0	10964.0
(9) $H + HO_2 \rightleftarrows OH + OH$	1.50E+14	0.0	1000.0
(10) $H + HO_2 \rightleftarrows H_2 + O_2$	8.45E+11	0.65	1241.0
(11) $H + HO_2 \rightleftarrows O + H_2O$	3.01E+13	0.0	1721.0
(12) $O + HO_2 \rightleftarrows O_2 + OH$	3.25E+13	0.0	0.0
(13) $OH + OH \rightleftarrows O + H_2O$	3.57E+04	2.4	-2112.0
(14) $H + H + M \rightleftarrows H_2 + M$	1.00E+18	-1.0	0.0
(15) $H + H + H_2 \rightleftarrows H_2 + H_2$	9.20E+16	-0.6	0.0
(16) $H + H + H_2O \rightleftarrows H_2 + H_2O$	6.00E+19	-1.25	0.0
(17) $H + OH + M \rightleftarrows H_2O + M$	2.21E+22	-2.0	0.0
(18) $H + O + M \rightleftarrows OH + M$	4.71E+18	-1.0	0.0
(19) $O + O + M \rightleftarrows O_2 + M$	1.89E+13	0.0	-1788.0
(20) $HO_2 + HO_2 \rightleftarrows H_2O_2 + O_2$	4.20E+14	0.0	11982.0
(20a) $HO_2 + HO_2 \rightleftarrows H_2O_2 + O_2$	1.30E+11	0.0	-1629.0
(21) $OH + OH(+M) \rightleftarrows H_2O_2(+M)$	1.24E+14	-0.37	0.0
low	3.04E+30	-4.63	2049.0
Troe [0.470 100.0 2000.0 1.0E+15]			
(22) $H_2O_2 + H \rightleftarrows HO_2 + H_2$	1.98E+06	2.0	2435
(23) $H_2O_2 + H \rightleftarrows OH + H_2O$	3.07E+13	0.0	4217.0
(24) $H_2O_2 + O \rightleftarrows OH + HO_2$	9.55E+06	2.0	3970.0
(25) $H_2O_2 + OH \rightleftarrows H_2O + HO_2$	2.40E+00	4.042	-2162.0

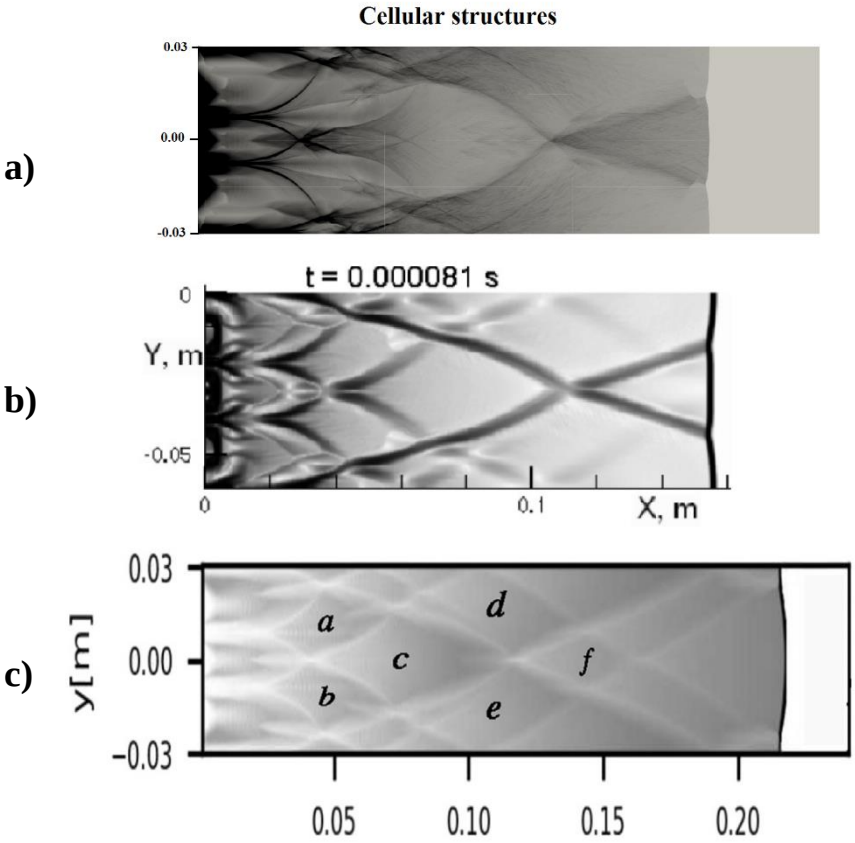

Figure 4-21: Detonation cellular structure development close to the ignition sources; a) VCEFoam, b) (Kirillov *et al.*, 2005), c) (Marcantoni, Tamagno and Elaskar, 2017)

Figure 4-21 shows the development of the detonation cellular structure close to the ignition sources. In the present work, the cellular structure has been captured by tracing the triple points in the domain. For tracing triple points, the maximum pressure in each time step of the solution has been stored in memory, and as a result, the cellular pattern could have been captured. In Figure 4-21 other previous CFD works have been included for comparison. It can be seen that the current captured cellular structure is closer to the previous CFD analysis of Kirillov (Kirillov *et al.*, 2005) which can be seen in Figure 4-21-b.

Table 4-3: Comparison of cellular structure cell size for H2/Air mixtures.

Reference	α (m) (Cell length)	λ (m) (Cell height)	c^{ar}(m) (Aspect ratio λ/α)	Reaction kinetic
Marcantoni et. al (Marcantoni, Tamagno and Elaskar, 2017)	0.074	0.032	0.43	Marinov (Marinov, Westbrook and Pitz, 1996)
Kirillov et. al (Kirillov *et al.*, 2005)	0.078	0.033	0.42	Marinov (Marinov, Westbrook and Pitz, 1996)
Eckett (Eckett, 2001)	0.054	0.03	0.55	8species/24reactions (Burks and Oran, 1981)
Oran et. al (Oran *et al.*, 1998)	0.055	0.03	0.54	8species/24reactions (Burks and Oran, 1981)
Lefebvre & Oran (Lefebvre and Oran, 1995)	0.077	0.03	0.42	Two steps model (Oran *et al.*, 1981)
Lefebvre et. al (Experimental) (Lefebvre, Weber and Oran, 1997)	0.17	0.09	0.52	Smoke foil
VCEFoam (present work)	0.785	0.033	0.0420	Marinov (Marinov, Westbrook and Pitz, 1996)

Table 4-3 shows a comparison of cellular structure cell size for H2/Air mixtures. In this table, the detonation cell length (α), Cell height (λ, also called cell size), and the cell dimension aspect ratio ($c^{ar} = \lambda/\alpha$), have been provided for different numerical and experimental observations. It can be seen that the predicted cell size of the present work (VCEFoam) are in acceptable agreements with results of Kirillov et al. (Kirillov *et al.*, 2005), Marcantoni et al.

(Marcantoni, Tamagno and Elaskar, 2017) and Lefebvre & Oran (Lefebvre and Oran, 1995). Note that the numerical setup (boundary and initial conditions) in the present work, is similar to the numerical work done by Kirillov et al. (Kirillov *et al.*, 2005) , Marcantoni et al. (Marcantoni, Tamagno and Elaskar, 2017) .

The experimental data presented by Lefebvre, Weber and Oran, (1997) shows a significant difference in cell size, compared to all the other numerical studies; however, the presented aspect ratio of the experimental observation is close to those given in (Oran *et al.*, 1998; Eckett, 2001). One of the possible reasons would be the case that in the experimental observation, due to having a strong ignition source, the first detonation cell was not clear in the shadowgraphs; therefore, the neighbour cell downstream of the tube has been presented. Hence, for further investigation, the same test case has been modelled with tube length extended to 0.5 m.

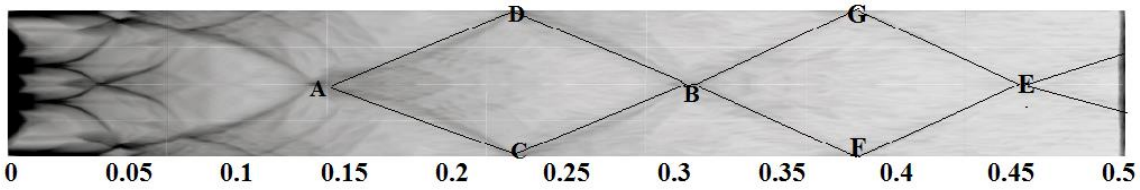

Figure 4-22: Cellular structure in the extended channel

The numerical schlieren of maximum pressure which indicates the cellular structure for the extended channel (to 0.5 m) is presented in Figure 4-22. During the initial stage, the cellular structure is similar to the one presented in Figure 4-21-a (shorter channel). However, in the middle of the domain towards the downstream end two much bigger cells have been formed (ACBD, and CFEG). These developed cells have a length of $\alpha_{ACBD} = 0.165\ m$ and $\alpha_{CFEG} = 0.15\ m$ which are very close to the value presented in the experimental observation ($\alpha_{Experiment} = 0.17\ m$).

Next, a qualitative comparison of the predicted detonation cell ACBD will be compared with other numerical works as well as an experimental observation.

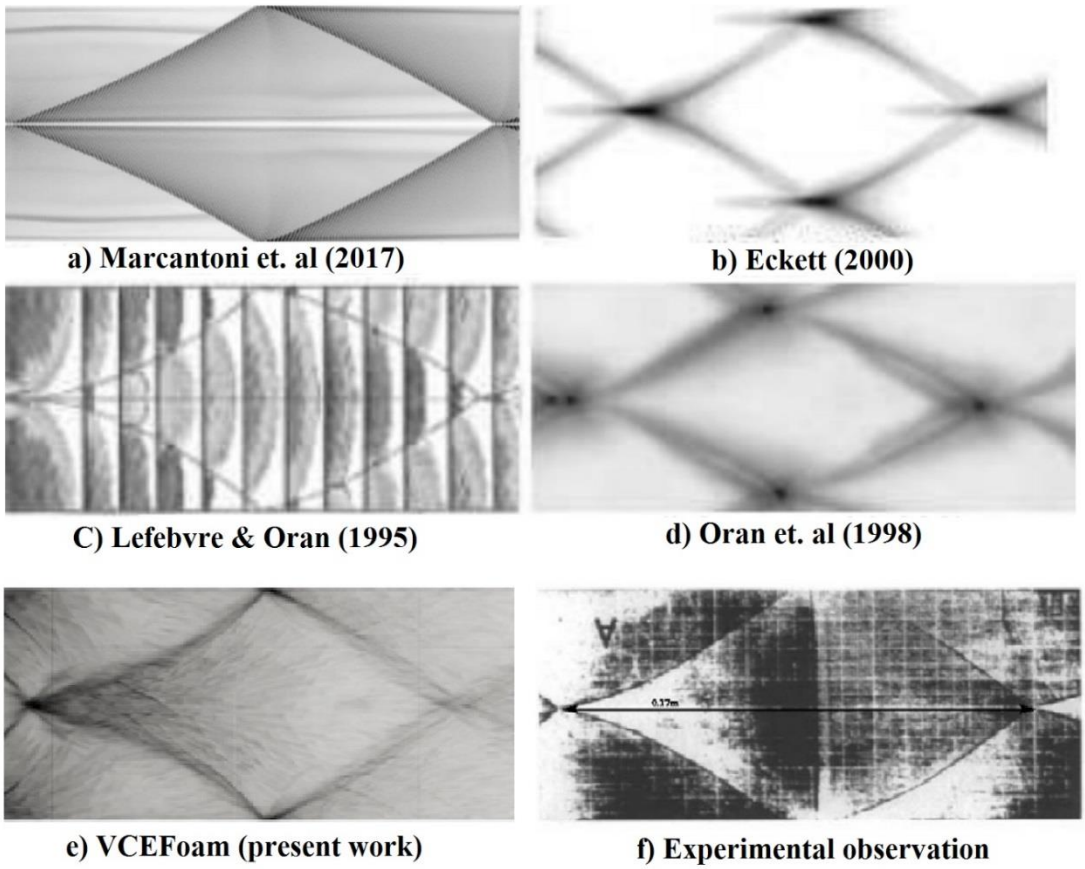

Figure 4-23: Comparison of Detonation cellular structure.

Figure 4-23 shows a comparison of detonation cellular structure in hydrogen/air mixture of various other CFD and experimental works. It can be seen that the current captured detonation cell (Figure 4-23-e) is in good agreement with other past similar works. The captured detonation cell in this study is more similar to the experimental observation as well as the work done by (Lefebvre and Oran, 1995), (Figure 4-23-c-f).

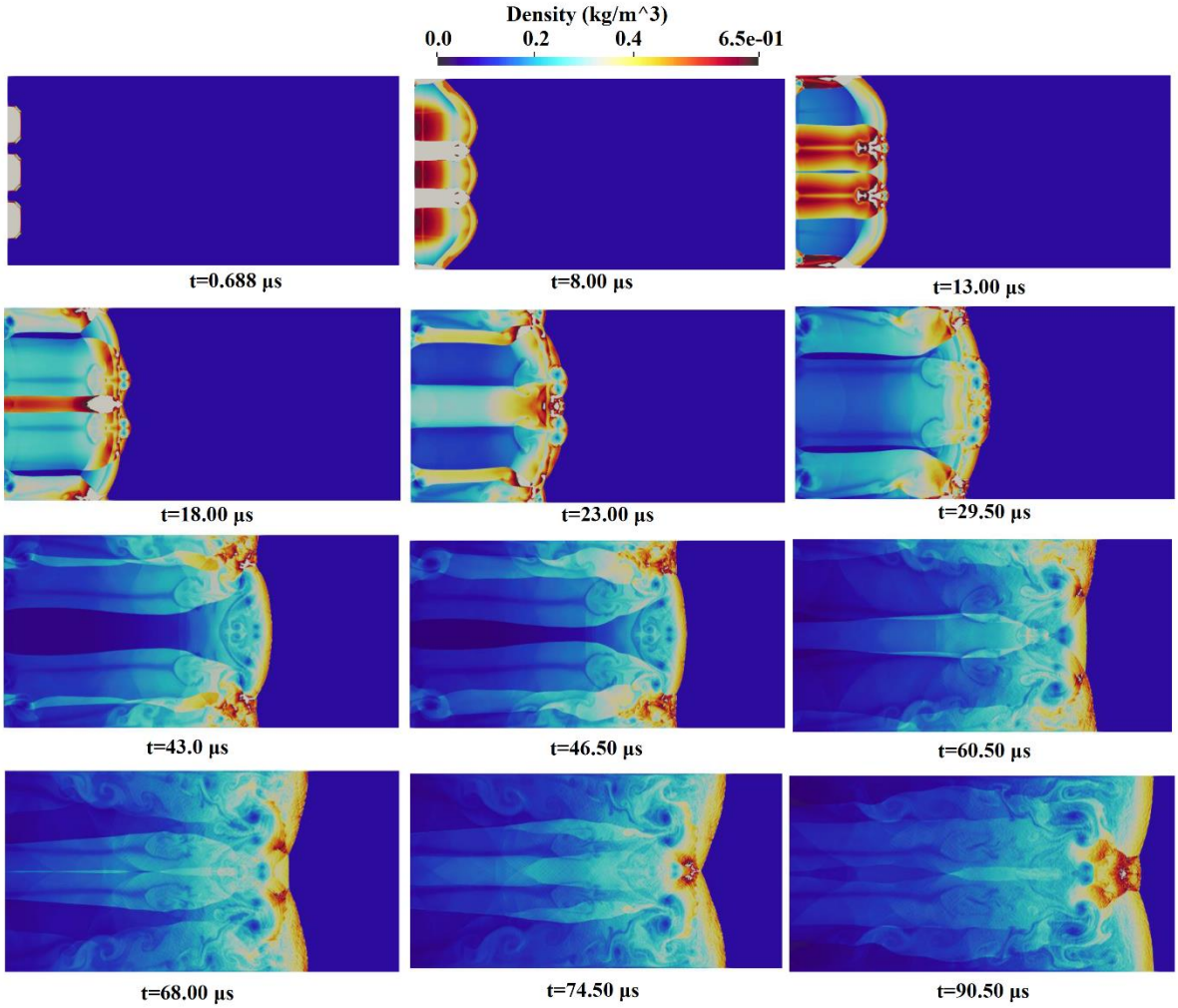

Figure 4-24: Density distribution: Cellular structure formation process: Evolution of triple points.

Figure 4-24 shows the density distribution of the cellular structure formation process. The evolution of triple points can also be seen in these snapshots. Figure 4-24 (t=0.688 µs) shows the three ignition areas which act as detonation initiations. Also, in the density snapshot, some small-scale features have been captured, such as forward and backward jets in the detonation fronts which indicates the RM instability.

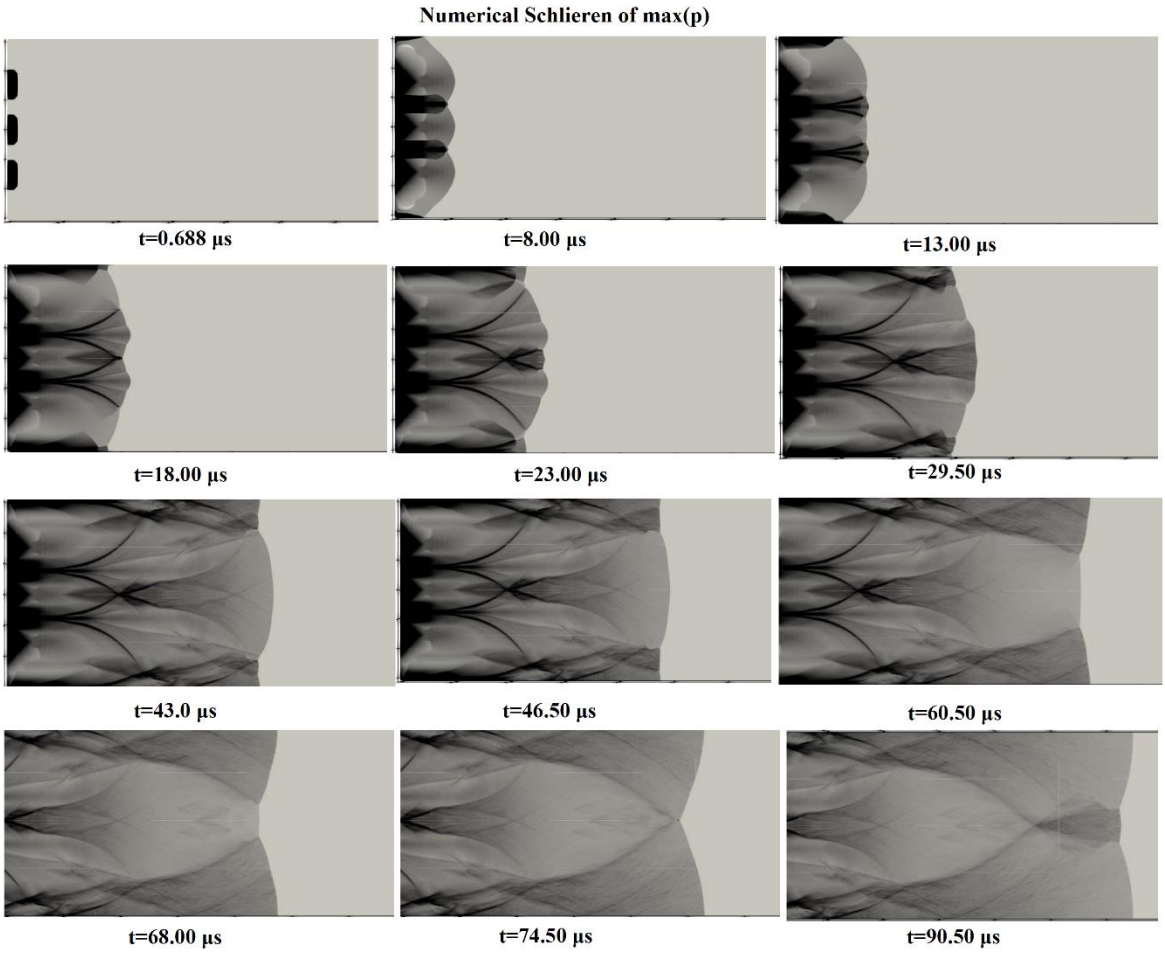

Figure 4-25: Numerical schlieren of maximum pressure distribution: Cellular structure formation process: Evolution of triple points.

Figure 4-25 shows numerical schlieren of the maximum pressure distribution of the cellular structure formation process. Also, the evolution of triple points can be seen in these snapshots. It can be seen that the first three perturbations have generated some triple points in the detonation front. Moreover, as a result of a secondary shock collision with the detonation front, a new triple point has been produced (23 µs). The trajectory of the triple points has produced some fish-cell sketches which represent cellular structure.

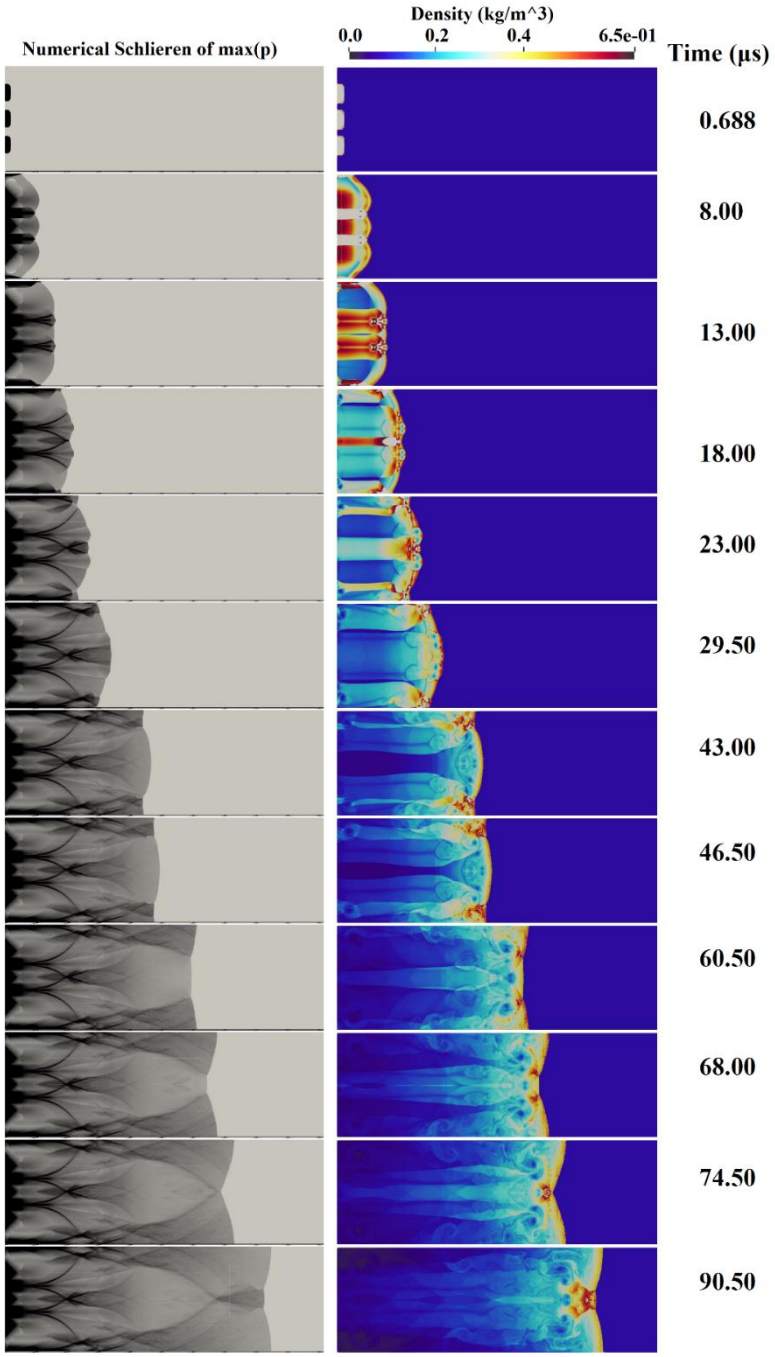

Figure 4-26: Trajectory of the triple points. Left: numerical schlieren of maximum pressure, right: density distribution.

Figure 4-26 shows the trajectory of the triple points, in which the left side shows the numerical schlieren of maximum pressure, and the right side presents the density distribution. The evaluation of triple points and how they produce a cellular structure can be found by comparing the numerical schlieren of maximum pressure and the density contours at the same time.

At t=0.688 μs, three ignition areas which act as detonation initiations can be found. At 8 μs, three semi-circular detonation fronts propagate downstream and also, as a result of interacting these detonation waves, two critical points (triple points) have been generated on the detonation front. Later, some shock waves reflect from both top and bottom walls before interacting with the other transverse and reflected shocks (at t=23 μs). This interaction of the reflected shock and detonation front will produce an additional triple point. From 29.5 μs onwards it can be seen that the two triple points are moving from top and bottom towards the middle of the domain. At 74.40 μs it can be found that the two triple points meet each other in the middle of the domain, and as a result, another strongly localised detonation occurs. At 90.50 μs it can be seen that two triple points are diverging from the middle and moving towards the top and bottom. Eventually, by tracking these triple points, the trajectory of these points will show "fish-cell" sketches which represent detonation cellular structure.

4.5 Summary

For verification of the developed numerical model, four sets of verification problem have been considered:

5. Shock capturing: 1D Sod's shock tube problem
6. Supersonic wedge: 2D oblique shock
7. DDT test case: comparison between pressure-based and density-based solution
8. 2-D detonation initiation test case: cellular structure

Sod's shock tube problem and supersonic wedge for oblique shock problems have been modelled. In both 1D shock capturing test case and 2D oblique shock test case, the predicted

pressure, temperature distributions are in excellent agreement with the analytical solutions. The present results accurately capture the above-mentioned important characteristics of the flow, i.e. the rarefaction wave, the contact discontinuity, and the shock discontinuity. This has demonstrated that the density-based solutions can provide accurate shock capturing.

Furthermore, a DDT test case has been modelled to study the comparison between pressure-based and density-based solution methods. In the detonation initiation test case, the capability of the current numerical code in capturing the detonation cellular structure has been examined. A small test case has been modelled with using three high ignition point to produce detonation initiation. The CFD results have been compared against both quantitatively and qualitatively with the other previous works as well as an experimental observation. The captured detonation cell size was in good agreement with the other CFD works and the experimental observations. Also, the evaluation of triple points and cellular structure development has been investigated.

Chapter 5 Deflagration-to-Detonation Transition (DDT) in Medium Scale

5.1 Flame acceleration and Transition to Detonation

While the vast majority of explosions in the industry are deflagrations, a worst-case scenario can emerge if the transition from deflagration to detonation occurs during the explosion. Deflagrations require congestion and confinement to generate significant overpressures; by contrast, detonations inherently produce high overpressure and have the potential to propagate through large unobstructed and unconfined areas without substantial weakening.

Although DDT in homogenous mixtures has been widely investigated (Ciccarelli and Dorofeev, 2008), relatively fewer studies have addressed the effects of spatial gradients in mixture composition. Kuznetsov *et al.*, (2011) conducted large-scale experiments of FA and DDT in an obstructed semi-confined flat layer of a hydrogen-air mixture with transverse concentration gradients and found that DDT propensity in semi-confined mixtures with concentration gradients might be determined by the maximum local hydrogen concentration for globally lean mixtures. Vollmer, Ettner and Sattelmayer, (2012) and Boeck, Hasslberger and Sattelmayer, (2014); Boeck, (2015); Boeck *et al.*, (2016) reported a strong effect of concentration gradients on FA and DDT in an entirely closed channel at laboratory-scale. However, Boeck et al. (Boeck *et al.*, 2016) also observed that in a channel with obstructions, only in lean mixtures with an average hydrogen concentration below about 24%, concentration gradients promote FA and DDT, whereas for richer mixtures the presence of gradients leads to weaker FA and retards DDT. The authors proposed a mixture-averaged analytical model for flame speed (σS_L) to predict this effect. By contrast, for unobstructed channels, gradients always led to stronger FA and earlier DDT, independent of the average hydrogen concentration, due to flame surface area enlargement is driven by spatial gradients in flame speed.

This chapter aims at generating a physical understanding of flame acceleration (FA), onset of detonation and detonation propagation in H2–air mixtures with transverse concentration gradients in an entirely confined area. Since extensive knowledge on these processes has been built up over the decades for homogeneous mixtures, the strategy is to identify similarities and differences induced by concentration gradients. The focus is clearly placed on the influence of mixture, in contrast to the often investigated influence of obstructions geometry.

The present work numerically investigates several cases that were studied experimentally by Boeck et al. (Boeck *et al.*, 2016). In addition to comparison with the measurements for model validation, detailed predictions of the field variables which were not measured in the experiments are analysed to examine the effects of concentration gradients further. DDT locations can be identified with high accuracy in the numerical simulations, whereas this is challenging in experiments due to limited optical access and limited data acquisition rates.

5.2 The experiments considered:

DDT experiments of Boeck et al. (Boeck *et al.*, 2016) are considered which compare homogeneous and inhomogeneous hydrogen-air mixtures regarding flame speed and overpressure. The experiments were conducted in a horizontal channel with and without internal obstructions. As shown in Figure 5-1, the channel measured 5.4 m (L) × 0.3 m (W) × 0.06 m (H). Two obstructed configurations is considered: seven flat-plate obstacles with a blockage ratio of 60% (BR60), and 30% (BR30) in different cases, were placed in a region $0.25m < x < 2.05m$ from the ignition location at the left end of the channel with an obstacle spacing of 0.3 m while the remaining channel length was unobstructed. The obstacle thickness is 0.012 m (shown in Figure 5-2). In addition, an unobstructed configuration (BR00) is considered where all obstacles were removed.

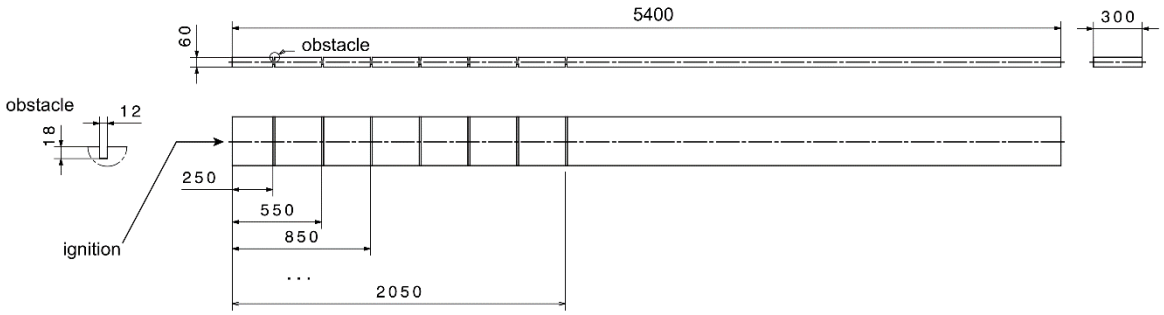

Figure 5-1: Geometry of the explosion channel, obstructed configuration (BR60). Dimensions are in (mm).

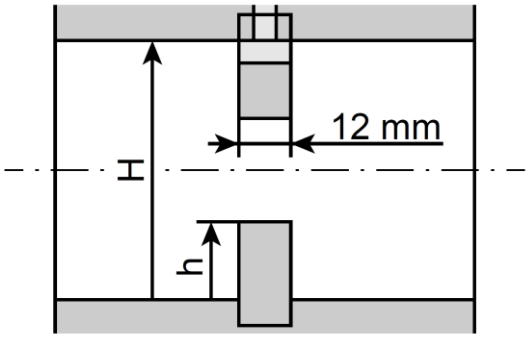

Figure 5-2: Side view schematic of obstacle configuration (Boeck *et al.*, 2016).

5.2.1 Mixture concentration:

Concentration gradients as shown in Figure 5-3 were generated by gas injection through the channel top plate, formation of a hydrogen layer near the channel ceiling, and subsequent diffusion. The gradients were oriented vertically, thus perpendicular to the main direction of flame propagation. The mixture was ignited by a weak electric spark centred at x = 0 m. Measurements were conducted for flame-tip velocity using photodiodes, obtaining local flame speed by linear interpolation between arrival times, and overpressure using piezo-electric

pressure transduces at the channel ceiling. See (Boeck *et al.*, 2016) for further details on the experiment and diagnostics. Vertical concentration gradients are presented in Figure 5-3.

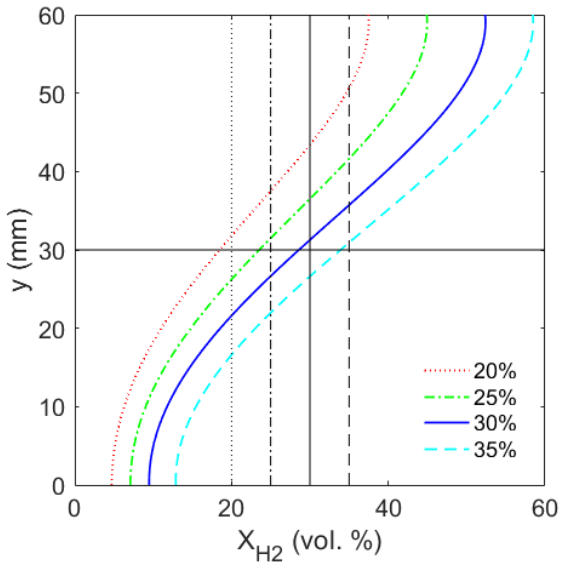

Figure 5-3: Hydrogen concentration profiles across the channel height of the average Hydrogen mixture between 20 and 35 vol.%

5.3 Numerical setup

For numerical modelling, the developed density-based code VCEFoam (Khodadadi Azadboni et al., 2017; Khodadadi Azadboni, Heidari and Wen, 2018; Khodadadi Azadboni, Wen and Heidari, 2019) is used with the Monotone Integrated Large Eddy Simulation (MILES) approach. Within VCEFoam, compressible Navier–Stokes equations with a hydrogen-air reaction mechanism which contains 9 species and 21 detailed reactions (Ó Conaire et al., 2004) are solved. The HLLC scheme (Batten, Leschziner and Goldberg, 1997) for shock capturing and the Runge-Kutta scheme (Borm, Jemcov and Kau, 2011) for the time discrete schemes are used, which include the dual time scheme and the physical time step. The solver and numerical schemes have been previously tested and been verified in chapter 4. In MILES turbulence methods, the local dissipation, can smoothly transport energy from the large scale, (which

eddies are resolved), to the smaller unresolved scales. This will be done by the natural dissipation effects which is available in these nonlinear monotone approaches.

In DDT where, the flow is highly reactive, the temperature increases lead to higher flow viscosity, υ, which reduces the Reynolds number and alters the dissipation scale. Therefore, the Kolmogorov length scale, $\left(\frac{\upsilon^3}{\varepsilon}\right)^{\frac{1}{4}}$ and time scale, $\left(\frac{\upsilon}{\varepsilon}\right)^{\frac{1}{2}}$, are even larger in highly reactive flow and hence, even smaller grid resolution would be required compared to a low temperature flow (Heidari, 2012).

Figure 5-4 shows the schematic diagram of the computational domain.

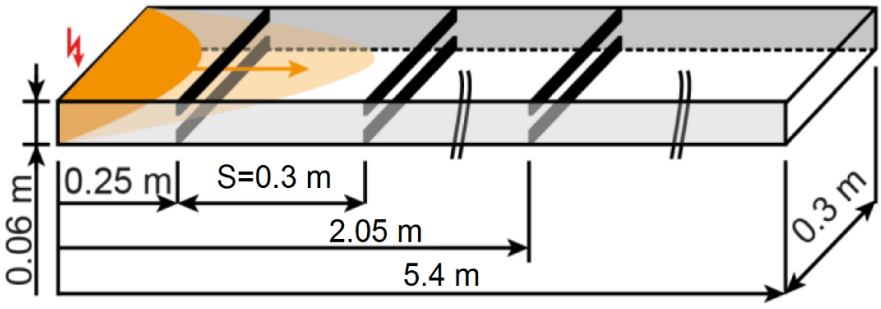

Figure 5-4: Schematic diagram of the computational domain.

Ignition has been modelled by using patch cells within a radius of 10 mm around the point of ignition (x=0, y=0.03m) to the burnt state (isobaric, adiabatic burnt mixture).

The following are the initial conditions:

- dt (time step) = $2 \times e - 07$
- Max Courant=0.3
- Inlet and outlet are closed so, all of the boundaries were; wall
- No slip boundary condition has been considered.
- For mesh independency four different mesh resolutions have been considered:
    1. dx1 (cell size for case 1 (coarse)) = 4 mm

2. dx2 (cell size for case 2 (medium)) = 100 µm
3. dx3 (cell size for case 2 (fine)) =10 µm
4. dx4 (cell size for case 2 (very fine)) =6 µm

- OpenMpi with OpenFOAM has been used for parallel processing.
- The initial hydrogen distribution varies in a vertical direction.
- The initial flow velocity is zero everywhere.

The models have been simulated on an HPC cluster, for these simulation 128 cores were used to simulate the DDT phenomena in the 5.4m channel (which is a medium scale test case). Moreover, using 128 cores, on a high-resolution mesh (10 µm) and a 21-step reaction mechanism requires around 28-35 days to simulate the whole DDT process.

5.3.1 Mesh Sensitivity Analysis

One of the important aspects of the CFD modelling is, making sure that the results of the numerical model are independent to the grid size. Two test cases (BR60% and 30% inhomogeneous mixture of H2/Air), with the initial and boundary condition in section 6.3, have been modelled with four different mesh resolutions.

The four different mesh resolution size has been selected as the following:

- coarse size mesh: 4 mm
- Medium size mesh: 100 µm
- Fine mesh: 10 µm
- Very fine mesh (Highest resolution mesh): 6 µm

The results of the overpressure probe as well as the flame tip velocities for these four cases have been compared with the experimental measurements.

Figure 5-5 shows the overpressure vs time and Figure 5-6 shows the flame tip velocity vs time, for the four mesh resolutions, in 60% blockage ratio (BR60), and 30% inhomogeneous mixture of hydrogen/air.

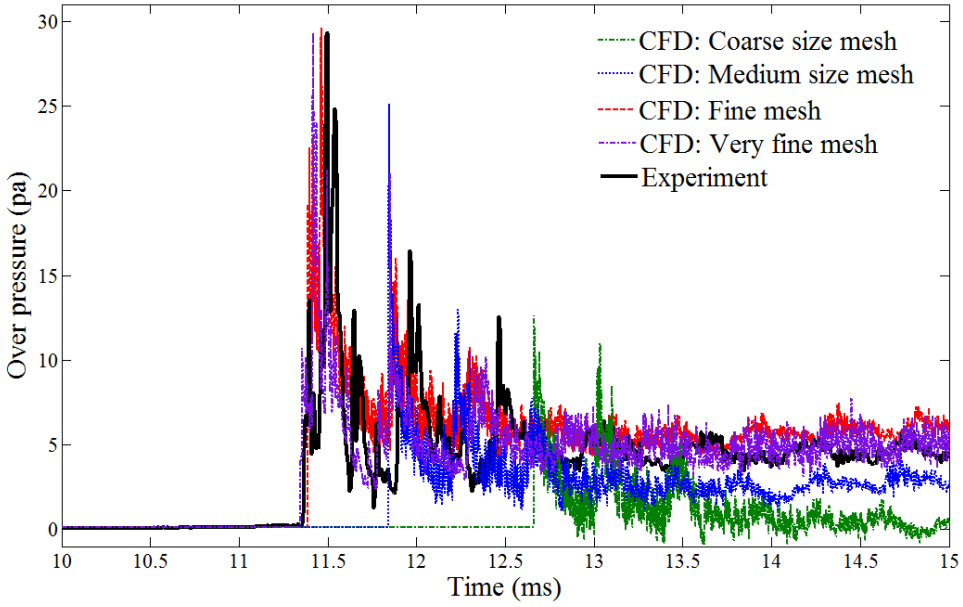

Figure 5-5: Grid independency study: overpressure vs time for 30% hydrogen/air mixture with BR60; probe location at x=1.4 m.

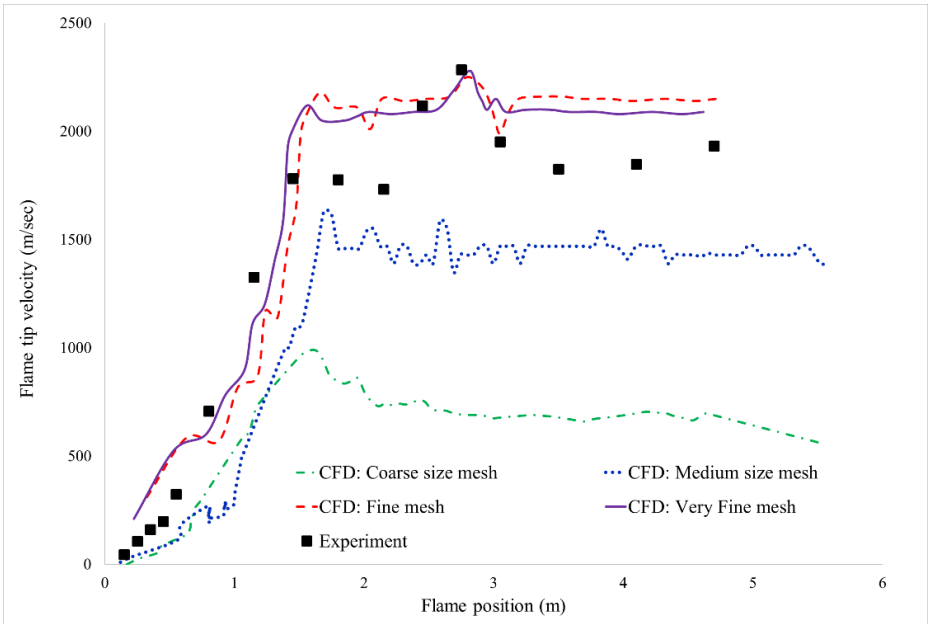

Figure 5-6: Grid independency study: Flame tip velocity vs flame position for 30% hydrogen/air mixture with BR60.

Figure 5-5 and Figure 5-6 show that by increasing the mesh resolution, from coarse to fine, the results of overpressure, as well as the flame tip velocity, become very close to the experimental measurements. It can be found that the coarse mesh, could not capture the transition to detonation phenomena and with this resolution, only the flame acceleration (deflagration) was captured. However, the results on the medium size mesh become closer to the experimental measurements, even though the CJ detonation velocity and the CJ pressure were not reproduced accurately. Finally it can be seen that the red and purple lines in Figure 5-5 and Figure 5-6, which represent the fine mesh (10 μm) and very fine mesh (6 μm), are in very good agreement with the experimental measurements (black squares in Figure 5-5 and Figure 5-6), and in both cases the CJ velocity and CJ pressure ratio, have been captured accurately. Hence, it can be seen that by refining the mesh from 10 μm to 6 μm, the results do not change significantly, therefore, it can be concluded that the results on the fine mesh (10 μm), are mesh independent. Therefore, for saving computational cost, 10 μm mesh resolution is used in this present study.

Also, as mentioned earlier in the inhomogeneous mixtures, the HRL varies across the domain due to concentration gradients, between 30 and 50 grid points per HRL (1/HRL). This resolution exceeds the resolution of previous 2-D DDT simulations in the literature (Sharpe, 2001; Gamezo, Ogawa and Oran, 2007; Ogawa, Oran and Gamezo, 2013; Emami *et al.*, 2015). Sharpe (Sharpe, 2001) observed that the results for grid resolutions above 20 1/HRL are sufficient. The present geometry is significantly larger than widely simulated mm-scale channels, and a resolution higher than what was used here would exceed presently available computational resources. Additional to the validation provided in this thesis, mesh sensitivity and validation can be found in previous publications (Khodadadi Azadboni *et al.*, 2017, 2019; Khodadadi Azadboni, Heidari and Wen, 2018; Khodadadi Azadboni, Wen and Heidari, 2019). In this study, adaptive mesh refinement was used to provide a minimum cell size of 10 μm, equivalent to a minimum of 30 grid points per half-reaction length.

5.4 Case studies:

For the considered experiment (Boeck *et al.*, 2016), different sets of configurations and fuel concentration have been studied. The other category is modelling Homogeneous and inhomogeneous mixture. Three different geometry configuration such as; BR00 (0%Blockagre ratio, smooth channel), BR30 (30 % blockage ratio), and BR60 (60% blockage ratio), have been considered in this study. Also, in order to study the effect of a concentration gradient, different mixture concentrations have been investigated in both homogenous and inhomogeneous mixtures.

As summarised in Table 5-1, a total of 17 conditions were simulated for different hydrogen concentrations in both homogeneous and inhomogeneous mixtures with and without obstructions.

Table 5-1: Test conditions numerically simulated.

Hydrogen concentration (%)	**Homogeneous**			**Inhomogeneous**		
	Unobstructed	BR60	BR300	Unobstructed	BR60	BR300
20		✓			✓	✓
25	✓			✓		
30	✓	✓	✓	✓	✓	✓
35	✓			✓		✓
40				✓	✓	✓

5.5 Results:

5.5.1 DDT in an unobstructed channel (BR00)

Table 5-2 provides a summary of the phenomena observed in the numerical simulations and experiments in the unobstructed channel configurations considered. It can be seen that in the unobstructed channel with the homogeneous mixture, DDT only occurs in the very rich mixture such as 35% hydrogen. However, in the inhomogeneous mixture, the transition to detonation occurs even in the lean mixture such as 25 % hydrogen concentration (Khodadadi Azadboni *et al.*, 2019).

Table 5-2: Summary of transition to detonation in the unobstructed channel.

Average Hydrogen concentration	**Homogeneous**	**Inhomogeneous**
20 %	No DDT (maximum flame speed = 45 m/s)	No DDT (maximum flame speed = 200 m/s)
25 %	No DDT (maximum flame speed = 150 m/s)	DDT at x=4.55 m
30 %	No DDT (maximum flame speed = 1000 m/s)	DDT at x=4.6 m
35 %	DDT at x=4.9 m	DDT at x=4.78 m

Table 5-2, shows that for non-uniform mixtures, run-up distance increase with increasing the average concentration. Boeck et al. (Boeck, Hasslberger and Sattelmayer, 2014) proposed a simple integral model for predicting the effective flame speed in non-uniform mixtures. Flame speed, being the product of expansion ratio and burning velocity, peaks at about X_H2 > 35%. Since run-up distance to DDT scales with flame speed, the presence of regions with X_H2 > 35% leads to an increase in run-up distance, which is the case for mixtures with global hydrogen concentrations beyond 25%.

5.5.1.1 Lean mixture (25% hydrogen concentration)

As shown in Figure 5-8 and , for the inhomogeneous mixture with 25% concentration, the predicted flame tip velocities, as well as overpressure, are in reasonably good agreement with the measurements. The flame tip velocity rises continuously in the channel. Transition to detonation occurs at x≈4 m. By contrast, in the homogeneous mixture, the flame acceleration is weak and maximum overpressure is far below CJ pressure.

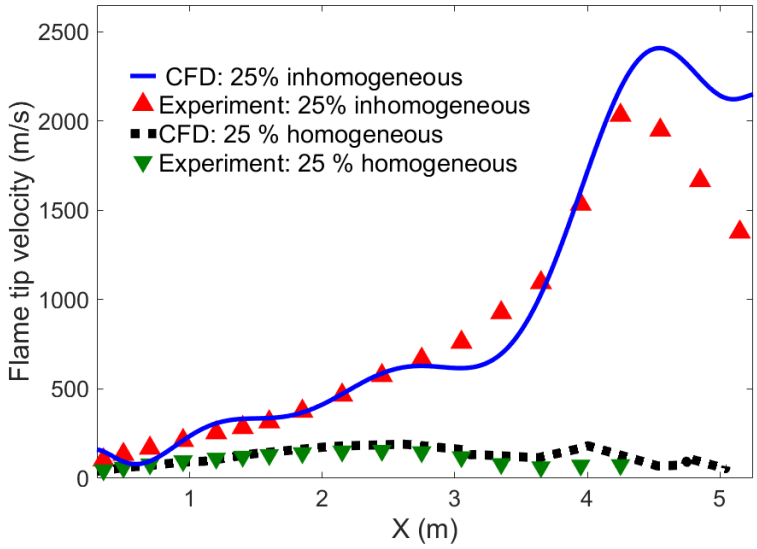

Figure 5-7: Comparison of the flame tip velocities between homogeneous and inhomogeneous mixtures with 25% hydrogen concentration (BR00). Experimental data (markers) and numerical predictions (lines).

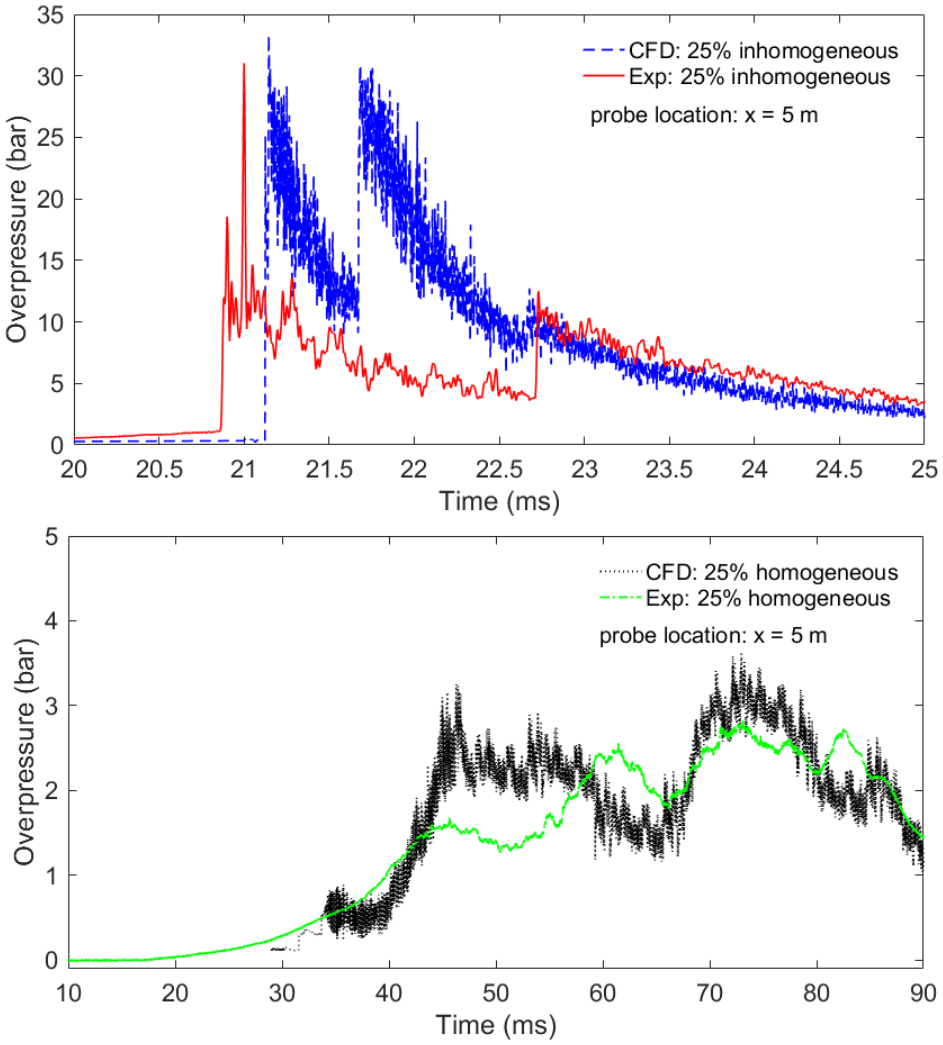

Figure 5-8: Comparison of overpressure at x = 5 m between the homogeneous (top) and inhomogeneous (bottom) mixtures at 25% hydrogen concentration (BR00).

As shown in Figure 5-8 and , in the lean mixture, DDT only happens in the inhomogeneous mixture. For the homogeneous case, the flame speed increases to a maximum value of 150 m/s while for the inhomogeneous case, the flame speed reached around 2400 m/s, which is above CJ velocity limit.

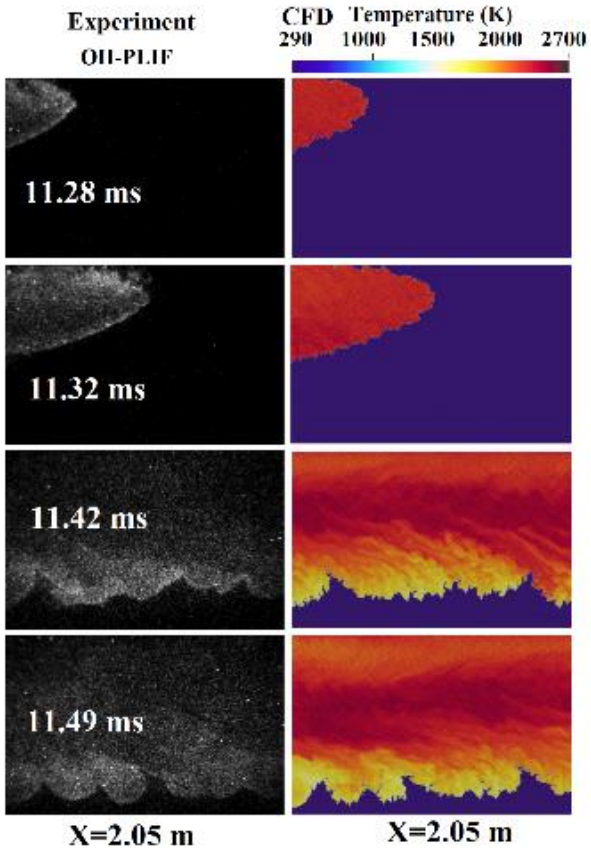

Figure 5-9: The sequence of flame acceleration, BR00, Inhomogeneous 25% (Left: OH-PLIF measurements; Right: the predicted temperature fields).

Figure 5-9 shows a qualitative comparison between the experimental OH-PLIF images of the leading flame edge and predicted temperature fields for the 25% inhomogeneous unobstructed channel. The leading edge of the flame propagates along the channel top wall, and the overall surface area of the flame is significantly enlarged. This effect governs strong flame acceleration in mixtures with concentration gradients in the unobstructed channel configuration. Wrinkling of the flame front is observed, but it is unclear whether it is due to intrinsic flame instabilities or flow instability related to the gradients in the horizontal flow velocity ahead of the flame (Khodadadi Azadboni *et al.*, 2019).

5.5.1.2 Near-stoichiometric mixture (30 % hydrogen concentration)

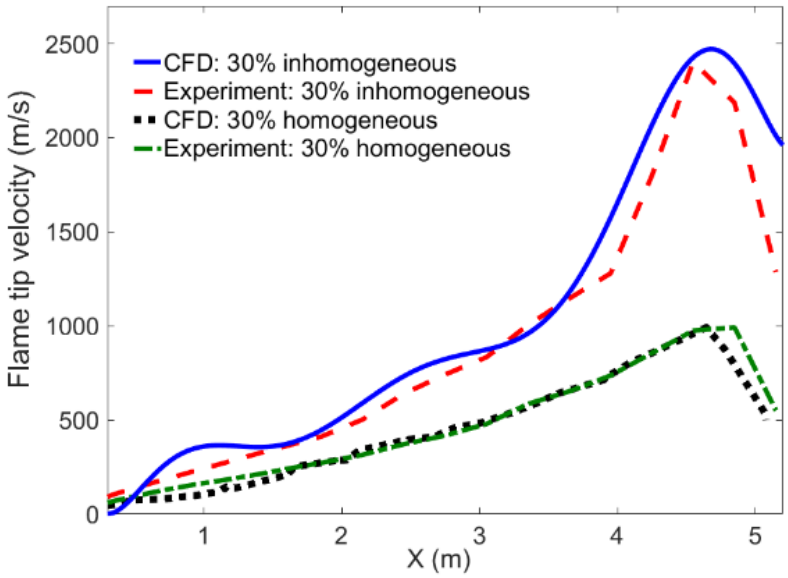

Figure 5-10: Comparison between the flame tip velocities in homogeneous and inhomogeneous mixtures at 30% hydrogen concentration.

Figure 5-10 shows that the predicted and measured flame tip velocities are in reasonably good agreement for both the homogeneous and inhomogeneous mixtures with an average 30% hydrogen concentration. Transition to detonation occurs in the inhomogeneous mixture at x ≈ 4 m similar to the lean case. However, FA in the homogeneous mixture is significantly stronger in the 30% hydrogen case compared to 25%, leading to a significant increase in peak pressure.

Figure 5-11 presents pressure histories at x=5 m from experiments and simulations. High peak pressures near 40 bar in case of the inhomogeneous mixture indicate that onset of detonation occurred close to the pressure transducer. In the case of the homogeneous mixture, multiple pressure peaks are observed.

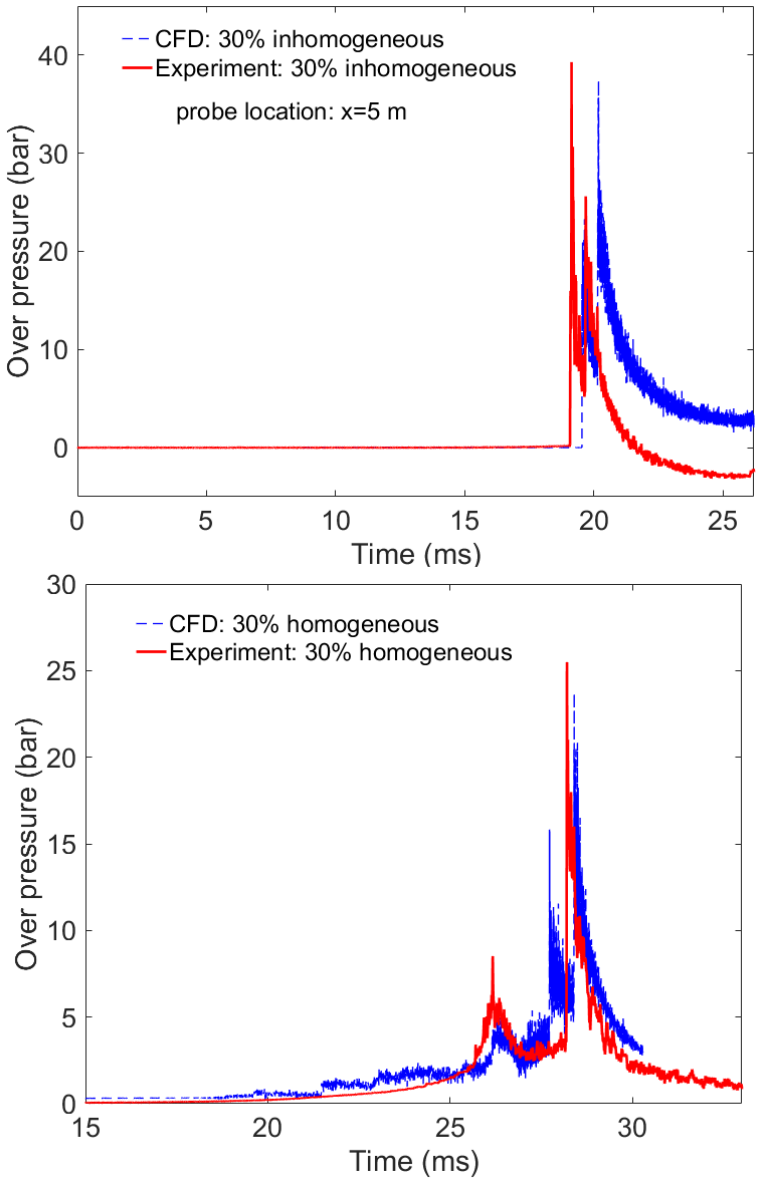

Figure 5-11: Comparison between overpressure at x=5m in the BR00 case and mixtures at 30% hydrogen concentration, top: inhomogeneous and bottom: homogeneous.

Figure 5-11, Figure 5-12, and Figure 5-13 show a good agreement on the pressure transducer measurement of experiment and numerical modelling. In the unobstructed homogeneous mixture of 30% hydrogen/air, the flame will rich to end wall of the channel after 26ms, and at this time the overpressure is around 7 bar, which is less than the CJ pressure ratio. In Figure 5-11, the 30% homogeneous, at x=5m, shows a maximum pressure of 25 bar, which is due to

shock reflection from the end of the channel. However, the unobstructed case with 30% inhomogeneous mixture, the overpressure at x=5 m, rises to around 39 bar, which exceeds the CJ pressure, and it indicates that transition to detonation has occurred (Khodadadi Azadboni *et al.*, 2019).

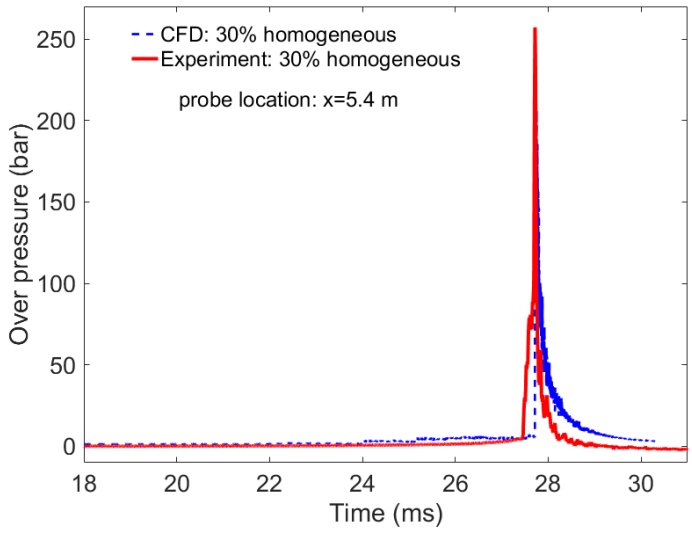

Figure 5-12: Comparison between overpressure, in homogeneous mixtures at 30% average hydrogen concentration; pressure probe located at x=5.4 m.

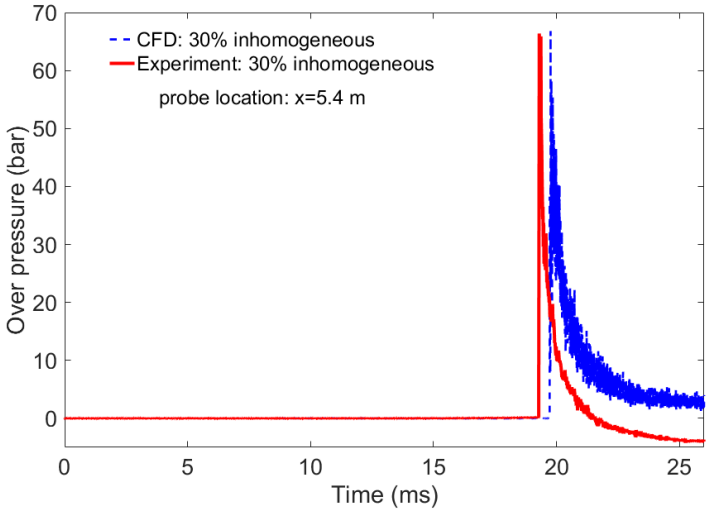

Figure 5-13: Comparison between overpressure, in inhomogeneous mixtures at 30% average hydrogen concentration; pressure probe located at x=5.4 m.

Figure 5-12, Figure 5-13, present pressure histories at x = 5.4 m, in the experiments and simulations for homogenous and inhomogeneous mixtures. The maximum overpressure in these plots are much higher than the one presented in Figure 5-11, and this is thought to be due to the shock reflection from the end of the closed channel leading to much higher overpressures.

Figure 5-14 shows the combustion wave near the end wall in 30% homogeneous mixture. The leading shock wave reflects at the end wall without any evidence of ignition behind the reflected shock waves, indicating that ignition delay times in the post-reflected shock gas are larger than the time available between shock reflection and the arrival of the trailing deflagration. However, during the interaction of the reflected shock wave with the trailing deflagration, a local explosion is observed which leads to the onset of detonation. This leads to high peak pressures which are consistent with the measurements shown in Figure 5-11 and Figure 5-12.

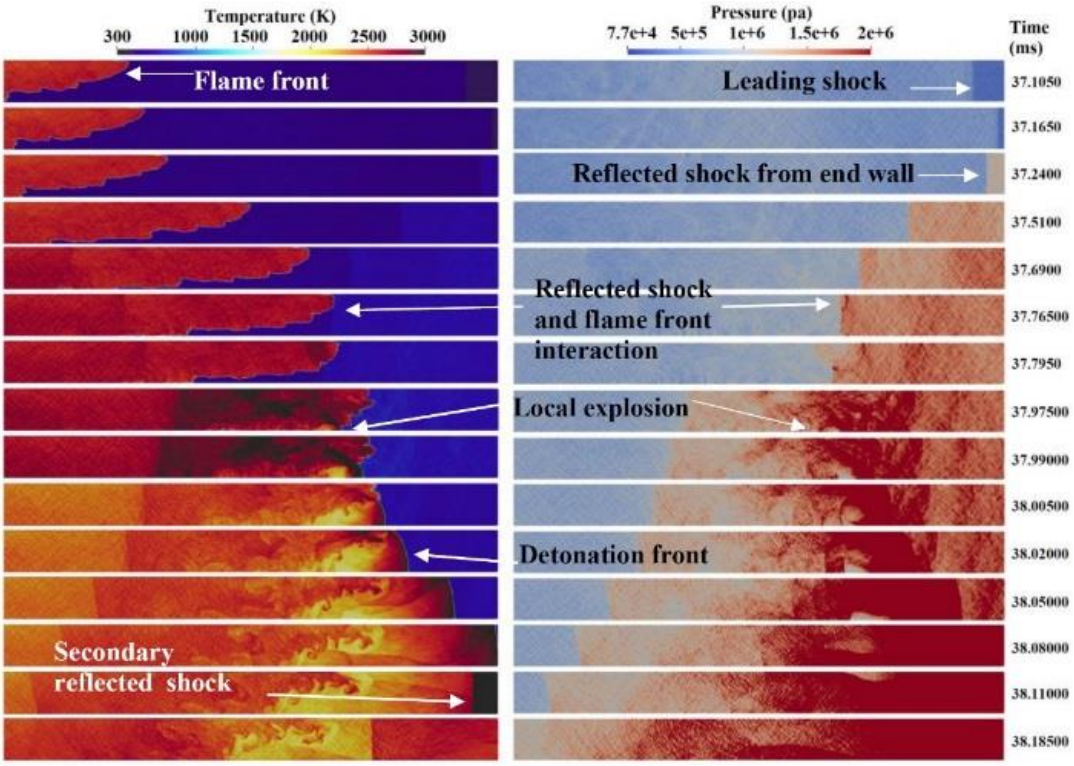

Figure 5-14: The predicted temperature (right) and pressure (left) fields for reflected shock at the end of the channel for 30% homogeneous hydrogen mixture (x=4.8 m to x=5.4 m).

5.5.1.3 Rich mixture (35 % hydrogen concentration)

Figure 5-15 shows reasonable agreement between the predicted and measured flame tip velocities for the inhomogeneous mixture with 35% hydrogen concentration. However, the maximum relative differences between the predicted CFD result and experimental measurement is around 22 % (around x=3.5m). DDT occurs in both the homogeneous and inhomogeneous mixtures. Flame propagation is slower in the homogeneous mixture than in the inhomogeneous mixture (this can be seen in Figure 5-15 as well as in the pressure plot shown in Figure 5-16). Very high peak pressure at the transducer location, x = 5 m, indicate that onset of detonation occurred near this location in the homogeneous mixture, whereas onset occurred earlier (x < 5 m) in the inhomogeneous mixture, resulting in a detonation propagating past the transducer with near CJ peak pressures.

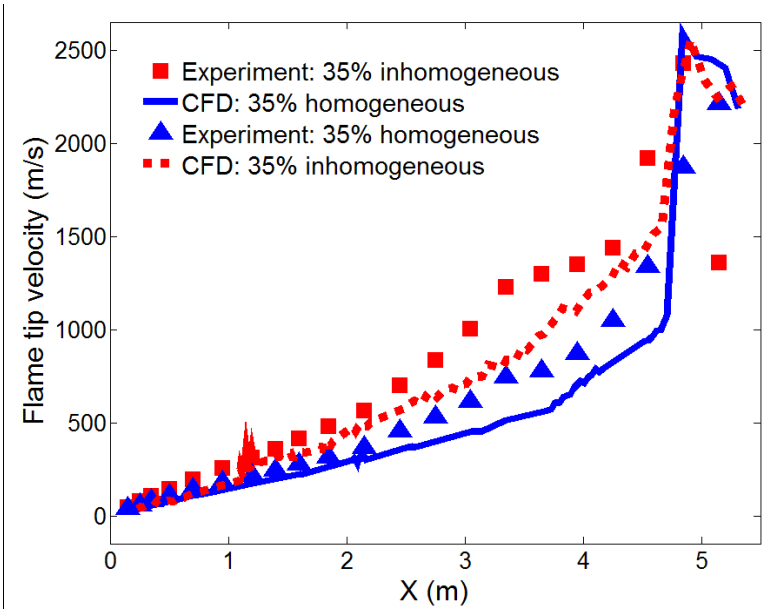

Figure 5-15: Comparison between the flame tip velocities in the inhomogeneous and homogeneous mixtures with 35% hydrogen concentration.

Figure 5-16, Figure 5-17 and Figure 5-18, show a relatively good agreement between the predicted and measured overpressure for the homogeneous and inhomogeneous mixtures with

an average 35% hydrogen concentration. In both homogeneous and inhomogeneous cases, the overpressures are more than CJ pressure, and at the end of the channel (around x=5 m), DDT has occurred. At x=5 m, the maximum overpressure in the homogeneous case is much higher than the inhomogeneous case (the maximum overpressure in the homogeneous case is: 100 bar, and in an inhomogeneous case is 27 bar).

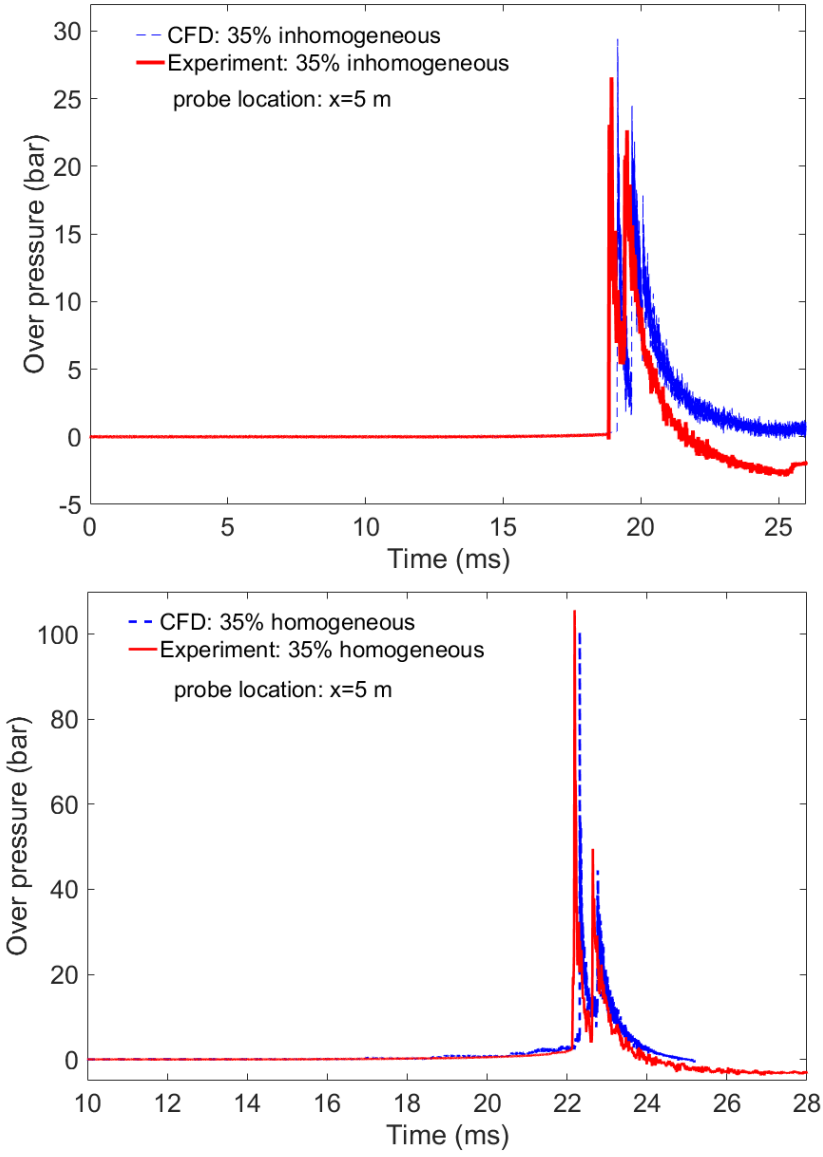

Figure 5-16: Comparison between predicted and measured overpressure at x=5m in the BR00 case and mixtures at 35% hydrogen concentration, top: inhomogeneous and bottom: homogeneous.

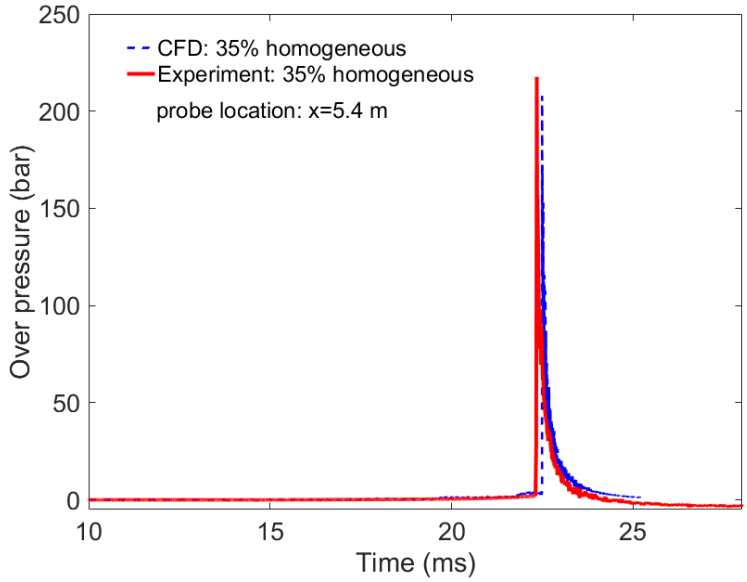

Figure 5-17: Comparison between predicted and measured overpressure, in homogeneous mixtures at 35% average hydrogen concentration; pressure probe located at x=5.4 m (right).

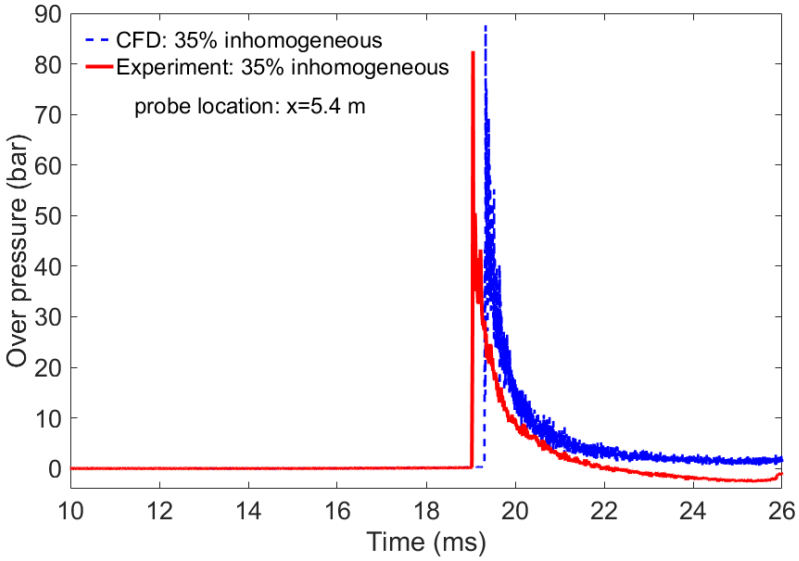

Figure 5-18: Comparison between predicted and measured overpressure, in inhomogeneous mixtures at 35% average hydrogen concentration; pressure probe located at x=5.4 m (right).

Figure 5-17 and Figure 5-18, presents pressure histories at x = 5.4 m from experiments and simulations for the homogenous and inhomogeneous mixture. The maximum overpressure in these plots (which are recorded from the end of channel x=5.4m), are much higher than the one presented in Figure 5-16 (x=5 m). This can be due to the shock reflection from the end of the closed channel.

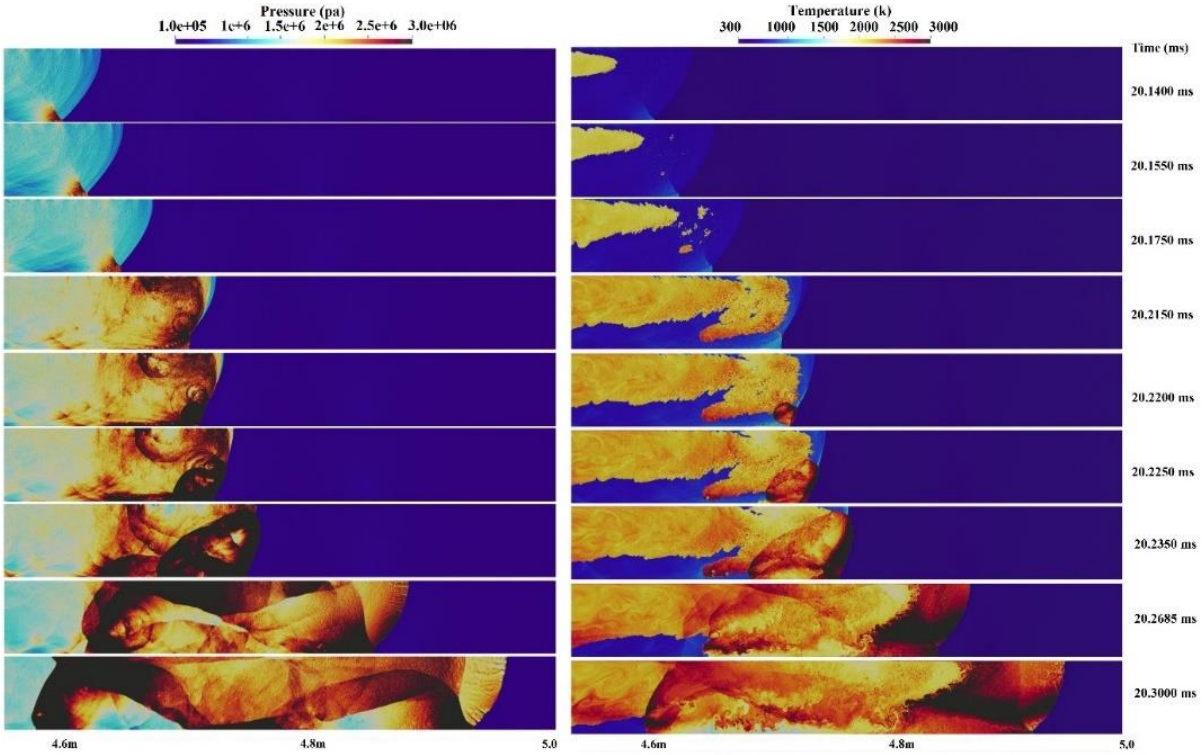

Figure 5-19: Pressure (left) and Temperature fields for DDT in the inhomogeneous 35% hydrogen-air mixture.

Figure 5-19 shows pressure and temperature fields during the flame acceleration and transition to detonation in the inhomogeneous 35% mixture. It can be seen that the DDT process occurs close to the end of the channel (4.6<x<5.0). Shock reflection off a solid wall and creation of a hot spot in the turbulent boundary layer behind a leading shock in an unobstructed channel, has occurred (Figure 5-19-t=20.1750ms). The location of hot spot generation in this flow field is random, and this can be due to; existing of temperature and pressure fluctuations behind the reflected shock, and also, induction time being highly sensitive to temperature fluctuations. Therefore, in the wall boundary layer behind a leading shock, a hot spot can form and cause

the onset of detonation. It is known that a localised explosion initiating detonation may either occur between the leading shock and the turbulent flame brush or in the direct vicinity of the flame.

5.5.1.4 Very rich mixture (40 % hydrogen concentration)

An unobstructed channel with 40% inhomogeneous mixture of hydrogen/air, has been considered.

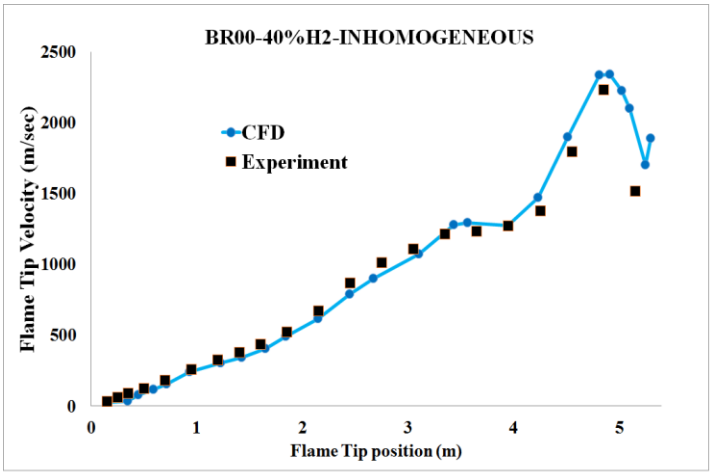

Figure 5-20: Comparison of the predicted and measured flame tip velocity for 40 % inhomogeneous hydrogen concentration in the unobstructed channel (BR00).

As shown in Figure 5-20, the predicted flame tip velocities are in reasonably good agreement with the measurements. The flame tip velocity rises continuously in the channel.

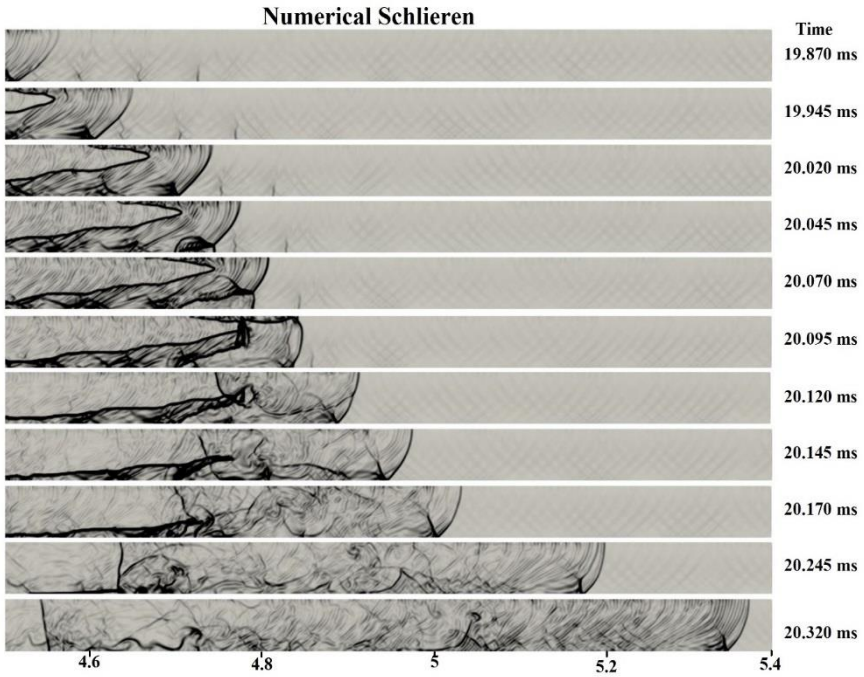

Figure 5-21: Numerical Schlieren (magnitude of density gradient) contours for onset of detonation in the inhomogeneous H2/Air mixture with 40% Vol and BR00.

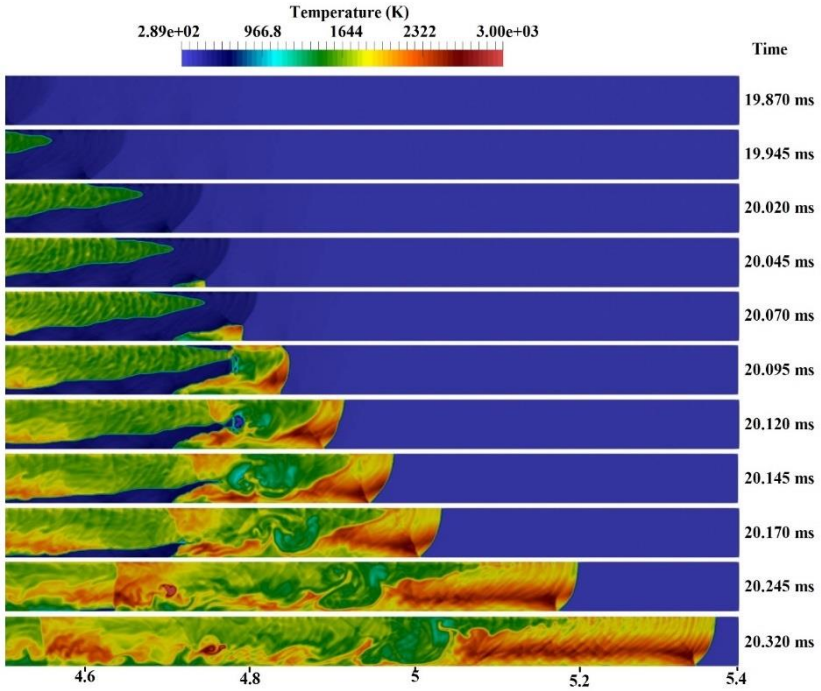

Figure 5-22: Temperature contour during the transition to the detonation in unobstructed channel (0% blockage ratio, BR00).

Figure 5-20 to Figure 5-22, show that in accordance with the experiments (Boeck *et al.*, 2016), the transition to detonation is initiated almost at the end of the channel (x=4.79m), and it's due to shock reflection at the upstream faces from the channel wall, leading to localised explosions in the leading shock wave. Figure 5-21shows numerical schlieren images (magnitude of the density gradient), and Figure 5-22 temperature fields of the onset of detonation, in the inhomogeneous mixture and unobstructed channel. The accelerated hydrogen flame propagates towards downstream of the channel with having a leading shock. At 20.045ms, a weak local explosion occurs near the bottom wall, where the mixture is lean. At 20.095ms, this local explosion interacts to the flame front, and the generated explosion is moving towards the flame front. The overpressure is around 20 bar, which satisfies the CJ detonation pressure ratio condition. Moreover, Figure 5-20 shows that at x=4.8 m, the flame tip velocity is at its maximum value. At 20.120 ms, the flow became supersonic, and the transition to detonation is complete (Khodadadi Azadboni, Heidari and Wen, 2018).

5.5.2 DDT in a channel with a 30% blockage ratio (BR30)

Four sets of simulations have been carried out for a blockage ratio BR=30, and average hydrogen concentrations of 20%, 30%, 35% and 40%. The numerical setup is the same as mentioned in section 5.3.

5.5.2.1 Lean mixture (20% hydrogen concentration)

As shown in Figure 5-23, the predicted flame position and flame tip speed are in reasonably good agreement with the measurements (Boeck *et al.*, 2016). However, around x=4m the maximum relative differences between the predicted CFD result and experimental measurement is around 35%. This can be due the inaccuracy of the photodiodes measurements for the velocity above 1000m/sec (this has been reported by (Boeck *et al.*, 2016)). In Figure

5-23, the mixture is lean with 20 percent inhomogeneous hydrogen concentration by average. Figure 5-23 and Figure 5-24 show that after the flame interacts with the very first obstacle, (which is located at x=0.25m), due to turbulence generation, the flame velocity increases (Khodadadi Azadboni, Heidari and Wen, 2017b). After flame passing all 7 obstacles (the last obsctale located at x=2.05m), the flame tip velocity increased to 1361 m/sec, which is still less than the D_{CJ} detonation speed. The D_{CJ} detonation speed for 20% hydrogen is 1716 m/s. Later, after the accelerated flame interacts with a generated shock at x=2.75m of the channel, the lean hydrogen flame transited to detonation (can be seen in Figure 5-23).

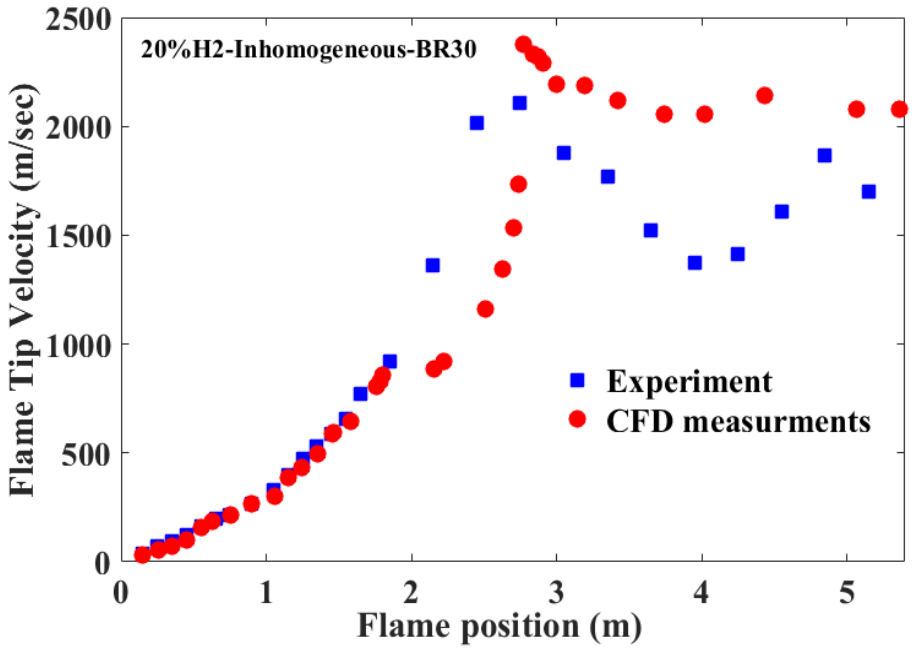

Figure 5-23: Comparison of the predicted and measured flame tip velocity for 20 % inhomogeneous hydrogen concentration in the 30% BR channel.

Figure 5-24 shows the onset of detonation in the 20% inhomogeneous hydrogen concentration, in the rectangular channel with 30 % blockage ratio (BR30).

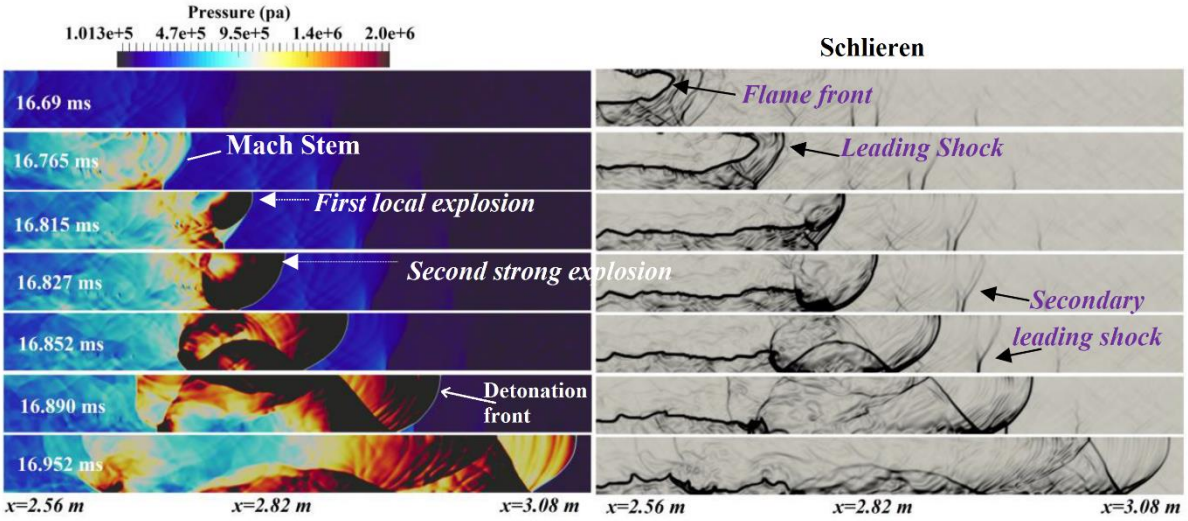

Figure 5-24: Pressure (left) and numerical Schlieren (right) with the magnitude of density gradient showing the onset of detonation in the inhomogeneous 20% hydrogen-air mixture.

In Figure 5-24, the frame at 16.69 ms shows a weak shock wave generated in front of the hydrogen flame front, and then at 16.765 ms, the shock is strengthened sufficiently to trigger the Mach steam and strong incident shock near the bottom wall, where the mixture is lean. Then at 16.815 ms, the first localised explosion happened near to the upper wall due to shock-flame interactions. This is a stronger explosion than the first one. The two local explosions interacted in the middle of the channel and resulted in much stronger explosions. At 16.852 ms, a secondary planer leading shock can be seen to propagate in front of the detonation wave. These predictions are also in line with previous experiments of Thomas (Thomas, 2012) and Kuznetsov et al. (Kuznetsov *et al.*, 1998), who found that in mixtures with concentration gradients, a secondary shock is observed as the incident shock passes through the interface layer. Subsequently, at 16.890 ms, this secondary shock and detonation wave interacted with each other, and a stronger detonation front was generated in the flame front. Figure 5-23 also shows that at this location (2.89m), the flame tip velocity is at its maximum. At 16.952 ms, the flow became supersonic, and the deflagration completely transited to detonation (Khodadadi Azadboni, Heidari and Wen, 2017b).

5.5.2.2 Near-stoichiometric mixture (30% hydrogen concentration)

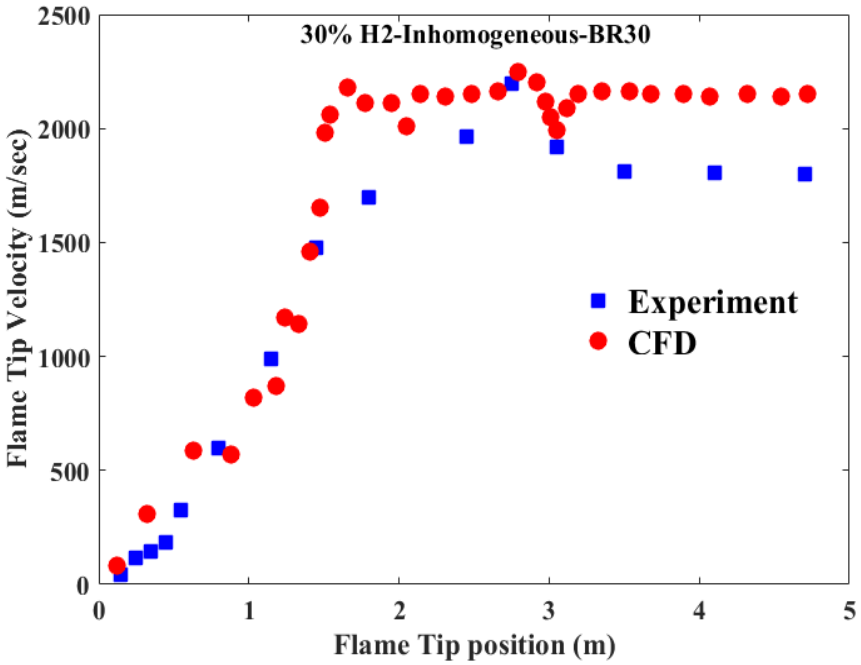

Figure 5-25: Comparison of the predicted and measured flame tip velocities for 30 % inhomogeneous hydrogen concentration in the 30% BR channel.

As illustrated in Figure 5-23, the predicted flame position and flame tip speed are in reasonably good agreement with the measurements (Boeck *et al.*, 2016). However, after the transition to detonation (around x>1.75m) the maximum relative differences between the predicted CFD result and experimental measurement is around 21%. As stated earlier, this discrepancy can be due the inaccuracy of the photodiodes measurements for the velocity above 1000m/sec (this has been reported by (Boeck *et al.*, 2016)). In Figure 5-25, the flame velocity rises continuously in the obstructed part of the channel (around the 7th obstacle, $x \leq 2.05$ m) due to flame interaction with the obstacles, resulting in combustion-induced expansion and turbulence generation. Figure 5-26 shows, the transition of accelerated hydrogen flame to detonation in

the inhomogeneous 30% mixture with 30 % blockage ratio (Khodadadi Azadboni, Heidari and Wen, 2017b).

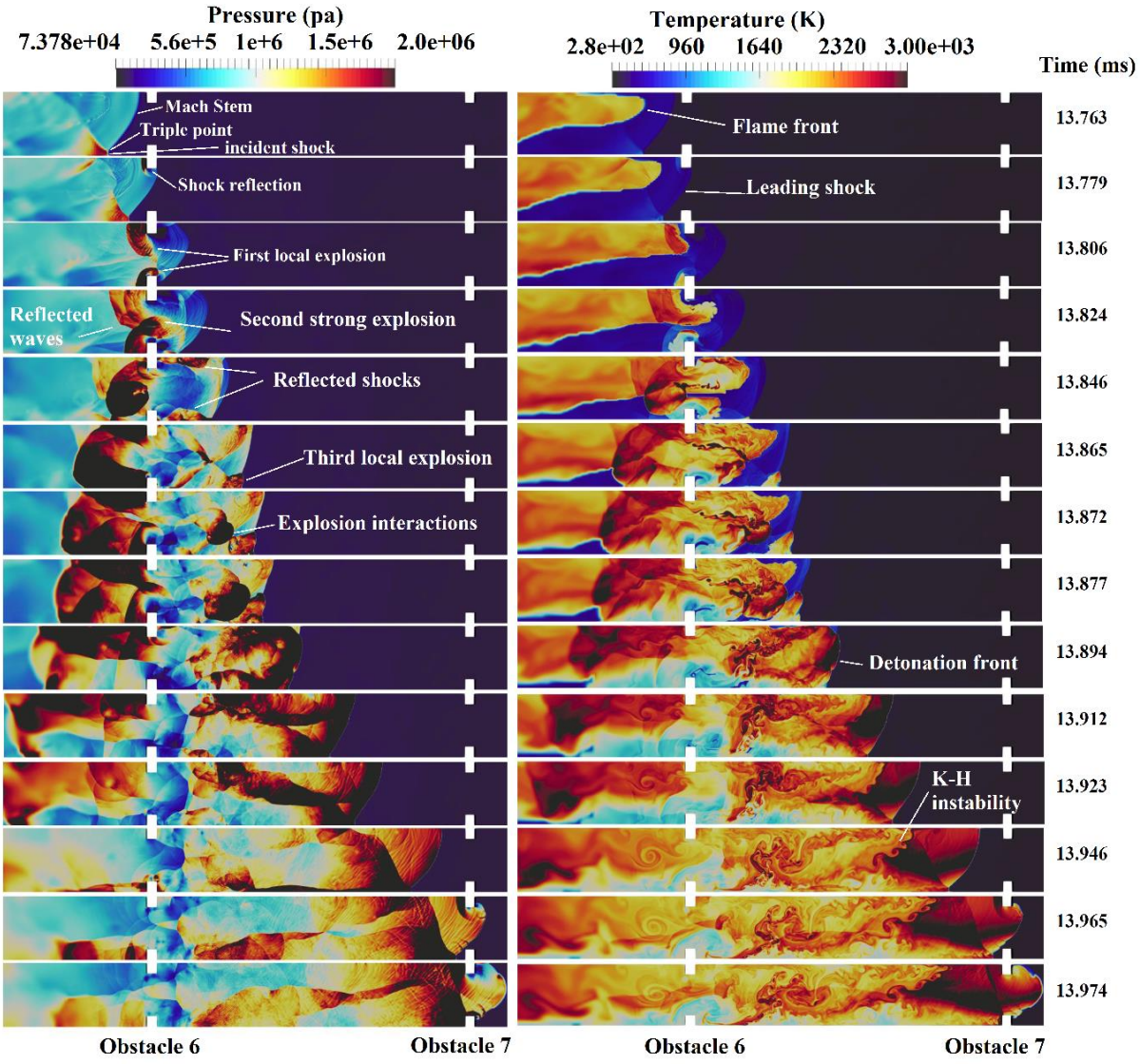

Figure 5-26: Pressure (left) and Temperature fields for DDT in the inhomogeneous 30% hydrogen-air mixture.

Figure 5-25, and Figure 5-26, show that after passing the 6th obstacle, the flame speed reached around 2100 m/s, which is the same as CJ detonation velocity of the stoichiometric hydrogen-air mixture. After the flame and detonation wave passed the last obstacle which is located in

x=2.05 m, the flame speed reached to a maximum of around 2200 m/s before decreasing slowly. The detonation speed of homogenous mixture of hydrogen/air in atmospheric condition and the stoichiometric range is around 1480-2150 m/s while in the present study while the predicted flame speed of 1450 to 2250 m/s in the present non-homogenous mixture just covers a slightly wider range. at 13.806 ms, the first localised explosions occurred near the obstacles on the both bottom and top wall. It is also noted that in the bottom wall, the mixture is almost lean with the concentration being around 10%, and the local speed of sound is around 361m/s (Khodadadi Azadboni, Wen and Heidari, 2019). At 13.806 ms, close the top obstacle, due to the interaction of reflected shock and flame front, this first localised explosion, formed. However, the local explosion on the vicinity of the bottom obstacle occurred, because of the generated hot spot near to the reflected shock from the obstacle. After DDT occurred, two shear layers have generated in the burned gas. Small scale vortices which indicate Kelvin Helmholtz (KH) instability, can be found in the shear layers (Khodadadi Azadboni, Heidari and Wen, 2017b).

In Figure 5-26 a number of forward and backwards jets can be seen at the interface of the burnt and unburnt gases, illustrating the existence of RM instability. , RM instability is one of the main hydrodynamic instabilities in DDT which is due to high gradients of pressure and density. There is a strong misalignment of the density gradient and pressure gradient at the interface between the flame front and pressure wave. This can trigger baroclinic torque ($\nabla\rho \times \nabla p$) which is generated as a result of baroclinic vorticity $\left({\nabla\rho \times \nabla p}/{\rho^2}\right)$, and is responsible for RM instability.

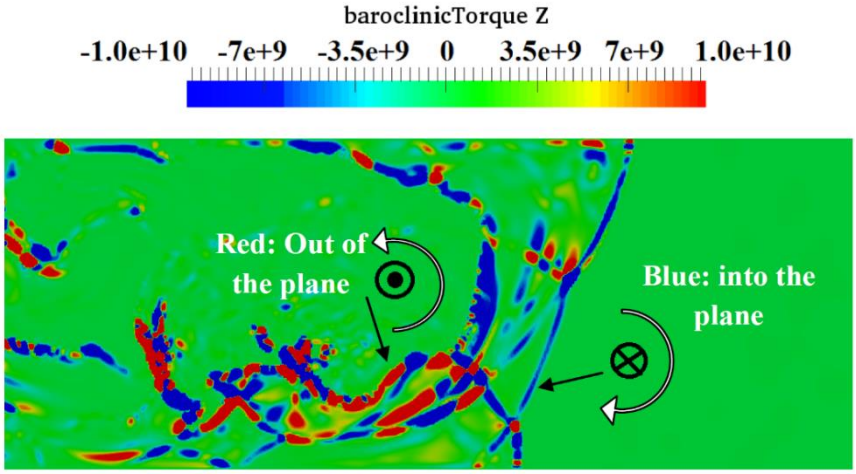

Figure 5-27: The contour of the predicted Baroclinic torque in Z direction time 13.95 ms.

This misalignment in a baroclinic torque which generates vorticity can be seen in Figure 5-27. while shock refracts from the interface of burned and unburned gas, misalignments in the density and pressure gradients occur. This results in generation of baroclinic vorticity through the production of baroclinic torque along the contact discontinuity causing the perturbations to grow in amplitude (Mazaheri, Mahmoudi and Radulescu, 2012; Mahmoudi, Mazaheri and Parvar, 2013). The misalignments between baroclinic vorticities are due to the cross-multiplication of gradient of density to the gradient of pressure (the misalignment is illustrated in Figure 5-28) (Khodadadi Azadboni *et al.*, 2017).

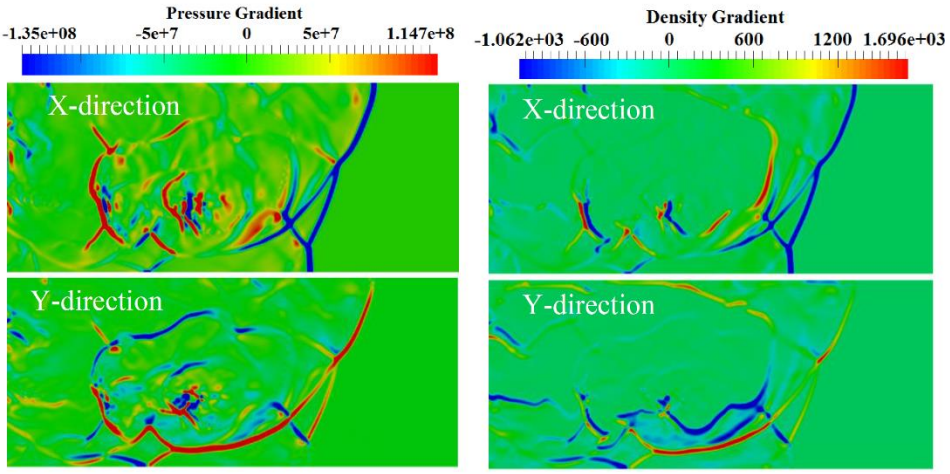

Figure 5-28: Pressure gradient (left), and density gradient (right), in X and Y directions for BR 60 and time 8.08 ms (Khodadadi Azadboni et al., 2017).

Figure 5-28 shows that in the same direction either X or Y, the pressure and density gradient vectors in the same regions are inline, i.e. they are either both negative or positive. On the other hand, in different directions, these vectors are misaligned. As shown in Figure 5-28, some parts of the baroclinic torque vectors are red (a positive vector which points away from the page), and some parts are blue (a negative vector which points towards the page). These results illustrate the existence of both positive and negative baroclinic vorticities in the flow field (Khodadadi Azadboni *et al.*, 2017).

Figure 5-29 shows the predicted baroclinic torque for the region around obstacles 6 and 7 at different times. It is evident that the baroclinic torque increases with time, promoting RM instability, FA and DDT. Figure 5-29-(a, b and c) show that the locations of the maximum baroclinic torque are aligned with locations of Mach stem on the bottom wall. Based on Figure 5-28 and Figure 5-29-d, it can be concluded that the DDT occurred at where there are maximum baroclinic torque and RM instability.

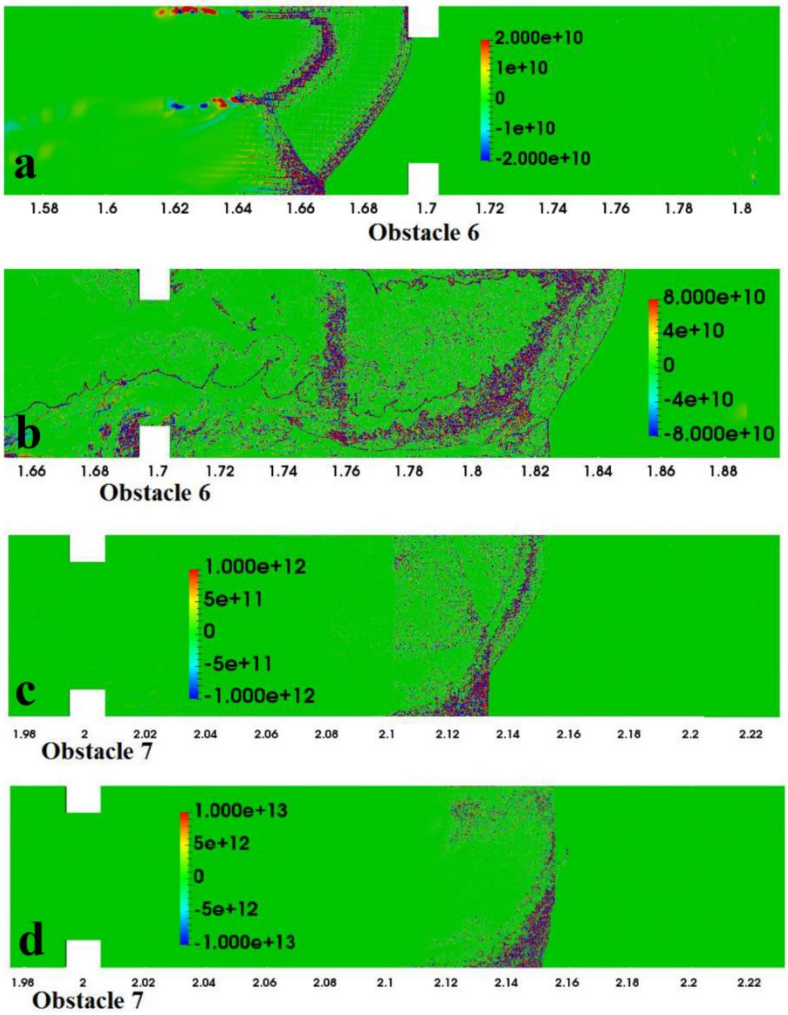

Figure 5-29: The contours of the predicted Baroclinic torque in the Z direction for BR 30 and a) time=13.79 ms, b) time=13.91 ms, c) time=14.48 ms and d) time=14.50 ms.

Figure 5-27 and Figure 5-29 show that more baroclinic vorticities are generated in the vicinity of the leading shock and Mach stem. In other regions, baroclinic torque exists just along the interface between the flame and strong shock waves. The vicinity of the Mach stem and flame shock interfaces are, therefore, the regions with most prone to have RM instabilities. This is also evidenced by the presence of forward or backward jets, resulting in mushroom shape flow patterns along the interface.

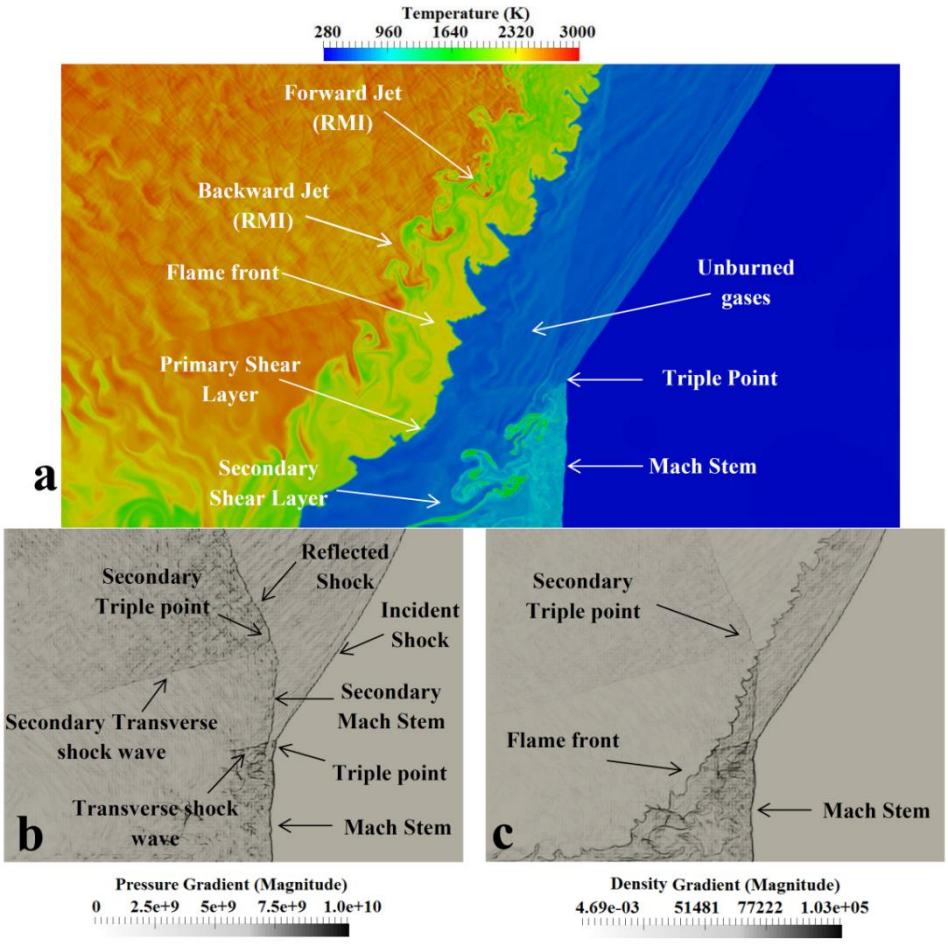

Figure 5-30: RM instability diagram in BR 30 and time=13.79 ms, a) The predicted temperature contour illustrating RM instability b) pressure gradient contour and c) density gradient contour (Khodadadi Azadboni et al., 2017).

Figure 5-30-a, shows the temperature contour illustrating the occurrence of RM instabilities at the flame front. The typical mushroom shapes RM instability are seen in the form of forward and backward jets. The interaction of the shock with the flame front is also accompanied by the existence of density differences between the burnt and unburnt gases. The backward jets in the primary shear layer propagated into the hot and burned gases and can be consumed shortly in the pool of hot products.

Figure 5-30-b, and -c, show the shock flame structure in the numerical schlieren of pressure gradient and density gradient, respectively. Overall, Figure 5-30 shows a strong shock wave propagating ahead of the flame front. A group of shock waves propagated down the channel before the flame arrival. These shocks diffracted around the obstacles, inducing flow, and enhancing shear layer turbulence behind the obstacle plates. As a result of the interaction of Mach stem with a transverse shock wave and the incident shock, a triple point has been generated in the flow field (which can be seen in Figure 5-30-b). Moreover, due to the generation of the secondary transverse shock wave and interaction of this wave with the secondary Mach stem and the reflected shock wave, another triple point appeared in the flow field, which can be seen in Figure 5-30-b, and named as a secondary triple point.

It is known that Baroclinic vorticity generation can enhance flame wrinkling on small scales and macroscopic flame distortion on large scales (Radulescu *et al.*, 2005). Thomas et al. (Thomas, Bambrey and Brown, 2001)experimentally demonstrated the great potential of shock-flame interaction in flame acceleration. Kholkhlov et al. (Khokhlov *et al.*, 1999; Khokhlov, Oran and Thomas, 1999), likewise found that shock-flame interaction is important to accelerate flames to critical conditions for the onset of detonation. They believed that large-scale RM instability was the primary mechanism increasing the heat release rate during the interaction of a flame with a single shock through macroscopic flame surface area growth while small-scale instability decays quickly and hence can only contribute for a short time.

5.5.2.3 35% hydrogen concentration (rich mixture)

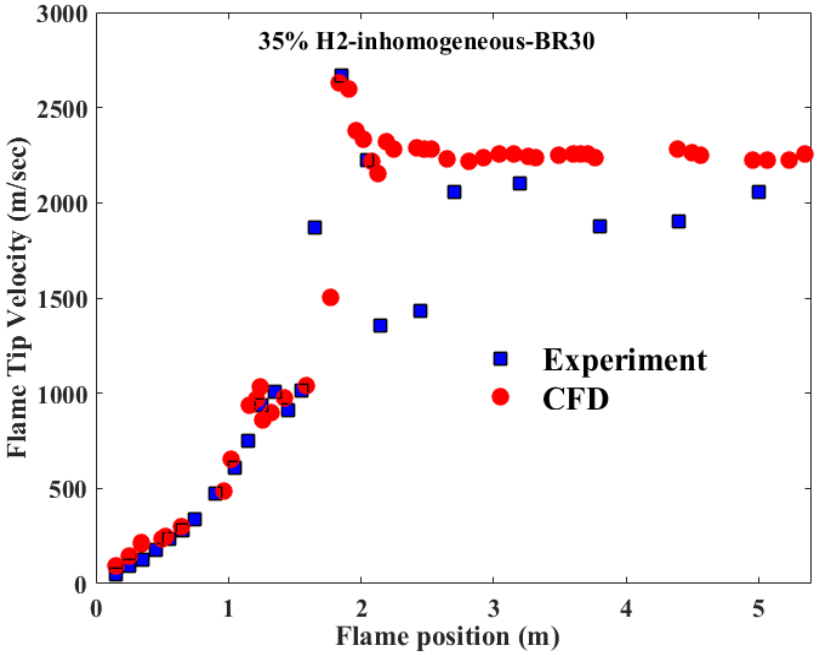

Figure 5-31: Comparison of the predicted and measured flame tip velocities for 35 % inhomogeneous hydrogen concentration in the 30% BR channel.

Figure 5-31 shows a relatively good agreement between the predicted and measured flame tip velocities for the inhomogeneous mixture with an average 35% concentration. Similar to the earlier results, after the transition to detonation (in this case around x>2m) the maximum relative differences between the predicted CFD result and experimental measurement is around 15%. As stated earlier, this discrepancy can be due the inaccuracy of the photodiodes measurements for the velocity above 1000m/sec (this has been reported by (Boeck *et al.*, 2016)). Comparing the results in Figure 5-31 with those in Figure 5-25 and Figure 5-23, show that the maximum flame tip velocity is much higher in the 35% concentration case compared to the 30% and 20% cases. the maximum flame speed in the 30% concentration was higher than the 20 % case, which indicated that between 20% to 35% concentrations, increasing the hydrogen concentration would lead to an increase in the maximum flame tip velocity.

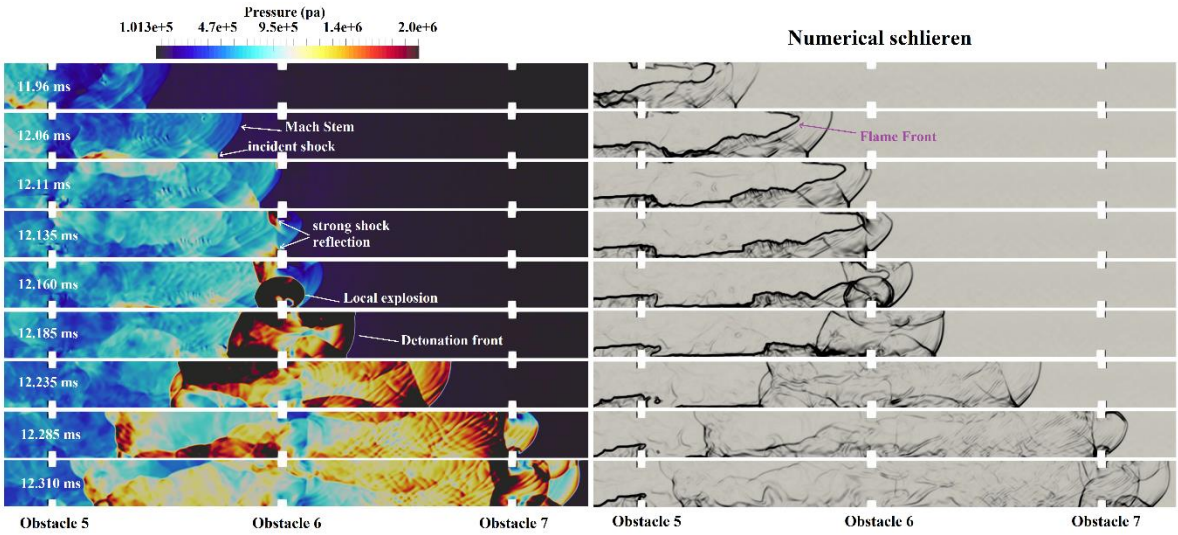

Figure 5-32: Pressure (left) and numerical schlieren (right, the magnitude of density gradient) fields of onset of detonation in the inhomogeneous 35% hydrogen-air mixture.

Figure 5-32 shows the onset of detonation in the inhomogeneous 35% mixture which located around obstacle 5 and 6. On the right-hand side that at 11.96 ms a planer shock is moving downstream of the flame front. Then due to an interaction of the leading shock and hot spots, a Mach steam has formed. At 12.06 ms. However, this hot spot and incident shock was not strong enough to trigger detonation. Then at 12.135 ms, combining the information on both the right- and left- hand sides in Figure 5-32, it can be seen that the strong reflected shocked formed, due to shock and flame front interaction next to obstacle 6 in the upper wall. Also, near the bottom wall due to shock reflection from the obstacle a hot spot has been generated, but this hot spot did not lead to a detonation. Then, at 12.160 ms this explosion wave generated a strong explosion near the bottom wall. Subsequently, the transition to detonation occurred at 12.185 ms. From the detonation structure at 12.235 ms, it can be demonstrated that the gas compressed by the shock wave is free of disturbances and all the chemical energy released in the reaction zone goes to support the detonation. The process eventually reached a steady state, and the shock wave propagated at nearly the C-J velocity. However, at 12.285 ms, while the detonation front interacted the obstacle, the flame tip velocity decreased as well as the overpressure. This is thought to be due to the existence of turbulence behind the shock wave

which influenced the interaction between the shock wave and the reaction zone. Although turbulence can accelerate the flame front and assist the onset of detonation (e.g. Figure 8 at 12.185 ms), here at 12.285 ms, it increased losses of energy and quenched the flame by mixing the burned and cold unburned gases; thus, decreasing the amount of chemical energy available to support the detonation. Then, at 12.310 ms, the two reflected shock waves from upper and lower wall interacted downstream of the flame front and generated a steady detonation wave, which propagated along the channel (Khodadadi Azadboni, Heidari and Wen, 2017b).

Figure 5-32 also illustrated that in the case of 35% hydrogen concentration, the transition of hydrogen flame to detonation happens earlier than the other cases with less average hydrogen concentration. Hence it can be concluded that by increasing the average hydrogen concentration from 20% to 35%, the flame will transit to detonation faster and in less distance to the ignition point. It is interesting that in this case, the first local explosion happens near the bottom wall.

5.5.2.4 Very rich mixture (40% hydrogen concentration)

Figure 5-33, shows the predicted flame tip velocities are in reasonable agreement with the measurements of the 40% hydrogen concentration, in a channel with a 30 % blockage ratio. In comparison with the unobstructed channel (Figure 5-21, Figure 5-22 and Figure 5-23), the flame has transited to detonation much earlier (in BR00, DDT occurred at x=4.79m, however in BR30, the DDT took place at around x=2.15m). Therefore, it can be concluded that obstacle has a significant impact on flame acceleration and transition to detonation (Khodadadi Azadboni, Heidari and Wen, 2018).

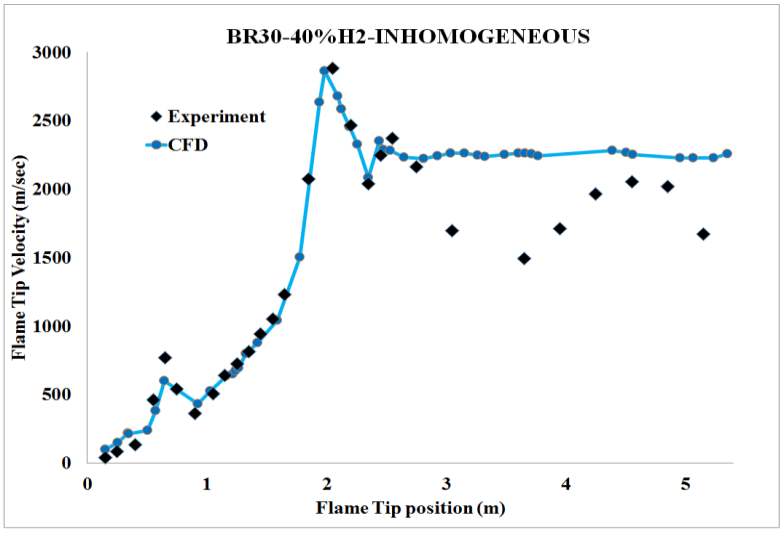

Figure 5-33: Comparison of the predicted and measured flame tip velocity for 40 % inhomogeneous hydrogen concentration in the 30% BR channel.

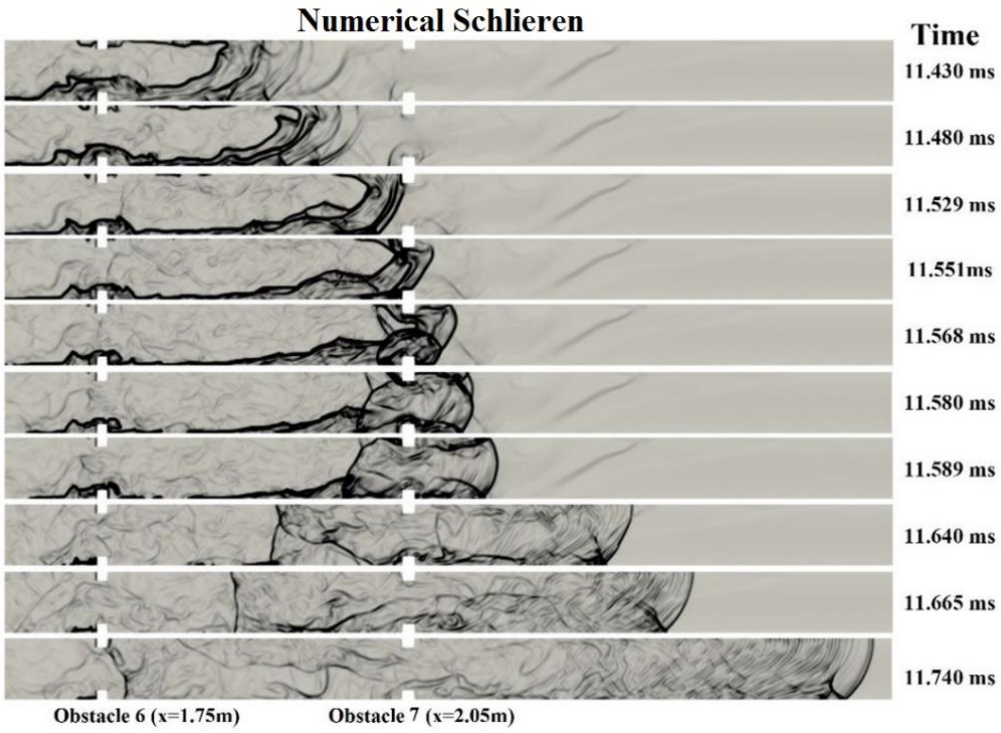

Figure 5-34: Numerical schlieren (magnitude of density gradient) contours of deflagration to detonation for inhomogeneous H2/Air mixture of 40% Vol and BR30

5.5.2.5 Conclusions

Numerical studies have been conducted to investigate DDT in an inhomogeneous mixture of hydrogen-air in an obstructed channel with 30% blockage ratio (BR=30) for four different average hydrogen concentration, i.e. 20%, 30%, 35% and 40% by volume. The predicted flame position and flame tip velocities are in reasonably good agreement with the measurements of Boeck et al. (Boeck *et al.*, 2016) for all three cases. In all the three cases the first localised explosion has triggered, due to the interaction of reflected shock from obstacle and flame front. The local explosion further developed to form the leading detonation wave. The increase in the fuel concentration was found to increase the FA and faster transition to detonation. Also, the increase in the BR was found to increase the FA and slow down the possibility of transition to detonation in the present configuration.

The role of hydrodynamic instabilities and the effect of baroclinic torque and RM instability have also been studied. The forward jet and backward jets which are a mushroom form flow represent the RM instability on the interface between the burned and unburned gas. The forward jets were found to impact on the shock front causing the appearance of a secondary triple point on the initial Mach stem on the flame front. The forward jet in the first shear layer was found to be consumed faster than those in the secondary shear layer. On the contrary, the backward jet consumed slower in the first shear layer than in the secondary shear layer. This is thought to be due to the existence of an unburned gas region between these two shear layers. The jets moving toward the burned pockets are moving slower than those going towards the unburned gas. The results support that RM instability is the primary source of turbulence generation in the present case.

5.5.3 DDT in a channel with a 60% blockage ratio (BR60)

Three sets of simulations (with different mixture concentrations), have been carried out for the 60 % blockage ratio channel (BR=60). The average hydrogen concentrations of these three cases are: 20%, 30% and 40%, respectively. The numerical setup is as the same mentioned in section 6.3.

5.5.3.1 Lean mixture (20% hydrogen concentration)

Figure 5-35 shows flame speed data from experiments and simulations with 20% hydrogen-air mixtures in the obstructed channel. In contrast to the 30% case, FA for the inhomogeneous mixture is stronger in the obstructed section compared to a homogeneous mixture. The difference is small but discernible in the obstructed section both in experiments and simulations. In the unobstructed section, the flame speed plateaus in the homogeneous mixture whereas it keeps increasing in the inhomogeneous case. This steady acceleration in the unobstructed section in the inhomogeneous mixture was attributed to continuous enlargement of the flame surface area due to the concentration gradient (Boeck, Hasslberger and Sattelmayer, 2014; Boeck, 2015) and is captured in the numerical simulation. This effect will be revisited in more detail later for the entirely unobstructed channel. A sudden increase in flame tip velocity at $x \approx 4$ m indicates a transition to detonation in the simulation (which can be found in the pressure- numerical schlieren contour in Figure 5-37). This was not visible as clearly in the measurements, where a more gradual increase in flame speed to 1700 m/s was measured towards the channel end. The large spacing of photodiodes used for velocity measurements in this region could not resolve sharp changes in the flame speed so that it is not entirely clear whether DDT occurred in the experiment (Khodadadi Azadboni *et al.*, 2019).

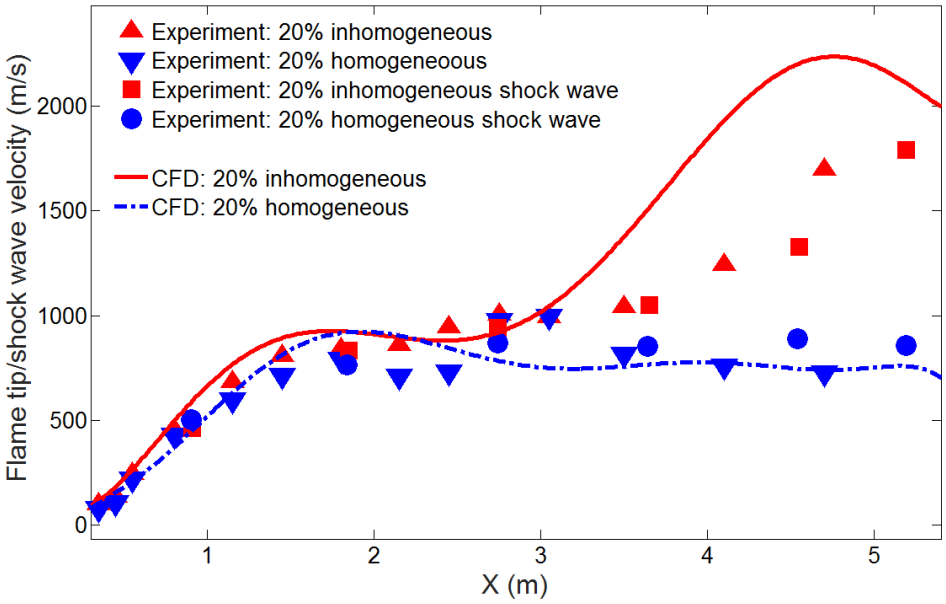

Figure 5-35: Comparison of the flame tip velocities between homogeneous and inhomogeneous mixtures with 20% hydrogen concentration (BR60). Experimental data (markers) and numerical predictions (lines).

Figure 5-36 presents pressure histories from experiments and simulations taken at x = 4.1 m. Pressure traces show the substantial difference in explosion strength between the homogeneous and inhomogeneous mixture, with peak pressure for the inhomogeneous mixture more than twice higher for the homogeneous mixture. The overpressure in the inhomogeneous case exceeds CJ pressure (based on Figure 2-1, calculated CJ pressure for 20% hydrogen is around 13.5 bar), which suggests that transition to detonation has occurred upstream of the pressure measurement location. The second peak pressure at t = 21 ms represents the reflected wave from the channel end plate. By contrast, comparably low overpressure in the homogeneous case suggests that a fast deflagration passes the pressure transducer.

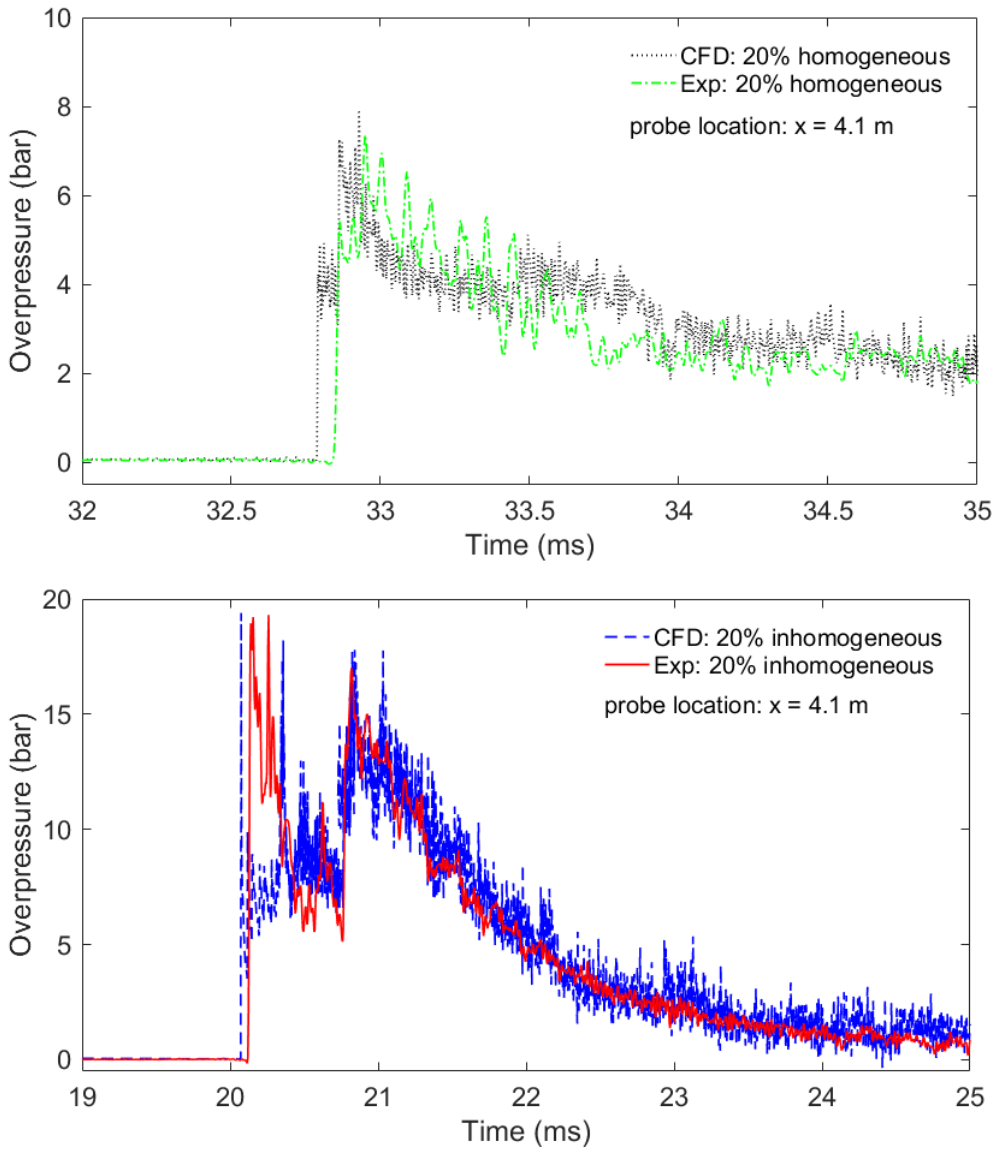

Figure 5-36: Comparison of overpressure at x = 4.1 m between the homogeneous (top) and inhomogeneous (bottom) mixtures at 20% hydrogen concentration (BR60).

Figure 5-37 presents numerical pressure and schlieren fields of detonation onset in the inhomogeneous mixture. The leading flame tip is initially located near the channel top wall, and the flame is elongated due to the concentration gradient providing highest local mixture reactivity near the channel ceiling. A local explosion is observed near the leading flame tip,

initiating the onset of detonation and driving a shock wave diagonally forward toward the channel bottom. This process is in qualitative agreement with the experimental observations in unobstructed channels and mixtures with concentration gradients (Ciccarelli and Dorofeev, 2008; Kuznetsov *et al.*, 2011; Thomas, 2012; Vollmer, Ettner and Sattelmayer, 2012; Boeck, 2015; Boeck *et al.*, 2016).

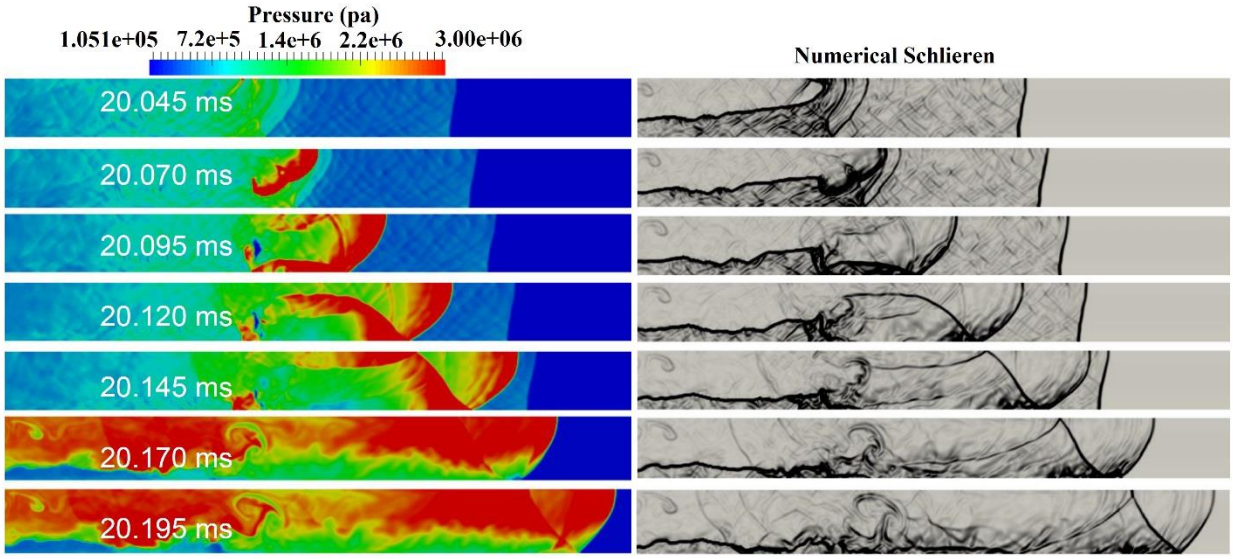

Figure 5-37: Pressure (left) and numerical schlieren (right) fields of detonation onset in the inhomogeneous 20% hydrogen-air mixture. The field-of-view extends from x = 3.75 m to x = 4.16 m.

5.5.3.2 Near-stoichiometric mixture (30% hydrogen concentration)

As shown in Figure 5-38, the predicted flame tip velocities are in reasonably good agreement with the measurements. For both the homogeneous and inhomogeneous mixtures, the flame tip velocity rises continuously in the obstructed part of the channel. FA is slightly stronger in the homogeneous mixture. Figure 5-38 shows flame speed data from BR60 experiments and simulations for 30% mixture. For both homogeneous and inhomogeneous mixtures, the flame tip velocity initially rises monotonically in the obstructed part of the channel (0 m < x < 2.05 m) and reaches values around 2000 m/s, indicating the transition to detonation within the obstructed channel section. It is difficult to determine the precise location of the onset of

detonation solely from flame speed measurements due to insufficient resolution. Initial FA is slightly stronger in the homogeneous mixture. The simulated flame tip velocities are in reasonably good agreement with the measurements (Khodadadi Azadboni *et al.*, 2019).

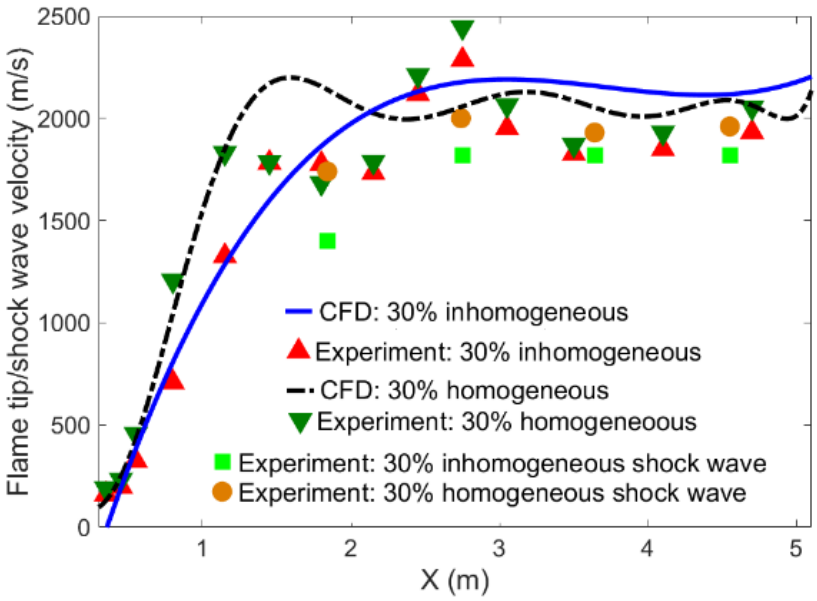

Figure 5-38: Comparison between the flame tip velocities for the homogeneous and inhomogeneous mixtures with 30% hydrogen concentration.

Pressure histories from experiments and simulations are compared in Figure 5-39 at a transducer location of x = 1.4 m. The pressure history for the homogeneous mixture shows a sharp increase in pressure at t = 12.4 ms to its peak value; by contrast, the inhomogeneous mixture shows an initial pressure increase at t = 11.4 ms to about 14 bar, a subsequent short decrease, and a sharp secondary increase to its peak value of about 30 bar at t = 11.5 ms. The step-wise increase in pressure and high secondary peak pressure observed for the inhomogeneous mixture suggests that the onset of detonation occurred in the immediate vicinity of the pressure transducer, at x = 1.4 m. By contrast, the single pressure increase observed for the homogeneous mixture suggests that the onset of detonation has occurred earlier, upstream of the transducer, and a detonation wave passes the transducer. In the

homogenous mixture, the onset of detonation happened around x= 1.15 m. This also will conclude that, although in the inhomogeneous mixture flame propagates faster, but the onset of detonation occurs later than the homogenous case. These initial observations are supported in the following by analysis of numerical schlieren sequences (Khodadadi Azadboni *et al.*, 2019).

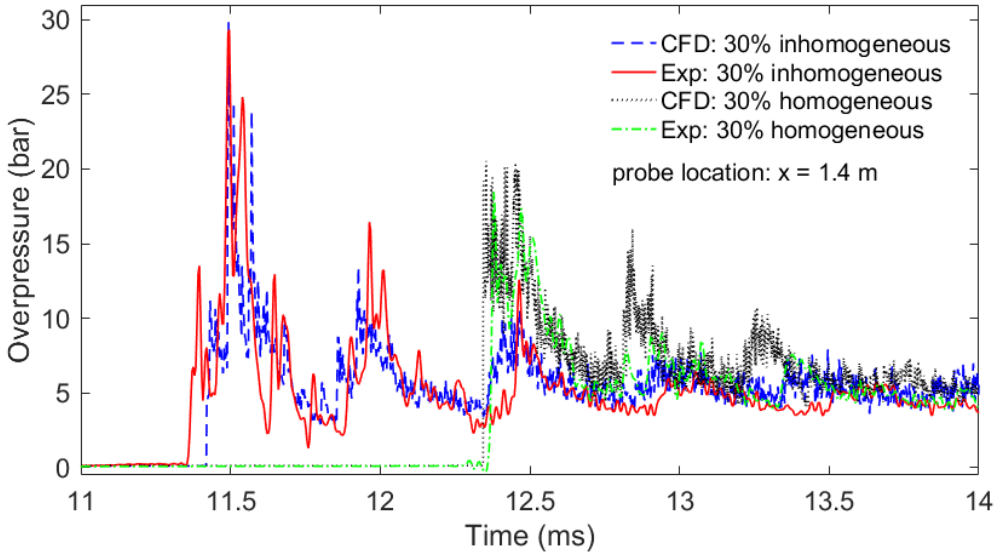

Figure 5-39: Comparison of overpressure at x = 1.4 m between the homogeneous and inhomogeneous mixtures at 30% hydrogen concentration (BR60).

Figure 5-40 shows the pressure and temperature fields generated from the simulations of the inhomogeneous mixture. In accordance with the experiments (Ciccarelli and Dorofeev, 2008; Kuznetsov *et al.*, 2011; Thomas, 2012; Vollmer, Ettner and Sattelmayer, 2012; Boeck, 2015; Boeck *et al.*, 2016), DDT is initiated by precursor shock reflection at the upstream faces of an obstacle, leading to local explosions behind the reflected shock wave and the onset of detonation either directly from the local explosions or from secondary hot-spots downstream of the obstacle. In the homogeneous mixture onset of detonation occurs between the obstacles located at x=0.85 m and x=1.15 m, whereas in the inhomogeneous mixture, the onset takes

place at the obstacle at x=1.45 m (can be seen in Figure 5-42). However, experiments show a detonation velocity deficit in the inhomogeneous mixture (L. R. Boeck *et al.*, 2016).

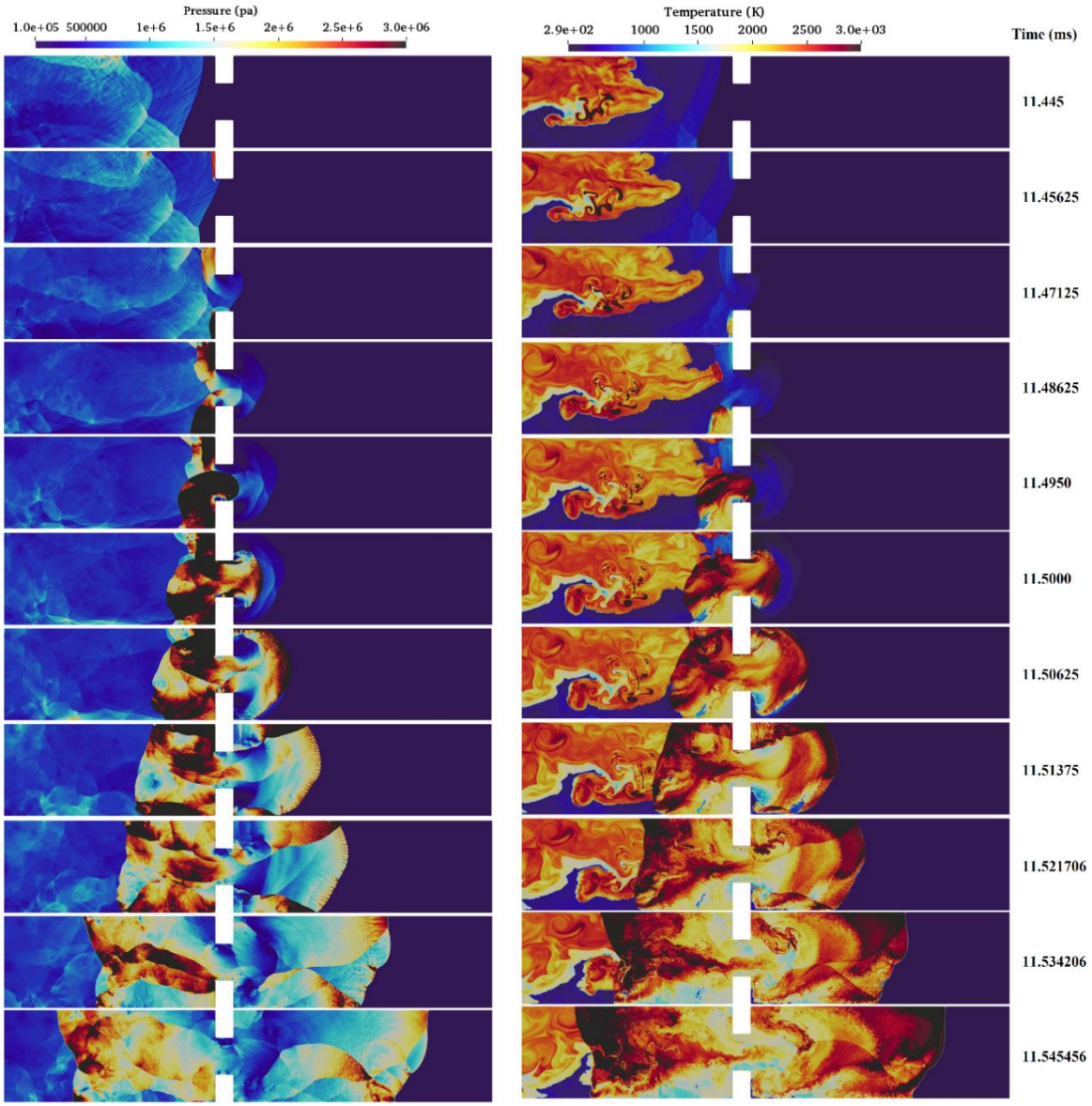

Figure 5-40: The predicted pressure (left) and temperature fields for the inhomogeneous with 30% hydrogen concentration. The obstacle in the field of view (FOV) is located at x=1.45 m.

Figure 5-38, Figure 5-39 and Figure 5-40, show that after the flame passed the 4th obstacle (x=1.45 m), the flame speed reached around 2100, which is above the CJ detonation velocity of the stoichiometric hydrogen-air mixture. It is also noted that the first local explosion occurred near the bottom wall (due hot spot generation near the reflected shock from obstacle), where the mixture is most lean with the volumetric hydrogen concentration is around 10% and the local speed of sound is around 361m/s (Khodadadi Azadboni *et al.*, 2016b). After the transition to detonation process, two shear layers formed in the burned gas, and small-scale vortices which indicate K-H instability were generated (Figure 5-41).

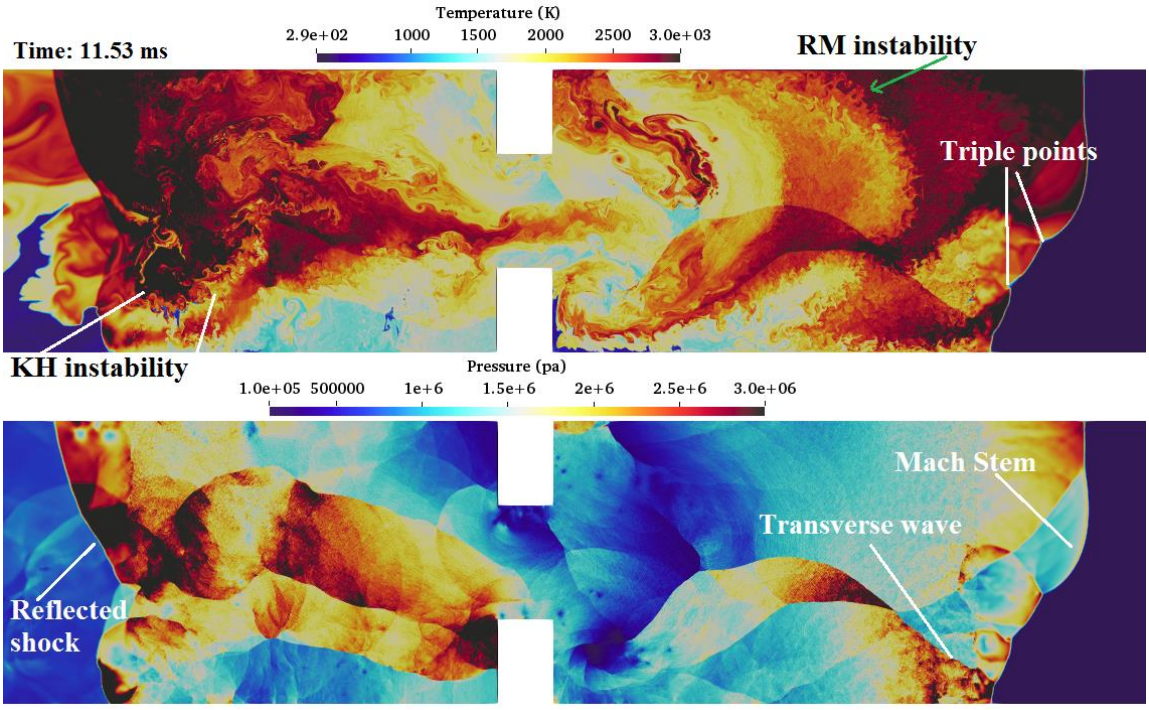

Figure 5-41: Small-scale features: The predicted temperature (top) and pressure (bottom) fields for the inhomogeneous with 30% hydrogen concentration. The obstacle in the field of view (FOV) is located at x=1.45 m, time: 11.53 ms.

Figure 5-41 shows the small-scale features in a snapshot of the onset of detonation in pressure and temperature fields generated from the inhomogeneous predictions at time=11.53 ms. The temperature field in Figure 5-41 shows small vortices in the shear layer generated in the burned area, which indicate the KH instability. The temperature field shows forwards and backwards mushroom shape jets in the burned area, which indicate as RM instability. The pressure field

in Figure 5-41, captured the details of detonation structure, the Mach stem, transverse shock as well as the reflected shock wave which are marked in the figure.

The numerical Schlieren in Figure 5-42 shows the onset of detonation in a BR60 channel for homogeneous (left) and inhomogeneous (right) mixture with 30% hydrogen concentration. It can be seen that the concentration gradients change not only the flame shape but also the formation of leading shocks and vortices behind the obstacles. In both cases, local DDT is initiated by precursor-shock reflection at the upstream faces of an obstacle, leading to local explosions behind the reflected shock wave and an over-driven detonation wave which eventually decays toward the CJ state. For the homogeneous mixture, secondary hot-spots are generated downstream of the obstacle which accomplishes the onset near the centre axis of the channel. At 12.39 ms, precursor shock waves are seen in front of the flame. The following frames show strong acceleration of the flame towards the precursor shocks and, eventually, the formation of a detonation wave. For the inhomogeneous mixture, local explosions at the upstream obstacle face directly cause the onset of detonation at 11.485 ms. In the homogeneous mixture onset occurs between obstacles, at x = 1.3 m, whereas in the inhomogeneous mixture, the onset takes place slightly later, at the obstacle at x = 1.45 m, which is consistent with initial observations from experimental and simulated flame speed and pressure histories. In the homogeneous mixture, at time 12.39 ms, triple leading shocks are moving in front of the flame, and suddenly at 12.435 ms, due to strong shock flame interaction in the middle of the channel, the accelerating flame have transited to detonation; then the shock and flame propagate together. However, in the inhomogeneous mixture, the transition to detonation took longer and further down from the channel entrance. Also, the mechanism of transition to detonation in the inhomogeneous mixture is different due to having different induction time along the height of the channel (Khodadadi Azadboni *et al.*, 2019).

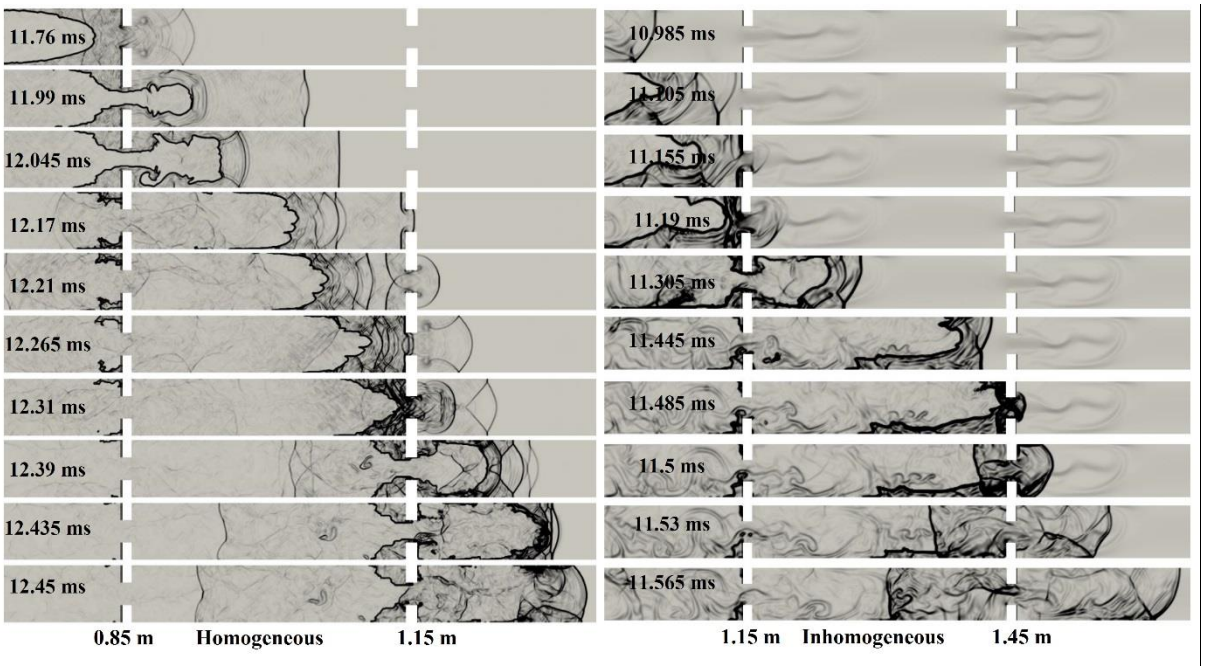

Figure 5-42: Numerical schlieren fields in the 30% hydrogen concentration with BR60. (Right: homogeneous 30% hydrogen mixture, left: inhomogeneous 30% hydrogen mixture).

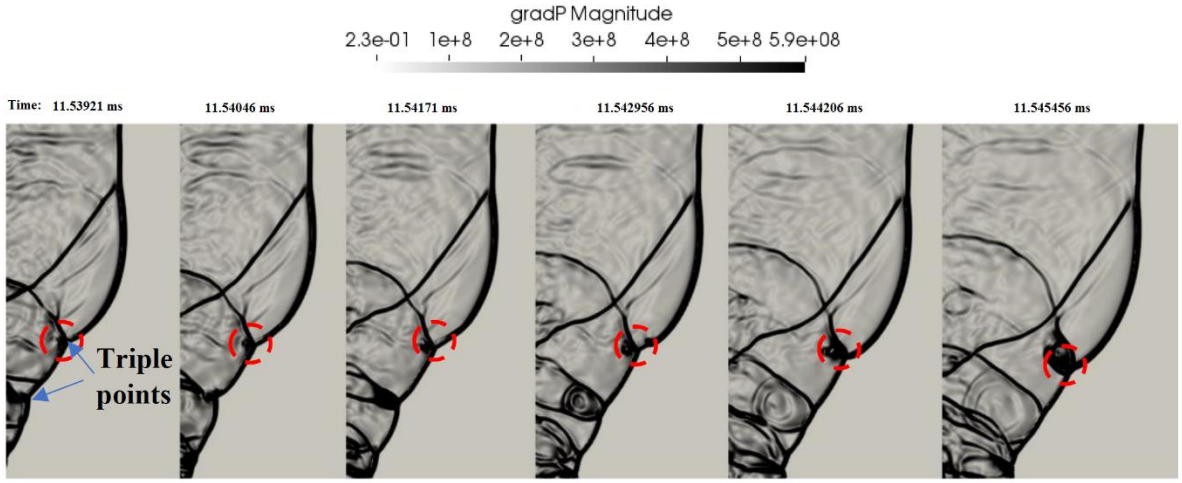

Figure 5-43: Triple points developments: Magnitude of pressure gradient evaluation right after DDT in the inhomogeneous 30% hydrogen-air mixture. The obstacle in the FOV is located at x=1.45 m.

Figure 5-43, shows the evaluation of triple points right after the onset of detonation, in the inhomogeneous 30% in an average hydrogen-air mixture. One of the triple points has been marked with a red circle line. It can be seen that as expected the triple points are moving in the detonation wave, and that is because of detonation cell generation.

5.5.3.3 Very rich mixture (40% hydrogen concentration)

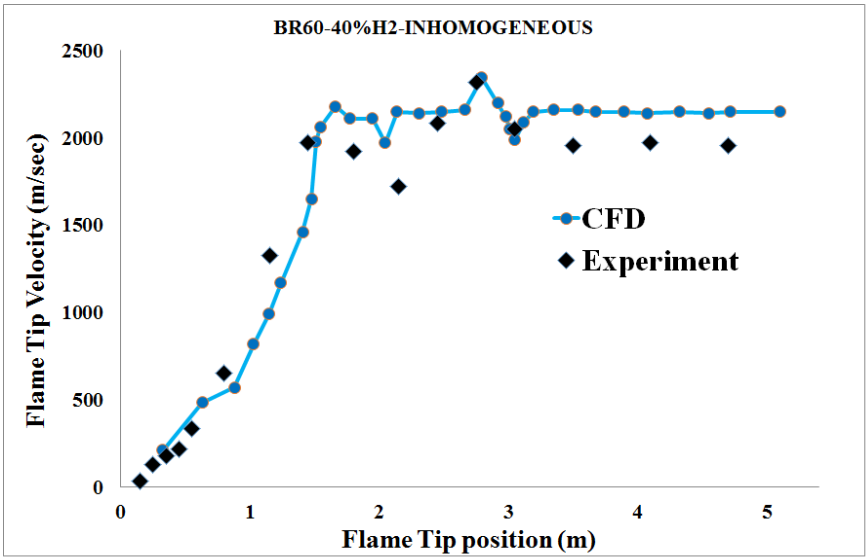

Figure 5-44: Comparison of the predicted and measured flame tip velocity for 40 % inhomogeneous hydrogen concentration in the 60% BR channel.

Figure 5-44, shows an excellent quantitative agreement in the predicted flame tip velocities with the experimental measurements (Boeck *et al.*, 2016) for the 40% hydrogen concentration, in a channel with a 60 % blockage ratio. Also, the maximum flame speed in the BR30 occurred sooner than the BR00 case, which indicated that within the studied range of between 0% to 60% blockage ratio configuration, increasing the blockage ratio would lead to faster in flame acceleration (FA).

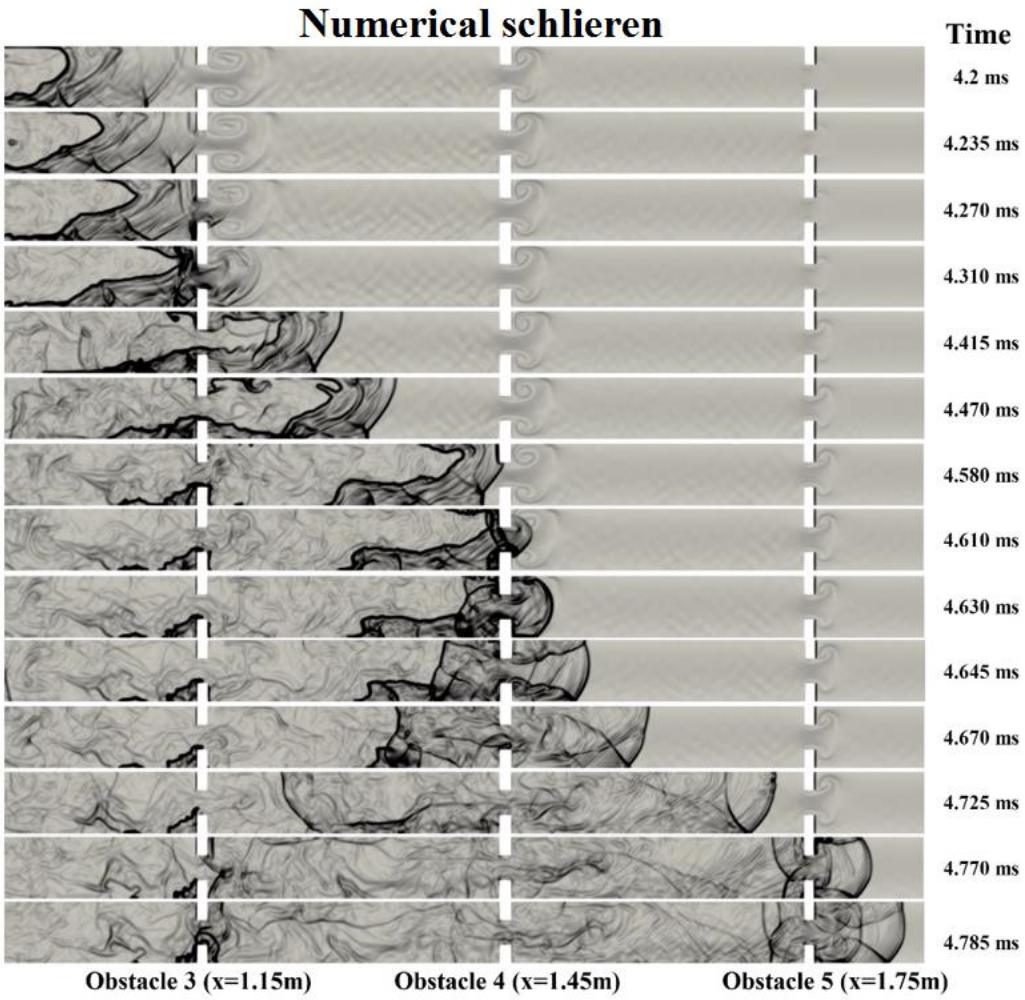

Figure 5-45: Numerical schlieren (magnitude of density gradient) contours of deflagration to detonation for inhomogeneous H2/Air mixture of 40% Vol and BR60.

Figure 5-45 shows the onset of detonation in the inhomogeneous 40% hydrogen/air mixture which located around obstacle 3, 4 and 5 at 4.2 ms a leading shock is moving ahead of the flame front. At 4.31 ms near to the upper wall, the reflected shock from the third obstacle, interacts the flame front, but that interaction was not strong enough to trigger the first local explosion (Khodadadi Azadboni, Heidari and Wen, 2018). At 4.580ms, Figure 5-45, the first weak explosion happens due to the interaction of the reflected shock from obstacle 4 and burnt gas. Then, at 4.610 ms this explosion wave generated a strong secondary explosion in the middle of the channel. Subsequently, the transition to detonation occurred at 4.630 ms. At 4.645ms, two shock waves from the bottom and top wall, in the downstream of obstacle 5,

reflected. These reflected shock waves interact in the middle of the channel and generate a stronger leading shock wave The process eventually reached a steady state, and the shock wave propagated at nearly the C-J velocity(Khodadadi Azadboni, Heidari and Wen, 2018).

Figure 5-45 also illustrated that in the case of a 60 percent blockage ratio, the transition to detonation happens earlier than the other cases with less blockage ratio. Hence it can be concluded that by increasing the blockage ratio from 0% to 60%, the flame will reduce the run-up distance.

5.6 Summary

Numerical studies have been conducted to investigate flame acceleration and transition to detonation in both homogeneous and inhomogeneous hydrogen-air mixtures in obstructed and unobstructed channel configurations. The developed VCEFoam solver has been used within OpenFOAM, for these simulations. For the considered experiment (Boeck *et al.*, 2016), different sets of configurations and fuel concentration have been studied. Three different geometry configuration such as: BR00 (0% Blockage ratio, smooth channel), BR30 (30 % blockage ratio), and BR60 (60% blockage ratio), have been considered in this study. Also, in order to study the effect of a concentration gradient, different mixture concentrations have been investigated in both homogenous and inhomogeneous mixtures. A total of 17 conditions were simulated for different hydrogen concentrations in both homogeneous and inhomogeneous mixtures with and without obstructions. The numerical predictions were compared against previous experiments. Overall, the predicted flame tip velocities, overpressures, and locations of detonation onset are in reasonably good agreement with the measurements. For both homogeneous and inhomogeneous mixtures with 30% hydrogen concentration, the onset of detonation occurs within the obstructed channel section, but the homogeneous mixtures show slightly faster flame acceleration and earlier onset. For the cases with 20% hydrogen concentration, the transition to detonation is observed only for the inhomogeneous mixture

where the concentration gradient enables stronger flame acceleration, especially in the unobstructed channel section in comparison with the homogeneous mixture.

The increase in the fuel concentration was found to increase the FA and faster transition to detonation. Also, the increase in the BR was found to increase the FA and slow down the possibility of transition to detonation in the present configuration. The role of hydrodynamic instabilities and the effect of baroclinic torque and RM instability have also been studied. The forward jet and backward jets which are a mushroom form flow represent the RM instability on the interface between the burned and unburned gas. The results support that RM instability is the primary source of turbulence generation in the present case.

The results of the three different blockage ratio configurations (BR00, BR30 and BR60), demonstrated the effects of the blockage ratio in DDT. The increase in the blockage ratio was found to increase the FA and faster transition to detonation.

This study confirms previous findings that transverse concentration gradients in channels can lead to substantially stronger FA and a higher propensity for DDT in comparison with homogeneous mixtures with the same average hydrogen concentration. In the unobstructed channel configuration, the onset of detonation is observed at the channel walls near the turbulent flame brush. High average hydrogen concentrations in conjunction with a concentration gradient are required to trigger DDT in the unobstructed channel. Flames in the gradient mixtures are observed to elongate while propagating along the unobstructed channel, whereas the homogeneous mixture shows an almost symmetric flame concerning the channel centerline.

Chapter 6 Vapour cloud explosion on an industrial scale

This chapter discusses vapour cloud explosion (VCE), generated from the release of evaporated LNG or natural gas which has already been dispersed and ignited. VCE explosion incidents usually occur outdoors while huge amount of fuel is dispersed (Woodward and Pitblado, 2010). VCE, can be categorized into two primary types: detonations and deflagrations. Detonations are much more destructive. Detonations usually happen in highly reactive fuels such as acetylene, hydrogen, and ethylene. LNG and Methane mixtures are usually considered as low to medium reactivity, which in most of the incidents they do not detonate (Foss *et al.*, 2003). It has been reported in the literature that LNG deflagration develops to detonation (DDT) only when the vapour cloud is either partially confined or it is within a highly congested region with several obstacles and blockages (Bjerketvedt, Bakke and van Wingerden, 1997).

6.1 Numerical approach in large scale modelling

In most of the relevant literature, hydrogen and methane/LNG fuel are commonly investigated in regard to explosion safety matters. In several studies, due to the high reactivity nature of hydrogen, this fuel has been considered as a worst-case scenario. Hydrogen in fuel mixtures also has the highest energy content by mass, but the lowest by volume (Wen, Madhav Rao and Tam, 2010). Hydrogen fuel is typically stored under higher pressures (30-300 bars) than other gaseous fuels, in order to achieve a higher energy density. Accidental release of hydrogen, during its handling, can lead to the formation of an ignitable mixture in a very short time. The potential use of hydrogen as a vehicle fuel would demand safe handling guidelines and a good understanding of the explosion hazards associated with installation, production and transportation.

The results presented in chapter 6, have confirmed the capability of the current numerical model to reproduce the small-scale features in DDT phenomena, as well as the structure of a detonation front. Such simulations are costly, due to the very high-resolution mesh, with some simulations taking around 35-45 days using 256 CPU cores of Kingston university's cluster. In this section, some large-scale studies have been selected to determine the applicability of the developed codes for modelling three-dimensional, real scale DDT studies. Therefore, the modelling very large scale and three-dimensional cases with the same resolution as mentioned in the previous chapter would be impossible and very cost effective. In this chapter, a robust combustion model will be added to the already developed density-based code, for modelling three-dimensional large-scale DDT and detonation scenarios.

Heidari et al. (Heidari *et al.*, 2011; Heidari, 2012), have shown that the detonation front can be artificially thickened by adjusting the chemistry so that the available grid can resolve the artificially thickened wavefront. The main difficulty with this approach is the lack of a proper reaction mechanism which works on such coarse grids. Consequently, the reaction mechanism would be grid-resolution dependent, so grid independency studies are not applicable. They also stated that the chemical reaction mechanism should be tuned and validated for any grid resolution. This method would add more complications. A similar approach, in which the chemical reaction mechanism has to be tuned based on the grid size has been introduced by (Yáñez *et al.*, 2011). This study aims to present a more general and robust approach for modelling large scale scenarios.

Ettner et al. (Ettner, Vollmer and Sattelmayer, 2014) and Hasslberger et al. (Hasslberger, Boeck and Sattelmayer, 2015) recently introduced a more robust combustion model for modelling large scale explosion scenarios (Ettner, Vollmer and Sattelmayer, 2014; Hasslberger, Boeck and Sattelmayer, 2015). The presented combustion model is based on a flame wrinkling model and autoignition model. Hasslberger et al. (Hasslberger, Boeck and Sattelmayer, 2015) found that the original flame wrinkling approach of Weller (Weller, 1993) will underestimate the deflagration in lean mixtures (particularly in the RUT experiments test cases, which will be discussed in section 6.2). Flame instabilities such as Darrieus-Landau and thermal-diffusive

instabilities, play a significant role during the modelling of DDT scenarios in lean mixtures (such as RUT cases). (Landau, 1944). In lean mixtures, the thermal diffusive instabilities are more important because of the difference between the thermal and mass transport across the burned and unburned areas. Since the RUT cases have a very lean hydrogen/air mixture, this is an important criterion and should be taken into account in the numerical code. Thus, in order to overcome the underestimation in deflagration of lean mixtures, the combustion model needs to resolve these instabilities.

Therefore, in this section, the developed density-based solver VCEFoam (which has been described and verified in chapter 3 and 4), has been modified for explosion modelling for industrial scale applications. The main solver modification is a different combustion modelling approach (which has been mentioned in the transport equation), and the rest of the equations in the solver remains the same. In this approach, two different source term will consider in the transport equation. One source term will model the deflagration process and the second source term will capture the detonation phase. Also, in the deflagrative source term, the effect of flame instabilities such as Darrieus-Landau (DL) and Rayleigh Taylor (RT) instabilities in flame surface wrinkling factor has been taken into account in addition to turbulence induced flame surface wrinkling. For modelling the thermal diffusive instabilities in large-scale models, the Muppala's combustion model (Muppala *et al.*, 2005, 2009) has been implemented and added as a subroutine in the numerical code, for modelling the large-scale scenarios. This model has been utilised in both pure and mixed fuels, within different Lewis number conditions, in both RANS and LES turbulent contexts (Muppala *et al.*, 2005, 2009; Vendra and Wen, 2018).

As mentioned above MILES and LES methods, represents more small-scale details in the flow fields. LES is a reasonable compromise between URANS and Direct Numerical Simulation (DNS), however, it is only applicable in small scale and medium scale scenarios (Hasslberger, 2017). In many LES subgrid scale models, significant part of the turbulence spectrum must be resolved, in which it requires to provide grid sizes, in the inertial range. Clearly, for three-dimensional large industrial scale, using LES, MILES, and DNS methods are impossible. Also, for safety studies, it is mainly important to predict the key characteristics factors, such as overpressure, flame speeds. Therefore, consider the industrial application, in this section, all of the large-scale test cases will be modelled in three dimensional with an Unsteady Reynolds-

Averaged Navier-Stokes (URANS) turbulence model. A statistical turbulence models, also known as Unsteady Reynolds-Averaged Navier-Stokes (URANS) models has been used in this large-scale modelling. Grid cell size is in the order of integral turbulence scales. Computational costs are clearly higher than using a simpler approach (e.g. RANS k-epsilon model), but still it is within an acceptable level. These approaches define the current standard in engineering fields. The URANS model, is globally unsteady but statistically averaged flow fields, including gas dynamic effects. Similarly, the important interaction between energy and momentum, specifically, the conversion of chemically bounded energy to kinetic energy is included in the model (Hasslberger, 2017). Also, based on a comparison of turbulence and chemistry time scales, the transition between different regimes of premixed combustion can be accounted for. Regarding DDT phenomena, the triggering event itself is a highly stochastic, localized and rare event but URANS is able to predict its statistical probability (Hasslberger, 2017).

6.1.1 Combustion modelling in large scale scenarios:

The transport equation for reaction progress variable is as below:

$$\frac{\partial(\bar{\rho}\tilde{c})}{\partial t}+\frac{\partial(\bar{\rho}\tilde{c}\tilde{u}_j)}{\partial x_j}-\frac{\partial}{\partial x_j}(\bar{\rho}D_{eff}\frac{\partial\tilde{c}}{\partial x_j})=\bar{\omega}_{c,ignition}+\bar{\omega}_{c,deflagrative} \tag{6.1}$$

In the Eq. 6.1, there are two source terms in the transport equation; $\bar{\omega}_{c,def}$, $\bar{\omega}_{c,ign}$ these are the deflagrative and detonative source term respectively. In this equation, the overbar symbol represents the Reynolds-averaging function, and the tilde symbol represents the Favre-averaging function. The flame wrinkling approach is based on a flamelet model, which tracks the flame front (c) between the burnt ($c=1$) and unburnt area ($c=0$) (Weller, 1993; Ettner, Vollmer and Sattelmayer, 2014; Hasslberger, Boeck and Sattelmayer, 2015).

In Eq. 6.1, D_{eff} represents the effective mass diffusion, which includes a laminar term (D), and a turbulent term (D_T). The turbulent diffusivity term can be derived using a turbulent Schmidt

number (Sc_T) and an eddy viscosity parameter (μ_T), which can be derived from the turbulence model.

$$D_{eff} = D + D_T = D + \frac{1}{Sc_T}\frac{\mu_T}{\bar{\rho}} \tag{6.2}$$

For modelling flame acceleration, the deflagrative source term has been applied in the model. For modelling the transition to detonation stage, the auto ignition source term has been considered as follows:

$$\bar{\omega}_{c,ignition} = \bar{\rho}\frac{1-\tilde{c}}{\Delta t}H(\tilde{\tau}-1) \tag{6.3}$$

In the above equation, Δt denotes the current time step, H denotes the Heaviside function and τ is a ratio between the simulation time (t), to the autoignition delay time ($\tau = {}^{t}\!/_{t_{ignition}}$).

The ignition delay time $t_{ignition}$ of a mixture is a function of local temperature T, pressure p, and mixture composition. This local ignition delay time is calculated using multi-dimensional look-up tables, obtained from isochoric explosion calculations, which are in turn calculated using CANTERA (Goodwin, Moffat and Speth, 2009) and a detailed reaction mechanism. More detail about the detonation auto ignition delay time and its validation can be found in the following (Ettner, Vollmer and Sattelmayer, 2014; Hasslberger, Boeck and Sattelmayer, 2015).

The deflagrative source term can be defined as follows:

$$\bar{\omega}_{c,deflagrative} = \bar{\rho}_u G \Xi S_L \left|\nabla \tilde{c}\right| \tag{6.4}$$

In Eq. 6.4, ρ_u denotes the density of the unburned mixture of fuel and oxidiser.

The first source term in the transport equation, which is the deflagrative source term $\bar{\omega}_{c,deflagrative}$, will capture the flame acceleration and deflagration. It will be modelled by using the Weller combustion model (Weller, 1993). In this flame wrinkling model introduced by Weller (Weller, 1993), a factor G (where G is between 0 and 1), corresponds to the quenching of turbulent flames. In Eq. 6.4, Ξ is the flame wrinkling factor, which is the ratio of the turbulent burning velocity S_T, to the laminar burning velocity S_L:

$$\Xi = \frac{S_T}{S_L} \tag{6.5}$$

Further details about the deflagrative source term are provided in (Weller, 1993; Ettner, Vollmer and Sattelmayer, 2014; Hasslberger, Boeck and Sattelmayer, 2015).

In most of the CFD code used to model large-scale scenarios, and empirical correlation for the turbulent burning velocity S_T is used.

In the present model, an additional balanced transport equation will be considered, to resolve the subgrid flame wrinkling factor:

$$\bar{\rho}_u \Xi G_\Xi - \bar{\rho}(\Xi - 1) R_\Xi = 0 \tag{6.6}$$

In the above transport equation for the flame surface area, G_Ξ is the generation rate, and R_Ξ is the reduction rate. These can be described by the following:

$$G_\Xi = \frac{0.28}{\tau_\eta} \tag{6.7}$$

$$R_\Xi = G_\Xi \frac{\Xi_\Xi}{\Xi_\Xi - 1} = G_\Xi \frac{\Xi^*_{eq}}{\Xi^*_{eq} - 1} \tag{6.8}$$

In Eq. 6.7, τ_η is the Kolmogorov length scale and Ξ_Ξ or Ξ^*_{eq} is the equilibrium flame wrinkling factor when the source and sink term are balanced.

As previously stated, the present study different to what has already been presented by (Weller, 1993; Ettner, Vollmer and Sattelmayer, 2014; Hasslberger, Boeck and Sattelmayer, 2015), a specific model has been considered for modelling the thermal diffusive instabilities in the large-scale model.

In order to model Ξ^*_{eq}, the turbulent flame wrinkling factor, the algebraic reaction rate closure, proposed by Muppala et al., (Muppala *et al.*, 2005)is utilized in the present study. Muppala's combustion model can be applied in lean turbulent premixed combustion, under varying Lewis number (Le = thermal diffusivity/diffusion coefficient) conditions (Muppala *et al.*, 2009; Burke *et al.*, 2015). Moreover, it can apply in different turbulent models.

$$\Xi^*_{eq} = 1 + \frac{0.46}{Le}\mathrm{Re}_t^{0.25}\left(\frac{u'}{S_L}\right)^{0.3}\left(\frac{p}{p_{ref}}\right)^{0.2} \tag{6.9}$$

In Eq. 6.9, u' represents the rms velocity fluctuations, Le is the Lewis number, $\mathrm{Re_t}$ is the turbulent Reynolds number and p represents pressure.

In order to model the DL instabilities (affected by premixed lean mixtures), Vendra et al.(Vendra and Wen, 2018) have introduced a simple analytical expression which has already been proposed earlier by(Bauwens, Chaffee and Dorofeev, 2011). The presented approach by (Bauwens, Chaffee and Dorofeev, 2011; Vendra and Wen, 2018) has been implemented in the present numerical model.

$$\Xi_{DL} = \max\left[1, \alpha_{DL}\left(\frac{\Delta}{\lambda_c}\right)^{1/3}\right] \tag{6.10}$$

In Eq. 6.10, Ξ_{DL} represents the wrinkling factor due to the DL instability, λ_c is a cutoff wavelength of the DL instability proportional to the flame thickness (it is also called as a cutoff wavelength of unstable scales), and α_{DL} is a coefficient which is used to consider the

uncertainty in λ_c, Δ is the turbulent filter size. This model can be applied for both LES and URANS turbulence model.

Bauwens et al. (Bauwens, Chaffee and Dorofeev, 2008), have shown that, in the case of methane-air mixtures $\alpha_{DL}\left(\frac{\Delta}{\lambda_c}\right)^{1/3} < 1$, therefore, the flame instabilities will be resolved on the grid scale and the DL wrinkling factor will be equal to unity, $\Xi_{DL} = 1$. In the current study (as suggested by(Bauwens, Chaffee and Dorofeev, 2011; Vendra and Wen, 2018)) for lean hydrogen-air mixtures will use $\lambda_c = 7mm$ and $\alpha_{DL} = 1.3$ to match the initial flame propagation.

The RT instability can also increase the flame surface area significantly. A basic approach proposed, by(Bauwens, Chaffee and Dorofeev, 2011; Vendra and Wen, 2018), has been used in the current study to model the flame wrinkling factor due to the RT instability. The additional transport equation for RT modelling is as follows:

$$\frac{\partial(\Xi_{RT}\bar{\rho})}{\partial t} + \tilde{U}_s.\nabla\Xi_{RT} = \bar{\rho}_u G_{RT}(\Xi_{RT} - 1) - \bar{\rho}R_{RT}(\Xi_{RT} - 1) \tag{6.11}$$

In the above equation, Ξ_{RT} is the surface wrinkling factor due to the RT instability. G_{RT} and R_{RT} are the rate of generation and removal rate of RT flame wrinkling, respectively.

$$G_{RT} = 2(k_{RT}\frac{\sigma - 1}{\sigma + 1}\vec{a}\cdot\vec{n}_f)^{1/2} \tag{6.12}$$

$$R_{RT} = \frac{8\sigma S_L k_{RT}}{\pi} \tag{6.13}$$

Where in Eq. 6.12, σ is the expansion ratio, a is the flame acceleration (derived from flame displacement velocity) and k_{RT} is the unstable wavenumber, related to RT instability. In the

modelling of flame surface acceleration, values of k_{RT} (in Eq. 6.12 and Eq. 6.13) are considered to be constant for a given fuel mixture, and in the present study (as suggested in (Vendra and Wen, 2018)) it is assumed to be 6 m^{-1}.

The flame surface wrinkling factor will be updated with the above submodels, to predict DL and RT instabilities:

$$\Xi = \Xi_{eq} \times \Xi_{DL} \times \Xi_{RT} \tag{6.14}$$

Therefore, in the present model, the effect of flame instabilities such as DL and RT in flame surface wrinkling factor has been taken into account in addition to turbulence induced flame surface wrinkling.

In the DDT phenomena, when the flame front meets a blockage or an obstacle, the wrinkled flame regime will transition from a wrinkled flame to a turbulent flame regime, in which the mechanisms in control for the turbulence include Kelvin-Helmholtz (KH), or Ritchmeyr Meshkov (RM) instabilities. These hydrodynamic instabilities (KH and RM instabilities) will be triggered once the flame is accelerated over several obstacles. Therefore, the CFD model should be capable of capturing KH and RM instabilities. In order to capture the KH instability, which is due to having velocity gradient in the interface of the burned and unburned area, there should be high-resolution grids at these interfaces. To provide higher grid resolution, an adaptive mesh refinement (AMR), technique (as described in chapter 4) will be employed in the numerical code. While modelling the RM instability, the numerical code should be capable of capturing high pressure and density gradients in the flow fields. As described in chapter 4, the current numerical code is a density-based code, in which the capability of capturing high pressure and density gradient has been proven by presenting the Sod's shock tube problem as well as the 2D oblique shock problem case (presented in chapter 5).

Large-scale experimental test cases, with lean hydrogen fuel (RUT test cases), will be modelled in the following for validation purposes. The test includes both DDT and detonation initiation scenarios. After validating the model with hydrogen fuel, vapour cloud explosion in methane and LNG fuel will be studied.

6.2 Code validation for an industrial scale: RUT facilities

In order to validate the large-scale model presented in the previous section, the largest available indoor DDT and explosion experiments were chosen. These are conducted at the RUT facility at Kurchatov institute (Dorofeev *et al.*, 1996; Efimenko and Gavrikov, 2007).

The RUT facility geometry is one of the most complex configurations in the experimental test cases of DDT scenarios. Due to the complexity of the RUT geometry, these verification test cases have been simulated in three dimensions instead of two dimensional.

Three different experimental test cases have been selected for the purpose of verification. These cases differ with respect to geometry configuration (blockage ratio), fuel mixture concentration and nature of ignition source. In the first two selected test cases, the mechanism of flame acceleration (deflagration) and transition to detonation (DDT) will be investigated. Moreover, in addition to DDT scenario, a detonation initiation test case will be studied.

6.2.1 Experimental configuration and computational setup

RUT facility tests have been carried out at the Russian Research Centre ("Kurchatov Institute") (using hydrogen/air mixtures in a complex geometry (Dorofeev *et al.*, 1996, 1997). As shown in Figure 6-2, Figure 6-3 and Figure 6-4, the large scale RUT geometry has an inner volume of approximately 424 m^3 (without obstructions). The first obstructed channel has length x=34.6 m, height y=2.3 m and depth z=2.5 m. This channel is followed by a canyon, which is a sudden jump in cross-section. The canyon has length x=10.5 m, height y=6 m and depth z=2.5m. A third channel with is a curved ramp shape follows the canyon. The third channel has length x=20 m; height y=2.3 m and depth z=2.5 m.

Figure 6-1: View of the RUT facility (Efimenko and Gavrikov, 2007).

The following are the selected test cases:

1. RUT 16: DDT test case; 30% blockage ratio.

2. RUT 22: DDT test case; 60% blockage ratio.

3. RUT 09: (Detonation test case); Direct initiation.

The details of these test cases have been provided in Table 6-1.

Table 6-1: RUT test case details

	RUT16	RUT22	RUT09
Hydrogen fuel concentration	12.5 %	14 %	25.5 %
Blockage ratio	30 %	60 %	0 (smooth channel)
Number of obstacles	12 (with 2.5 m spacing)	6 (with 5 m spacing)	0 (smooth channel)

Inner volume (without obstruction)	423.9 [m^3]	423.7 [m^3]	242.5 [m^3]
Ignition source	spark	spark	200 g TNT
Main feature	DDT	DDT	Direct detonation initiation

For the RUT16, with 30% blockage ratio, twelve concrete obstacles were placed along the first channel with a spacing of 2.5 m. For the RUT22, with 60% blockage ratio, six concrete obstacles were placed along the first channel with a spacing of 5 m. These details can be found in Table 6-1. All boundaries have been assumed to have a no slip, adiabatic, wall boundary condition. The Initial temperature in these tests was 293 K, and the initial pressure in all the tests was considered 1 atm. In order to generate a CFD mesh, the geometries were first created by using CAD software (SolidWorks). The CFMesh (available in foam extended (Gschaider *et al.*, 2013) version of OpenFOAM) was then used to generate the mesh from the CAD (.STL) file. The average cell size was 0.02339 m, which produced around 17.2 million 3D hexahedral cells. A snapshot of the 3D hexahedral mesh for the RUT22 case is shown in Figure 6-5. As previously mentioned in section 7.1, in order to capture the flame front more accurately, AMR with two-level mesh refinement was used during the transient run. In these test cases, the reactive mixture is confined in a closed domain, therefore, all the boundaries are considered as no-slip wall boundary conditions. The initial temperature and pressure are 293 K and 1.013 bar, respectively. For the RUT 16, and RUT 22 cases, the spark ignition has been modelled via a patch of burned area with high temperature. The ignition spark location has been shown in Figure 6-3. For the RUT 09, the ignition has been modelled by using a small patch with high pressure and temperature, which is equivalent to 200 g TNT.

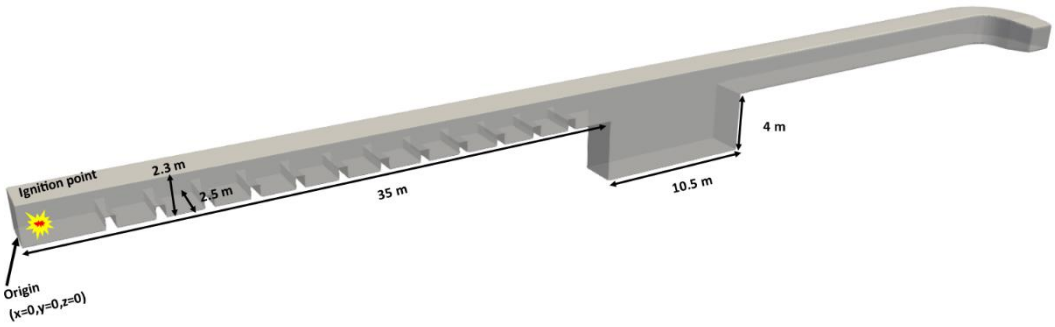

Figure 6-2: RUT 16 geometry configuration; 30% blockage ratio.

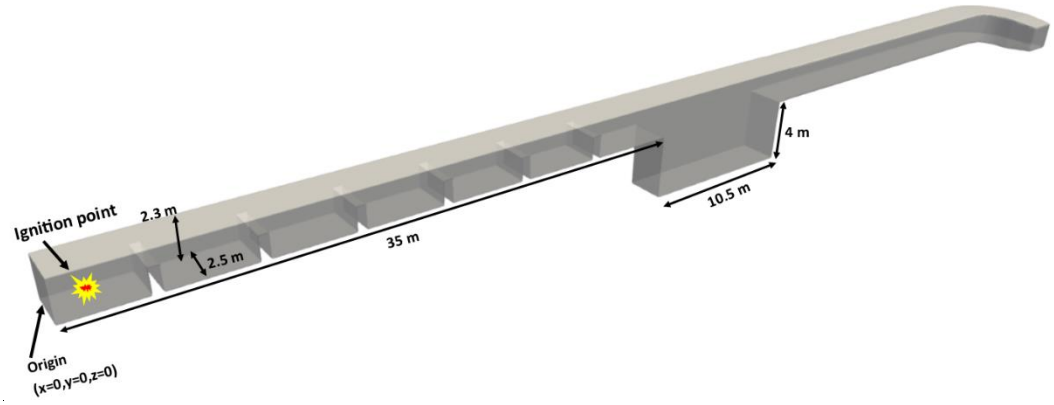

Figure 6-3: RUT 22 geometry configuration: 60 % blockage ratio.

Figure 6-4: RUT 09 geometry configuration: direct detonation initiation.

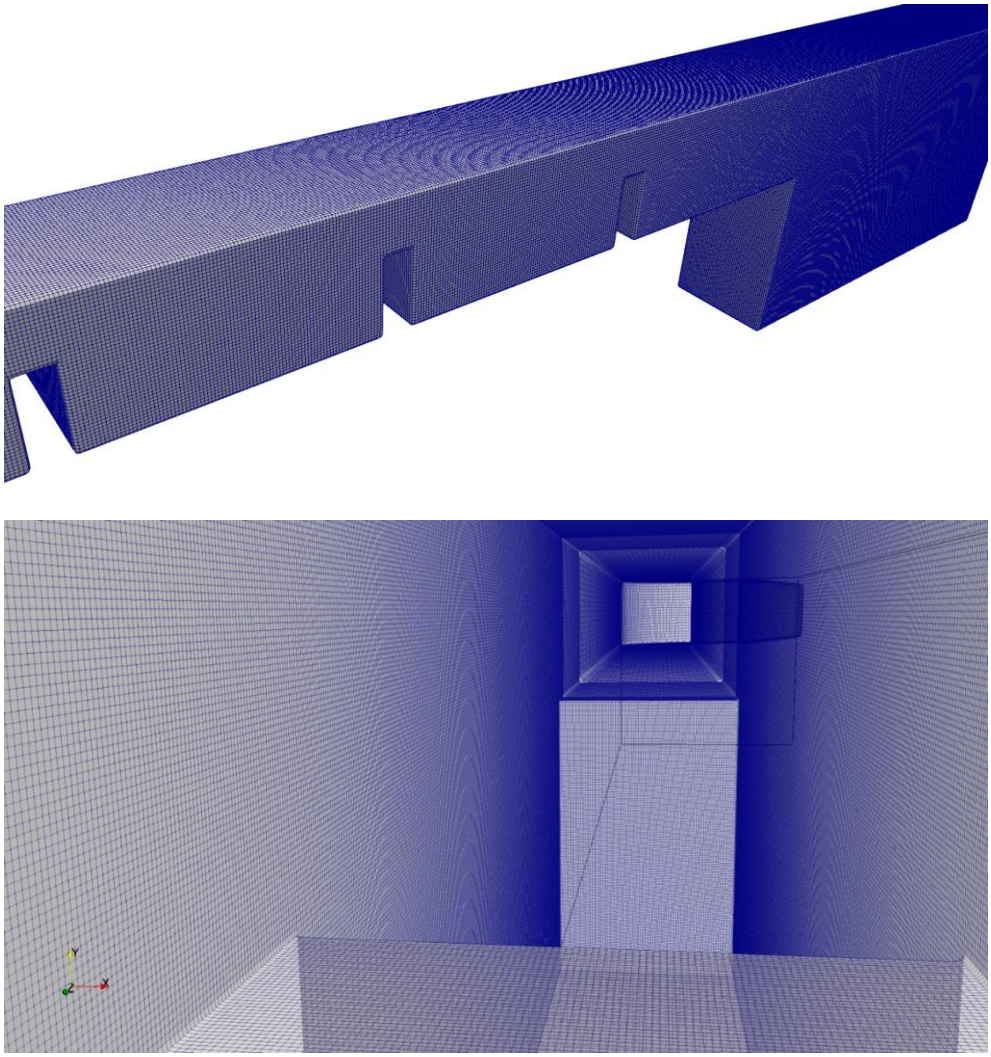

Figure 6-5: Snapshot of the 3D hexahedral mesh for the RUT22 case; top: outer part of the canyon, bottom: inner view of the channel.

Figure 6-2, Figure 6-3 and Figure 6-4, show the geometry configurations of RUT 16 with 30% blockage ratio, RUT 22 with 60% blockage ratio and RUT 09, detonation initiation case, respectively. In order to record the overpressure in the channel, a number of pressure transducers were installed in the domain. The locations of these pressure gauges are shown in both Figure 6-6 and Table 6-2.

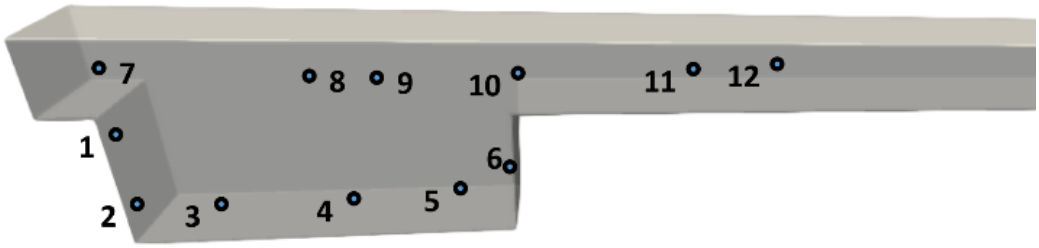

Figure 6-6: Pressure gauges position in the RUT cases.

Table 6-2: coordinates of the gauge sensors in the RUT facilities.

Gauge number	pressure transducers *coordinates*
01	(35.35, -1.0, 1.2)
02	(35.62, -2.5, 1.05)
03	(38.09, -2.5, 1.05)
04	(42.10, -2.5, 1.2)
05	(44.09, -2.5, 1.2)
06	(45.90, -2.5, 1.2)
07	(35.35, 1.0, 1.2)
08	(41.01, 1.0, 1.2)
09	(43.59, 1.0, 1.2)
10	(46.29, 1.0, 1.2)
11	(52.49, 1.0, 1.2)
12	(52.99, 1.0, 1.2)

6.2.2 Mesh Sensitivity Analysis

In order to demonstrate that the results of the large-scale cases, are independent of the grid size a mesh sensitivity study for one of the RUT cases has been provided. For this purpose, the RUT16 test case has been modelled with four different mesh resolutions.

- coarse size mesh: 42.102 cm
- Medium size mesh: 21.051 cm
- Fine mesh: 8.186 cm
- Very fine mesh (Highest resolution mesh): 2.339 cm.

Figure 6-7 shows the overpressure vs time, for the four mesh resolutions, in the RUT 16 test case.

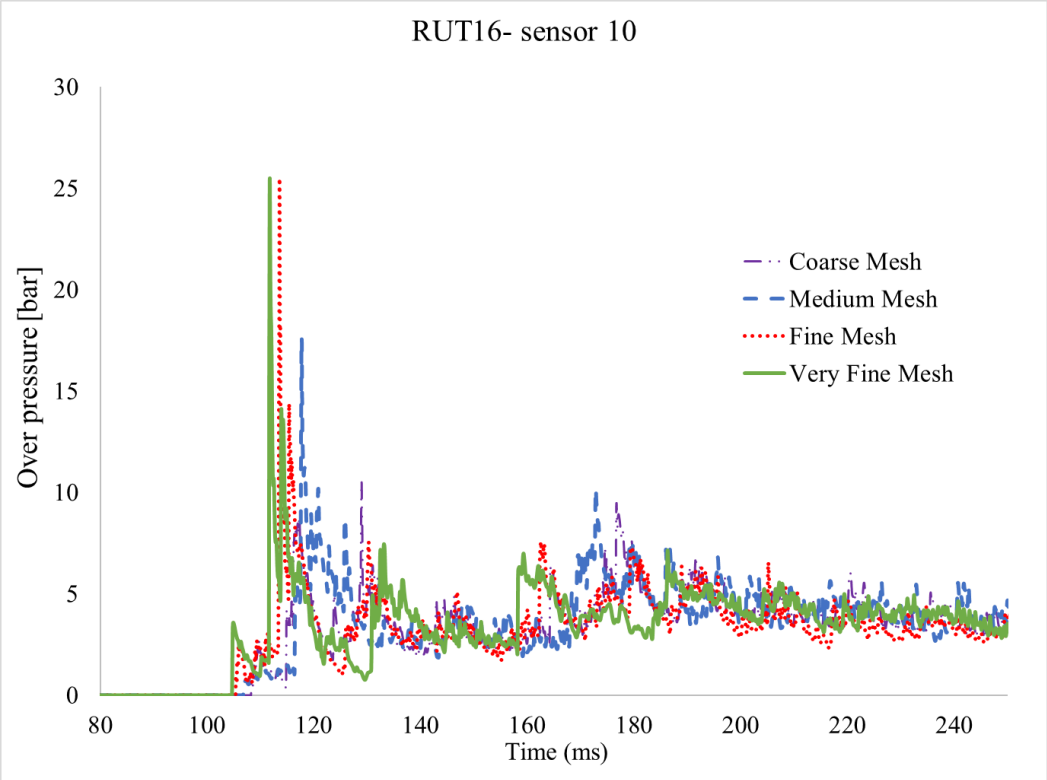

Figure 6-7: Grid independency study: overpressure vs time for the RUT 16 case; probe location at sensor 10.

Figure 6-7 demonstrate that by increasing the mesh resolution, from coarse to very fine mesh, the predicted overpressure become independent of grid size. It can be found that even coarse mesh, could not capture the transition to detonation phenomena and only the flame acceleration (deflagration) was captured. By refining the mesh from fine mesh (8.186 cm) to very fine mesh (2.339 cm), the results do not change significantly, therefore, it can be concluded that the results on the fine mesh (8.186 cm), are mesh independent. Therefore, for saving computational cost, 8.186 cm mesh resolution can be used in this present study.

Also, in the recent work done by Hasselberger et al. (Hasslberger, Boeck and Sattelmayer, 2015), they have found that using cell around 8 cm will be sufficient to predict accurate flame propagation and correct location of DDT.

6.2.3 Results of the RUT 16 case: 30% blockage ratio

The computational domain for the RUT 16 case is shown in Figure 6-2. 12 concrete obstacles with 30% blockage ratio were installed along the first channel (left side of the domain), with a spacing of 2.5 m. This specific experiment represents the lowest ever measured detonation limit (12.5 %) of hydrogen/air mixtures (Hasslberger, Boeck and Sattelmayer, 2015).

Figure 6-8 shows overpressure at the end wall of the canyon (sensor 6, which is marked in Figure 6-6), for the RUT 16 case. The results are compared with the experimental measurements and a similar CFD study by other researchers (Hasslberger, Boeck and Sattelmayer, 2015). The predicted overpressure is in good agreement with the experimental measurements. The transition to detonation in the lean Hydrogen/air mixture (12.5%) occurred in the canyon area. The present CFD model has captured the DDT phenomenon. However, the CFD model by Hasslberger et al. (Hasslberger, Boeck and Sattelmayer, 2015) was unable to capture DDT in this configuration and fuel mixture.

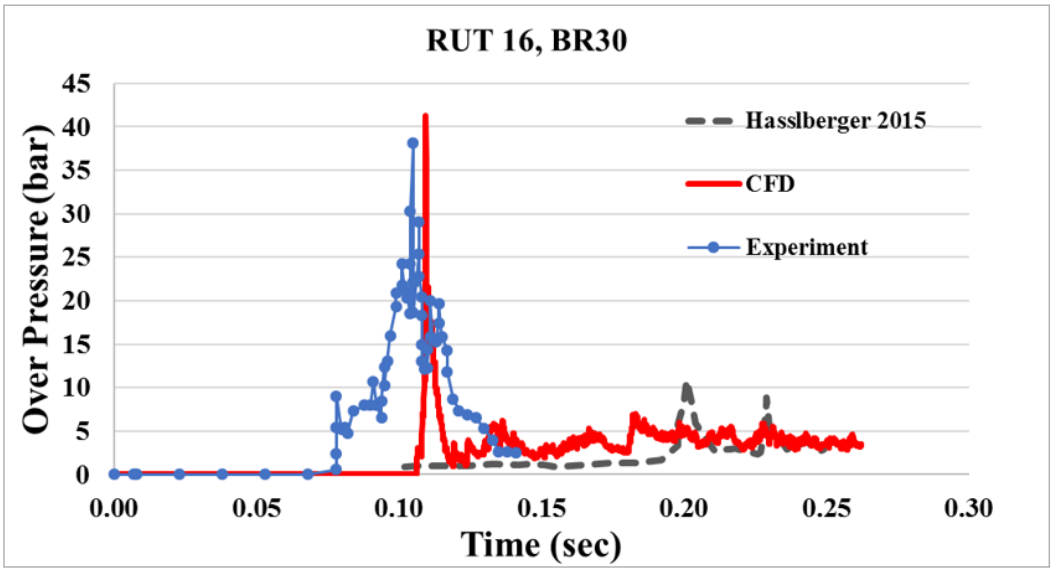

Figure 6-8: overpressure probe at the end wall of the canyon (sensor 6), for the RUT16.

Figure 6-9 shows the results of numerical schlieren of pressure for the RUT16 test case. It also shows two-dimensional front reconstructions from photodiode measurements (small circles). It can be seen that at 109 ms, an explosion wave is propagating towards the left in the bottom of the canyon (in Figure 6-9 it has been marked with red circle), by comparing this against the bottom picture in Figure 6-9, the same behaviour can be found in the experimental measurement. The solid lines in Figure 6-9 are explosion waves in the experiment. These explosion wave movements are in agreement with the predicted numerical schlieren. In this scenario, DDT happened near the end of the canyon, and the detonation wave propagated backwards into the second channel.

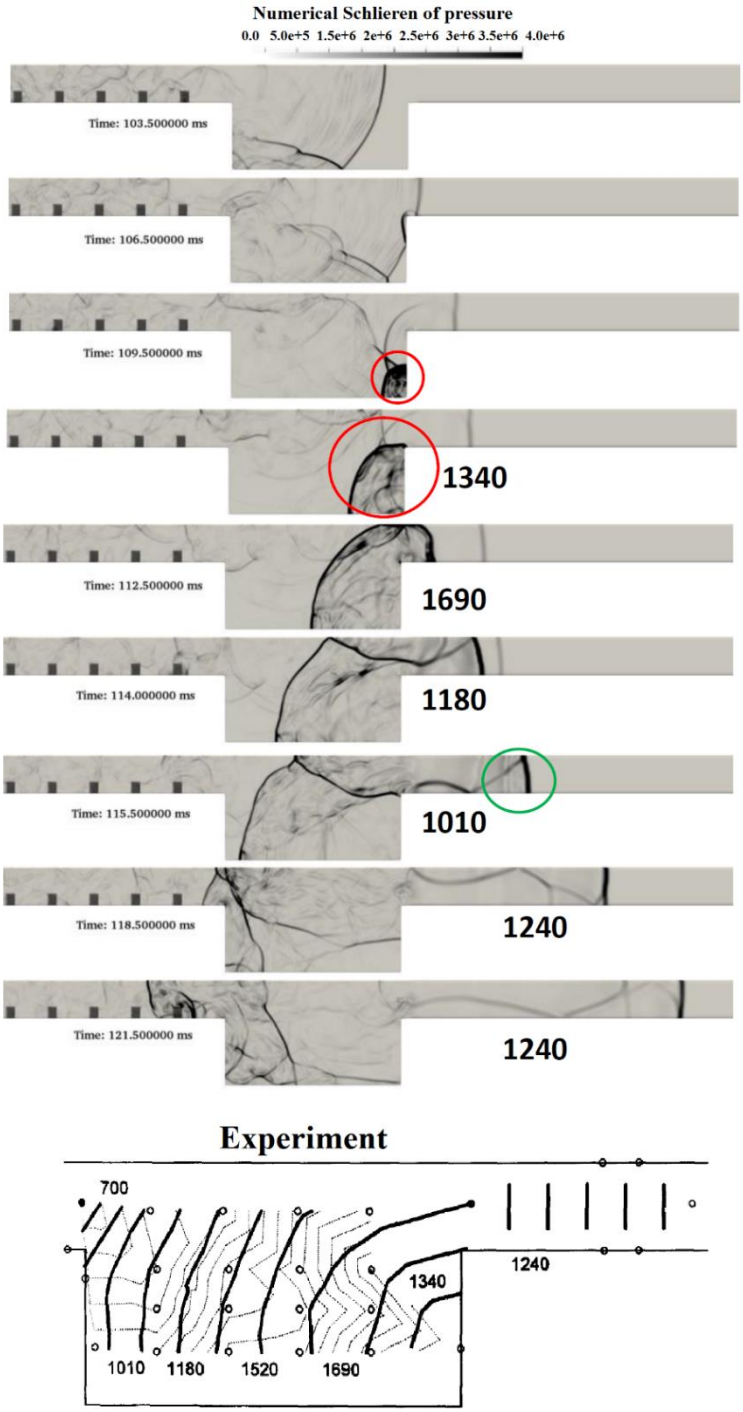

Figure 6-9: Top: numerical schlieren of pressure for RUT16, bottom: Small circles in the experiment; Flame front reconstructions from photodiode measurements, The solid lines are explosion waves in the experiment; Reproduced from (Dorofeev et al., 1996).

Figure 6-10, Figure 6-11 and Figure 6-12 show the numerical schlieren, pressure fields and the temperature isosurface representing during the DDT process for the RUT 16, BR 30% case. Figure 6-13 shows overpressure recordings in pressure sensors 1-12. These snapshots, as well as the pressure probe recordings, demonstrate that the lean hydrogen flame has been accelerated after interacting with the obstacles in the first part of the channel. It should be noted that DDT had not yet taken place in the first part of the channel. At 87 and 90 ms, in the pressure and temperature filed contours (which are Figure 6-11 and Figure 6-12), it can be seen that some localised explosion has occurred in the first channel. However, these localised explosions were not strong enough to trigger detonation. At 102 ms after ignition, it can be seen that, after the leading shock and flame front reached the bottom wall of the canyon, a reflected shock from the end wall of the canyon interacts with the flame front, and another weak localised explosion occurred, which did not trigger any detonation. Close to the flame front, a sudden pressure peak can be recognised. The reflected shock propagates faster in the burned mixture rather than in the unburned mixture. In both areas, the speed of sound can differ around the factor of two. In the locality of the pressure peak, a local explosion has generated. At the bottom of the canyon, the local explosion, eventually meets the Mach stem of the precursor shock. Later, at 109 ms, it can be seen that a strong explosion has occurred at the bottom right side of the canyon, moving towards the leading shock and flame front. By looking at Figure 6-11 and Figure 6-12, it can be found that the strong explosion has turned into a detonation wave, moving both downstream and upstream of the canyon. At 111.0 ms, the strong local explosion reflects off from the canyon end wall. This will lead to a secondary blast wave, propagating upward and backward direction (seen at 112.5 ms) – similar to what was observed in the experiment. Eventually, at 117.0 ms onwards, in the second channel, it can be found that the overdriven detonation wave, overtakes the precursor shock and decreases to a steady CJ detonation propagation.

In this case, the reflection of the leading shock at the canyon end wall, did not directly lead to the transition to detonation. The DDT was triggered through hot spots, and eventually by local explosions in a turbulent flame brush.

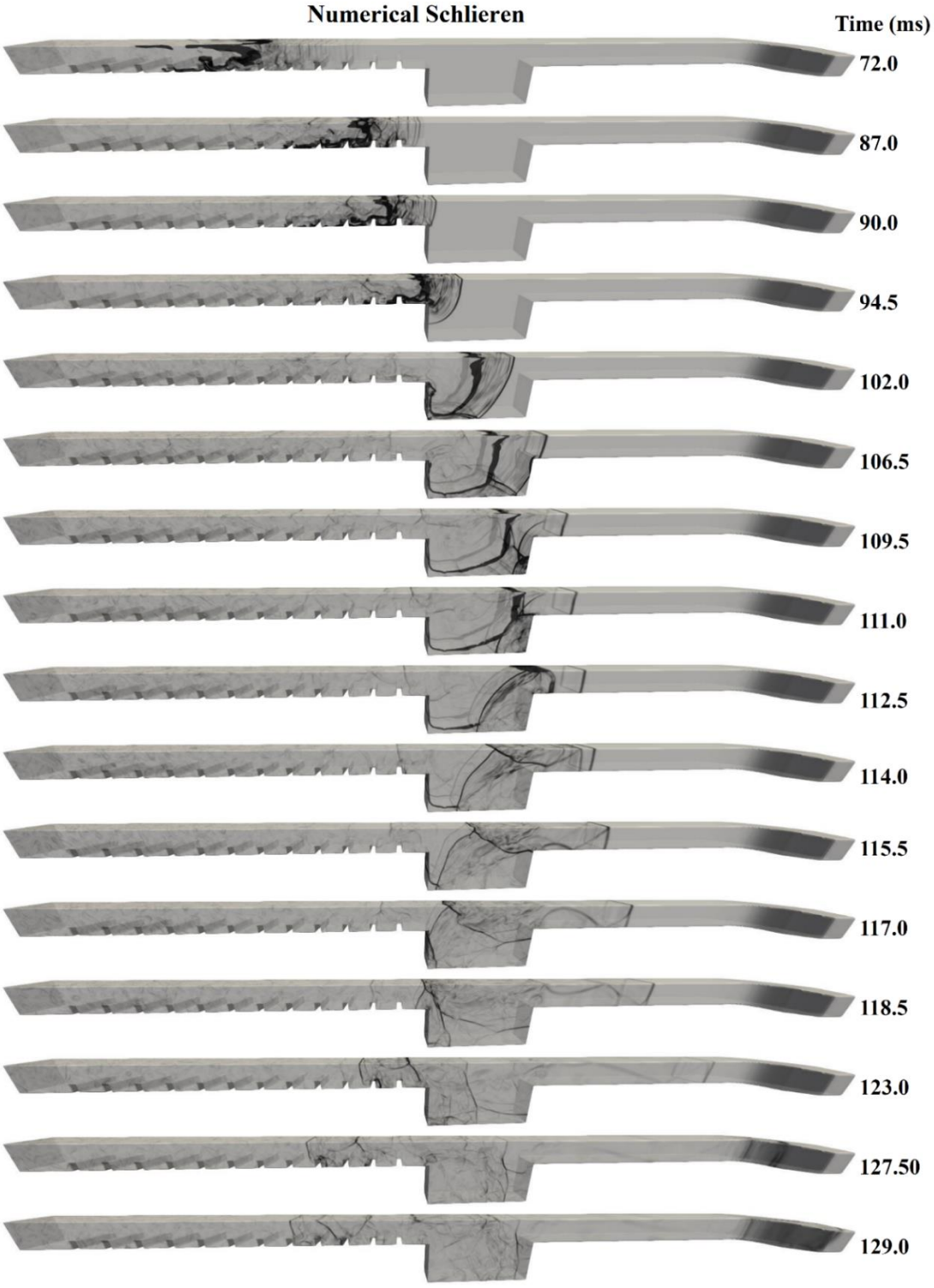

Figure 6-10: Numerical schlieren during the DDT process for the RUT 16, BR 30%.

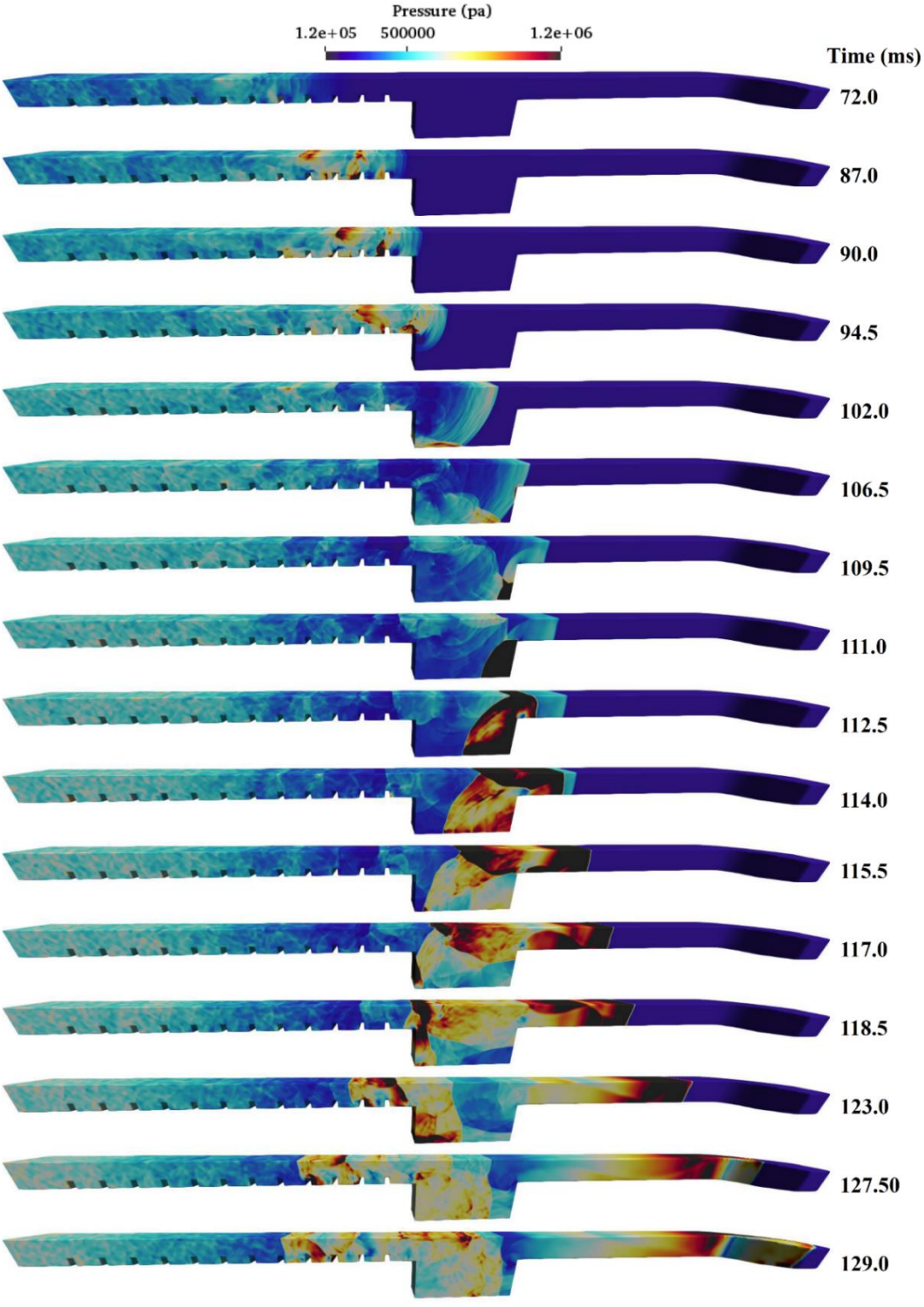

Figure 6-11: Pressure fields during the DDT process for the RUT 16, BR 30%.

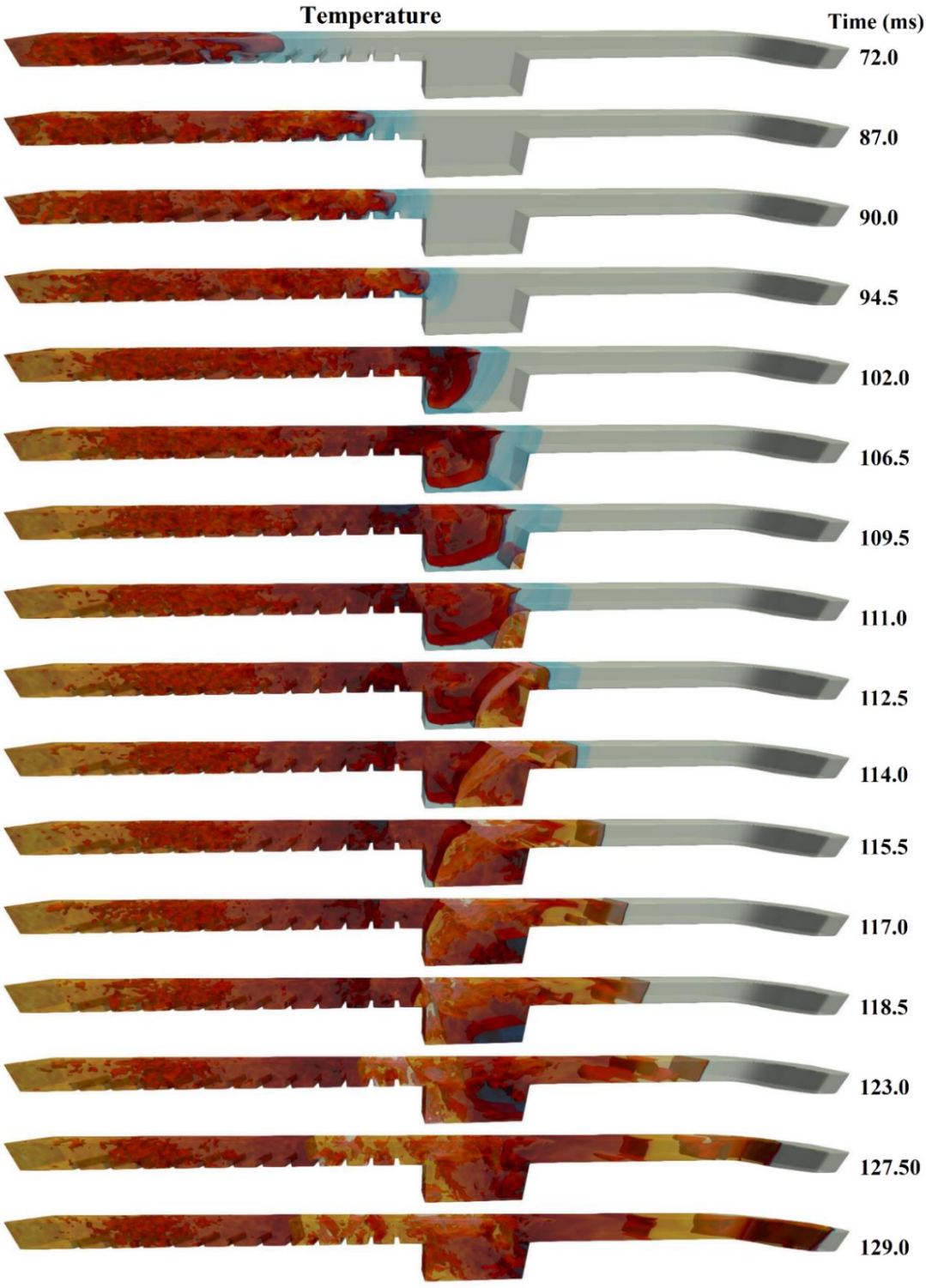

Figure 6-12: Isosurface of temperature at 2000 K during the DDT process for the RUT 16, BR 30%.

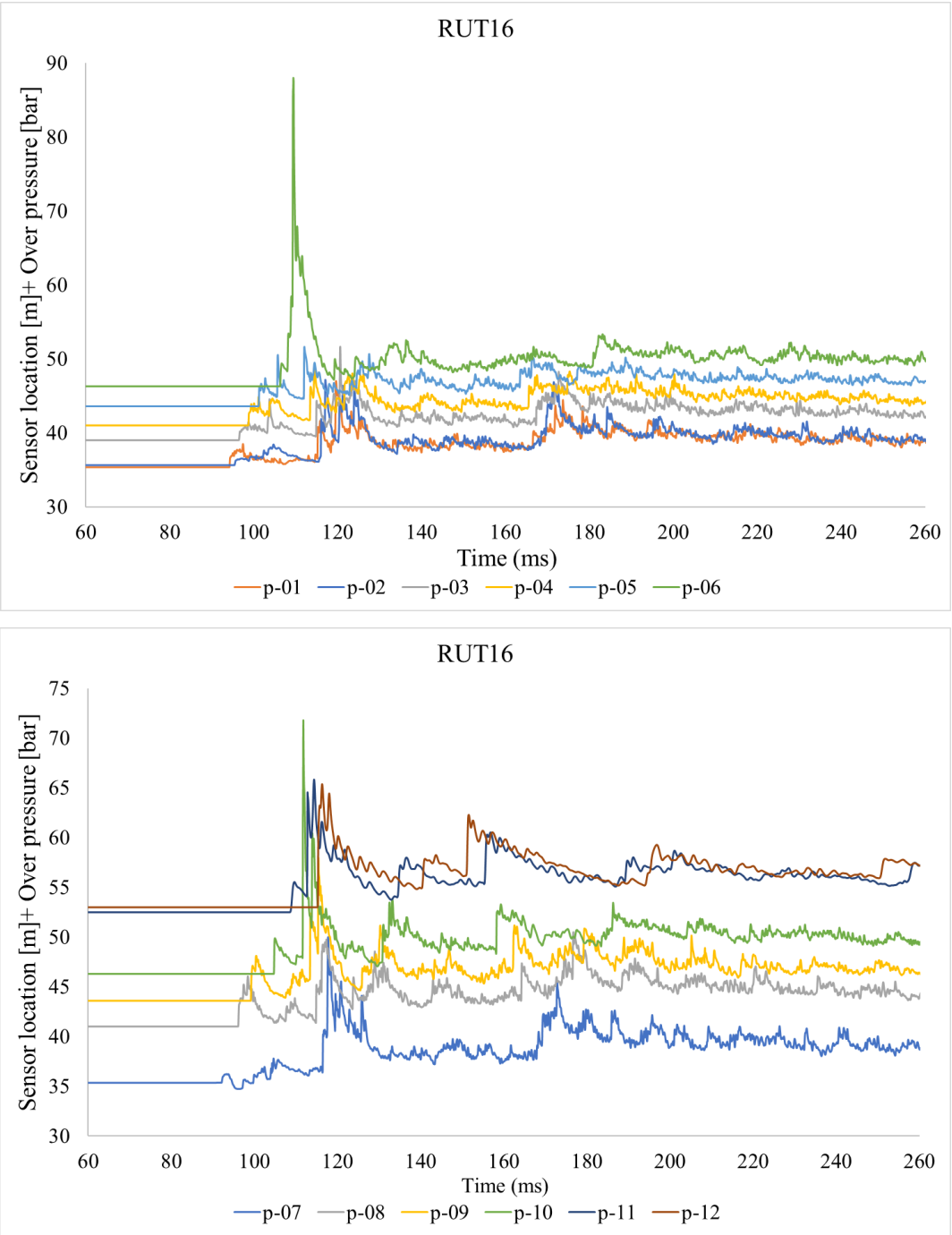

Figure 6-13: Overpressure recordings in RUT16; top: sensors 2 to 6, lower line of canyon area; bottom: sensor 7 to 11, upper line sensors.

Figure 6-13 shows the pressure recording for sensors 1 to 12; which are the lower- and upper-line pressure probes. In these plots, the transient overpressure recordings are shifted in space according to the x coordinate of the pressure probe position. As it has been stated in the geometry configuration, the canyon section is approximately from x=35 m to x=46 m. The maximum overpressure occurs in sensor 6, which is close to the end canyon wall. This will support the above-mentioned idea of "in this scenario, DDT was triggered from hot spots and ultimately by local explosions". After the sudden pressure increase, the generated local explosion from the bottom end wall of the canyon will meet the flame front, which will lead to a detonation wave propagating in the second channel.

6.2.4 Results of the RUT 22 case: 60% blockage ratio

The computational domain configuration for the RUT 22 case is shown in Figure 6-3. It is shown in the geometry configuration that six concrete obstacles with 60% blockage ratio were placed along the first channel with a spacing of 5 m.

Figure 6-14 shows a qualitative comparison of the predicted flame tip position against the available experimental measurement data. Figure 6-14 demonstrates a good agreement with the numerical prediction of the flame tip position and the experimental measurements. This space-time plot, in addition to representing a verification against the experiment, will demonstrate the flame acceleration behaviour.

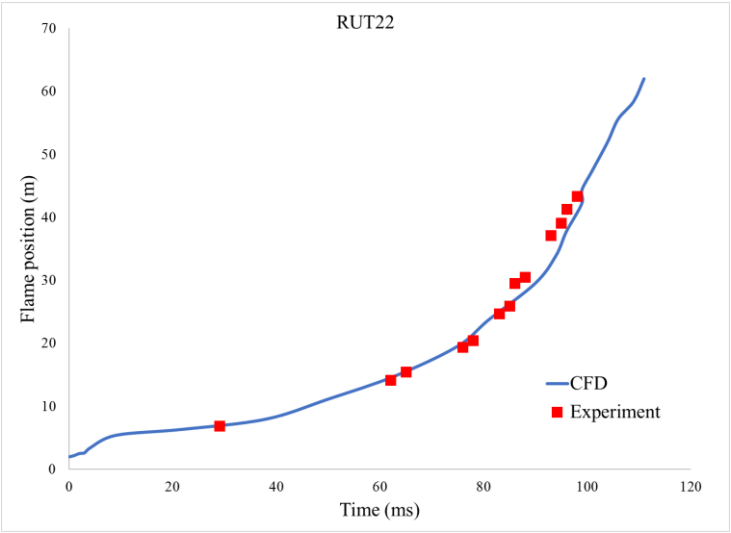

Figure 6-14: RUT22: Flame tip position vs time

For further investigation of the explosion behaviour, and the effect of flame interacting obstacles, additional pressure probes have been installed in the first left part of the channel. The exact coordinates of these pressure sensors are shown in Figure 6-15.

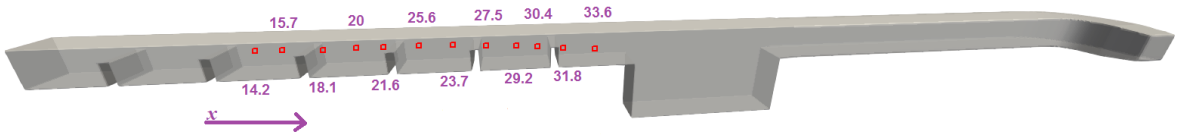

Figure 6-15: Location of pressure probes in the first channel of the RUT 22 case.

shows the overpressure recordings in RUT22 scenario. In which the top plot indicates the pressure recorded by sensors located in the first channel, middle plot: the pressure recorded by sensors 2 to 6 (lower line of canyon area), and bottom plot: the pressure recorded by sensor 7 to 11 (the upper line of the canyon area). For the pressure recording in the first obstructed channel, sensors are named based on their x coordinate. As shown in the geometry configuration, the canyon section is approximately from x=35 m to x=46 m. In these plots

shown in , the transient overpressure recordings are shifted in space according to the x coordinate of the pressure probe position.

In addition to pressure recordings, pressure, temperature and numerical schlieren fields (Figure 6-17, Figure 6-18 and Figure 6-19 respectively) are essential for analysing the DDT process in detail.

The top plot in demonstrates that, at 60 ms, the first sudden jump in overpressure occurs at sensor 18 (x=18.1m, close to the third obstacle), which is around 13 bar. Note that the CJ overpressure, for 14% hydrogen/air mixture, is 9.9 bar (Calculated by STANJAN (Reynolds, 1986)). This overpressure is above the CJ overpressure limit, but detonation did not occur (by looking at the temperature fields contour Figure 6-12). Around 70 ms maximum overpressure occurs at sensor 30 (x=27.5m; close to the last obstacle), which is around 20 bar. However, this strong localised explosion did not lead to detonation (from the temperature fields at 70.5 ms). The middle plot in shows that the maximum overpressure in the lower line of the canyon area is at sensor 6, which is close to the end canyon wall. This is due to the interaction of the reflected detonation waves from the left-end canyon wall and the bottom wall (this can be found at 81 ms in the numerical schlieren fields, Figure 6-19). Pressure recordings at sensor 11 and 12 (sensors in the second channel) demonstrate that a stable detonation wave is moving downstream of the channel (the recorded overpressure is around 13 bar, which is above CJ overpressure).

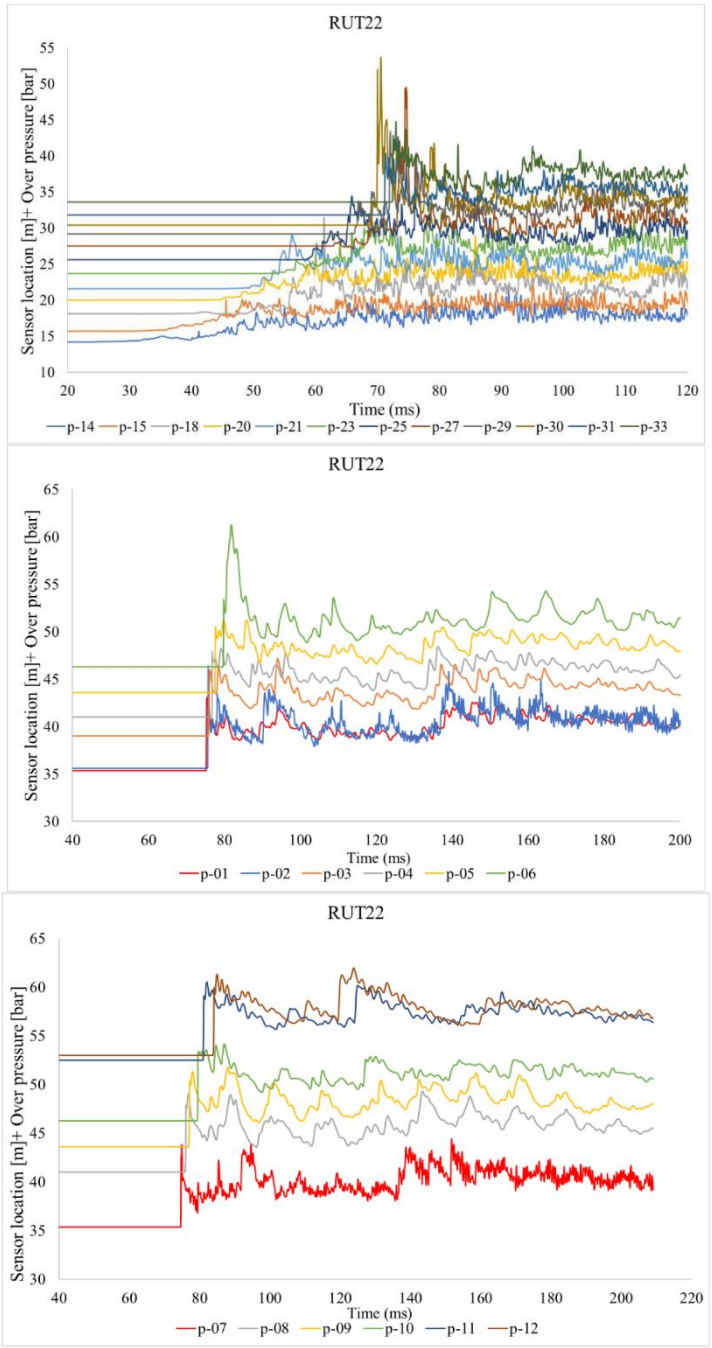

Figure 6-16: Overpressure recordings in RUT22; top: sensors are located in the first channel, middle: sensors 2 to 6, lower line of canyon area, and bottom: sensor 7 to 11, the upper line of the canyon area.

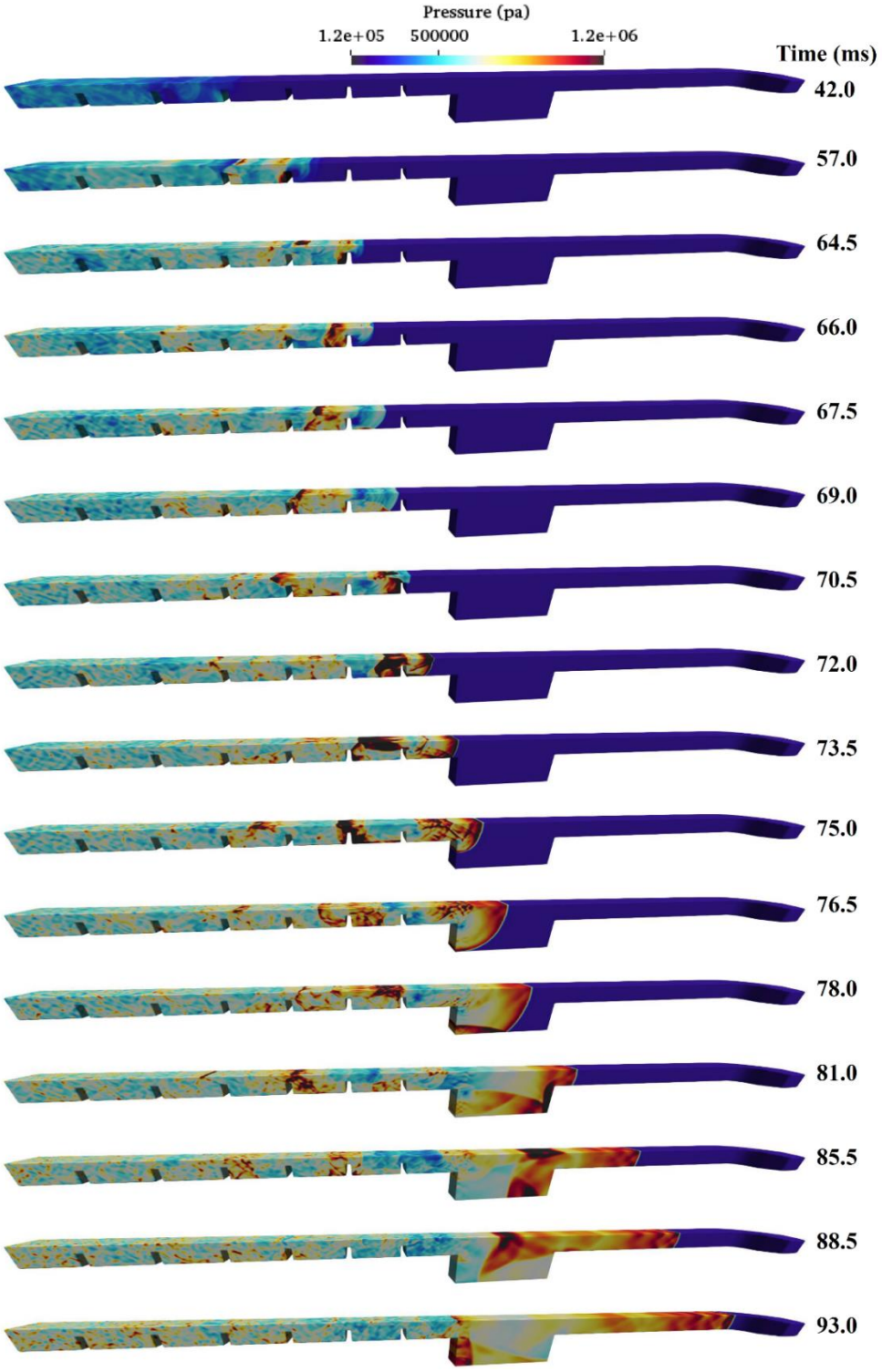

Figure 6-17: Pressure fields during the DDT process for the RUT 16, BR 60%.

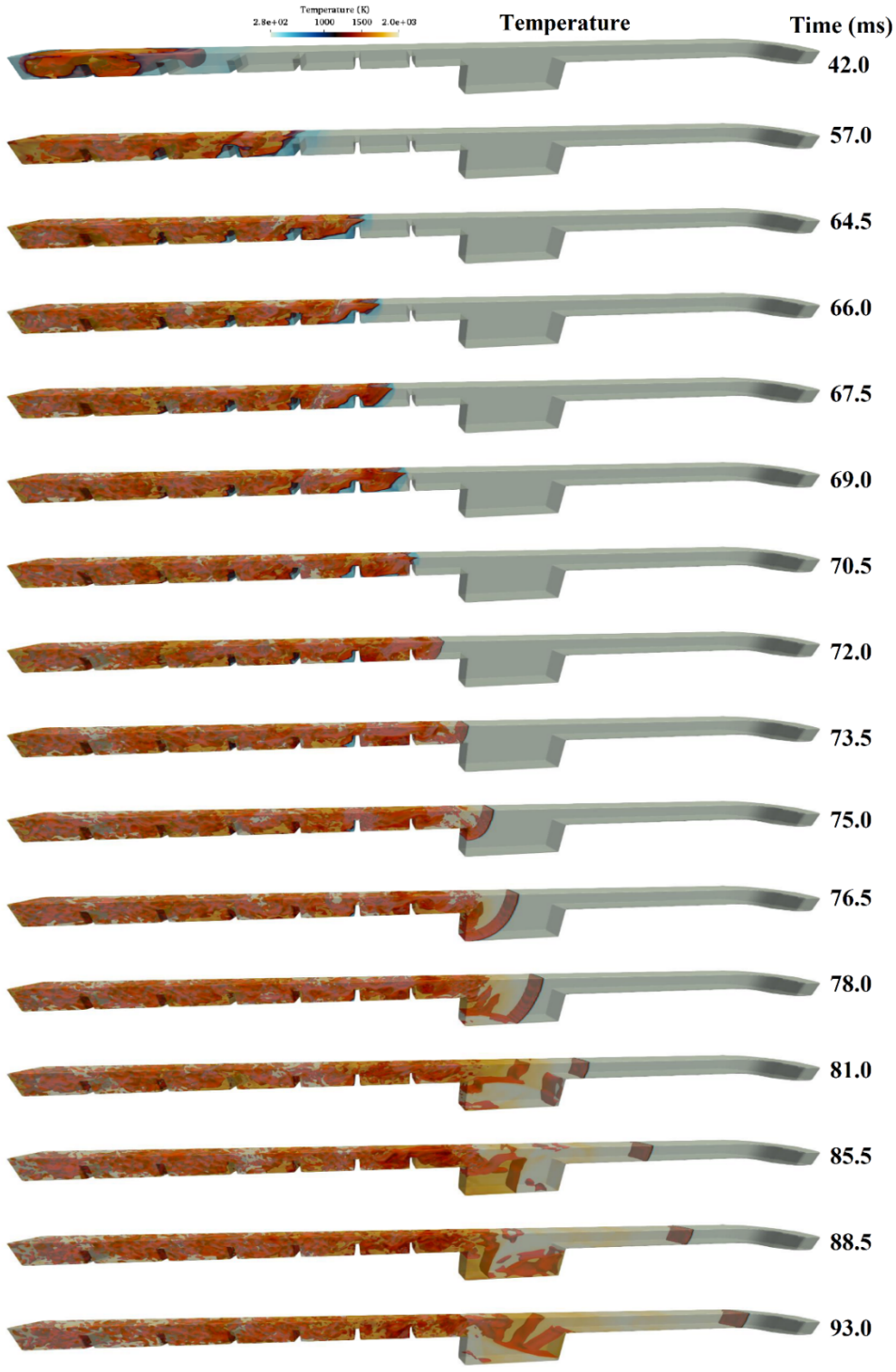

Figure 6-18: Isosurface of temperature at 2000 K during the DDT process for the RUT 22, BR 60%.

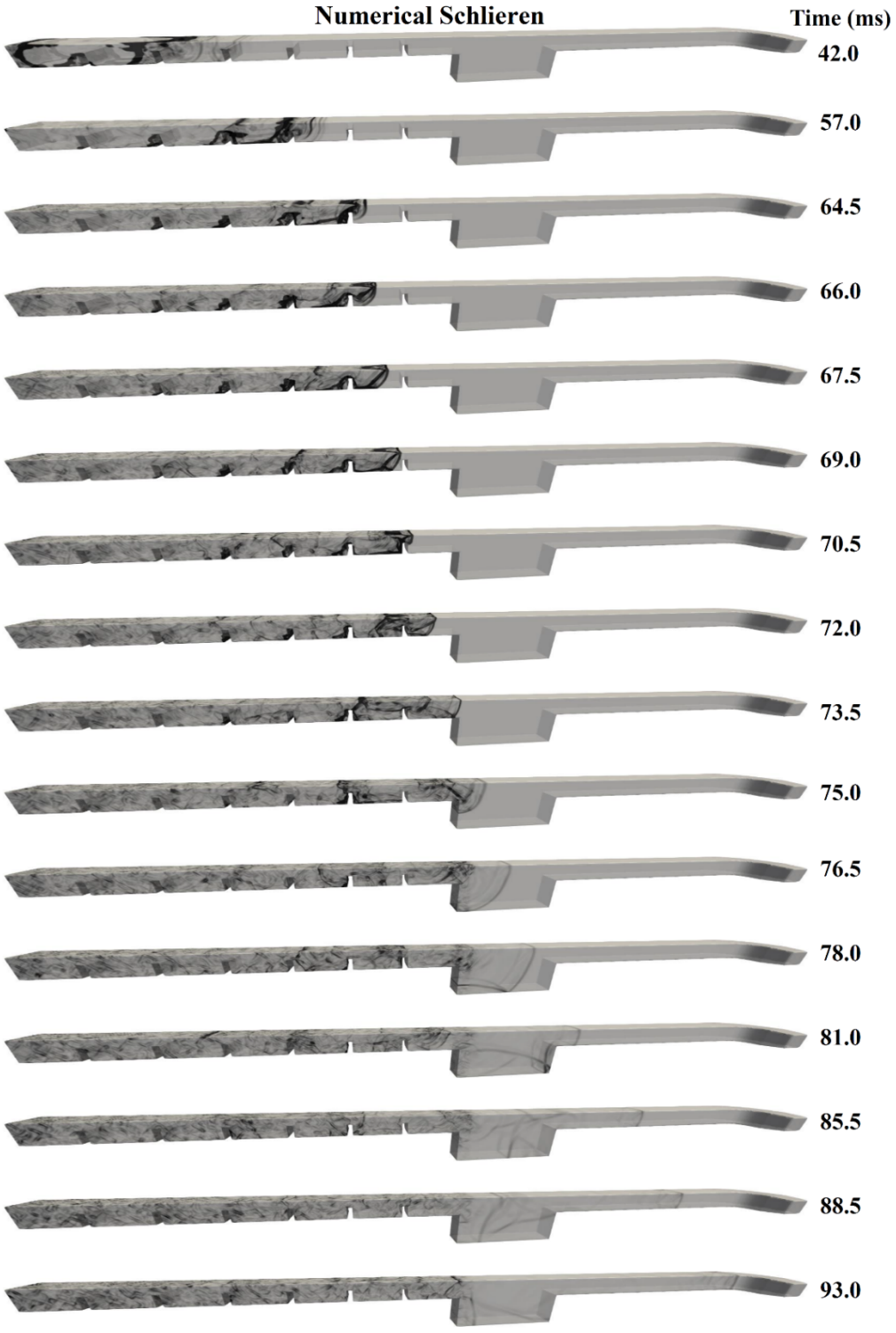

Figure 6-19: Numerical schlieren during the DDT process for the RUT 16, BR 60%.

Figure 6-17, Figure 6-18 and Figure 6-19 represent the pressure, temperature and numerical schlieren fields during the DDT process of the RUT 22 configuration, respectively. These snapshots, as well as the pressure probe recordings, and together with experimental observations(Dorofeev *et al.*, 1996, 1997), demonstrate that the lean hydrogen flame gradually accelerates and, unlike the previous scenario (RUT16), DDT occurs in the first channel and close to the last obstacle. From 42 to 70 ms, the leading shock waves and the flame front are detached and propagate towards the downstream channel. This indicates a flame deflagration (shown in Figure 6-17, Figure 6-18 and Figure 6-19).

At 64.5 ms after ignition, the reflected shocks from the 5th obstacle interact with the flame front. However, this interaction is not strong enough to cause a detonation. From the temperature fields (Figure 6-18- 64.5 ms) it is clear that the flame front and shock waves are still separated, hence DDT has not yet occurred in this snapshot. At 70.5 ms, close to the bottom wall in the vicinity of the last obstacle, a strong shock reflection occurs. This strong shock reflection interacts to the accelerated flame and causes a strong local explosion. However, since the flame front and shock are separated, the transition to detonation does not occur. Eventually, at 72 ms, the shock wave couples with the flame front at the top part of the channel, and transition to detonation will happen. This local explosion (induced by reflected shock waves and interaction to the flame), leads to the onset of detonation in the obstructed part of the channel (unlike RUT16 case). In the experimental observation (Dorofeev *et al.*, 1996) mentioned that, for this scenario (RUT 22), the transition to detonation was observed at the end of the obstacles sequence, which is in agreement with the current numerical predictions.

6.2.5 Results of the RUT 09 case: Unobstructed (Detonation initiation)

Unlike RUT 16 and RUT 22 (DDT cases), RUT 09 has been investigated by numerous authors in the past, and is known as a standard validation problem in large-scale detonation modelling. The computational domain configuration for the RUT 09 case is shown in Figure 6-4. Initial conditions and boundary conditions are the same as mentioned in section 6.1.1. Ignition has been initiated by using a small patch with high pressure and temperature. Like what has been

suggested by(Heidari *et al.*, 2011), the value of initiated pressure and temperature are equal to CJ detonation. For 25.5% hydrogen, T_{CJ}=2807.8 K and p_{CJ}=15.3 bar.

A detonation wave is directly initiated in the right side of the channel. The detonation wave propagates from the curved channel towards the canyon. The simulation was carried out for 35 ms; however, it takes the detonation front 17.3 ms, to reach the end of the channel. Overpressure has been recorded in the canyon section, as well as the end part of the first channel (sensor 7, 8 and 11 shown in Figure 6-6). These overpressures, predictions have been compared quantitively against the experimental measurements (shown in Figure 6-20). The quantitative comparison between the numerical prediction and the experimental measurements (Dorofeev *et al.*, 1996; Kotchourko, 2007), shows a good agreement.

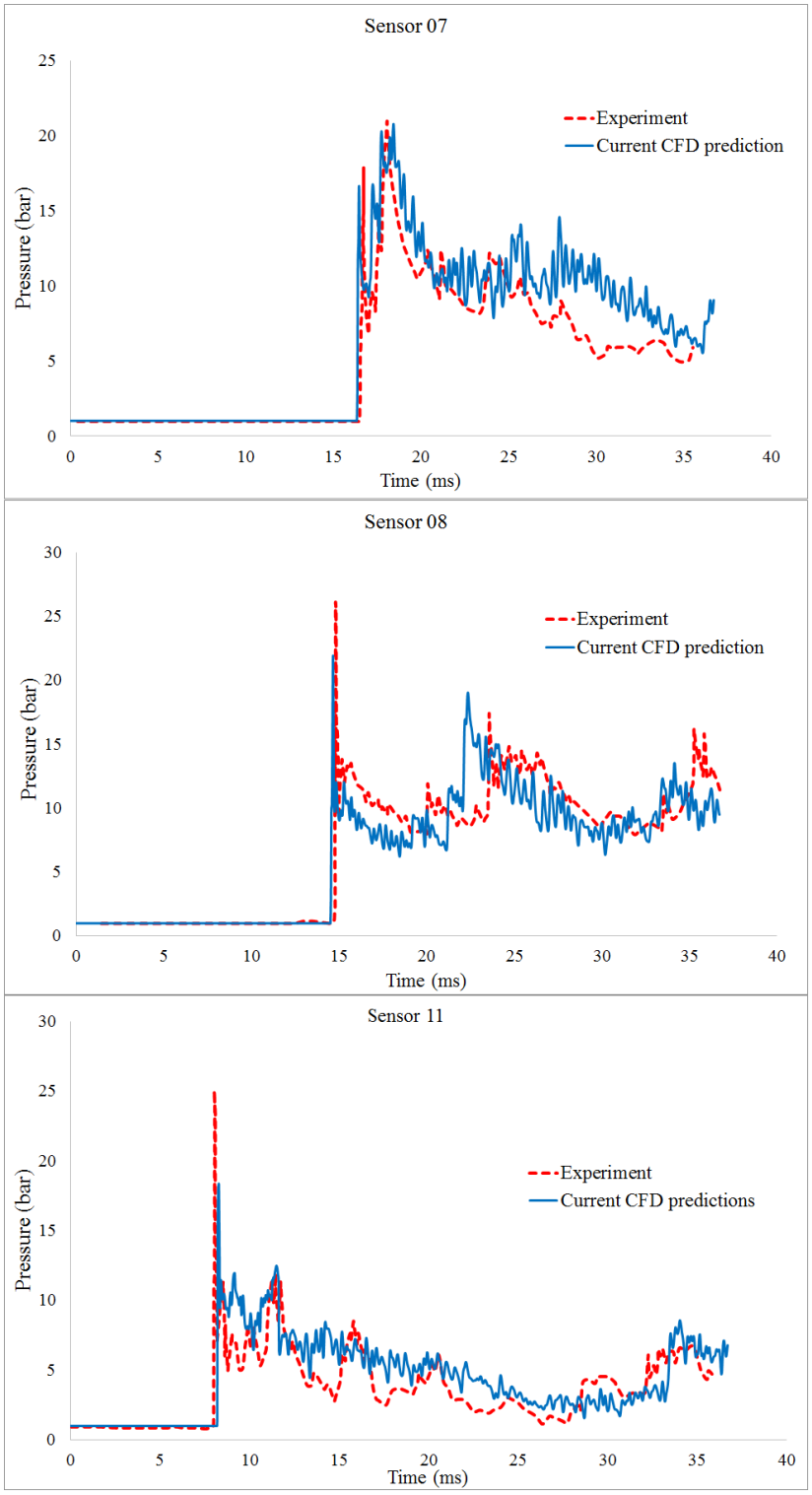

Figure 6-20: pressure recording for the RUT 09 case: sensor 7-11 top to bottom.

Figure 6-21: Numerical schlieren during the detonation propagation for the RUT 09 case.

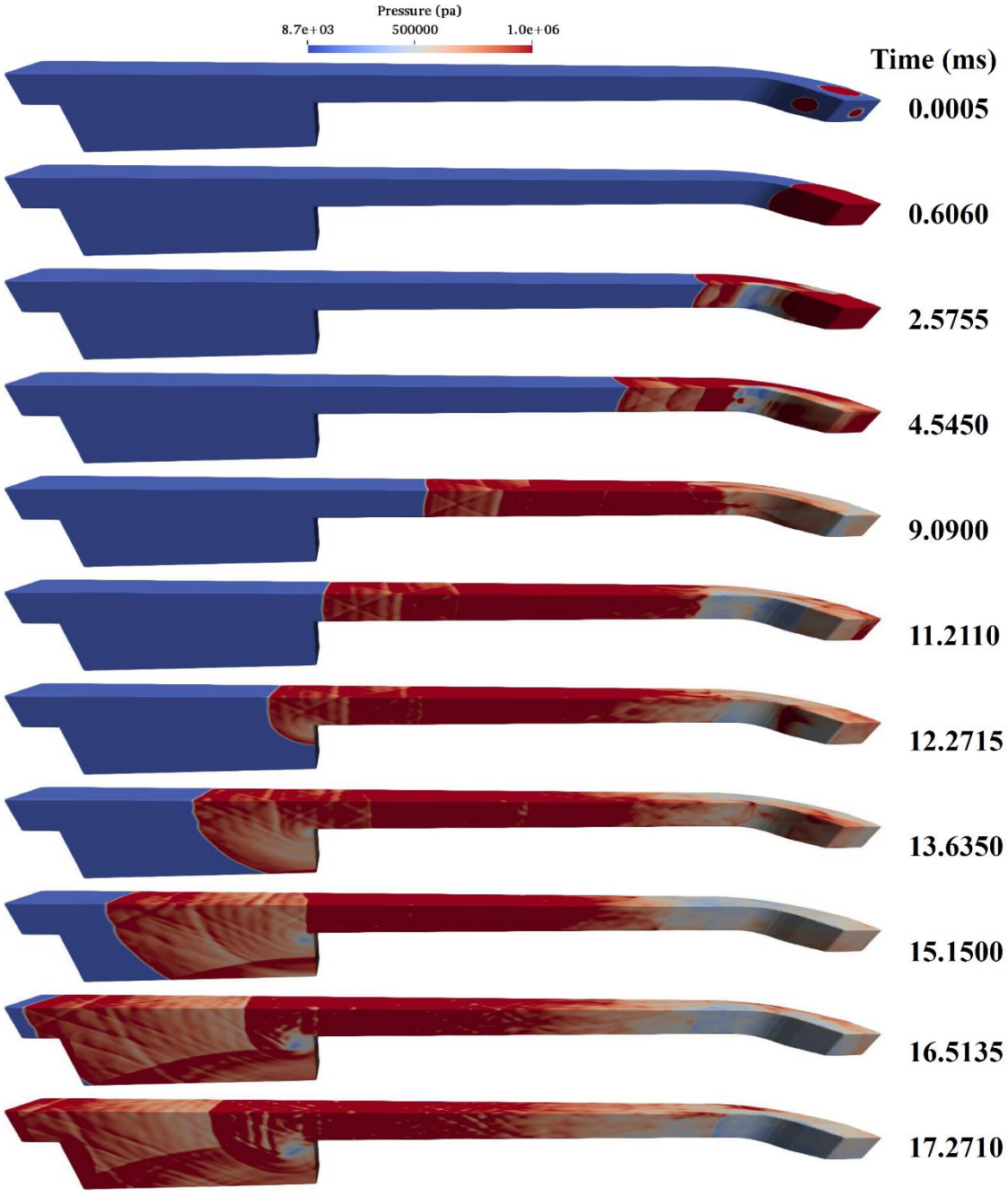

Figure 6-22: Pressure fields during the detonation propagation for the RUT 09 case.

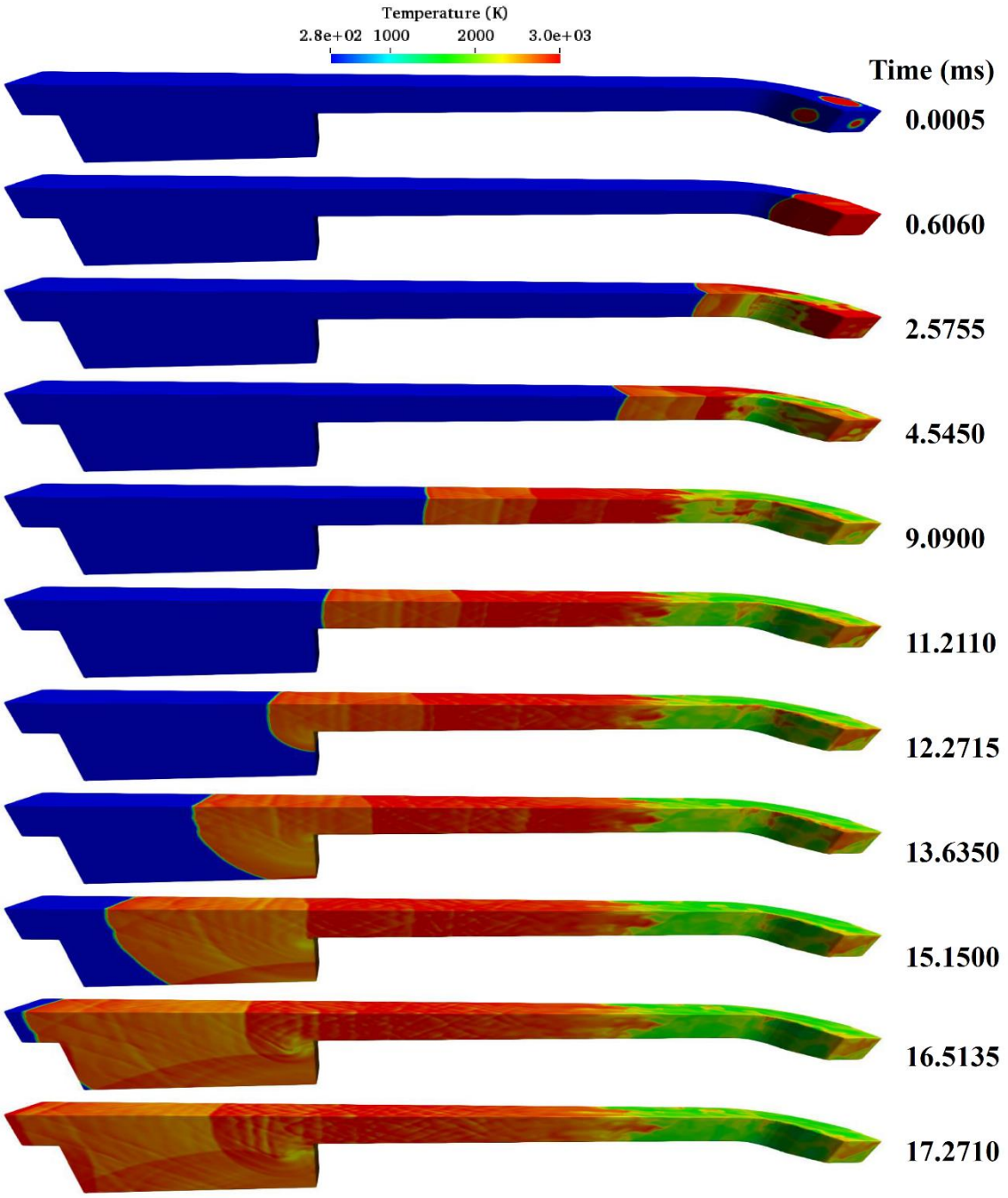

Figure 6-23: Temperature fields during the detonation propagation for the RUT 09 case.

Figure 6-21 shows the numerical schlieren, Figure 6-22 shows the pressure fields, and Figure 6-23 shows the temperature fields, during the detonation propagation for the detonation initiation case (RUT 09 case). These snapshots indicate that a stable detonation front is moving towards the canyon, and that the detonation front did not lead to a failure. At 4.5 ms, due to shock reflections from the channel walls, a high-pressure region can be found behind the leading detonation front. This can be known as a secondary shock wave, which moves behind the leading detonation front. At 16.5 ms, a strong interaction, between the reflected shock wave (from the bottom of the canyon) and the secondary shock wave, occurs in the middle of the canyon. This strong interaction leads to a higher overpressure in the detonation front. Based on the pressure transducer plots and the above contour plots, it can be demonstrated that the numerical code successfully predicted key safety features, such as detonation overpressure.

6.2.6 Summary:

Transition to detonation was observed in a lean mixture (with a minimum of 12.5% H2/air). In the scenario with a lean mixture of 12.5% H2/Air (RUT16), DDT did not occur in the first obstructed channel, but did occur in the canyon section. Due to localised explosions and reflections (which is shown in the snapshots, as well as the pressure recordings), behind the leading shock, several pressure waves have been generated. Eventually, in the vicinity of the end-wall of the canyon, the interactions between pressure waves and shock waves with the surrounding walls, led to the onset of detonation by a very strong local explosion. The detonation wave propagates backwards in the canyon, and it develops up to the end of the second channel. Similar to what has been reported by the experimental measurements, the recorded overpressures of the detonation front were about 11-15 bar (Dorofeev *et al.*, 1996). In the RUT 22 configuration with 14% hydrogen, the local explosion induced by reflected shock waves and interaction to the flame, unlike the RUT 16 case (12.5% hydrogen), leads to the onset of detonation in the obstructed part of the channel. The detonation initiation case (RUT09) has also been modelled and verified against experimental measurements. It can be determined that the numerical code has got a good capability in modelling DDT and detonation scenarios in large scale cases.

After verifying the numerical code in modelling DDT and detonation in large scale scenarios, vapour cloud explosion (VCE) of liquefied natural gas (LNG) will be studied. Two different possible incidents in LNG VCE will be considered; explosion modelling in onshore LNG plant and offshore LNG shipping.

6.3 Vapour cloud explosion modelling in an onshore LNG plant

One of the possible hazards in the onshore LNG plant is a vapour cloud explosion (VCE) phenomena. The importance of this study has been discussed earlier, in the introduction section. In this section, an LNG plant has been considered to have fuel leakage from one of its storage tanks. As a result of the leakage, liquid fuel will spill on the ground level and then it evaporates. The evaporated liquid natural gas has been ignited for explosion study purposes. The first hazard scenario which will occur is the LNG dispersion and evaporation. Dispersion and evaporation modelling have been simulated by one of the SafeLNG researchers (Macchi, 2018).

Macchi (Macchi, 2018) demonstrated that it can be assumed that LNG fuel is equivalent to pure Methane. LNG's composition will depend on the way it has been processed and its sources, however, the primary composition is Methane with about 85-95% percentage of the mixture, and the rest of the compositions are Propane, Ethane, Butane and Nitrogen. Table 6-3 shows the LNG Compositions from Different sources. From Table 6-3 can be found that the LNG with Alaska origin, contains 99.80% methane. Therefore, as it has been assumed by other researchers, in this study, the LNG can be considered as pure liquid methane.

Table 6-3: LNG Compositions from Different sources (mole %) (McCartney, 2002)

Species	Alaska	Trinidad	Algeria	Malaysia	Indonesia	Brunei	Australia	Oman	Qatar
N2	ND	0.00%	0.28%	0.32%	0.09%	0.00%	0.01%	0.00%	0.19%
Methane CH4	99.80%	92.26%	91.40%	91.15%	90.60%	89.40%	87.82%	87.66%	89.87%
Ethane C2H6	0.10%	6.39%	7.87%	4.28%	6.00%	6.30%	8.30%	9.72%	6.65%
Propane C3H8	ND	0.91%	0.44%	2.87%	2.48%	2.80%	2.98%	2.04%	2.30%
Iso-butane i-C4H10	ND	0.21%	0.00%	0.70%	ND	ND	0.40%	0.29%	0.41%
n-Butane n-C4H10	ND	0.22%	0.00%	0.66%	0.82%	1.30%	0.48%	0.30%	0.57%
Iso-pentane i-C5H12	ND	0.00%	0.00%	0.01%	ND	0.00%	0.00%	0.00%	0.01%
n-pentane n-C5H12	ND	0.00%	0.00%	0.00%	0.01%	0.00%	0.00%	0.00%	0.00%
Total	99.90%	100.00%	100.00%	100.00%	100.00%	99.80%	100.00%	100.00%	100.00%

ND = Not Determined

6.3.1 Fuel Dispersion in an onshore LNG plant:

The considered computational domain for this onshore LNG plant is shown in Figure 6-24. The computational domain size:$260m \times 100m \times 450m$.

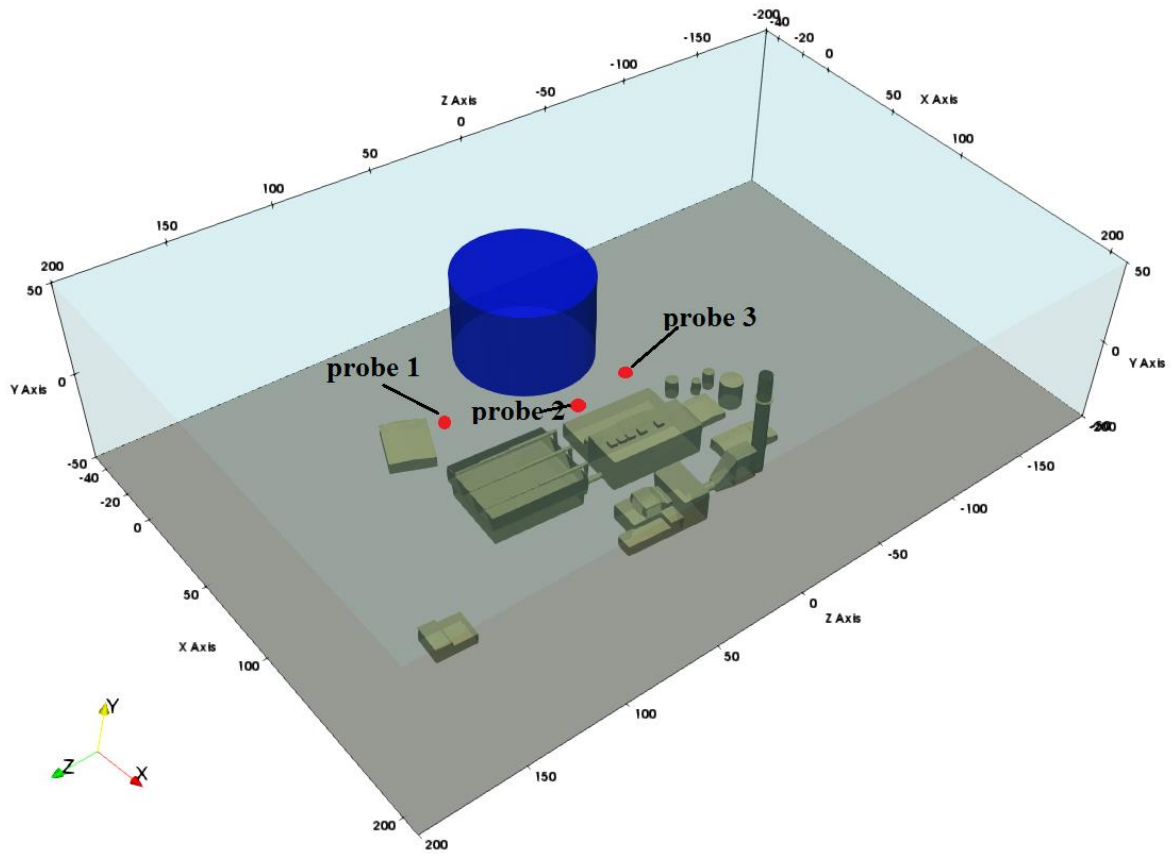

Figure 6-24: Geometry for an onshore LNG plant; the computational domain size:$260m \times 100m \times 450m$.

In the geometry shown in Figure 6-24, the largest LNG storage tank has 50 m height and 35 m radius. This onshore plant area is $200m \times 125m$, and the plant structures' height is varying from one another, with a maximum height of 60 m for the chimney. The LNG plant has been considered to have fuel leakage from one of its storage tanks. As a result of the leakage, liquid fuel will spill on the ground level and then it evaporates. In order to consider the worst-case scenario, the minimum distance from the tank to the plant has been considered which is

approximately 25 m, and the direction of fuel spill is directly towards the plants (Macchi, 2018). Then evaporated liquid natural gas has been ignited for explosion study purposes.

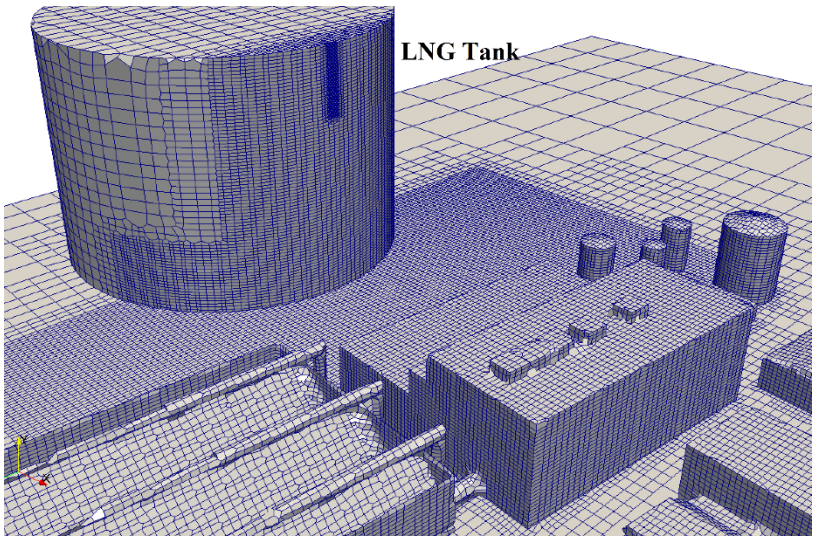

Figure 6-25: Generated mesh by snappy hex mesh for the onshore LNG plant.

Figure 6-25 shows the CFD mesh which has been generated by using the snappyHexMesh tool (available in OpenFOAM), with refinement boxes in the region of the liquid spill, the ground where the might will spread, and the vicinity of buildings where ignition will take place. The number of grid cells used in this mesh was approximately 4 million. For the LNG spill scenario, mesh sensitivity analysis has been done by (Macchi, 2018).

For the initial conditions, a constant temperature of 6°C, as well as low-value turbulence intensity, has been considered. No-slip wall boundary condition has been chosen for the ground, tank, and LNG plant. The mass flow rate of LNG has been considered to be 36 Kg/s. (Macchi, 2018) reported that the 36 kg/s leakage, could be a consequence of a large failure in the tank structure or high flow rate injected in the incident tank. Therefore, this large leakage, could leads to a larger area covered by the flammable vapour cloud. The URANS turbulence model was used to model the effects of turbulence.

In the following result of LNG spill which has been modelled by *cascadeFoam* (an in-house OpenFOAM solver developed by (Macchi, 2018)), are presented.

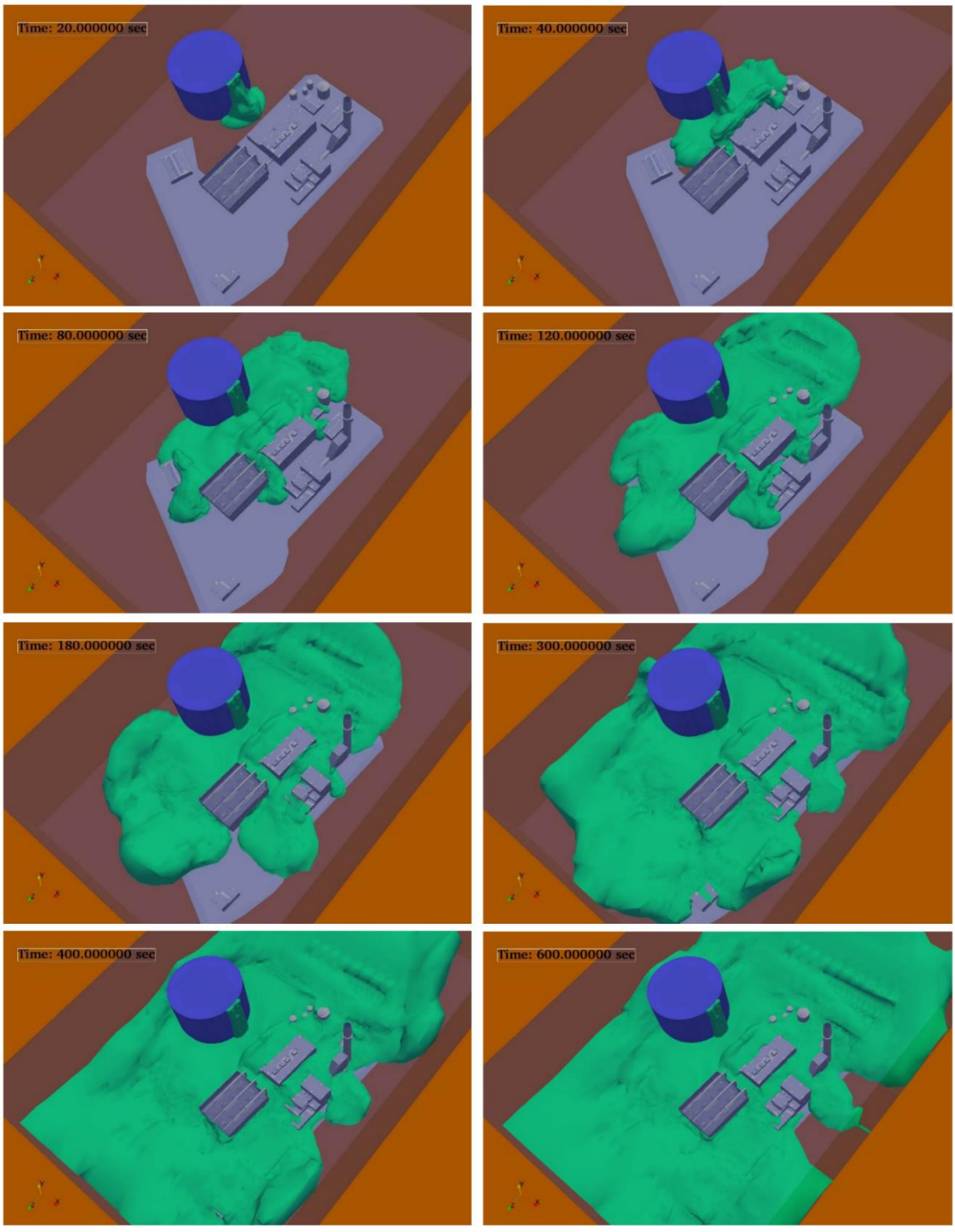

Figure 6-26: LNG spill in an onshore plant (LFL). Time: 20-600 seconds.

Figure 6-26 shows the contour of lower flammability limit (LFL) of the LNG spill, for the time between 20 to 600 seconds. The extent of LNG cloud for 600 seconds is shown into the domain. After this LNG release and spilling on the ground, the liquid fuel will evaporate and turn to natural gas. Also, in order to satisfy the mass balance, the amount of liquid fuel which will evaporate would match the mass flow rate released from the LNG tank.

6.3.2 Igniting the LNG flammable vapour cloud:

For the explosion modelling, a mesh refinement has been done in the current geometry. In this case, the base mesh has average cell size is approximately 35 cm (level 0), and by using AMR method, the first level of refinement (level 1) will have a cell size of 17.4 cm, and in the second level of refinement (level 2), it will become 8.7 cm. In the recent work done by Hasselberger et al. (Hasslberger, Boeck and Sattelmayer, 2015), they have found that using cell around 8 cm will be sufficient to predict accurate flame propagation and correct location of DDT. However, as expected, they have mentioned that with this grid size scale the small-scale features will not be captured.

Nevertheless, the purpose of this study is for safety analysis, and therefore it is not necessary to capture the microstructure and small-scale features. Similar to the approach done by Hasselberger et al. (Hasslberger, Boeck and Sattelmayer, 2015), in this very large-scale case, the URANS turbulence model has been used for turbulence modelling. The combustion modelling is as the same method described in section 6.1. Also, the reduced detailed reaction mechanism of NG-Air developed by Smooke (Smooke, 1991) which has 35 reactions, has been used in this study. Wang et al. (Wang *et al.*, 2018) showed that the induction times predicted by this reduced detailed chemical reaction is in a good agreement with the GRI 3.0 (Smith *et al.*, 2000) mechanism and as well as experimental results (GRI 3.0 mechanism is a standard detailed reference mechanism with 325 elementary reactions and 53 species). Ignition has been modelled via a patch of burned area with high temperature. The ignition spark location has been shown in Figure 6-27.

Then by having a spark ignition in the flammable LNG vapour cloud, the combustion process will be initiated. Therefore, the results of the dispersion model at the latest time (600 seconds),

will be used as initial conditions for the LNG explosion modelling. These results which include; mass fraction of the natural gas, temperature and pressure fields, will be imposed in the VCEFoam solver, with the same setup discussed in the previous section.

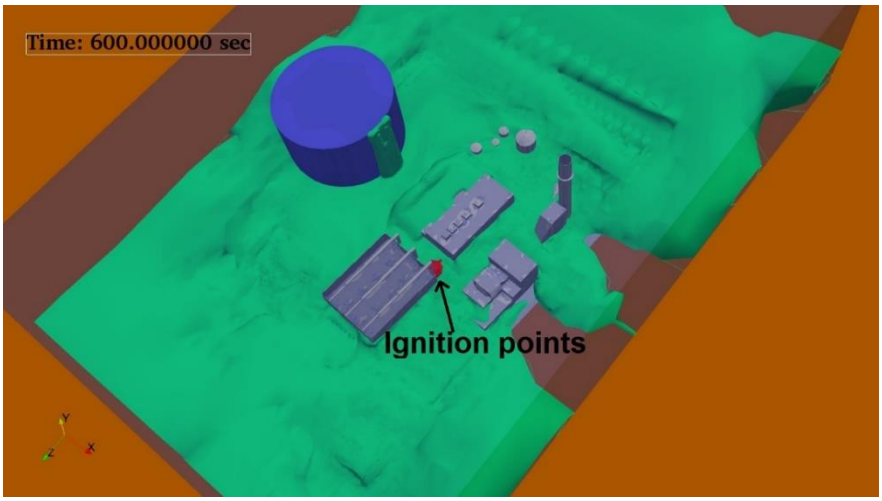

Figure 6-27: Onshore LNG explosion scenario: Ignition patch location in the computational domain.

In order to track the overpressure in this LNG explosion modelling, three different pressure probes have been considered in the domain. The coordinates of these pressure transducer are shown in Table 6-4.

Table 6-4: Location of the pressure transducer in the onshore LNG plant case.

Coordinate	X	Y	Z
Probe1	31.14	-44.85	72.74
Probe2	84.91	-50	29.8731
Probe3	50.71	-43.1118	7.50019

Figure 6-28 shows the transient overpressure for the onshore LNG plant case, in three different probe location. The location of these probe points is marked in Figure 6-24.

In Figure 6-28 can be found that the maximum overpressure in this explosion modelling is around 1.1 bar, which is far below the CJ detonation limit. The quasi-static CJ detonation wave pressure for stoichiometric methane/air mixtures, is 16.6 bar. Therefore, in this scenario, LNG flame acceleration was not enough to cause a detonation, and only a flame deflagration has been noticed.

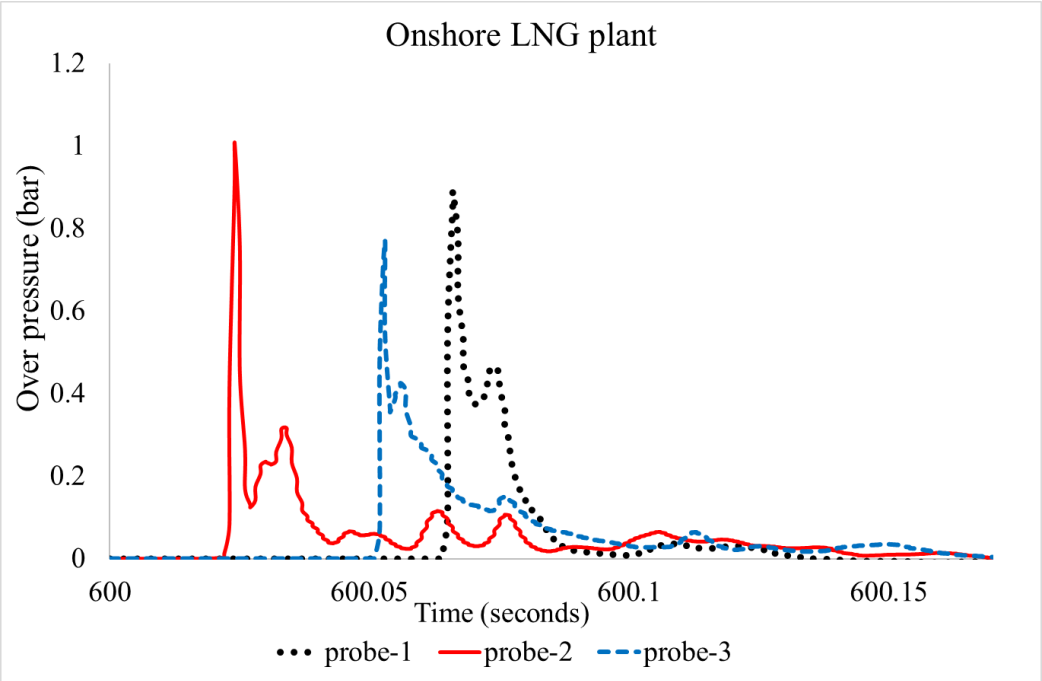

Figure 6-28: Transient overpressure for the onshore LNG plant case.

Figure 6-29 shows pressure distribution on a horizontal plane 2m above the floor level of the onshore LNG plant. These pressure contours support the predicted transient overpressure for presented in Figure 6-28. At 600.030250 seconds the first sudden increase in pressure field has been predicted. This pressure increase is due to the flame interaction to the adjacent building. Moreover, the sudden increase in overpressure can be found while the flame front interacts any other congested region. Then the predicted overpressure of the LNG flame front tends to decay once the flame front passes outside of an obstructed region.

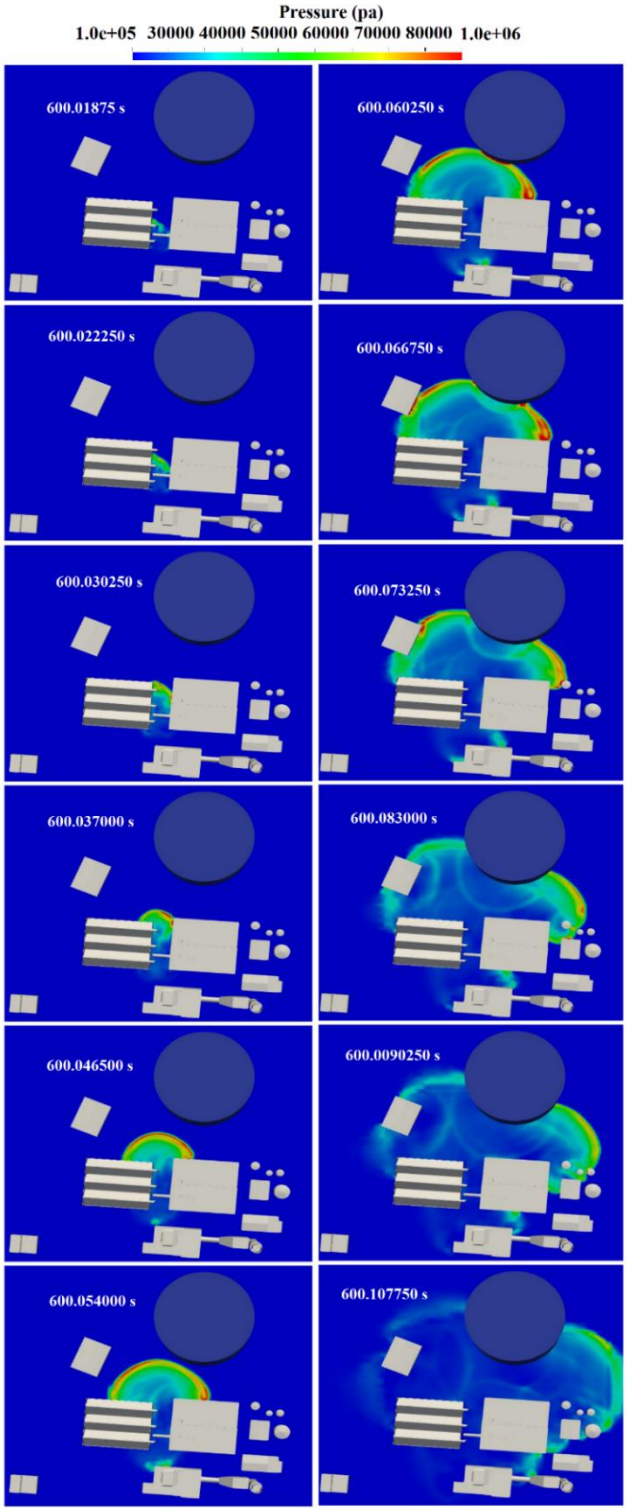

Figure 6-29: pressure distribution on 2m above floor level: onshore LNG plant.

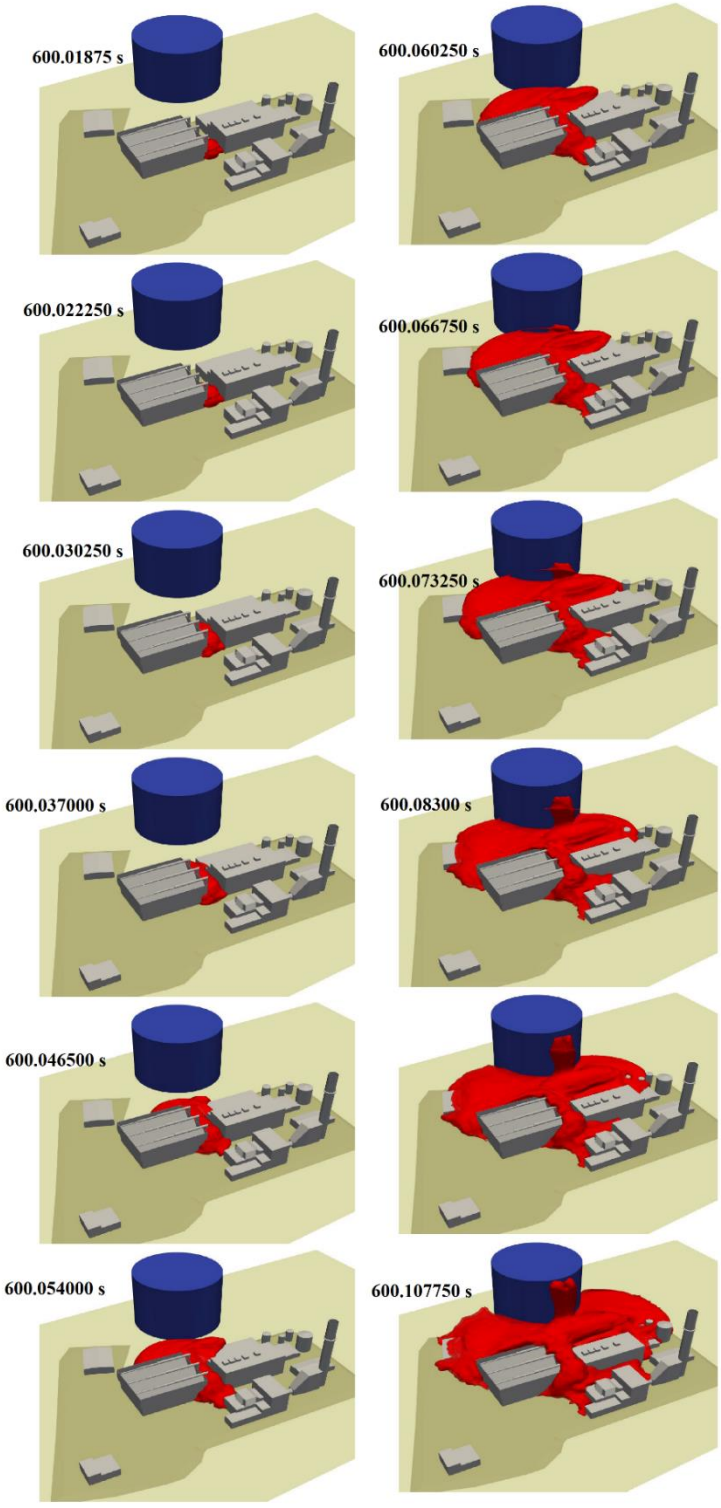

Figure 6-30: Isosurface of temperature at 1600 K: onshore LNG plant.

Figure 6-30 shows the isosurface of temperature at 1600 K, which indicates the evolution of the flame front resulting from the ignition of the LNG vapour cloud. By interacting the flame front to the adjacent building and obstruction, it can be found that the LNG flame will accelerate. By considering the results of pressure probe, pressure contour and temperature, it can be concluded that the LNG flame propagation only developed a deflagration and it did not lead to detonation.

6.4 Vapour cloud explosion modelling in an offshore LNG ship

As mentioned in the introduction chapter, LNG fuel characterises as one of the important potential energy sources in the world. One of the primary ways of transporting LNG is through marine transport. In order to address one of the vital safety concerns regarding the potential consequence for LNG shipping incidents and explosion hazards, in this section vapour cloud explosion will be studied in an offshore LNG carrier.

6.4.1 LNG shipping and explosion modelling

An offshore case with having 5 LNG oil tanker in a ship has been selected to model the flame deflagration. The computational domain for an offshore LNG shipping case is shown in Figure 6-31. The considered ship includes 5 LNG oil tanker which is bounded in a large domain ($350m \times 200m \times 400m$). The domain has been chosen to be very large, to avoid any boundary influence on the flame propagation in the ship.

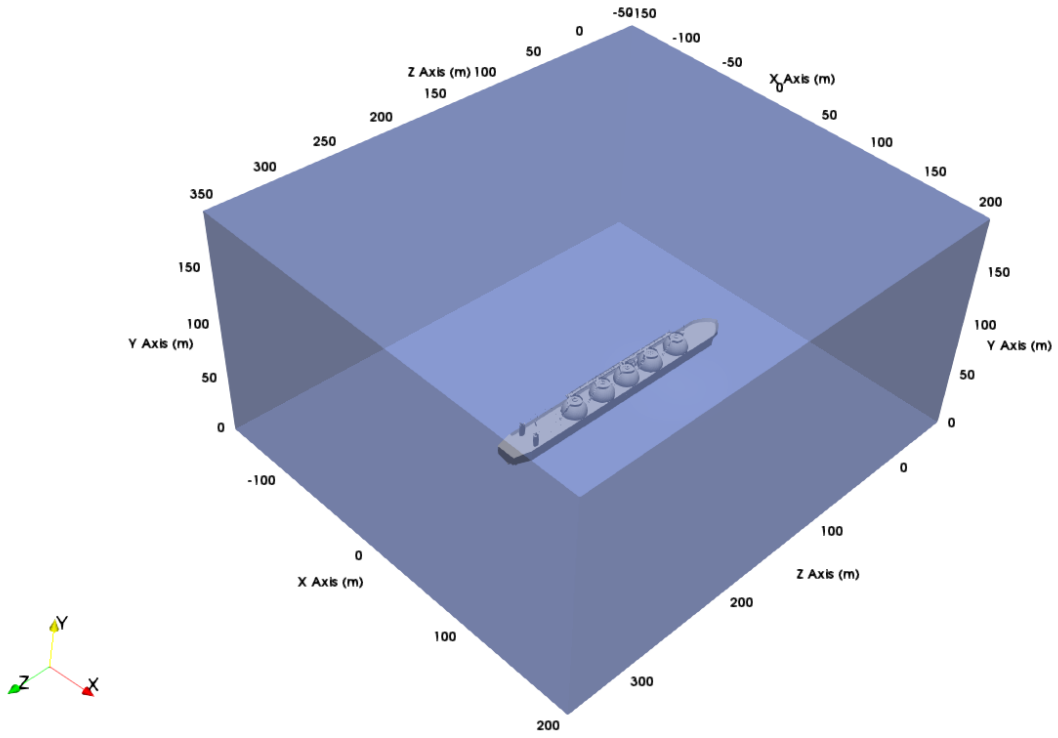

Figure 6-31: Computational domain for an offshore LNG shipping.

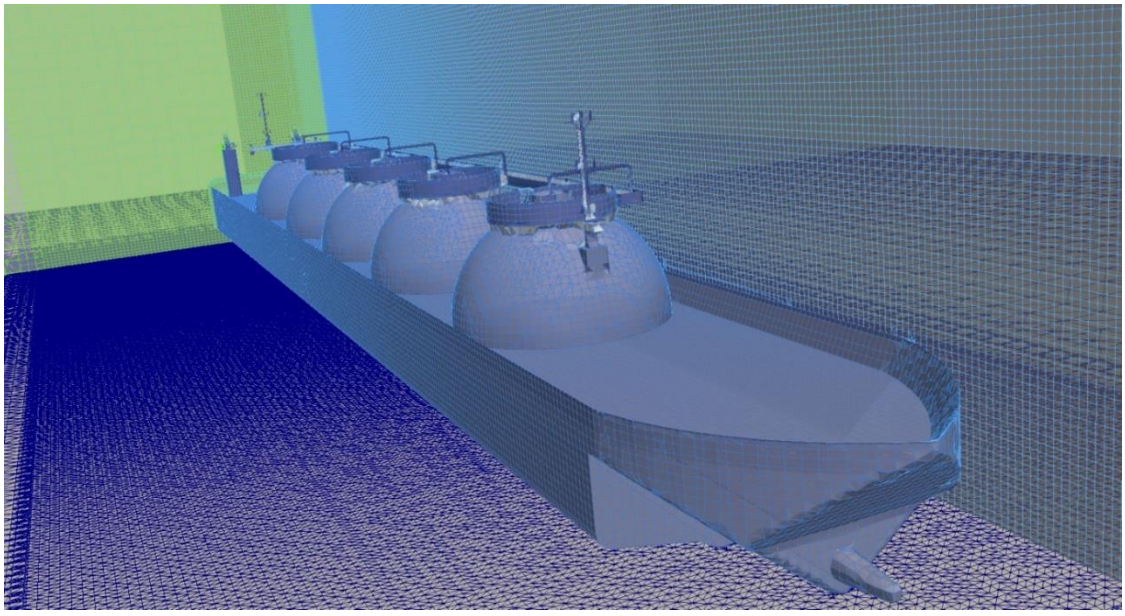

Figure 6-32: The base mesh generated by snappy Hex mesh for the offshore LNG ship case.

Figure 6-32 shows the base CFD mesh generated by snappy Hex mesh for the offshore LNG ship case. By using snappy hex mesh, some level of refinement has been applied to the base mesh, and the area closer to the ship is more refined than the further area. In this case, similar to the previous section (section 7.2), the base mesh has an average cell size considered to be approximately 35 cm (level 0). By using the AMR method, the first level of refinement (level 1) will provide a cell size of 17.4 cm, and in the second level of refinement (level 2), it will become 8.7 cm. Moreover, based on the literature for safety analysis, this mesh resolution is sufficient (Hasslberger, 2017). Also, it has been assumed that the LNG fuel has been already released and it has been evaporated. Therefore, the computational domain has been filled by a premixed stochiometric mixture of LNG/Air in this scenario.

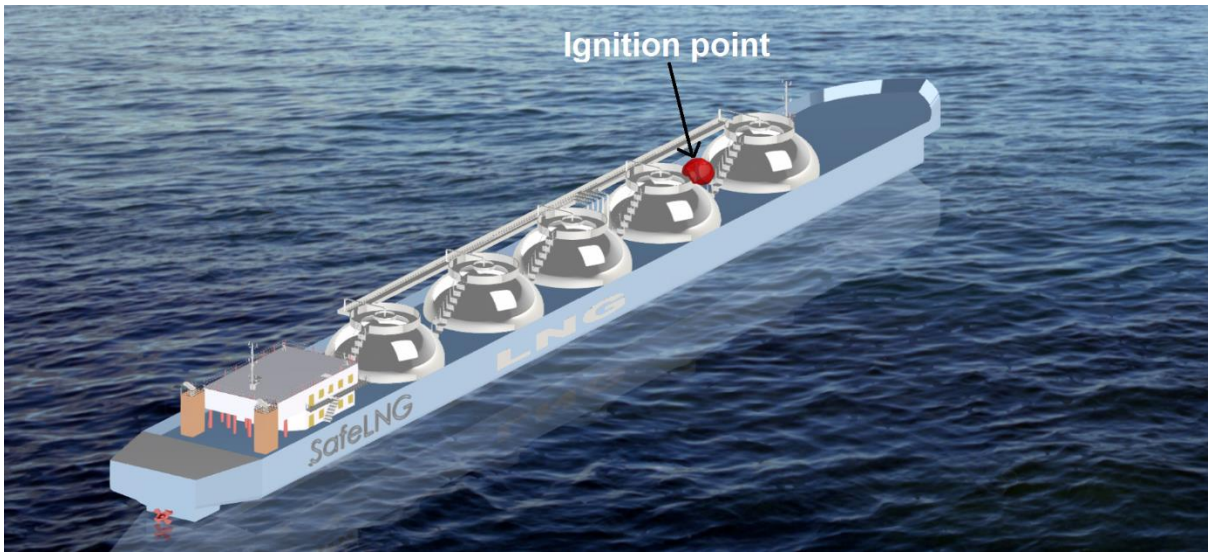

Figure 6-33: LNG shipping incident scenario: Ignition patch location in the computational domain.

The same approach as the previous sections has been utilized for modelling the spark ignition. The ignition patch has been assumed a high temperature and burned area. The ignition patch location in this scenario is shown in Figure 6-33. The numerical model has been simulated for 12 ms. It takes the LNG flame front, around 10 ms to reach the far left of the ship, from the ignition point. The results of LNG flame front propagation is provided in Figure 6-34.

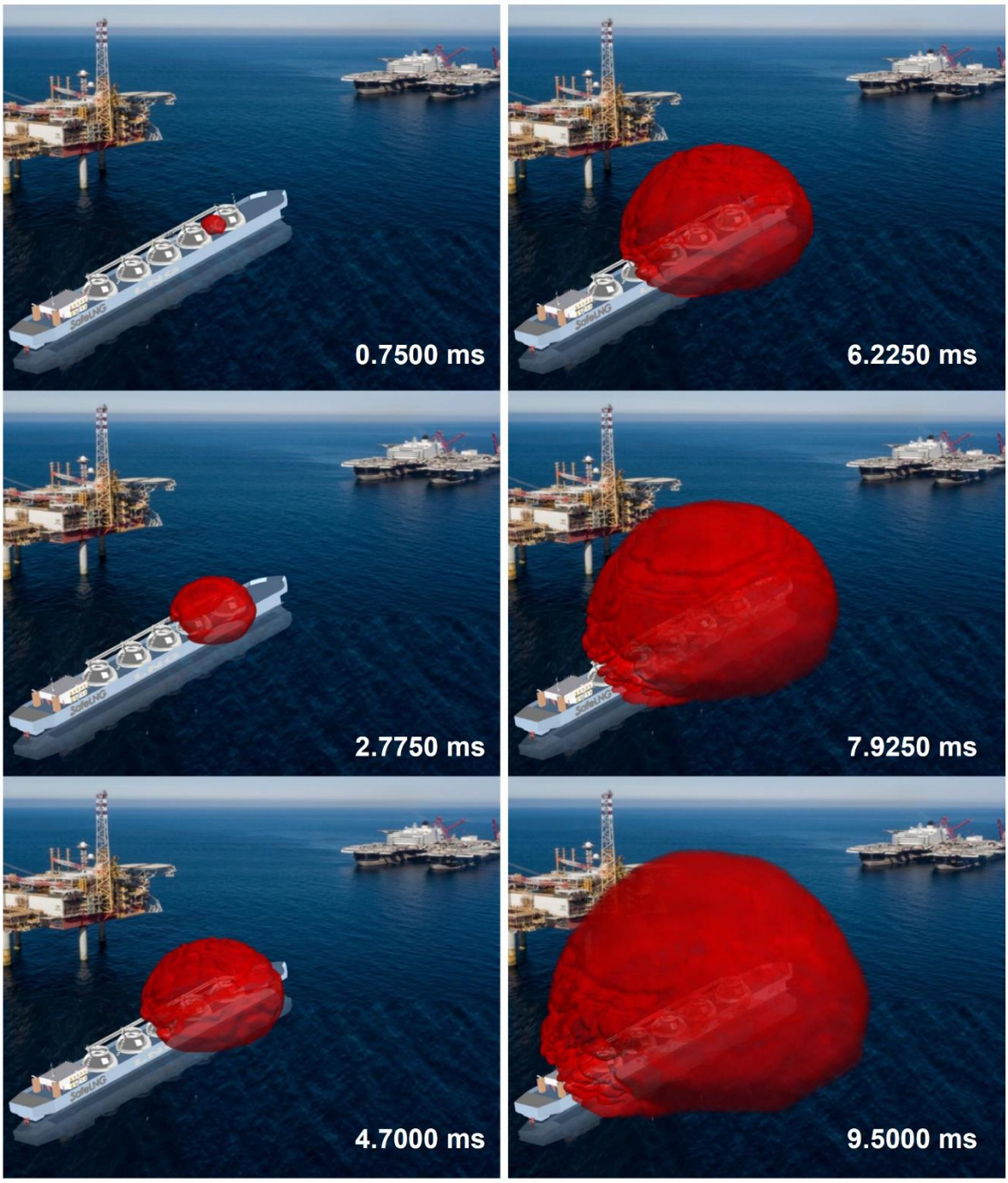

Figure 6-34: LNG flame front propagation in offshore LNG carrier- isosurface of temperature at 1600 K.

Figure 6-34 shows the LNG flame front propagation in offshore LNG carrier. These snapshots represent the isosurface of temperature at 1600 K. Due to the interaction of LNG flame front to the pier pylons, the flame front is accelerating. However, this flame acceleration is not as fast as the onshore case, whereas there was more obstruction in the plant. Also, it is notable that the current time scale is too large for a possible explosion scenario, and in this case, only flame deflagration has been captured. In the study done by (Pollock and Johnson, 2018), stated that in the offshore Marine LNG tanks, vapour cloud explosion (VCE), would not happen, due to not having enough congestion and obstruction to increase the flame speed. In Figure 6-35 the overpressure generated next to the second tank (probe 1), and fourth tank (probe 2).

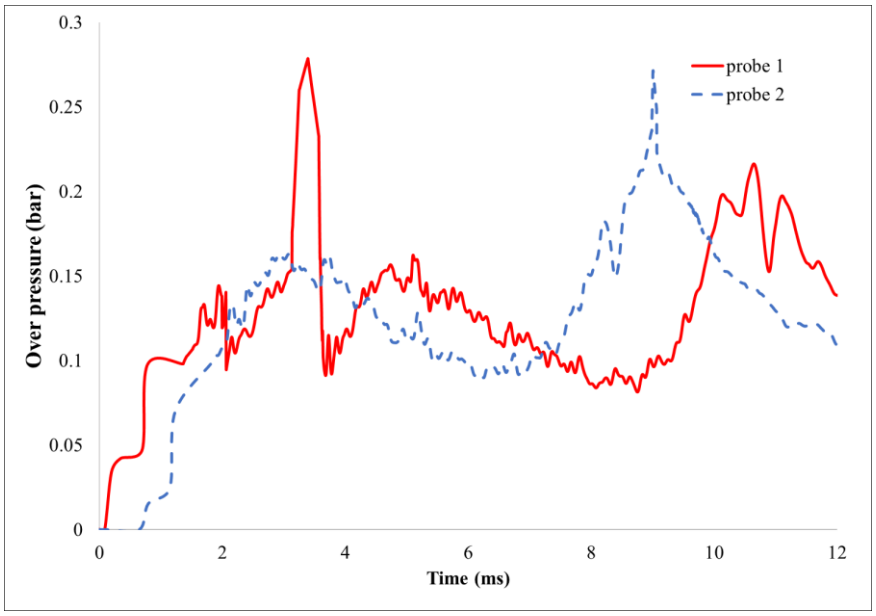

Figure 6-35: Transient overpressure for offshore LNG carrier case.

Figure 6-35 shows that the maximum overpressure in the offshore LNG explosion is around 0.3 bar (30000 pa), which is far from the CJ detonation pressure (for stoichiometric Methane/air mixture, CJ detonation pressure is around 16.6 bar). Therefore, in this scenario, VCE did not happen, and only flame deflagration has been captured. Also, compare to the onshore test case

in the previous section, it can be found that the predicted overpressure in offshore case, is far below the predicted overpressure in the onshore case (in the onshore LNG plant the maximum predicted overpressure was 1.1 bar, while in this offshore LNG carrier scenario maximum predicted overpressure was 0.3 bar). This is mainly due to having more congestion and obstruction in the onshore test case. This has also been reported by (Woodward and Pitblado, 2010; Algell, Bakosch and Forsman, 2012; Mokhatab *et al.*, 2015; Pollock and Johnson, 2018) which will support this matter.

6.5 Summary:

In this chapter, a robust CFD methodology has been presented for modelling very large scale (industrial scale), vapour cloud explosions. The developed numerical model presented in chapter six (for modelling medium scale VCE), has been modified for large scale explosion modelling. A specific model has been considered for modelling the impact of flame-instabilities, particularly the thermal diffusive instabilities, and DL instabilities in large-scale models. The numerical model has initially been validated with the largest ever conducted indoor DDT and explosion experiments in the RUT facilities. Two different DDT scenarios: DDT by local explosions near the turbulent flame brush, and DDT by shock-focusing, have been modelled (RUT 16 and RUT 22 cases respectively). Additional to the DDT verification cases, a detonation initiation test case (RUT09) has been modelled and verified against experimental measurements. Good qualitative agreement between the numerical prediction results and experimental measurements of RUT facilities has achieved (for all DDT and detonation cases).

After code verification, LNG vapour cloud explosion scenarios, generated from the release of an evaporated liquefied natural gas have been studied. Two different possible incidents in LNG VCE have been studied; explosion modelling in onshore LNG plant and offshore LNG shipping. For the onshore LNG explosion study; an LNG plant has been considered to have fuel leakage from one of its storage tanks. Because of the leakage, liquid fuel spilt on the ground level, and then it evaporates. The evaporated liquid natural gas has been ignited for explosion

study purposes. The LNG spill scenario has been modelled by *cascadeFoam* (an in-house OpenFOAM solver developed by (Macchi, 2018)), and the LNG explosion has been modelled by VCEFoam. The numerical results showed that by interacting the flame front to the buildings and obstructions, the LNG flame would accelerate. The maximum recorded overpressure in this explosion modelling is around 1.1 bar, which is far below the CJ detonation limit. As mentioned earlier, the quasi-static CJ detonation wave pressure, for stoichiometric methane/air mixtures, is 16.6 bar. Therefore, in this scenario, LNG flame acceleration was not enough to cause a detonation, and only a flame deflagration has been noticed.

The second considered LNG explosion incident was an offshore LNG carrier with having 5 LNG oil tanker. The domain has been chosen to be very large, to avoid any boundary influence on the flame propagation in the ship. CFD mesh generated by snappy Hex mesh for the offshore LNG ship case. By using snappy hex mesh, some level of refinement has been applied to the base mesh, and the area closer to the ship is more refined than the further area. Addition to this local refinement an AMR method has been carried out in the model for resolving higher resolution. The numerical results demonstrated that due to the interaction of LNG flame front to the pier pylons, the flame front is accelerating. Nevertheless, this flame acceleration is not as fast as the onshore case, whereas there was more obstruction in the plant. The maximum recorded overpressure in the offshore LNG explosion was around 0.3 bar (30000 pa), which is far from the CJ detonation pressure. Therefore, in this scenario, VCE did not happen, and only flame deflagration has been captured.

Chapter 7 Conclusion remarks and Future work

This chapter starts with the concluding remarks of the present works, and then some suggestions for future works will be recommended.

7.1 Conclusion

The dynamics of deflagration to detonation transition (DDT) and explosion modelling in very large scale (industrial scale) scenarios, been studied using the newly assembled density-based solvers (VCEFoam) within the frame of OpenFOAM CFD toolbox. The first stage of DDT involving flame acceleration at a subsonic level has been modelled using the pressure-based algorithm and while the DDT modelled by the density-based solver. To evaluate the convective fluxes contribution, Harten–Lax–van Leer–Contact (HLLC) scheme is used for accurate shock capturing. For verification of the developed numerical model, four sets of verification problem have been considered:

1. Shock capturing: 1D Sod's shock tube problem
2. Supersonic wedge: 2D oblique shock
3. DDT test case: comparison between pressure-based and density-based solution
4. 2-D detonation initiation test case: cellular structure

Sod's shock tube problem and supersonic wedge for oblique shock problems have been modelled. Furthermore, a DDT test case has been modelled to study the comparison between pressure-based and density-based solution methods. In the detonation initiation test case, the capability of the current numerical code in capturing the detonation cellular structure has been examined. A small test case has been modelled with using three high ignition point to produce detonation initiation. The CFD results have been compared against both quantitatively and qualitatively with the other previous works as well as an experimental observation. The captured detonation cell size was in good agreement with the other CFD works and the

experimental observations. Also, the evaluation of triple points and cellular structure development has been investigated.

After code verification, numerical studies have been conducted to investigate flame acceleration and transition to detonation in both homogeneous and inhomogeneous hydrogen-air mixtures in obstructed and unobstructed channel configurations (in medium scale). The developed VCEFoam solver has been used within OpenFOAM, for these simulations. For the considered experiment (Boeck *et al.*, 2016), different sets of configurations and fuel concentration have been studied. Three different geometry configuration such as: BR00 (0% Blockage ratio, smooth channel), BR30 (30 % blockage ratio), and BR60 (60% blockage ratio), have been considered in this study. Also, in order to study the effect of a concentration gradient, different mixture concentrations have been investigated in both homogenous and inhomogeneous mixtures. A total of 17 conditions were simulated for different hydrogen concentrations in both homogeneous and inhomogeneous mixtures with and without obstructions. The numerical predictions were compared against previous experiments. Overall, the predicted flame tip velocities, overpressures, and locations of detonation onset are in reasonably good agreement with the measurements. For both homogeneous and inhomogeneous mixtures with 30% hydrogen concentration, the onset of detonation occurs within the obstructed channel section, but the homogeneous mixtures show slightly faster flame acceleration and earlier onset. For the cases with 20% hydrogen concentration, the transition to detonation is observed only for the inhomogeneous mixture where the concentration gradient enables stronger flame acceleration, especially in the unobstructed channel section in comparison with the homogeneous mixture.

The increase in the fuel concentration was found to increase the FA and faster transition to detonation. Also, the increase in the BR was found to increase the FA and slow down the possibility of transition to detonation in the present configuration. The role of hydrodynamic instabilities and the effect of baroclinic torque and RM instability have also been studied. The forward jet and backward jets which are a mushroom form flow represent the RM instability on the interface between the burned and unburned gas. Also, the Baroclinic torque and the resulting Richtmyer–Meshkov (RM) instability are studied. The results support that RM

instability is the primary source of turbulence generation in the present case. These studies have shown that the overpressure at the transition stage is higher in the mixture with concentration gradients, in comparison with the homogeneous mixtures under similar test conditions.

The results of the three different blockage ratio configurations (BR00, BR30 and BR60), demonstrated the effects of the blockage ratio in DDT. The increase in the blockage ratio was found to increase the FA and faster transition to detonation. This study also, confirms previous findings that transverse concentration gradients in channels can lead to substantially stronger FA and a higher propensity for DDT in comparison with homogeneous mixtures with the same average hydrogen concentration. In the unobstructed channel configuration, the onset of detonation is observed at the channel walls near the turbulent flame brush. High average hydrogen concentrations in conjunction with a concentration gradient are required to trigger DDT in the unobstructed channel. Flames in the gradient mixtures are observed to elongate while propagating along the unobstructed channel, whereas the homogeneous mixture shows an almost symmetric flame with respect to the channel centerline.

Then vapour cloud explosion study has been carried out for industrial scale scenarios (very large scale). A robust CFD methodology has been presented for modelling very large scale, vapour cloud explosions scenarios. The developed numerical model presented in chapter six (for modelling medium scale VCE), has been modified for large scale explosion modelling. A specific model has been considered for modelling the impact of flame-instabilities, particularly the thermal diffusive instabilities, and DL instabilities in large-scale models. The numerical model has initially been validated with the largest ever conducted indoor DDT and explosion experiments in the RUT facilities. Two different DDT scenarios: DDT by local explosions near the turbulent flame brush, and DDT by shock-focusing, have been modelled (RUT 16 and RUT 22 cases respectively). Additional to the DDT verification cases, a detonation initiation test case (RUT09) has been modelled and verified against experimental measurements. Good qualitative agreement between the numerical prediction results and experimental measurements of RUT facilities has achieved (for all DDT and detonation cases).

After demonstrating the code verification, LNG vapour cloud explosion scenarios, generated from the release of an evaporated liquefied natural gas have been studied. Two different possible incidents in LNG VCE have been studied; explosion modelling in onshore LNG plant and offshore LNG shipping. For the onshore LNG explosion study; an LNG plant has been considered to have fuel leakage from one of its storage tanks. Because of the leakage, liquid fuel spilt on the ground level, and then it evaporates. The evaporated liquid natural gas has been ignited for explosion study purposes. The LNG spill scenario has been modelled by *cascadeFoam* (Macchi, 2018), and the LNG explosion has been modelled by VCEFoam. The numerical results showed that by interacting the flame front to the buildings and obstructions, the LNG flame would accelerate. The maximum recorded overpressure in this explosion modelling is around 1.1 bar, which is far below the CJ detonation limit (CJ detonation pressure, for stoichiometric methane/air mixtures, is 16.6 bar). Therefore, in this scenario, LNG flame acceleration was not enough to cause a detonation, and only a flame deflagration has been noticed.

The second considered LNG explosion incident was an offshore LNG carrier with having 5 LNG oil tanker. Addition to this local refinement an AMR method has been carried out in the model for resolving higher resolution. The numerical results demonstrated that due to the interaction of LNG flame front to the pier pylons, the flame front is accelerating. Nevertheless, this flame acceleration is not as fast as the onshore case, whereas there was more obstruction in the plant. The maximum recorded overpressure in the offshore LNG explosion was around 0.3 bar (30000 pa), which is far from the CJ detonation pressure. Therefore, in this scenario, VCE did not happen, and only flame deflagration has been captured. The results of the present work can be used in the context of safety to assess the potential risks of explosions in the energy industry.

7.2 Outlook for future work

The computational power and time are one of the main limiting aspects of the current work. Therefore, the author recommends for future work, to include the “in situ adaptive tabulation (ISAT) method”, in the numerical model. Utilising ISAT method along with a detailed reaction mechanism can reduce the computational cost, significantly.

Moreover, in the present work, only the vertical concentration gradient in DDT has been studied. Hence, it is advisable, in future work, to consider a horizontal concentration gradient.

Additionally, it is recommended that in future modelling works, prior to running parallel a simulation, in HPC (High Performance Computing) cluster; a parallel performance benchmark test case should be run and find out the optimum number of cores for future simulations.

Also, it can be recommended to further study the effect of different reaction mechanism in ignition delay time, as well as DDT run-up distance.

References

Algell, J., Bakosch, A. and Forsman, B. (2012) *Feasibility Study on LNG Fuelled Short Sea and Coastal Shipping in the Wider Caribbean Region*. SSPA Sweden AB.

Anderson, J. D. (1990) *Modern compressible flow: with historical perspective*. McGraw-Hill New York.

Ascher, U. M., Ruuth, S. J. and Spiteri, R. J. (1997) 'Implicit-explicit Runge-Kutta methods for time-dependent partial differential equations', *Applied Numerical Mathematics*. Elsevier, 25(2–3), pp. 151–167.

Aspden, A. (2006) *Monotone Integrated Large Eddy Simulation of Buoyant Turbulent Jets with Off-Source Heating*. University of Cambridge.

Batten, P., Leschziner, M. A. and Goldberg, U. C. (1997) 'Average-state Jacobians and implicit methods for compressible viscous and turbulent flows', *Journal of computational physics*. Elsevier, 137(1), pp. 38–78.

Bauwens, C. R., Chaffee, J. and Dorofeev, S. B. (2011) 'Vented explosion overpressures from combustion of hydrogen and hydrocarbon mixtures', *International Journal of Hydrogen Energy*. Elsevier, 36(3), pp. 2329–2336.

Bauwens, C. R., Chaffee, J. L. and Dorofeev, S. (2008) 'Experimental and numerical study of methane-air deflagrations in a vented enclosure', *Fire Safety Science*, 9, pp. 1043–1054.

Berthelot, M. and Vielle, P. (1882) 'On Explosive Waves', *Comptes Rendus Hebdomadaires des Seances de l Academie des Sciences*, 94, pp. 149–152.

Bjerketvedt, D., Bakke, J. R. and van Wingerden, K. (1997) 'Gas explosion handbook', *Journal of Hazardous Materials*. Elsevier {BV}, 52(1), pp. 1–150. doi: 10.1016/s0304-3894(97)81620-2.

Boeck, L. *et al.* (2016) 'The "GraVent DDT database"', *Shock Waves*. Springer, 26(5), pp. 683–685.

Boeck, L. R. (2015) *Deflagration-to-Detonation Transition and Detonation Propagation in H2 -Air Mixtures with Transverse Concentration Gradients*. Technical University of Munich. doi: 10.4085/1062-6050-46.1.85.

Boeck, L. R. *et al.* (2016) 'Detonation propagation in hydrogen–air mixtures with transverse concentration gradients', *Shock Waves*. Springer, 26(2), pp. 181–192.

Boeck, L. R., Hasslberger, J. and Sattelmayer, T. (2014) 'Flame acceleration in hydrogen/air mixtures with concentration gradients', *Combustion Science and Technology*. Taylor & Francis, 186(10–11), pp. 1650–1661.

Boris, J. P. *et al.* (1992) 'New insights into large eddy simulation', *Fluid dynamics research*. IOP Publishing, 10(4–6), p. 199.

Borm, O., Jemcov, A. and Kau, H.-P. (2011) 'Density based Navier Stokes solver for transonic flows', in *Proceedings of 6th OpenFOAM workshop, penn state university, USA*.

Breitung, W. *et al.* (2000) *Flame acceleration and deflagration to detonation transition in nuclear safety. state-of-the-art report by a group of experts.*

Burke, E. M. *et al.* (2015) 'Progress Towards a Validated Cantera-based Turbulent Flame Speed Solver', *Seventh Eur. Combust. Meet*, pp. 1–6.

Burks, T. L. and Oran, E. S. (1981) *A Computational Study of the Chemical Kinetics of Hydrogen Combustion.* NAVAL RESEARCH LAB WASHINGTON DC.

Byron, F. W. and Fuller, R. W. (1992) 'Mathematics of Classical and Quantum Physics Dover Publications', in *Inc.*

Chan, C. K. (1995) ‘Collision of a shock wave with obstacles in a combustible mixture’, *Combustion and Flame*. Elsevier {BV}, 100(1–2), pp. 341–348. doi: 10.1016/0010-2180(94)00139-j.

Chan, C. K. and Dewit, W. A. (1996) ‘Deflagration-to-detonation transition in end gases’, *Symposium (International) on Combustion*. Elsevier {BV}, 26(2), pp. 2679–2684. doi: 10.1016/s0082-0784(96)80103-2.

Chao, J. (2006) *Critical deflagration waves that lead to the onset of detonation*. McGill University.

Chapman, D. L. (1899) ‘VI. On the rate of explosion in gases’, *The London, Edinburgh, and Dublin Philosophical Magazine and Journal of Science*. Taylor & Francis, 47(284), pp. 90–104. doi: 10.1080/14786449908621243.

Ciccarelli, G. and Boccio, J. L. (1998) ‘Detonation wave propagation through a single orifice plate in a circular tube’, *Symposium (International) on Combustion*. Elsevier {BV}, 27(2), pp. 2233–2239. doi: 10.1016/s0082-0784(98)80072-6.

Ciccarelli, G. and Dorofeev, S. (2008) ‘Flame acceleration and transition to detonation in ducts’, *Progress in energy and combustion science*. Elsevier, 34(4), pp. 499–550.

Deiterding, R. (2003) ‘Numerical structure analysis of regular hydrogen-oxygen detonations’.

Deiterding, R. (2005) ‘Detonation structure simulation with AMROC’, in *International Conference on High Performance Computing and Communications*. Springer, pp. 916–927.

Döring, W. (1943) ‘On detonation processes in gases’, *Ann. Phys*, 43(421–436), p. 9.

Dorofeev, S. *et al.* (1997) ‘Large scale hydrogen–air–steam DDT experiments in the RUT facility. Test Series 1996’, *Report RRC KI 80-05*, 16.

Dorofeev, S. B. *et al.* (1996) ‘Deflagration to detonation transition in large confined volume of lean hydrogen-air mixtures’, *Combustion and flame*. Elsevier, 104(1–2), pp. 95–110.

Dorofeev, S. B. *et al.* (2000) 'Effect of scale on the onset of detonations', *Shock Waves*. Springer Nature, 10(2), pp. 137–149. doi: 10.1007/s001930050187.

Dorofeev, S. B. *et al.* (2001) 'Evaluation of limits for effective flame acceleration in hydrogen mixtures', *Journal of Loss Prevention in the process industries*. Elsevier, 14(6), pp. 583–589.

Eckett, C. A. (2001) 'Numerical and analytical studies of the dynamics of gaseous detonations'. California Institute of Technology.

Efimenko, A. and Gavrikov, A. (2007) 'Large scale hydrogen-air detonation experiments. The effect of ignition location and hydrogen concentration on loads', *Description of HySafe SBEP V13*.

Emami, S. *et al.* (2015) 'LES of flame acceleration and DDT in hydrogen–air mixture using artificially thickened flame approach and detailed chemical kinetics', *international journal of hydrogen energy*. Elsevier, 40(23), pp. 7395–7408.

Ettner, F., Vollmer, K. G. and Sattelmayer, T. (2014) 'Numerical simulation of the deflagration-to-detonation transition in inhomogeneous mixtures', *Journal of Combustion*. Hindawi, 2014.

Explosion Dynamics Laboratory (no date) *California Institute of Technology: shock and Detonation Toolbox*. Available at: http://shepherd.caltech.edu/EDL/public/flammability.html (Accessed: 11 March 2018).

Ferziger, J. H. and Peric, M. (2012) *Computational methods for fluid dynamics*. Springer Science & Business Media.

Fickett, W. and Davis, W. C. (2000) *Detonation: theory and experiment*. Courier Corporation.

Foss, M. M. *et al.* (2003) 'LNG safety and security', *Center for Energy Economics (CEE)*.

Fraccarollo, L. and Toro, E. F. (1993) 'A Shock–Capturing Method for Two Dimensional

Dam–Break Problems', in *Proceedings of the Fifth International Symposium in Computational Fluid Dynamics, Sendai, Japan*.

Fraccarollo, L. and Toro, E. F. (1995) 'Experimental and numerical assessment of the shallow water model for two-dimensional dam-break type problems', *Journal of hydraulic research*. Taylor & Francis Group, 33(6), pp. 843–864.

Frolov, S. M. (2012) 'Acceleration of the deflagration-to-detonation transition in gases: From Shchelkin to our days', *Combustion, Explosion, and Shock Waves*. Pleiades Publishing Ltd, 48(3), pp. 258–268. doi: 10.1134/s0010508212030021.

Gaathaug, A. V. (2015) *Experimental Study of Deflagration to Detonation Transition in Hydrogen-Air Mixtures*. Telemark University College.

Gamezo, V. N., Ogawa, T. and Oran, E. S. (2007) 'Numerical simulations of flame propagation and DDT in obstructed channels filled with hydrogen-air mixture', *Proceedings of the Combustion Institute*. Elsevier {BV}, 31(2), pp. 2463–2471. doi: 10.1016/j.proci.2006.07.220.

Gavrikov, A. I., Efimenko, A. A. and Dorofeev, S. B. (2000) 'A model for detonation cell size prediction from chemical kinetics', *Combustion and Flame*. Elsevier {BV}, 120(1–2), pp. 19–33. doi: 10.1016/s0010-2180(99)00076-0.

Goodwin, D. G., Moffat, H. K. and Speth, R. L. (2009) 'Cantera: An object-oriented software toolkit for chemical kinetics, thermodynamics, and transport processes', *Caltech, Pasadena, CA*.

Greenshields, C. J. *et al.* (2010) 'Implementation of semi-discrete, non-staggered central schemes in a colocated, polyhedral, finite volume framework, for high-speed viscous flows', *International journal for numerical methods in fluids*. Wiley Online Library, 63(1), pp. 1–21.

Greenshields, C. J. (2015) 'OpenFOAM user guide', *OpenFOAM Foundation Ltd, version*, 3(1), p. 47.

Grinstein, F. F., Margolin, L. G. and Rider, W. J. (2007) *Implicit large eddy simulation: computing turbulent fluid dynamics*. Cambridge university press.

Grune, J. *et al.* (2013) 'Experimental investigation of hydrogen{\textendash}air deflagrations and detonations in semi-confined flat layers', *Journal of Loss Prevention in the Process Industries*. Elsevier {BV}, 26(2), pp. 317–323. doi: 10.1016/j.jlp.2011.09.008.

Gschaider, B. *et al.* (2013) *foam-extend*. Available at: https://sourceforge.net/projects/foam-extend/ (Accessed: 24 March 2018).

Harten, A., Lax, P. D. and van Leer, B. (1983) 'On upstream differencing and Godunov-type schemes for hyperbolic conservation laws', *SIAM review*. SIAM, 25(1), pp. 35–61.

Hasslberger, J. (2017) *Numerical Simulation of Deflagration-to-Detonation Transition on Industry Scale*. Technische Universität München.

Hasslberger, J., Boeck, L. R. and Sattelmayer, T. (2015) 'Numerical simulation of deflagration-to-detonation transition in large confined volumes', *Journal of Loss Prevention in the Process Industries*. Elsevier, 36, pp. 371–379.

Heidari, A. *et al.* (2011) 'Numerical simulation of large scale hydrogen detonation', *International Journal of Hydrogen Energy*. Elsevier, 36(3), pp. 2538–2544.

Heidari, A. (2012) *Numerical simulation of Deflagration to Detonation Transition in Hydrogen Explosion*. Kingston University London.

Hirschfelder, J. O. *et al.* (1964) *Molecular theory of gases and liquids*. Wiley New York.

Hugoniot, P. H. (1887) 'Sur la propagation du mouvement dans les corps et spécialement dans les gaz parfaits, 2e Partie', *Journal de l'École Polytechnique. Paris*, 57, pp. 3–97.

Issa, R. I. (1986) 'Solution of the implicitly discretised fluid flow equations by operator-splitting', *Journal of computational physics*. Elsevier, 62(1), pp. 40–65.

Jouguet, E. (1905) 'On the propagation of chemical reactions in gases', *J. de mathematiques*

Pures et Appliquees, 1(347–425), p. 2.

Kee, R., Coltrin, M. and Glarborg, P. (2003) 'Chemically Reacting Flow: Theory & Practice'. New Jersey: John Wiley and Sons.

Khodadadi Azadboni, R. *et al.* (2016a) 'Numerical simulation of flame acceleration and transition from deflagration to detonation using OpenFOAM', in *The 11th OpenFOAM® Workshop*. Guimaraes, Portugal, pp. 357–372. doi: 10.1007/978-3-319-60846-4_26.

Khodadadi Azadboni, R. *et al.* (2016b) 'Numerical simulation of flame acceleration and transition from deflagration to detonation using OpenFOAM', in. Guimaraes.

Khodadadi Azadboni, R. *et al.* (2017) 'Numerical modeling of deflagration to detonation transition in inhomogeneous hydrogen/air mixtures', *Journal of Loss Prevention in the Process Industries*. Elsevier, 49, pp. 722–730. doi: 10.1016/J.JLP.2017.04.024.

Khodadadi Azadboni, R. *et al.* (2019) 'The effect of concentration gradients on deflagration-to-detonation transition in a rectangular channel with and without obstructions – A numerical study', *International Journal of Hydrogen Energy*. Pergamon, 44(13), pp. 7032–7040. doi: 10.1016/j.ijhydene.2019.01.157.

Khodadadi Azadboni, R., Heidari, A. and Wen, J. X. (2017a) 'Numerical modelling of flame acceleration and transition to detonation in hydrogen/air mixtures with concentration gradient', in *International Conference on Hydrogen Safety-ICHS2017*. Hamburg (Germany): International Association for Hydrogen Safety "HySafe", p. 163. Available at: https://hysafe.info/wp-content/uploads/2017_papers/163.pdf (Accessed: 14 March 2019).

Khodadadi Azadboni, R., Heidari, A. and Wen, J. X. (2017b) 'Numerical modelling of flame acceleration and transition to detonation in hydrogen/air mixtures with concentration gradient', in *INTERNATIONAL CONFERENCE ON HYDROGEN SAFETY*. Hamburg: HySafe. Available at: https://hysafe.info/ichs2017/.

Khodadadi Azadboni, R., Heidari, A. and Wen, J. X. (2018) 'A Computational Fluid Dynamic Investigation of Inhomogeneous Hydrogen Flame Acceleration and Transition to

Detonation', *Flow, Turbulence and Combustion*, 101(4), pp. 1009–1021. doi: 10.1007/s10494-018-9977-4.

Khodadadi Azadboni, R., Wen, J. X. and Heidari, A. (2019) 'Numerical Modeling of Flame Acceleration and Transition from Deflagration to Detonation Using OpenFOAM®', in *OpenFOAM®*. Cham: Springer International Publishing, pp. 357–372. doi: 10.1007/978-3-319-60846-4_26.

Khodadadi Azdaboni, R., Malekbala, M. R. and Azadboni, F. K. (2013) 'Evaluate shock capturing capability with the numerical methods in openfoam', *Thermal Science*, 17(4), pp. 1255–1260. doi: 10.1007/s10784-015-9298-1.

Khokhlov, A. M. *et al.* (1999) 'Interaction of a shock with a sinusoidally perturbed flame', *Combustion and flame*. Elsevier, 117(1–2), pp. 99–116.

Khokhlov, A. M., Oran, E. S. and Thomas, G. O. (1999) 'Numerical simulation of deflagration-to-detonation transition: the role of shock–flame interactions in turbulent flames', *Combustion and Flame*. Elsevier, 117(1–2), pp. 323–339.

Kirillov, I. A. *et al.* (2005) 'Sensitivity to detonation and detonation cellular structure of H 2-O 2-air-H 2 O 2 gas mixtures', in *First International Conference on Hydrogen Safety, Pisa, Italy*, pp. 8–10.

Kotchourko, A. (2007) *safety of hydrogen as an Energy carrier*. Available at: http://www.hysafe.org/documents?kwd=SBEP.

Kristoffersen, K. (2004) *Gas explosions in process pipes*. Telemark University College. Available at: http://hdl.handle.net/11250/2437791 (Accessed: 13 March 2018).

Kumar, P. P. *et al.* (2015) 'Numerical comparison of hydrogen-air reaction mechanisms for unsteady shock-induced combustion applications', *Journal of Mechanical Science and Technology*, 29(3), pp. 893–898. doi: 10.1007/s12206-015-0202-2.

Kurganov, A., Noelle, S. and Petrova, G. (2001) 'Semidiscrete central-upwind schemes for

hyperbolic conservation laws and Hamilton--Jacobi equations', *SIAM Journal on Scientific Computing*. SIAM, 23(3), pp. 707–740.

Kurganov, A. and Tadmor, E. (2000) 'New high-resolution central schemes for nonlinear conservation laws and convection–diffusion equations', *Journal of Computational Physics*. Elsevier, 160(1), pp. 241–282.

Kuznetsov, M. *et al.* (2005) 'DDT in a smooth tube filled with a hydrogen–oxygen mixture', *Shock Waves*. Springer, 14(3), pp. 205–215.

Kuznetsov, M. *et al.* (2011) 'Hydrogen–air deflagrations and detonations in a semi-confined flat layer', in *Proceedings of the Sixth International Seminar on Fire & Explosion Hazards (FEH6)*. doi: 10.3850/978-981-08-7724-8 02-05.

Kuznetsov, M. S. *et al.* (1998) 'Detonation propagation, decay, and reinitiation in nonuniform gaseous mixtures', in *Symposium (International) on Combustion*. Elsevier, pp. 2241–2247.

Kuznetsov, M. S., Alekseev, V. I. and Dorofeev, S. B. (2000) 'Comparison of critical conditions for {DDT} in regular and irregular cellular detonation systems', *Shock Waves*. Springer Nature, 10(3), pp. 217–223. doi: 10.1007/s001930050009.

Landau, L. D. (1944) 'On the theory of slow combustion', *Acta Physicochim (USSR)*, 19, pp. 77–85.

Law, C. K. (2010) *Combustion physics*. Cambridge university press.

Lee, J. H., Knystautas, R. and Chan, C. K. (1985) 'Turbulent flame propagation in obstacle-filled tubes', *Symposium (International) on Combustion*. Elsevier {BV}, 20(1), pp. 1663–1672. doi: 10.1016/s0082-0784(85)80662-7.

Lee, J. H. S. (1977) 'Initiation of Gaseous Detonation', *Annual Review of Physical Chemistry*. Annual Reviews 4139 El Camino Way, P.O. Box 10139, Palo Alto, CA 94303-0139, USA , 28(1), pp. 75–104. doi: 10.1146/annurev.pc.28.100177.000451.

Lee, J. H. S. (2008) *The detonation phenomenon*.

Van Leer, B. (1974) ‘Towards the ultimate conservative difference scheme. II. Monotonicity and conservation combined in a second-order scheme’, *Journal of computational physics*. Elsevier, 14(4), pp. 361–370.

Lefebvre, M. H. and Oran, E. S. (1995) ‘Analysis of the shock structures in a regular detonation’, *Shock Waves*. Springer, 4(5), pp. 277–283.

Lefebvre, M. H., Weber, J. W. and Oran, E. S. (1997) ‘Numerical Simulations of a Marginal Detonation: Wave Velocities and Transverse Wave Structure’, in *IUTAM Symposium on Combustion in Supersonic Flows*. Springer, pp. 347–358.

Lindstedt, R. P. and Michels, H. J. (1989) ‘Deflagration to detonation transitions and strong deflagrations in alkane and alkene air mixtures’, *Combustion and Flame*. Elsevier {BV}, 76(2), pp. 169–181. doi: 10.1016/0010-2180(89)90065-5.

Macchi, M. (2018) *LNG/Fuel cascades and flammable cloud formation*, *Kingston University London*. Kingston University London.

Mahmoudi, Y., Mazaheri, K. and Parvar, S. (2013) ‘Hydrodynamic instabilities and transverse waves in propagation mechanism of gaseous detonations’, *Acta Astronautica*. Elsevier, 91, pp. 263–282.

Mallard, E. and Le Chatelier, H. (1881) ‘On the propagation velocity of inflammation in gaseous explosive mixtures’, *Compt. Rend. Acad. Sci. Paris, France*, 93, p. 145.

Marcantoni, L. F. G., Tamagno, J. and Elaskar, S. (2017) ‘Two-dimensional numerical simulations of detonation cellular structures in H2O2Ar mixtures with OpenFOAM®’, *International Journal of Hydrogen Energy*. Elsevier, 42(41), pp. 26102–26113.

Marinov, N. M., Westbrook, C. K. and Pitz, W. J. (1996) ‘DETAILED AND GLOBAL CHEMICAL KINETICS MODEL FOR’, *Transport phenomena in combustion*, 1, p. 118.

Mazaheri, K., Mahmoudi, Y. and Radulescu, M. I. (2012) ‘Diffusion and hydrodynamic instabilities in gaseous detonations’, *Combustion and Flame*. Elsevier, 159(6), pp. 2138–

2154.

McCartney, D. (2002) ‘Gas Conditioning for Imported LNG’, in *82nd Annual Convention Gas Processors Association*.

Meyer, J. W., Urtiew, P. A. and Oppenheim, A. K. (1970) ‘On the inadequacy of gasdynamic processes for triggering the transition to detonation’, *Combustion and Flame*. Elsevier {BV}, 14(1), pp. 13–20. doi: 10.1016/s0010-2180(70)80005-0.

Moen, I. and Lee, J. H. (1980) ‘The mechanism of transition from deflagration to detonation in vapor cloud explosion’, *Progress in Energy and Combustion Sciences*, 6, pp. 359–389.

Mokhatab, S. *et al.* (2014) ‘Handbook of Liquefied Natural Gas’, in *Handbook of Liquefied Natural Gas*. Elsevier. doi: 10.1016/B978-0-12-404585-9.05001-7.

Mokhatab, S. *et al.* (2015) *Handbook of liquefied natural gas*. Elsevier.

Moukalled, F., Mangani, L. and Darwish, M. (2016) *The Finite Volume Method in Computational Fluid Dynamics*. doi: 10.1007/978-3-319-16874-6.

Muppala, S. P. R. *et al.* (2005) ‘Development of an algebraic reaction rate closure for the numerical calculation of turbulent premixed methane, ethylene, and propane/air flames for pressures up to 1.0 MPa’, *Combustion and Flame*. Elsevier, 140(4), pp. 257–266.

Muppala, S. P. R. *et al.* (2009) ‘Experimental and analytical investigation of the turbulent burning velocity of two-component fuel mixtures of hydrogen, methane and propane’, *international journal of hydrogen energy*. Elsevier, 34(22), pp. 9258–9265.

Von Neumann, J. (1942) ‘THERORY OF DETONATION WAVES1’.

Nogueira, X. *et al.* (2010) ‘Implicit large eddy simulation of non-wall-bounded turbulent flows based on the multiscale properties of a high-order finite volume method’, *Computer Methods in Applied Mechanics and Engineering*. Elsevier, 199(9–12), pp. 615–624.

Ó Conaire, M. *et al.* (2004) ‘A comprehensive modeling study of hydrogen oxidation’,

International journal of chemical kinetics. Wiley Online Library, 36(11), pp. 603–622.

Ogawa, T., Oran, E. S. and Gamezo, V. N. (2013) 'Numerical study on flame acceleration and DDT in an inclined array of cylinders using an AMR technique', *Computers & Fluids*. Elsevier, 85, pp. 63–70.

Ohnishi, S. *et al.* (no date) *STUDY ON THE BEHAVIOR OF AN LNG TANK FOUNDATION UNDER THE ULTIMATE LIMIT STATE USING A DEMOLISHED TANK*. Available at: https://www.gti.energy/wp-content/uploads/2018/12/Storage-7-Shunsuke_Ohnishi-LNG17-Poster.pdf (Accessed: 11 March 2019).

OpenFOAM Ltd (2015). Available at: https://openfoam.org/ (Accessed: 18 March 2015).

Oran, E. S. *et al.* (1981) 'Numerical simulations of detonations in hydrogen-air and methane-air mixtures', in *Symposium (International) on Combustion*. Elsevier, pp. 1641–1649.

Oran, E. S. *et al.* (1998) 'A numerical study of a two-dimensional H2-O2-Ar detonation using a detailed chemical reaction model', *Combustion and Flame*. Elsevier, 113(1–2), pp. 147–163.

Oran, E. S. and Boris, J. P. (1993) 'Computing turbulent shear flows—a convenient conspiracy', *Computers in Physics*. AIP, 7(5), pp. 523–533.

Patankar, S. (1980) *Numerical heat transfer and fluid flow*. CRC press.

Peraldi, O., Knystautas, R. and Lee, J. H. (1988) 'Criteria for transition to detonation in tubes', *Symposium (International) on Combustion*. Elsevier {BV}, 21(1), pp. 1629–1637. doi: 10.1016/s0082-0784(88)80396-5.

Poinsot, T. and Veynante, D. (2005) *Theoretical and numerical combustion*. RT Edwards, Inc.

Pollock, N. and Johnson, M. (2018) *Review of Vapour Cloud Explosion and BLEVE Risk*. Available at: www.dnvgl.com.

Radulescu, M. I. *et al.* (2005) ‘The ignition mechanism in irregular structure gaseous detonations’, *Proceedings of the Combustion Institute*. Elsevier, 30(2), pp. 1859–1867.

Rankine, W. J. . (1870) ‘{XV}. On the thermodynamic theory of waves of finite longitudinal disturbance’, *Philosophical Transactions of the Royal Society of London*. The Royal Society, 160, pp. 277–288. doi: 10.1098/rstl.1870.0015.

Reynolds, W. C. (1986) ‘The element potential method for chemical equilibrium analysis: implementation in the interactive program STANJAN’, *Technical Rept.* Dept. of Mechanical Engineering, Stanford Univ.

Sagaut, P. (2006) *Large eddy simulation for incompressible flows: an introduction*. Springer Science & Business Media.

Sharpe, G. J. (2001) ‘Transverse waves in numerical simulations of cellular detonations’, *Journal of Fluid Mechanics*. Cambridge University Press, 447, pp. 31–51.

Shchelkin, K. (1947) ‘Occurrence of detonation in gases in roughwalled tubes’, *Soviet Journal of Technical Physics*, 17.

Shepherd, J. E. (2009) ‘Detonation in gases’, *Proceedings of the Combustion Institute*. Elsevier, 32(1), pp. 83–98.

Sherman, M. P., Tieszen, S. R. and Benedick, W. B. (1989) *FLAME facility: The effect of obstacles and transverse venting on flame acceleration and transition on detonation for hydrogen-air mixtures at large scale*. Nuclear Regulatory Commission.

Smith, G. P. *et al.* (2000) ‘GRI-Mech 3.0’, *URL http://www. me. berkeley. edu/gri_mech*.

Smooke, M. D. (1991) *Reduced kinetic mechanisms and asymptotic approximations for methane-air flames: a topical volume*. Springer.

Sod, G. A. (1978) ‘A survey of several finite difference methods for systems of nonlinear hyperbolic conservation laws’, *Journal of Computational Physics*. Elsevier {BV}, 27(1), pp. 1–31. doi: 10.1016/0021-9991(78)90023-2.

Soloukhin, R. I. (1961) 'Deflagration to detonation transition in gases', *Soviet Prikladn Mech i Techn Phys (Appl Mech Tech Phys)*, 4, p. 128.

Speight, J. G. (2007) *Natural gas : a basic handbook*. Gulf Pub. Co.

Stamps, D. W., Benedick, W. B. and Tieszen, S. R. (1991) *Hydrogen-air-diluent detonation study for nuclear reactor safety analyses*. Nuclear Regulatory Commission, Washington, DC (USA). Div. of Systems ….

Tabor, G. and Weller, H. G. (2004) 'Large eddy simulation of premixed turbulent combustion using Ξ flame surface wrinkling model', *Flow, Turbulence and Combustion*. Springer, 72(1), pp. 1–27.

Teodorczyk, A. (2008) 'Scale effects on hydrogen{\textendash}air fast deflagrations and detonations in small obstructed channels', *Journal of Loss Prevention in the Process Industries*. Elsevier {BV}, 21(2), pp. 147–153. doi: 10.1016/j.jlp.2007.06.017.

Teodorczyk, A., Lee, J. H. S. and Knystautas, R. (1989) 'Propagation mechanism of quasi-detonations', *Symposium (International) on Combustion*. Elsevier {BV}, 22(1), pp. 1723–1731. doi: 10.1016/s0082-0784(89)80185-7.

Teodorczyk, A., Lee, J. H. S. and Knystautas, R. (1991) 'The structure of fast turbulent flames in very rough, obstacle-filled channels', *Symposium (International) on Combustion*. Elsevier {BV}, 23(1), pp. 735–741. doi: 10.1016/s0082-0784(06)80324-3.

Thomas, G. (2012) 'Some observations on the initiation and onset of detonation', *Philosophical Transactions of the Royal Society A: Mathematical, Physical and Engineering Sciences*. The Royal Society, 370(1960), pp. 715–739. doi: 10.1098/rsta.2011.0368.

Thomas, G., Bambrey, R. and Brown, C. (2001) 'Experimental observations of flame acceleration and transition to detonation following shock-flame interaction', *Combustion Theory and Modelling*. Taylor & Francis, 5(4), pp. 573–594. doi: 10.1088/1364-7830/5/4/304.

Toro, E. F. (2009a) *Riemann Solvers and Numerical Methods for Fluid Dynamics*. Berlin, Heidelberg: Springer Berlin Heidelberg. doi: 10.1007/b79761.

Toro, E. F. (2009b) 'The HLL and HLLC Riemann Solvers', in *Riemann Solvers and Numerical Methods for Fluid Dynamics*. Berlin, Heidelberg: Springer Berlin Heidelberg, pp. 315–344. doi: 10.1007/b79761_10.

Toro, E. F. (2013) *Riemann solvers and numerical methods for fluid dynamics: a practical introduction*. Springer Science & Business Media.

Toro, E. F. and Chakraborty, A. (1994) 'The development of a Riemann solver for the steady supersonic Euler equations', *The Aeronautical Journal*. Cambridge University Press, 98(979), pp. 325–339.

Toro, E. F., Spruce, M. and Speares, W. (1994) 'Restoration of the contact surface in the HLL-Riemann solver', *Shock waves*. Springer, 4(1), pp. 25–34.

Urtiew, P. and Oppenheim, A. (1966) 'Experimental observations of the transition to detonation in an explosive gas', *Proceedings of the Royal Society of London. Series A. Mathematical and Physical Sciences*. The Royal Society, 295(1440), pp. 13–28. doi: 10.1098/rspa.1966.0223.

Vågsæther, K. (2010) *Modelling of gas explosions*. Telemark University College – NTNU.

Vendra, C. M. R. and Wen, J. X. (2018) 'Numerical modelling of vented lean hydrogen deflagations in an ISO container', *International Journal of Hydrogen Energy*. Elsevier.

Versteeg, H. K. and Malalasekera, W. (2007) *An introduction to computational fluid dynamics: the finite volume method*. Pearson education.

Vollmer, K. G., Ettner, F. and Sattelmayer, T. (2012) 'Deflagration-to-detonation transition in hydrogen/air mixtures with a concentration gradient', *Combustion Science and Technology*. Taylor & Francis, 184(10–11), pp. 1903–1915.

Wang, C. *et al.* (2018) 'Influence of chemical kinetics on detonation initiating by temperature

gradients in methane/air', *Combustion and Flame*. Elsevier, 197, pp. 400–415.

Weller, H. G. (1993) 'The development of a new flame area combustion model using conditional averaging', *Thermo-fluids section report TF*. Citeseer, 9307.

Weller, H. G. *et al.* (1998) 'Application of a flame-wrinkling LES combustion model to a turbulent mixing layer', in *Symposium (International) on Combustion*. Elsevier, pp. 899–907.

Wen, J. X., Madhav Rao, V. C. and Tam, V. H. Y. (2010) 'Numerical study of hydrogen explosions in a refuelling environment and in a model storage room', *International Journal of Hydrogen Energy*, 35(1), pp. 385–394. doi: 10.1016/j.ijhydene.2009.10.052.

White, F. M. and Corfield, I. (2006) *Viscous fluid flow*. McGraw-Hill New York.

Wilke, C. R. (1950) 'Diffusional properties of multicomponent gases', *Chem. Eng. Progress*, 46, pp. 95–104.

Woodward, J. L. and Pitblado, R. M. (2010) *LNG Risk Based Safety*, *LNG Risk Based Safety*. John Wiley & Sons, Inc. doi: 10.1002/9780470590232.

Xiao, H., Houim, R. W. and Oran, E. S. (2015) 'Formation and evolution of distorted tulip flames', *Combustion and Flame*. Elsevier, 162(11), pp. 4084–4101.

Yáñez, J. *et al.* (2011) 'A comparison exercise on the CFD detonation simulation in large-scale confined volumes', *international journal of hydrogen energy*. Elsevier, 36(3), pp. 2613–2619.

Yu, S. (2015) 'Large Eddy Simulation of Deflagration to Detonation Transition using Artificial Thickening', *PhD Thesis*, pp. 1–6.

Zeldovich, Y. B. (1950) 'On the theory of the propagation of detonation in gaseous systems'.

Appendix A List of publications from this research

In this section, the list of publications from this research is provided.

A.1 Journal Papers:

1. **R. Khodadadi Azadboni**, A. Heidari, L.R. Boeck, & J.X. Wen, "the effect of concentration gradients on deflagration-to-detonation transition in a rectangular channel with and without obstructions - A numerical study", International Journal of Hydrogen Energy, vol: 44 (13) pp: 7032-7040, 2019. https://doi.org/10.1016/j.ijhydene.2019.01.157

2. **R. Khodadadi Azadboni**, A. Heidari, J.X. Wen, "A Computational Fluid Dynamic Investigation of Inhomogeneous Hydrogen Flame Acceleration and Transition to Detonation", Journal of Flow Turbulence and Combustion, vol: 101 (4) pp: 1009-1021, 2018. https://doi.org/10.1007/s10494-018-9977-4

3. **R. Khodadadi Azadboni**, J.X. Wen, A. Heidari & C.J. Wang, "Numerical Modelling of Deflagration to Detonation Transition in Inhomogeneous Hydrogen/Air Mixtures", Journal of Loss Prevention in the Process Industries – Elsevier, vol: 49 pp: 722-730, 2017. http://dx.doi.org/10.1016/j.jlp.2017.04.024

A.2 Book Chapter:

- **R. Khodadadi Azadboni**, J.X. Wen, A. Heidari, 2017, "Numerical modeling of flame acceleration and transition from deflagration to detonation using OpenFOAM". In J. Miguel Nóbrega, Hrvoje Jasak eds., "OpenFOAM®: Selected papers of the 11th

Workshop", Springer. ISBN: 9783319608457, pp. 357–372. doi: 10.1007/978-3-319-60846-4_26.

- https://link.springer.com/chapter/10.1007%2F978-3-319-60846-4_26

A.3 Conference presentations:

1. **R. Khodadadi Azadboni**, A. Heidari, & J.X. Wen, "Numerical Analysis of Flame Acceleration and Onset of Detonation in Homogenous and Inhomogeneous Mixture", The 27th International Colloquium on the Dynamics of Explosions and Reactive Systems (ICDERS), Beijing, China, 28 July – 2 August 2019.

2. **R. Khodadadi Azadboni**, J.X. Wen, A. Heidari, & L.R. Boeck, "Numerical Study of Deflagration-to-Detonation Transition in Homogenous and Inhomogeneous Hydrogen-Air Mixtures", The 26th ICDERS, Boston, USA, 30 July – 4 August 2017.

3. **R. Khodadadi Azadboni**, A. Heidari, J.X. Wen, "CFD Analysis of Deflagration to Detonation Transition in Homogenous and Inhomogeneous Hydrogen-Air Mixtures", Conference of UK Turbulent Reacting Flows Consortium (UKCTRF) in Southampton, UK, 2017. **(First prize has been awarded)**.

4. **R. Khodadadi Azadboni**, J.X. Wen & A. Heidari "A Computational Fluid Dynamic Investigation Of Inhomogeneous Hydrogen Flame Acceleration And Transition To Detonation", 10th Mediterranean Combustion Symposium (10^{th} MCS), Naples, Italy, September 17-21, 2017. (**Awarded as a selected paper).**

5. **R. Khodadadi Azadboni**, A. Heidari, J.X. Wen, "Predicting LNG Vapour Cloud Explosions", The 92^{nd}'s FABIG Technical Meeting: New Developments for Design Against Cryogenic Releases, Aberdeen and London, UK, 27 & 28 September 2017.

6. **R. Khodadadi Azadboni**, J.X. Wen & A. Heidari "Numerical Modelling Of Flame Acceleration And Transition To Detonation In Hydrogen/Air Mixtures With Concentration Gradient", International Conference On Hydrogen Safety (ICHS 2017), September, 11-13 2017 - Hamburg (Germany). (**Awarded as a selected paper**).

7. **R. Khodadadi Azadboni**, J.X. Wen, A. Heidari, S.P.R. Muppala & C.J. Wang, "Numerical investigation of Hydrodynamic instability in deflagration to detonation transition in inhomogeneous mixture", The 36th International Symposium on Combustion, 4P132, Seoul, Korea | July 31 – August 5, 2016.

8. **R. Khodadadi Azadboni**, J.X. Wen, A. Heidari & C.J. Wang, "Numerical Modelling of Deflagration to Detonation Transition in Inhomogeneous Hydrogen/Air Mixtures", 11th

International Symposium on Hazards, Prevention, and Mitigation of Industrial Explosion (ISHPMIE) in Dalian, China, 2016. (**Awarded as a selected paper**).

9. **R. Khodadadi Azadboni**, J.X. Wen, A. Heidari, S.P.R. Muppala & C.J. Wang, "Numerical Simulation Of Flame Acceleration And Transition From Deflagration To Detonation Using OpenFOAM", The 11th OpenFOAM Conference in -Portugal, 2016.
10. **R. Khodadadi Azadboni**, J.X. Wen, A. Heidari, S.P.R. Muppala & C.J. Wang, "CFD Modelling Of Non-Uniform Hydrogen Flame Propagating Across Obstacles And Inducing Detonation", Conference of UK Turbulent Reacting Flows Consortium (UKCTRF) in Durham, 2016.